Ultrafine grained nickel processed by powder metallurgy : microstructure, mechanical properties and thermal stability

Lucia Garcia de La Cruz

Normandie Université

THÈSE

Pour obtenir le diplôme de doctorat

Spécialité PHYSIQUE

Préparée au sein de l'Université de Caen Normandie

Ultrafine grained nickel processed by powder metallurgy : microstructure, mechanical properties and thermal stability

Présentée et soutenue par
Lucia GARCIA DE LA CRUZ

Thèse soutenue publiquement le 14/10/2019 devant le jury composé de		
M. GUY DIRRAS	Professeur des universités, Université Paris 13 Paris-Nord	Rapporteur du jury
M. CLAUDE ESTOURNES	Directeur de recherche au CNRS, Université Toulouse 3 Paul Sabatier	Rapporteur du jury
M. YANNICK CHAMPION	Directeur de recherche, INP - ENSE3 à Grenoble	Président du jury
Mme ANNE-LAURE HELBERT	Maître de conférences HDR, Université Paris 11 Paris-Sud	Membre du jury
M. CLEMENT KELLER	Maître de conférences, INSA de Rouen Normandie	Membre du jury
Mme MAYERLING MARTINEZ CELIS	Maître de conférences, Université Caen Normandie	Membre du jury
M. ERIC HUG	Professeur des universités, Université Caen Normandie	Directeur de thèse

Thèse dirigée par ERIC HUG, Laboratoire de cristallographie et sciences des materiaux (Caen)

UNIVERSITÉ CAEN NORMANDIE

ED 591 PSIME

RISMA

"*Few things in nature seem more inanimate than a piece of metal. The casual observer sees only his own reflection in its bright, still surface and nothing of its world within. This internal world is, however, a place of ceaseless activity. Electrons dash from end to end at immense speeds, atoms move and exchange places* […]".

Sir Alan Cottrell
"An Introduction to Metallurgy"

ACKNOWLEDGEMENTS

The work in the present manuscript was performed at the CRISMAT laboratory in Caen, thus thanks must be given first, to the director, Wilfrid Prellier. Je tiens ensuite à remercier les membres du jury, d'abord à Claude Estournes et Guy Dirras, les rapporteurs. Merci d'avoir lu ma thèse avec intérêt, pour les rapports sur mon manuscrit, pleins des bons remarques et critiques qui m'aident à avoir une meilleure vue de l'ensemble de mes travaux, ainsi que pour les questions et remarques lors de ma soutenance. Ensuite à Yannick Champion, président du jury, pour ses commentaires très enrichissantes qui donne envie de continuer à apprendre sur la déformation plastique des métaux. Anne-Laure Helbert pour ses commentaires très intéressantes sur le traitement de données EBSD. Clément Keller, gracias por tus preguntas un tanto particulares, pero sobre todo gracias por tu ojo crítico sobre mi trabajo y por ayudar a mejorarlo. A mi querida Mayerling Martinez, por tus palabras el día de mi defensa, que plasmaron el arduo camino de una tesis, con el añadido de hacerla en el extranjero, y que hicieron llorar a más de uno. Gracias por enseñarme a utilizar un Jeol 2010, por miles de respuestas, por discusiones científicas y personales (dentro y fuera del laboratorio), así como por tu sonrisa y buen humor. Je tiens maintenant à remercier à Éric Hug, mon directeur de thèse, pour avoir vu une chercheuse en moi lors de mon Erasmus, où je voyais juste de la curiosité. Merci de m'avoir laissé suivre les thématiques que je trouvais plus intéressantes, pour les voyages scientifiques (Saint Etienne, Dublin et Nancy) et le séjour en Allemagne, ainsi que pour les cours à Caligny qui m'ont permis d'apprendre énormément.

Je vais continuer par remercier le personnel du CRISMAT et CNRT qui m'ont aidé d'une manière ou autre ces dernières années. L'équipe de microscopie, Xavier, Muriel et Richard. Pour leur aide concernant la préparation des échantillons pour observation ainsi que l'utilisation des microscopes MEB et MET. Egalement à Bernadette Domenges, pour les heures passées au Dual-Beam, et les images et vidéos qui m'ont permis de mieux comprendre les résultats obtenues dans les études de diffusion. Merci aussi pour les mesures effectuées chez Presto Engineering, sans ton aide, le Chapitre V de ce manuscrit n'aurait pas été possible. Je remercie aussi les personnes du premier étage du CNRT pour leur aide et bonne humeur, les deux Christelle, Sylvain, les deux Christophe et d'une manière très spécial à Jérôme, pour répondre à mes mil questions, pour être gentil quand j'arrivais avec un moule SPS cassé et pour son sourire constante. Egalement à Guillaume Riquet avec qui j'ai survécu un master et une thèse, merci de m'avoir écouté quand j'étais malheureuse et d'avoir fêté avec moi quand j'étais contente. Un grand merci à Marion Jore pour me faciliter toujours la vie, concernant la plus grande problématique en France… l'administration. Je veux remercier aussi le côté CRISMAT, car sans Sophie Dufourd et Laurence Hervé je n'aurai pas eu une partie importante de mes résultats. Je passe maintenant aux métallurgistes…merci à Maxime pour son innocence, à Cendrine pour être toujours prêt à répondre à mes questions et me donner des solutions, à Brice pour ses offres de café et sa joie contagieuse, à Florent

Moisy qui m'a beaucoup aidé à réfléchir sur l'observation des dislocations au MET et à Florent Picot, qui m'a beaucoup manqué cette dernière année mais qui me fait toujours rire et qui m'aide sans souci avec les problèmes Igor/Word/Powerpoint. Merci Florent pour les aventures vécues à Saint Etienne et Dublin, estás como una cabra ! Un remerciement appart mérite Antoine Gueydan, car grâce à lui l'exécution et interprétation des essais mécaniques a été possible, merci beaucoup pour ton aide expérimental ainsi que théorique, pour chercher du temps pour m'aider à chaque fois que j'avais besoin de quelque chose, pour nos discussions sur le frittage, la mécanique, la diffusion, l'enseignement… MUCHAS GRACIAS. Et finalement mes petites Pauline et Julie. Merci Pauline de m'avoir accompagné, on s'est aidé, on a travaillé ensemble et on a réussi ! (C'est incroyable mais on a écrit nos manuscrits et on est encore vivantes) Je te félicite pour ta thèse et je te souhaite que des bonnes choses pour la suite. Ma chère Julie, j'ai commencé à te connaître un peu mieux lors de la journée de l'école doctoral 2018 et encore plus lors de notre participation à « La Métallurgie Quel Avenir ! » Merci d'avoir aidé avec tout (en particulier pour tes corrections de français), pour écouter avec intérêt mes réflexions scientifiques au lieu de m'ignorer (ça aurait été complètement justifié) et encore plus pour tes questions ! Aussi simples que compliqués elles m'ont obligé à mettre par terre ce que je croyais savoir et recommencer de zéro avec un nouveau regard. Bonne courage pour ta dernière année de thèse ! Merci aux personnes qui n'était pas au laboratoire pendent les trois ans de thèse mais ont aussi contribué à ces travaux : Isabel, Pierre Antoine, Gwendoline, Margaux, Gaël, Mélanie, Jean Baptiste, Cédric, Etienne… et toute personne que j'ai pu oublier.

Before moving to the acknowledgement of people who have helped me stay sane these years, thanks are due to some scientific figures who I was lucky enough to meet along the way and are an example to follow. Gerhard Wilde and Sergiy Divinski. I only met Gerhard Wilde on one occasion in his office, but his general view of metallurgy and how in five minutes of conversation he understood my PhD subject and was able to give me some very good ideas of experiments to perform, blew me away. Thank you for giving me the opportunity to work in the Institute of Materials Physics in Münster. Sergiy Divinski, it was an honor working with you and your team, your knowledge on solid-state diffusion is inspiring. Thank you so much for taking time of your busy schedule to answer any questions I had and for helping me with anything I needed. I also want to acknowledge the people that helped me during my stay in Münster, Daniel, Josua, Stefan, Manoel, Friederike, Lishai, Rajeshwari…thank you so much! Finally, my role models, strong, brilliant, scientific women. Gracias Ángela Molina y Maite Chicote por vuestro apoyo, por contagiarme vuestra pasión por aprender y por ser un ejemplo a seguir tanto en el trato personal, como en vuestra manera de comunicar la ciencia y hacer investigación.

Finalmente quiero agradecer a todas las personas que me han acompañado en este camino, a veces complicado y a los que me han apoyado siempre, incluyendo esos momentos de debilidad en los cuales no me sentía capaz de terminar lo que con tanto entusiasmo había empezado. Merci à Thomas Paulmier,

Michel et Agnès d'avoir été ma famille normande. Pour votre aide, votre support, des repas, des verres, des soirées jeux de société… bref, MERCI BEAUCOUP. Gracias también a Almu-Chan por horas de video-llamadas, por no olvidarse de mí y estar siempre disponible para pasar tiempo conmigo cuando venía a Cartagena. A Patricia por su apoyo incondicional y por hacer el esfuerzo de venir a verme hasta en tres ocasiones a tierras normandas, incluyendo mi defensa de tesis. Fue muy especial para mí y te deseo lo mejor para terminar tu tesis doctoral. Un apoyo importante estos tres años han sido mis abuelos, Juanjo y Mari Nieves, con los cuales he intercambiado correos electrónicos con mis aventuras y desventuras. El mirar mi vida a través de sus ojos me ayudó en los momentos más difíciles a no olvidar lo afortunada que soy. Igualmente, mis abuelos Antonio y Mari Carmen, la fragilidad de mi abuelo y la fuerza de mi abuela, siempre tan ilusionados de recibir una llamada o una visita, me motivan a ir hacia delante y vivir la vida al máximo. De mis tíos (los adoro a todos), destacar a los que siempre han estado pendientes de esta aventura, Pili y Gonzalo, gracias por venir a visitarme a Münster y por mostrar tanto interés por mi trabajo. También, gracias a mi tía Maki por venir desde tan lejos para estar conmigo en la defensa de mi tesis dándome su cariño y su apoyo. Agradecer con todo mi cariño a mis suegros Felipe y María Luisa por estar siempre pendientes de nosotros, por sus visitas, las maletas cargadas de comida y de tuppers, y por acogerme como a una más de la familia desde el principio. Agradecer a mis hermanos su cariño y apoyo. A Fernando por estar siempre libre para hablar o incluso venir en mi ayuda hasta Alemania cuando estaba sola. A mi hermana Marta, que a pesar de los kilómetros que nos separan y la diferencia de hora, ha conseguido estar siempre a mi lado. A mi hermana Cristina, por las llamadas de wasap los sábados por la mañana junto con mi bebé Martín que me ayudaron a sobrellevar este último año, el más complicado de todos. Finalmente, gracias a mis padres, por todo. Su amor y apoyo incondicional, combinado con independencia y autonomía han hecho de mi la persona fuerte (aunque a veces flaquee) y autosuficiente que soy hoy. Gracias al trabajo duro pudieron proporcionarme, no solo una educación que ha culminado en la realización de una tesis doctoral, si no unas vivencias únicas en distintos lugares de España y del mundo que me han motivado a no temer a lo desconocido y embarcarme en aventuras como estos años en Francia. Sois un ejemplo para mí.

Para terminar, tengo que darle las gracias de todo corazón a mi compañero de viaje, Felipe. Hace nueve años comenzamos juntos este largo camino desde unas clases de química general en Murcia hasta una tesis doctoral. Sin tu ayuda a lo largo de estos años, no hubiera llegado ni a la mitad. Gracias por aguantarme, por levantarme cuando caigo y por confiar en mis capacidades cuando yo estoy segura de que no seré capaz de seguir. Espero seguir recorriendo el mundo contigo y aprendiendo de tu mano.

Table of contents

LIST OF ABBREVIATIONS AND SYMBOLS

BM	Ball milling	HV	Vickers hardness
CCD	Charge coupled device	IQ	Image quality
CG	Coarse grained	KAM	Kernel average misorientation
CI	Confidence index	LAGB	Low angle grain boundary
CSL	Coincidence site lattice	LEDS	Low-energy dislocation structures
DCAP	Dynamic channel angular pressing	LSC	Liquid scintillation counter
DIC	Digital image correlation	NsM	Nanostructured materials
EBSD	Electron backscatter diffraction	PCA	Process control agent
ECAP	Equal channel angular pressing	PM	Powder metallurgy
ED	Electrodeposition	PVD	Physical vapor deposition
FCC	Face centered cubic	SADP	Selected area diffraction pattern
FG	Fine grain	SEM	Scanning electron microscopy
FIB	Focused ion beam	SPD	Severe plastic deformation
GAM	Grain average misorientation	SPS	Spark plasma sintering
GBCD	Grain boundary character distribution	TEM	Transmission electron microscopy
GND	Geometrically necessary dislocations	TB	Twin boundary
GOS	Grain orientation spread	UFG	Ultrafine grained
HAB	High angle boundary	UTS	Ultimate tensile strength
HCP	Hexagonal close packed	WD	Working distance
HIP	Hot isostatic pressing	XRD	X-ray diffraction
HP	Hall-Petch		
HPT	High pressure torsion		

A	Weight of the sample in air	Δg_A	Kernel average misorientation
A_0	Pre-exponential factor	Δg_{Ax}	Kernel misorientation
A_d	Constant	E_a	Activation enthalpy
A_g	Geometrical factor	e_{ikl}	Permutation tensor
α_d	Parameter of dislocation interaction and configuration	ε	True strain
α_{ij}	Nye dislocation tensor	ε_f	Elongation to failure
B	Weight of the sample in EtOH	ε_u	Uniform elongation
b	Norm of the Burgers vector	F	Load
$\vec{b}$	Burgers vector	$\vec{F}$	Force
B_d	Constant	$\bar{g}$	Average orientation of a grain
β_d	Parameter that relates Λ and l_d	$\vec{\mathrm{g}}$	Diffraction vector
$\bar{c}$	Concentration of tracer	g^A	Orientation of a pixel
γ	Grain boundary energy per unit area	$g_{ij,k}$	Spatial gradient of orientation
γ_0	Constant	h	Thickness
γ_s	Shear strain	h_i	Initial thickness
d	Grain size	H_{c2}	Upper critical magnetic field
d_0	Constant	θ	Misorientation angle
d_c	Dislocation cell size	θ_h	Work hardening rate
D_d	Dislocation diffusion coefficient	i	Electric current
D_{gb}	Grain boundary diffusion coefficient	I_{hkl}	Intensity of the (hkl) peak
D_{gb}^{rel}	Self-diffusion coefficient for relaxed grain boundaries	J_c	Critical current density
D_s	Surface diffusion coefficient	k	Boltzmann constant
D_v	Lattice diffusion coefficient	k_g	Factor dependent of grain morphology
δ	Grain boundary width	k_{HP}	HP constant

K_H	Hollomon strain hardening coefficient	S	Seebeck coefficient
l_d	Average distance between dislocations	σ	True stress
λ	Angle between slip plane and tensile axis	σ_0	Friction stress
λ_c	Thermal conductivity	σ_y	Yield strength
Λ	Average distance traveled by a dislocation	t	Time
M (T)	Magnetization	T	Temperature
M_T	Taylor's factor	T_c	Critical temperature
μ	Shear modulus	T_m	Melting temperature
n	Normal direction to the grain boundary plane	τ	Critical shear
N	Total number of pixels in a grain	τ_c	Critical resolved shear stress
n_H	Hollomon strain hardening exponent	τ_{rel}	Relaxation time
$\vec{\xi}$	Line direction	φ	Angle between ⊥ to slip plane and tensile axis
o	Rotation axis	y	Depth
p	Twin boundary density	y_a	Dislocation annihilation distance
p_0	Constant	Ω	Atomic volume
P_d	Probability of dislocation annihilation	z	Line direction
R	The gas constant		
ρ	Density		
ρ_0	Density of auxiliary liquid		
ρ_d	Total density of dislocations		
ρ_L	Air density		
ρ_r	Electrical resistivity		
ρ_w	Dislocation density in the hard phase		

INTRODUCTION

Modern metallurgy is in need of new processing methods to improve the properties of well-known materials. For instance, strengthening by grain refinement allows for lighter structures with equivalent mechanical strength. Ultrafine grained (UFG) metals ($d < 1$ μm) fulfill the requirement of improved strength, however, other properties such as ductility or thermal stability deteriorate. A broad literature concerning UFG materials as well as nanostructured materials is available but it includes contradictions concerning their intrinsic properties. The processing method has a great impact on the final characteristics of specimens and complete studies on mechanical and physical properties measured on the same samples are lacking.

The synthesis of bulk UFG metals is mainly achieved by either Severe Plastic Deformation (SPD) or Powder Metallurgy (PM). SPD consists on severely deforming metallic specimens by applying high stress in order to overcome the energy necessary to refine the microstructure into very small grains. Powder metallurgy uses temperatures below the melting temperature to activate solid-state diffusion for consolidation of nanosized or nanostructured powders into nearly completely dense specimens. SPD techniques are more popular than powder metallurgy for the synthesis of UFG samples, as they enable the synthesis of specimens with a refined microstructure of 150-300 nm without additional contamination. Nevertheless, the refinement of grain size by severe deformation results in a metastable microstructure with elevated internal stresses. From a practical point of view, another drawback of SPD is the lack of homogeneity as well as the limited size and geometry of the specimens that limits their use. PM is adequate for producing bulk homogeneous UFG metals with low residual stresses. To this aim, fast sintering techniques provided of simultaneous pressing and heating of the powders are used. Spark Plasma Sintering (SPS) is a good option as its high heating rate reduces sintering time, limiting grain growth. With this technique, at a laboratory scale, cylinders with diameters of 10 - 80 mm can be processed with homogeneous characteristics throughout the volume of the samples. Scaling up to fulfill industrial needs is feasible as it consists on adjusting the amount of powder to the piece in construction. In fact, the first commercial products processed by these means are already in the market [1]. Recently [2], a patent for SPS dies for complex geometries was developed meaning that no forming after synthesis would be needed, which makes this technique even more attractive.

In fact, powder metallurgy is a steady developing industry, which is highly used in different domains such as aerospace electronics, nuclear energy industry, technologies for medical or dental use and specially in the automobile industry [3–5]. The main reasons to choose PM over other processing methods is the combination of the three qualities represented in Fig. I-1.

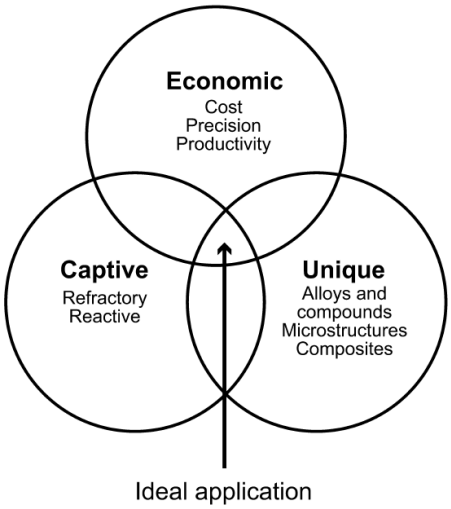

Fig. I-1 Venn diagram of the attributes sought when choosing a processing technique. Powder metallurgy techniques correspond to the intersection of the three circles [6].

The different PM processes enable the production of exclusive materials that are difficult or impossible to manufacture by other methods such as tungsten carbide, as well as unique alloys and microstructures [7–9]. Also, the PM market is very competitive as the manufacturing processes are material and energy efficient compared to other metal forming technologies such as casting, forging and screw machining (Fig. I-2). Moreover, the PM techniques are considered as green technologies as ~80 wt.% of the raw material used for manufacturing comes from recycled scrap[1]. The depletion of natural resources, energy and material wise, imposes the development of more efficient production techniques, making PM techniques very appealing.

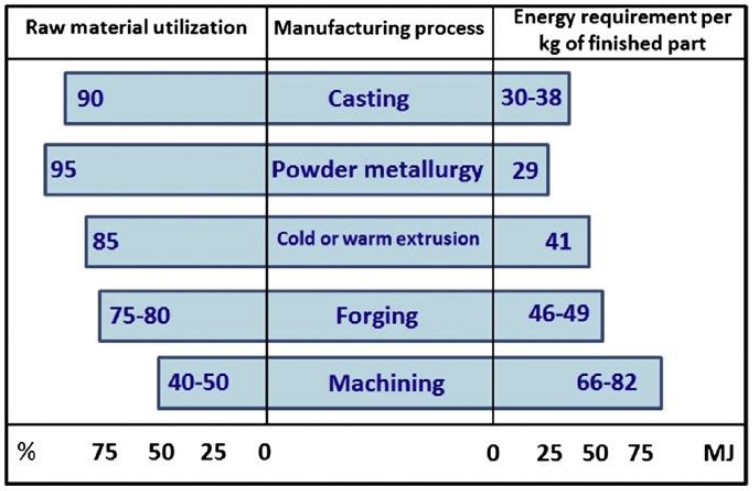

Fig. I-2 Comparison of raw material and energy consumption depending on the manufacturing process [10].

[1] « Vision 2025 Future Developments for the European PM Industry » The European PM Industry Roadmap, January 2015.

The properties of the pieces manufactured by PM can be adjusted by choosing the appropriate material and process, w the required microstructure [6]. A wide range of engineering materials can be processed to produce highly complex forms that require little or no machining afterwards (Fig. I-3). The conventional procedure is still highly used, which consists on pressing a mixture of metal powder and lubricant in a die to form the so-called green compact, heating it afterwards to produce the metallic piece. Nevertheless, for the last two decades, other PM techniques have been developed to adjust to new needs. Such techniques include metal injection molding, hot isostatic pressing and additive manufacturing.

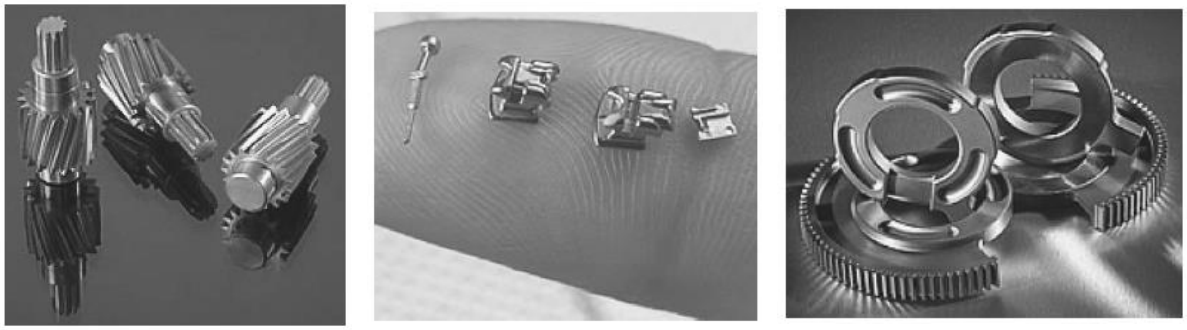

(a) (b) (c)

Fig. I-3 Pieces displaying complex forms manufactured by PM. Helical gear and spur pinion (a). Orthodontic system bracket, slide and hook (b). Sector gear and fixed rings (c) [6].

This brief introduction to the PM industry shows the interest on further studying the properties of materials processed by these means. Moreover, the combination of the benefits of PM with the strengthening of UFG microstructures seems highly promising and frames the context of the present study.

UFG samples can be produced by PM using nanopowders or nanostructured powders. Previous works have focused on the use of nanopowders, which unfortunately exhibit an important amount of oxides. Nevertheless, the use of nanostructured powders obtained by ball milling (BM) enables the synthesis of samples of oxide free refined microstructure under certain conditions. To date, a complete study of the possibilities of coupling BM and SPS for UFG processing is lacking. The purpose of this study is to investigate UFG nickel, from the synthesis of the powder and densification by SPS, to the mechanical and physical properties of samples with different grain sizes. Choosing nickel as a well-known model material enables the comparison of the results collected in this study with a large body of literature and sets the bases for future studies performed on more complex materials.

First, specimens with grain sizes in the UFG domain were processed from different precursor powders. To this aim, BM parameters were modified to produce diverse powders from the as-received commercial powder. The powders were afterwards consolidated by SPS, which was chosen as sintering

technique for the short processing time and good density results. Careful characterization of the sintered microstructures was performed by electron backscatter diffraction analyses, highlighting grain size, grain boundary character distribution and relative misorientations. Furthermore, relative internal stresses are discussed by means of grain orientation spread as well as from the identification of dislocation structures by transmission electron microscopy for selected samples.

Then, uniaxial tensile testing was performed for samples of different grain sizes to characterize the following mechanical properties: yield stress, ultimate tensile strength (UTS), uniform deformation and deformation to failure. In addition, the strain-hardening mechanisms were investigated for a better understanding of the effect of refining the microstructure to the UFG range on plastic deformation. The deformed microstructure at fracture for selected samples was studied to enlighten strain-hardening discussions as well as to investigate the presence of specific dislocation structures in the deformed state.

Finally, the behavior of microstructures under thermal energy (heat) was studied in two ranges. On the one hand, at low temperature (400 K), grain boundary diffusion was investigated by means of radiotracer experiments to examine high diffusivity paths. On the other hand, at high temperature (up to 1123 K), the stability of the microstructure as well as retrograde sintering of samples processed from BM powders was studied. The conclusion of this manuscript will combine the different results obtained in this study providing a general overview of the synthesis/microstructure/properties relation of UFG samples processed by PM.

CHAPTER I. STATE OF THE ART ON NANOSTRUCTURED AND UFG METALS

1. Definition and context

Metals with microstructures that display a grain size (d) in the (100-1000 nm) range are known as UltraFine Grain (UFG) materials. Situated between conventional coarse-grained polycrystalline metals ($d > 10$ µm) and nanostructured materials (NsM) ($d < 100$ nm), UFG metals present remarkable physical, chemical and mechanical properties. In the last 60 years, the development of the modern defect theory as well as the advance of technology has enabled the physical explanation of these properties, especially with high-resolution methods such as transmission electron microscopy. A review article published by H. Gleiter in 1992 [11] gives an overview of the promising possibilities of both NsM and UFG. In his multiple papers [12–14] he describes the peculiarities of NsM which he describes as disordered solids with a high density of defects (Fig. I-1).

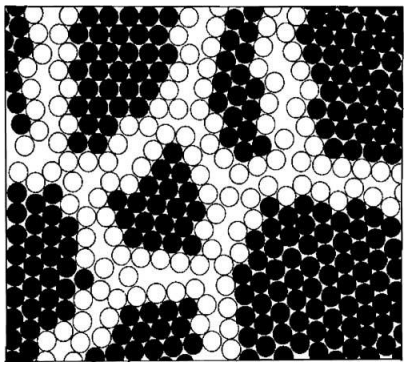

Fig. I-1 NsM in 2D with circles representing the atoms of the structure. Filled circles represent atoms in the bulk of the crystals and open circles atoms situated in grain boundary regions [12].

Most functional and mechanical properties are controlled or largely influenced by vacancies, dislocations, and grain or phase boundaries. Thus, a large volume fraction of these defects entails new physical mechanisms that modify the macroscopic behavior of materials. Bulk UFG materials can be obtained by two main processes, severe plastic deformation (SPD) or powder metallurgy. Investigations on the former are more numerous and started with the pioneer work of Bridgman in 1935 [15] where the effect of applying high shearing stress combined with high hydrostatic pressure on pure metals was investigated. Bridgman was awarded with the Nobel Prize in Physics on 1946 for “the invention of an apparatus to produce extremely high pressures and for the discoveries he made therewith in the field of high-pressure physics”. His work sets the bases for the development of High Pressure Torsion (HPT) in the former Soviet Union, where in the 1980’s V.M. Segal and his colleagues contributed immensely to

the development of the SPD techniques [16]. In fact, UFG metals had been used for centuries, starting in China around 500 B.C. [17], but the scientific approach of associating a refined microstructure with the specific properties displayed by these materials arrived in the late 1980's with the works of R.Z. Valiev [18–20]. From this moment on, thousands of investigations have been carried out focusing on these techniques, and are still today in full development.

Powder metallurgy itself has a long history as well, many objects of ancient civilizations used the principles of sintering to fabricate metallic pieces specially from metals and alloys with high melting points such as iron, steel or later on, platinum [3]. It had been called "the lost art" [21] as it practically disappeared in Europe for centuries to be reborn in the 18th century. The production of UFG metals from nanopowders and nanostructured powders started in the 1990's. Unlike the SPD techniques, research concerning UFG metals processed by powder metallurgy are less abundant in in literature.

2. Processing methods

The processing technique chosen to produce UFG/NsM materials highly influences the obtained microstructure. Thus, a classification of such materials attending to their processing technique is regularly used. A general approach is to differentiate between "top-down" and "bottom-up" techniques. In the case of "top-down" techniques microstructure refinement is achieved by severe plastic deformation by structural disintegration of the coarse grained microstructure [22]. HPT, equal channel angular pressing (ECAP) and mechanical milling are included in this category. The bottom-up approach consists on starting from elemental blocks (atoms, molecules, clusters) and use them to build up the structures like in powder metallurgy, electrodeposition or physical vapor deposition. A qualitative introduction of these techniques is necessary to acknowledge their effect on the processed UFG specimens.

2.1. *Severe Plastic Deformation*

Microstructure refinement by SPD is achieved in consecutive stages of plastic deformation usually represented by multiples passes through the experimental set-up. Different models are proposed to discuss the physical mechanisms that lead to the formation of the UFG microstructures. These include dislocation density based models as well as more exotic models such as grain subdivision from lattice curvature development or dynamic plastic deformation. An outlook of these models is summarized by Y. Estrin *et al.* in [23]. For dislocation cell-forming materials (such as nickel), dislocation density based models are the most commonly accepted. Dislocation cell structures are considered to become the final grain structures, from increasing misorientation between neighboring cells. In a first stage, dislocation

cells become low angle grain boundaries (LAGBs), evolving to high angle grain boundaries (HABs) at higher strain levels.

There exists numerous SPD techniques, a good overview of these technologies can be found elsewhere [23], but in this section only HPT, ECAP and BM are shortly described.

HPT

The high pressure torsion method consists on applying a high pressure on a disc-like sample of reduced dimensions (typically 10 mm in diameter and 1 mm in thickness), followed by the application of torsional straining from rotation of the die (Fig. I-2).

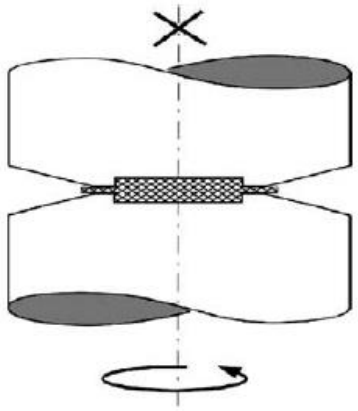

Fig. I-2 Schematic illustration of HPT processing set-up [24].

Despite the limited dimensions of the specimens, HPT is very attractive to researches as it enables processing of microstructures with equiaxed grains of smaller size than other SPD techniques as well as a higher fraction of HAB [25]. The most important advantage of HPT and SPD techniques in general, is the controlled contamination and porosity. In addition to reduced dimensions, the main disadvantage of HPT is a controversial lack of radial homogeneity [24–27]. This is still under discussion as some authors claim that a reasonable level of homogeneity can be ensured provided the applied pressure is high enough and a sufficient number of passes is performed [28,29].

ECAP

Equal channel angular pressing is, together with HPT, the most studied SPD technique. In this method, a sample is pressed through a die containing two channels, intersecting at an angle φ that is generally close to 90° (Fig. I-3 (a)). Both channels are equal in cross-section and the sample, in the form of rod or bar, is machined to fit within the die. When the sample passes through the channel and is forced around the sharp corner, an elevated level of shear strain is induced. Both, the channel angle between the two channels (φ) and the angle that defines the outer arc of curvature between them (Ψ) affect the

imposed strain. Despite the intense strain, the specimen emerges from the die with the initial cross-sectional dimensions (Fig. I-3 (b)), which is a characteristic feature of ECAP versus other metalworking methods such as rolling or drawing. Higher strain levels can be attained by repetitively pressing the same specimen through the set-up. Moreover, by rotating the sample, different slip systems can be activated on consecutive passes [30].

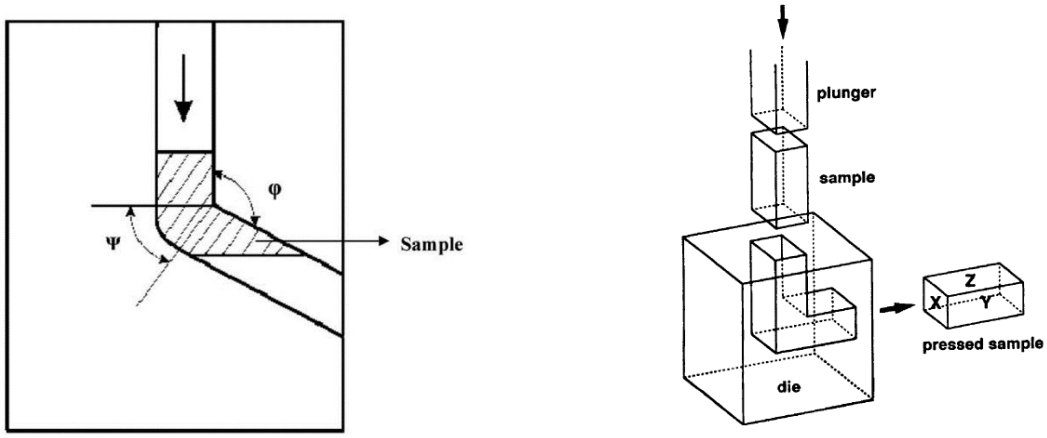

(a) (b)

Fig. I-3 Illustration of the section of an ECAP die, where Ψ and φ are the two internal angles (a). Authors [22], highlight the sheared part of the sample in the front end shape. Schematic representation of an ECAP facility [31] (b). The arrow in both illustrations indicates the direction of the pressure applied to the sample.

The characteristic microstructure of ECAP processed samples present grains bigger in size than in HPT processed samples, an elongated morphology and crystallographic texture [32,33]. On the other hand, this technique is less limited in dimensions as bigger specimens can be processed. Hardness measurements across the surface of ECAP samples, show slight differences between the center and the edge of the specimens [34,35], suggesting microstructural heterogeneities.

Mechanical milling

Mechanical milling as nanostructuring technique consists on the repeated cyclic deformation of powders by high-energy forces created from collisions of the milling medium (balls in the case of ball milling (BM) (Fig. I-4 (a)) with the powder. The response to these forces is different depending on the nature of the precursor powder, brittle or ductile (Fig. I-4 (b)). In ductile materials (Fig. I-4 (c)) particles deform and change in morphology, from spheres to pancake shape and finally to flake shape particles. As described in [21], once cold welding of particles is achieved, microforging begins followed by a closed repeating loop of fracture, microforging and agglomeration until the desired result is accomplished. Once the process is completed, the resulting powder exhibits a different morphology and particle size, as well as high defect density and refined crystallite size. These changes are highly dependent on milling parameters.

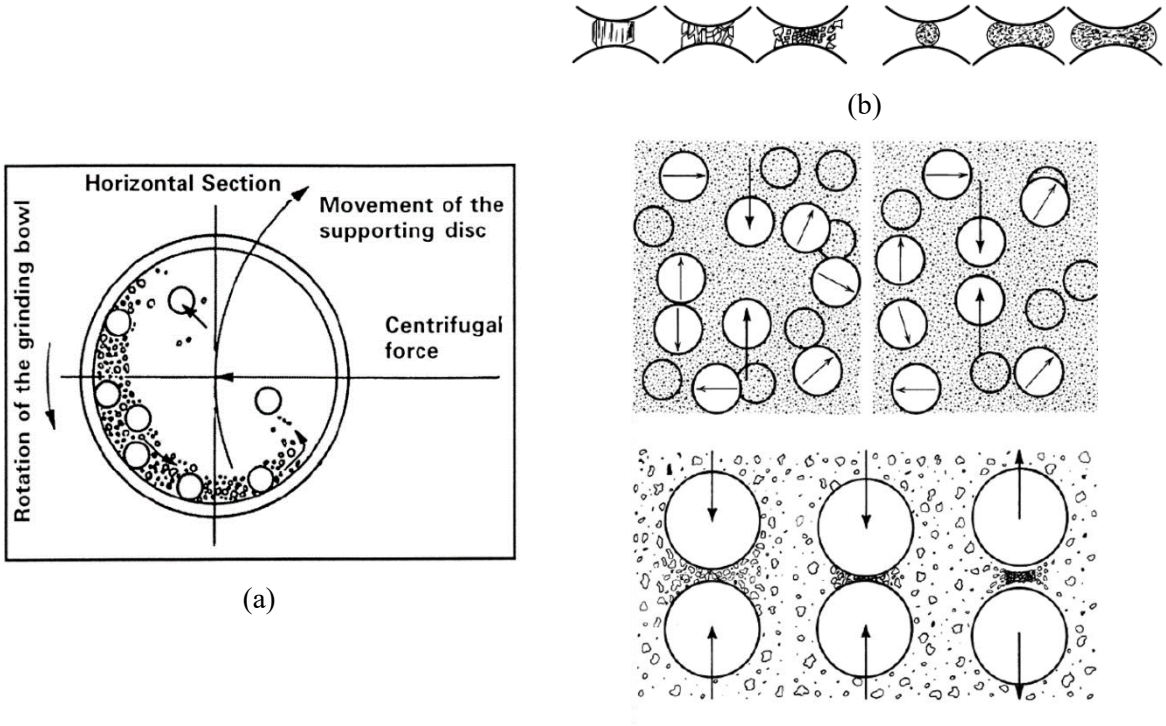

Fig. I-4 Schematic representation of the BM process [36] (a). Response of a brittle material particle (left) and a ductile particle (right) to the compressive force between two balls (b) [21]. Stages of the milling process from the randomly agitated charge of balls and powder (upper illustration) to compaction and welding of powder particles (lower illustration) [21].

From a historic point of view, BM was developed together with mechanical alloying. John Benjamin and his co-workers at the International Nickel Company in the late 1960's [37] were the first to promote its use for the production of complex oxide dispersion-strengthened alloys. The increasing interest for this method in the following decades expanded the comprehension of the mechanisms involved in powder synthesis by BM. This lead to the employment of this technique for nanostructuration as well as other means such as solid state amorphization. As an example, in the 1990's BM of a Ni powder was performed, which exhibited grain sizes below 100 nm and very high elastic strains measured by X-ray diffraction (XRD) [20,38].

Unlike the previously described techniques, the essential characteristic of BM is the production of powdered materials that must be consolidated afterwards. In addition, all classes of materials (including brittle compounds) are adaptable to this method, which can be easily scaled up for the production of significant quantities of material [39]. As a counterpart, a higher level of contamination is encountered from the additives used to reduce cold-welding, oxidation or the wear of the milling media. This drawback can be hindered by cautiously choosing the appropriate milling parameters.

2.2. *Powder Metallurgy*

Powder metallurgy (PM) represents the second group of bulk UFG processing methods and belongs to the bottom-up techniques. These synthesis methods have been overlooked for this purpose as oxides are formed in the surface of nanopowders preventing proper sintering, which results in more brittle materials [40,41]. Nevertheless, the use of deformed nanostructured powders obtained by mechanical milling can produce oxide free specimens under certain conditions.

Sintering of powders occurs by solid-state diffusion when heat is applied to a body containing pores. The reduction in the surface area associated to the existing porosities is the driving force in this process. In addition, restoration, recrystallization and grain growth take place during sintering to minimize the free energy of the system. Using powder metallurgy to synthesize UFG metals can be challenging as finding the proper sintering parameters is crucial for good densification, and grain growth has to be limited as much as possible. The most used sintering techniques for consolidation of nanosized or nanostructured powders are hot isostatic pressing and spark plasma sintering. The combination of pressure and heating makes them ideal to produce bulk samples in a short time, limiting grain growth.

Hot Isostatic Pressing (HIP)

The HIP method consists on consolidating a powdered material by the application of high temperature and isostatic pressure simultaneously. In this process, the isostatic pressure arises from molecules or atoms of gas that collide with the surface of the piece. At every point, the pressure is the same and it is applied in a direction normal to the surface making densification very homogeneous. The pressure medium is an inert gas, usually high purity Ar. For the synthesis of UFG metals, nanopowders are placed in an envelope made of metal or glass that will shrink with the powder during sintering to yield a densified final product with the wanted geometry and dimension (Fig. I-5).

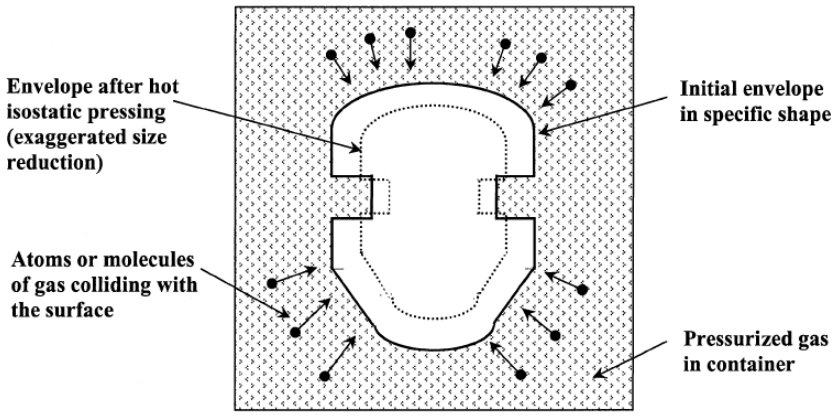

Fig. I-5 Schematic illustration of the HIP process, the reduction of the shape placed in the encapsulating envelope is exhibited [42].

Temperatures used in HIP processing are usually higher than 0.7 T_m (melting temperature) to lower yield strength and increase diffusivity for pore closure [42]. The main advantages of this method is high density [43] and uniformity in the processed specimens, which arise from the homogeneously applied pressure. However, a higher average sintering temperature than SPS sintering has to be employed producing samples with bigger grain sizes [41].

Spark Plasma Sintering (SPS)

Spark plasma sintering is one of the techniques known as pulsed electric current sintering, which are characterized by the use of an electric current as heat supplier. As for HIP processing, continuous pressing assists the sintering process in SPS. The advantages of SPS sintering include lower sintering temperature, shorter holding time, fast heating rates and improved kinetics of densification [44,45]. The special characteristics of the SPS method are believed to be achieved by the heat generation mechanisms induced by the electric current [46] (rather than conventional heat supply as for HIP) and the rapid bonding between particles that results from the applied pressure [47]. E. Olevsky *et al*. [48] suggest that mass transport by electromigration might be the explanation for the faster diffusion observed in pulsed electric current sintering. In addition, fast heating rates allow for bypassing the non-densifying mechanisms that occur at lower temperature.

Although SPS processing can produce metallic as well as ceramics and composite specimens, the sintering mechanisms (Fig. I-6) during synthesis will differ depending on the material. Z. Trzaska *et al.* [49] studied the kinetics and microscopic mechanisms of densification of an annealed Ni powder by SPS. The authors proposed a densification mechanism dependent on the plastic deformation of the regions close to the contact point between particles. Essentially, a high dislocation density develops from the compressive forces covering ¼ of the radius of the particles and diffusion in dislocations by dislocation climb represents the rate-controlling mechanisms for densification. In addition, stress relaxation is believed to occur by restoration alone, without recrystallization.

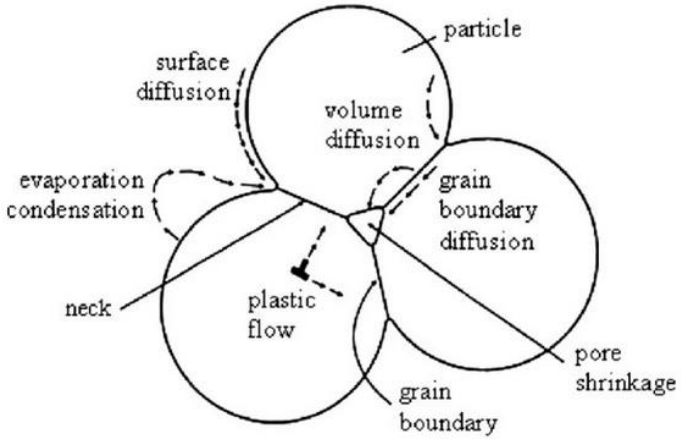

Fig. I-6 Mass transport mechanisms available during sintering [50].

Homogeneous, disc-like UFG samples can be easily obtained by SPS sintering up to a diameter of 50 mm-80 mm. Several parameters (pressure, temperature, time, pulsed or continuos current, etc.) can be modified to attain different microstructures [51–56]. The main disadvantages of this technique are the same as for HIP, residual porosity, higher contamination levels than SPD and bigger minimum grain size.

2.3. *Nanostructuration of thin films*

Finally, the bottom-up techniques used to produce thin films are presented as they enable the synthesis of UFG/NsM metals down to the smallest grain size possible, several nanometers. Although not used in the synthesis of samples in the present work, literature concerning UFG nickel samples prepared by these techniques is contemplated for discussion thus, a brief introduction is necessary. The main techniques used to produce nanostructured and UFG thin films are electrodeposition (ED) and physical vapor deposition (PVD).

ED consists on growing a film on a substrate by electrical pulses that force the deposition of cations as crystalline and amorphous patches (Fig. I-7). This technique has the potential of processing samples with grain sizes as small as 20 nm in a variety of sizes and shapes, and enables the synthesis of porosity free samples with a thickness up to a few mm when the appropriate conditions are used [57]. The disadvantages of this technique includes contamination from the additives used for the synthesis, as well as preferred crystallographic orientation, variable residual and internal stresses, a lack of homogeneity of the microstructure and low thermal stability [58–61].

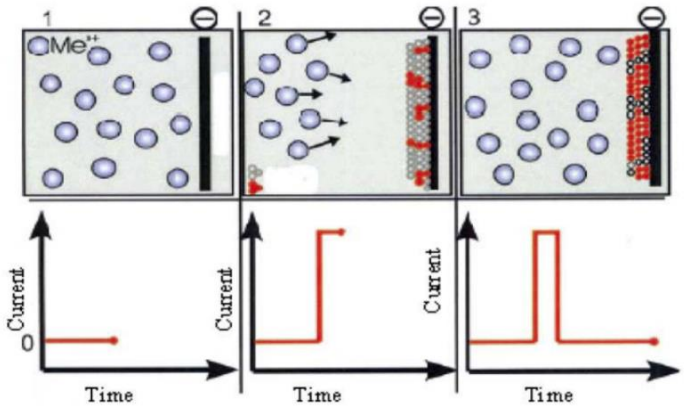

Fig. I-7 Schematic representation of the ED process at three different times as a function of electrical current [22].

PVD techniques involve the generation of vapor phase species via evaporation, sputtering, laser ablation or ion beam, and consequent deposition on a substrate. Advantages and disadvantages are mostly the same as ED, although contamination is highly reduced in PVD techniques. Interestingly, a particularity of PVD prepared Ni is abnormal grain growth [62,63].

3. Properties of UFG metals

3.1. *Macroscopic properties of UFG metals*

The aim of processing NsM/UFG metals and alloys is obtaining specimens that exhibit unique macroscopic properties. A growing body of literature has examined such properties, including some review articles such as the one by M. A. Meyers *et al.* [22] from 2006. In this section, a summary of the mechanical properties of UFG/NsM metals is presented, for samples obtained with different processing techniques. Additionally, some macroscopic functional properties will be briefly introduced for a global outlook of the possibilities of UFG metals.

Mechanical properties in UFG/NsM metals

One of the main issues of UFG/NsM metals is that they display in general, lower ductility than their coarse grain counterparts [64]. However, high ductility has also been reported for UFG copper and nickel [65–69]. The ductility of a specimen is measured as the elongation to failure in standard tensile testing [70] and is considered as low when it represents less than 5 % elongation to failure [68]. The contradictions found in literature result, partially, from the use of nonstandard tensile specimens, as the size and geometry of the samples notably affects the measurement. Y.T. Zhu *et al.* [71] have written a paper on this purpose, concluding that for a better comparison, uniform elongation should be used as it is less affected by the dimensions of the sample. In such case, the beginning of necking will determine the ductility of the sample. The onset of necking, for a constant strain rate ($\dot{\varepsilon}$), is given by the Considère criterion [72]:

$$\left(\frac{\partial\sigma}{\partial\varepsilon}\right)_{\dot{\varepsilon}} \leq \sigma \tag{1.1}$$

where $\left(\frac{\partial\sigma}{\partial\varepsilon}\right)$ is the strain hardening rate (θ_h) and σ the flow stress. From this criterion, it follows that ductility and strain hardening are highly related. Thus, a possible cause for low ductility in UFG/NsM metals is a reduced hardening rate when grain size is refined. In such cases the crossing point of the hardening rate with the increasing flow stress would appears sooner, triggering necking [73,74]. The hardening rate highly depends on the ability of the specimens to accumulate dislocations, organized in different structures, which act as obstacles to dislocation glide. In the UFG regime, the mean free path of dislocations is limited by the grain boundaries, and dislocation storage is lessened by dynamic recovery and annihilation of dislocations at grain boundaries, leading to a decrease in the hardening rate [75,76]. In fact, a reduced or inexistent strain hardening in UFG metals has been reported in compression testing for FCC metals such as copper, body centered cubic (BCC) metals such as iron Fe [22] and

hexagonal close packed metals (HCP) such as Titanium [77]. For a further discussion concerning strain hardening in UFG/NsM metals, refer to Chapter IV of this manuscript.

In addition to the strain hardening hypothesis concerning the low ductility of UFG/NsM metals, M.A. Meyers *et al.* [22] propose three other possible sources: processing artifacts (such as pores), tensile instability and crack nucleation due to shear instability. The decrease in ductility is more acute in NsM than in UFG metals. Fig. I-8 (a), displays the yield strength of NsM normalized by the yield strength of conventional grain size samples, showing a very strong reduction of elongation to failure in most cases. In the case of UFG metals, Fig. I-8 (b) shows that a good compromise can be found for some metals such as copper or titanium.

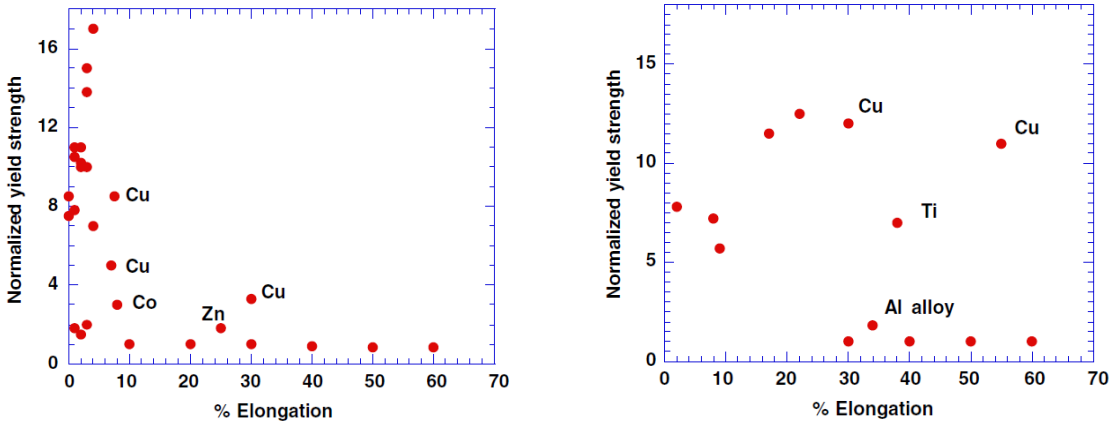

Fig. I-8 Comparison of normalized yield strength against elongation to failure for nanocrystalline metals (a) and UFG metals (b) [22].

In the cases where enhanced ductility was reported, the authors propose several mechanisms. For instance, “non-equilibrium” grain boundaries, present in SPD processed samples, provide a large number of dislocations available for slip. A high density of dislocations and an elevated excess volume characterizes such boundaries, which enable grain rotation at room temperature contributing to improving strain hardening [78]. Also, material-dependent features such as the presence of twin boundaries will contribute to higher ductility [22,79,80].

An example of the evolution of the tensile mechanical properties for samples in the UFG range with different grain size can be depicted in Fig. I-9 for commercially pure Al (Fig. I-9 (a)) and for Ti-added ultra-low carbon IF (interstitial-free) steel (Fig. I-9 (b)) [81]. An increasing elongation to fracture can be depicted with increasing grain size as well an evolution in the aspect of the curves, in both materials. When the grain size is reduced below a critical value, inhomogeneous yielding characterized by a yield drop occurs followed by necking soon after yielding (Fig. I-9).

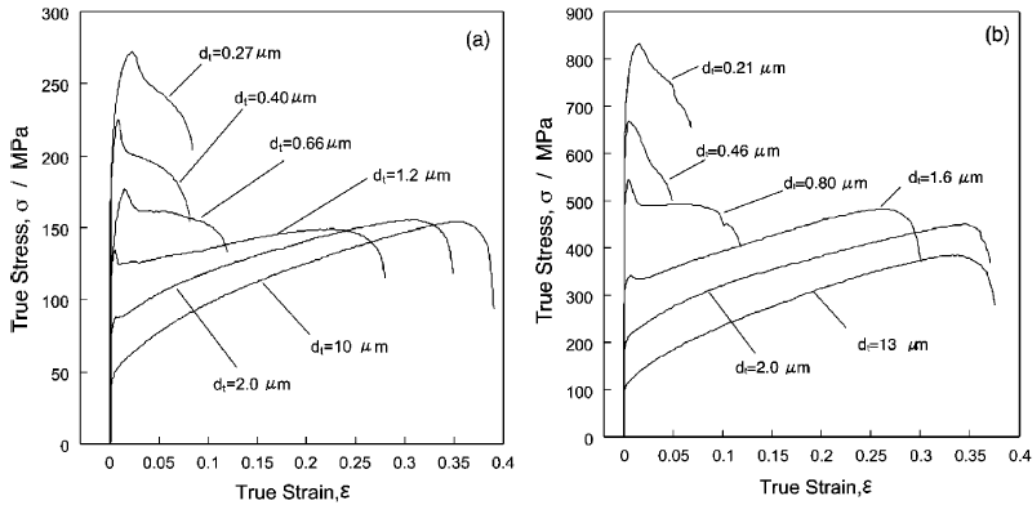

Fig. I-9 True stress-true strain plots corresponding to UFG 1100-Al (a) and IF steel (b) processed by SPD and consequent annealing to obtain different grain sizes [81].

C.Y. Yu *et al*. [73] suggested that the yield drop is associated with a lack of mobile dislocations characteristic of UFG structures. Mobile dislocations are related to shear strain (γ_s) by the expression $\gamma_s = bNA$, where b is the norm of the Burgers vector, N the number of mobile dislocations and A the area crossed by a moving dislocation. In the UFG regime, grain boundaries act as dislocation sources and sinks thus, N would depend on the generation/annihilation ratio. In addition, as the grain size is reduced, the surface area of the grain boundaries increases and A decreases. If the density of mobile dislocations is not high enough, a higher velocity of dislocations is required to fulfill the applied strain rate, which demands higher stress and translates into a yield peak. The same authors explain the low ductility displayed for smaller UFG grain sizes, from the high rate of dislocation annihilation at room temperature, which hinders strain hardening. Because annihilation highly depends in temperature, they performed tensile tests at 77 K (Fig. I-10). At this temperature, much higher ductility if observed in addition to work hardening in samples in the UFG regime.

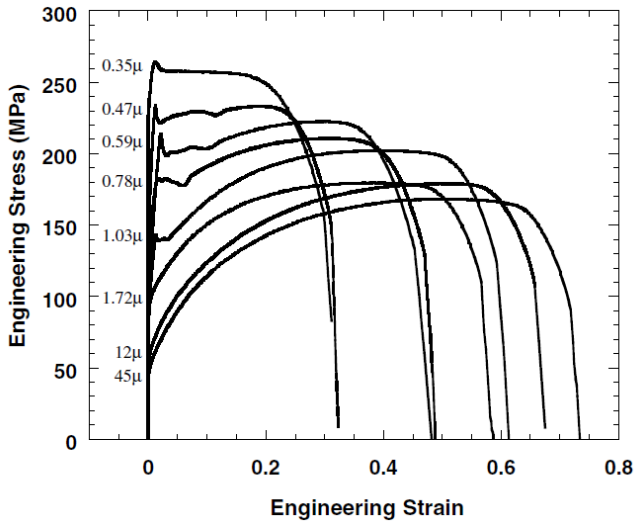

Fig. I-10 Engineering tensile stress-strain curves for commercially pure aluminum (AA1050) obtained by SPD and annealing [73].

Concerning mechanical testing at high temperature, the lack of thermal stability of most pure UFG metals makes testing at relatively high temperature ($T > 0.5\ T_m$) complicated. On the other hand, in some UFG processed alloys the presence of second phases or precipitates guarantee the stability of the microstructure and they display superplastic properties at high temperature [16,82]. To achieve superplasticity, two conditions must be fulfilled, small grain size (below 10 µm) and a testing temperature relatively high to ensure high diffusion. It has been shown that the main superplastic flow mechanism is grain boundary sliding, which entails the movement of grains in a polycrystal over each other without elongation of the grains [83]. This mechanism requires intragranular slip as an accommodation mechanism, which in coarse grained metals is delayed by subgrain boundaries. Nevertheless, in UFG metals, a grain size smaller than the equilibrium subgrain size, enables the traveling of dislocations across the grain, the formation of pile-ups and dislocation climb into another grain boundary, which facilitates grain boundary sliding [83].

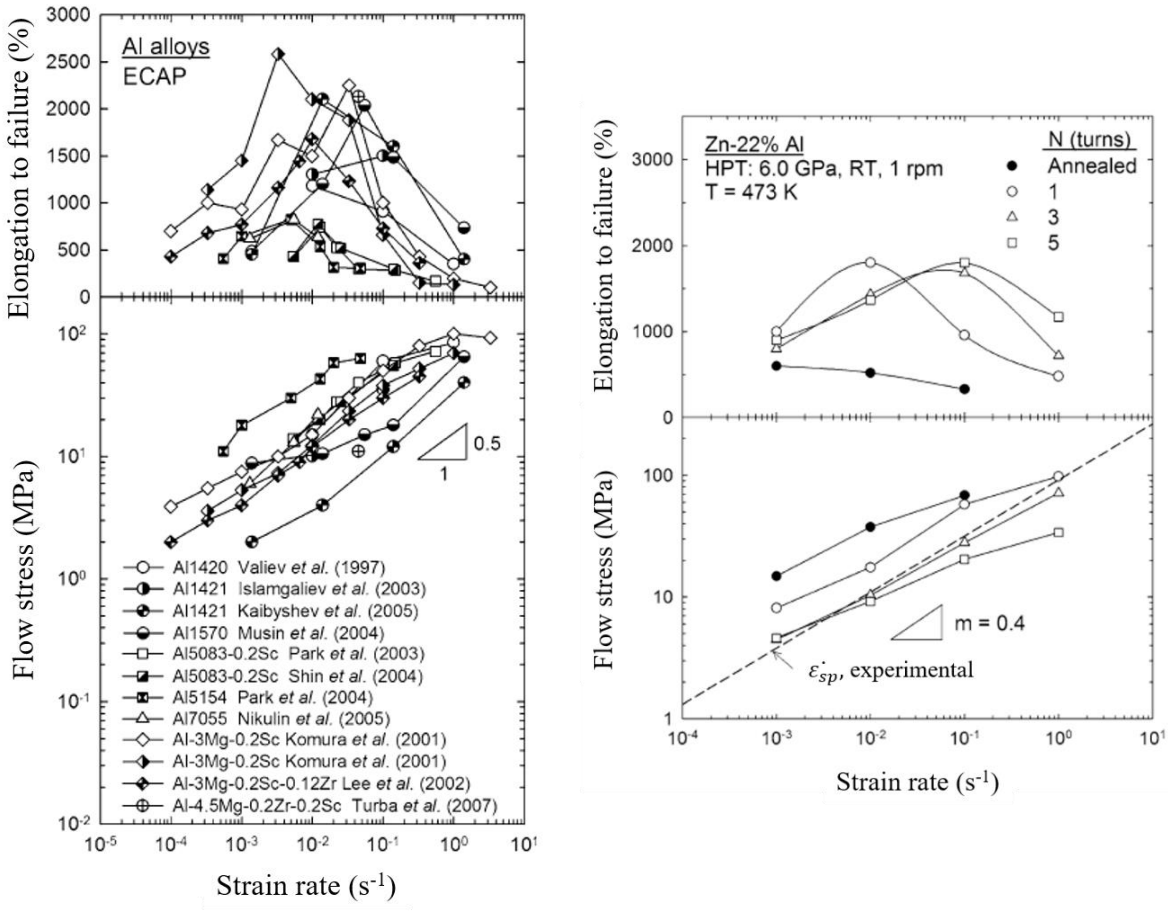

(a) (b)

Fig. I-11 Elongation to failure (upper) and flow stress (lower) against strain rate for ECAP processed Al alloys (a) and for HPT processed a Zn-22% Al alloy [83].

Examples of good superplastic properties can be observed for aluminum alloys prepared by ECAP (Fig. I-11 (a)) and a zinc alloy prepared by HPT with different numbers of turns (Fig. I-11 (b)). Despite the maximum elongation to failure being at a strain rate of ~10^{-3} s^{-1}, in Al alloys, good superplasticity is also observed at faster strain rates. Likewise, in Zn-22% Al, high elongation to failure is displayed at fast strain rates when the microstructure is well homogenized.

Now, let us consider the mechanical properties of UFG and nanostructured nickel obtained by different processing techniques. The tensile stress-strain curves of SPD processed and SPD + annealing Ni samples are shown in Fig. I-12 (a) [66]. State 1 corresponds to a sample processed by ECAP + cold rolling, state 2 corresponds to state 1 + HPT and the number 200 added to some samples indicates an annealing treatment at 200 °C for 1 h. It can be seen that the specimen prepared by ECAP + cold rolling and annealing at 200 °C for 1 h displays the maximum ductility (12 %). This value is not negligible specially when related to a yield strength of 835 MPa, nevertheless, uniform elongation is below 5 %. After yielding, an important hardening followed rapidly by heterogeneous deformation is depicted. Unlike Al, in this case no yield drop is observed.

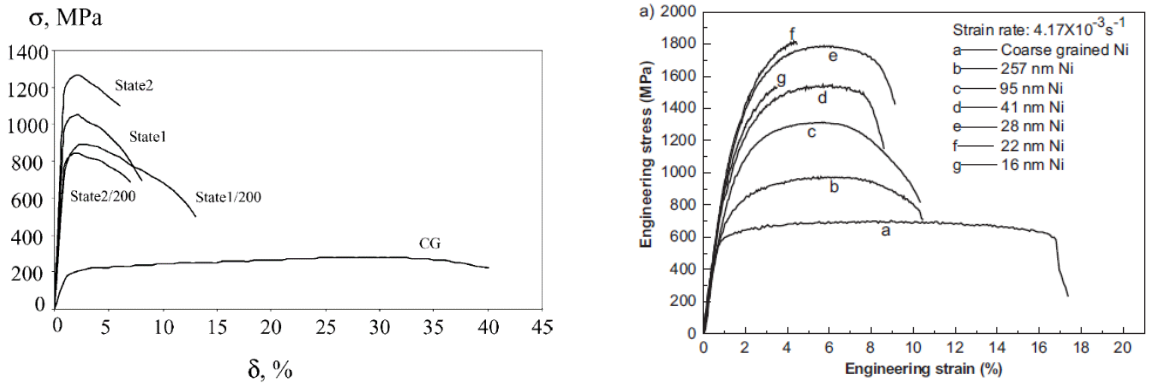

(a) (b)

Fig. I-12 Tensile engineering stress-strain curves for UFG Ni processed by SPD [66] (a) and by ED [69] (b).

Concerning nanostructured Ni prepared by ED, Fig. I-12 (b) shows that within the nanosized regime, big differences in ductility and strength can be depicted. Acceptable ductility (up to 10 %) is displayed for samples of grain sizes above 25 nm, and low (below 5 %) for smaller grain sizes. The retained ductility at grain sizes below 50 nm is explained by X. Shen *et al.* [69] by means of heterogeneities in the microstructure. Such heterogeneities would allow for dislocation accumulation in larger grains creating a large deformation gradient. Consequently, an important number of geometrically necessary dislocations would accommodate the gradient accounting for the additional strain hardening.

Finally, for PM processed samples, information concerning ductility and strain hardening in tension is lacking for samples sintered from nanopowders as mechanical testing was performed in compression.

Regarding Ni samples processed by SPS from BM powders [84], Fig. I-13 displays the mechanical behavior of a nanostructures sample in the true stress-strain curve. The engineering stress-strain curve is not shown on the paper and elongation to fracture is not reported. Nevertheless, from Fig. I-13 good ductility can be anticipated.

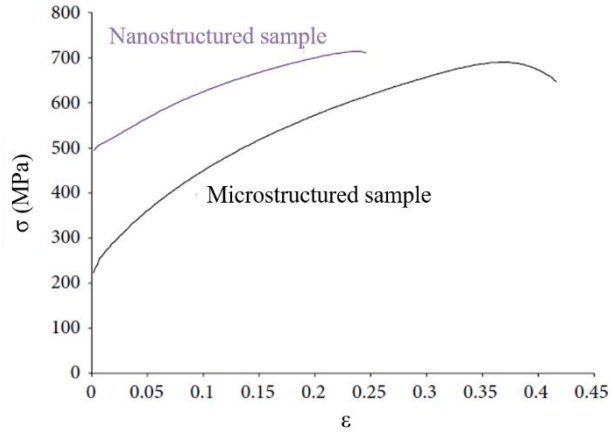

Fig. I-13 True stress-strain curves of two samples processed by SPS from BM powders (Nanostructured sample) and as-received powder (Microstructured sample) [84].

Influence of grain size in the UFG/NsM ranges on strength

Yield strength (σ_y) is known to evolve with grain size (d) following the Hall-Petch (HP) relation:

$$\sigma_y = \sigma_0 + k_{HP}\frac{1}{\sqrt{d}} \tag{1.2}$$

where σ_0 is the friction stress in the absence of grain boundaries, and k_{HP} represents the HP constant, which reflects on the sensibility of the material to the presence of grain boundaries. It can be inferred from eq. (1) that a refinement of the grain size implies a strengthening of the material, which leads to the interest of fabricating materials with reduced grain sizes. The physical mechanism behind this equation, described by E.O. Hall [85], is the development of intragranular pileups of dislocations of the same sign at grain boundaries. When d is refined below a critical size a deviation from this trend towards lower stress values than expected has been reported [22]. In Fig. I-14, yield strength of different pure metals is plotted against grain size showing a breakdown of the HP trend. This deviation was attributed to a modification in the deformation mechanisms below a critical grain size value. Nevertheless, contradictory analyses and results can be found in literature concerning this deviation.

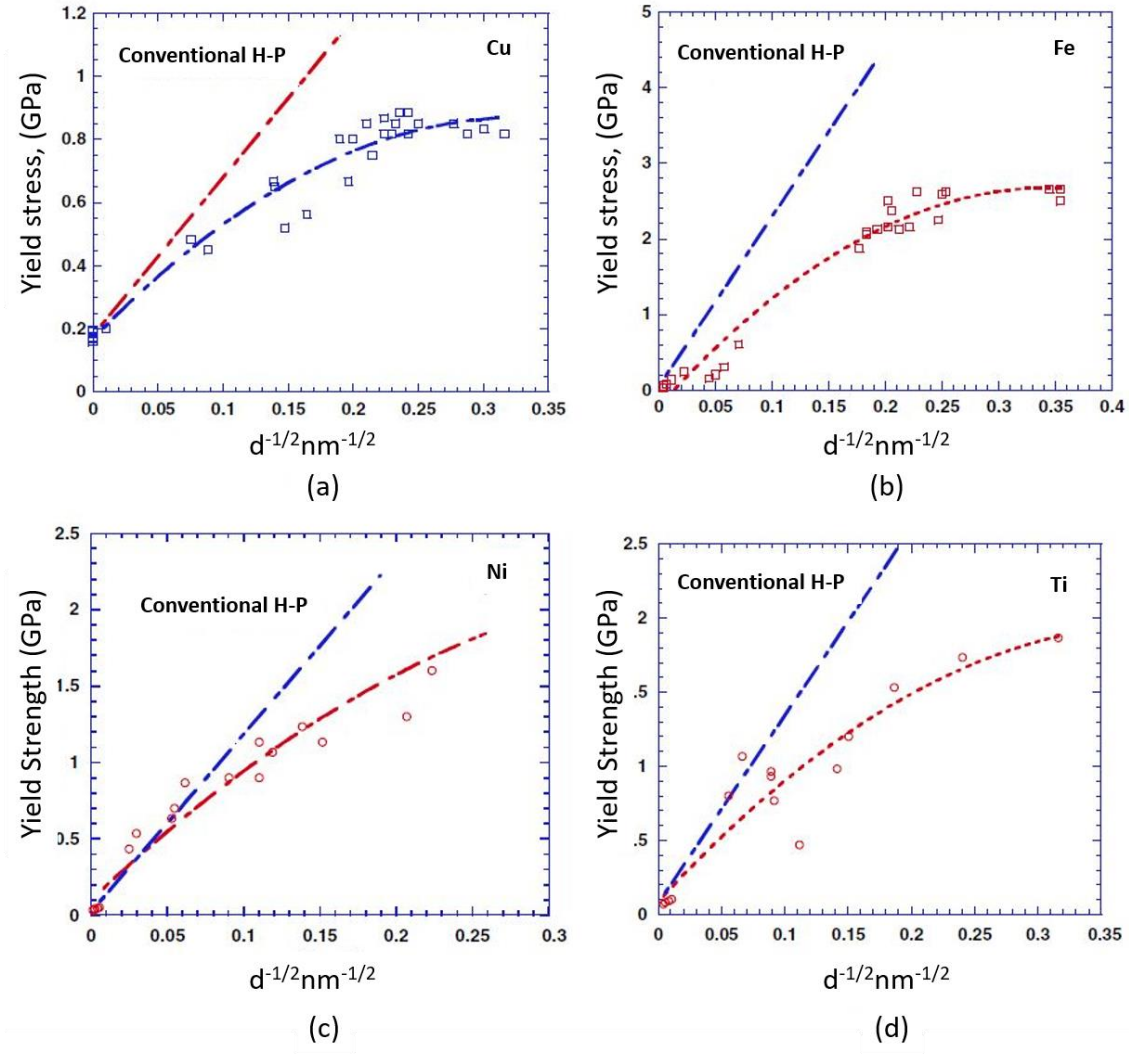

Fig. I-14 Deviation of the HP relation displayed in the UFG/nanosized range by copper (a), iron (b), nickel (c) and titanium (d) [22].

For copper (Fig. I-14 (a)) at very small grain sizes an inversion of the HP relation can be inferred. Some authors have in fact reported such inversion in nanostructured copper (Fig. I-15 (a)). The same phenomenon was observed for palladium, as well as several alloys, including Ni alloys (Fig. I-15 (b)-(c)). The negative slope was attributed to diffusional creep in NsM at room temperature, similarly to grain boundary sliding at high temperature for coarse grained samples. This was studied by discrete dislocation analysis, which confirmed this hypothesis [86]. However, the presence of flaws in the processed samples, leads to considering the inversion an artifact [87]. The difficulty of preparing defect free samples with grain sizes below 50 nm (where the inversion usually appears), makes the determination of the real trend still open to discussion.

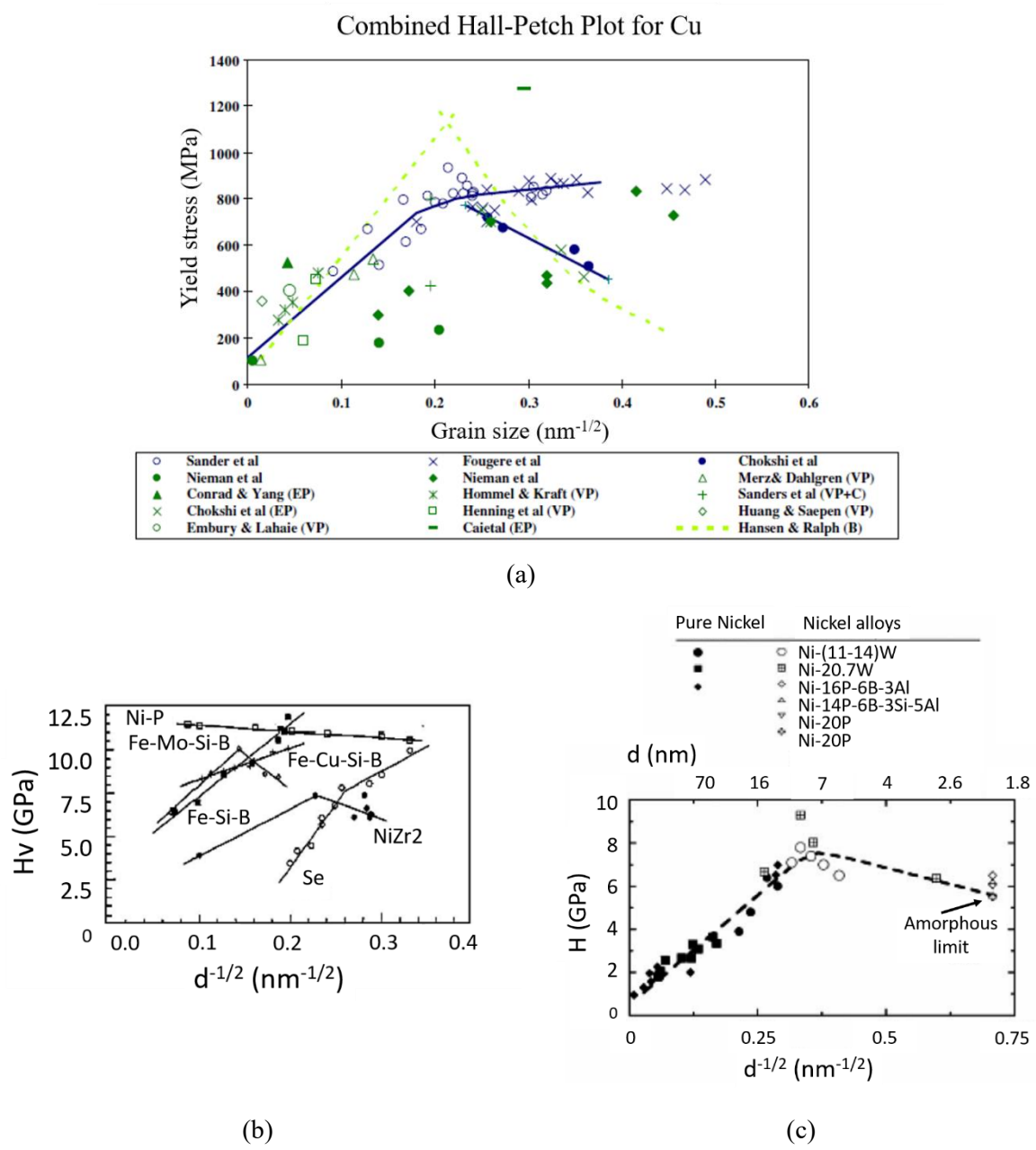

Fig. I-15 HP plot of Cu (a), several nanostructured alloys (b), pure Ni and nickel alloys (c) [22].

Several authors have investigated the influence of grain size in the UFG range on yield strength. For instance, K.S. Kumar et al. [64] proposed no deviation (Fig. I-16 (a)), whereas R.Z. Valiev [88] reported higher strength than that expected from the HP relation (Fig. I-16 (b), curve 2). The higher strength determined by R.Z. Valiev was explained by the presence of dislocation substructures and "non-equilibrium" grain boundaries in the case of Ni processed by HPT.

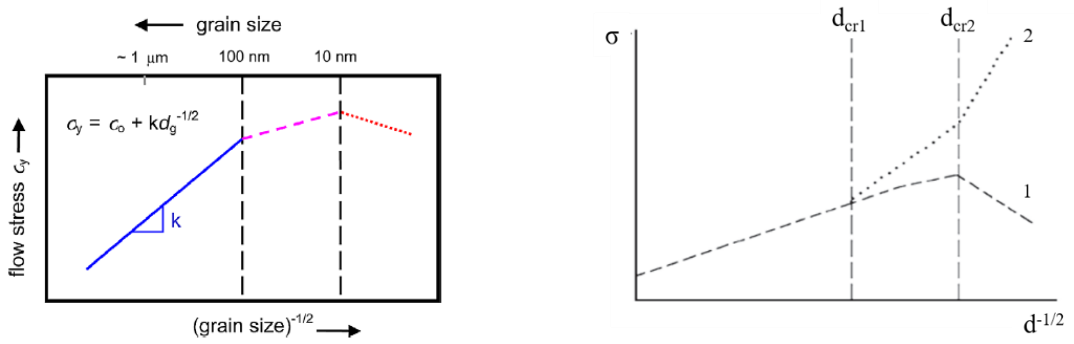

(a) (b)

Fig. I-16 Different hypothesis of the HP relation in the UFG regime, K.S. Kumar et al. [64] (a) and R.Z. Valiev [88].

Experimental results obtained for pure metals such as aluminum (Fig. I-17 (a)) or copper (Fig. I-17 (b)) obtained by different processing techniques, SPD and powder metallurgy respectively, display a behavior closer to the one predicted by R.Z. Valiev.

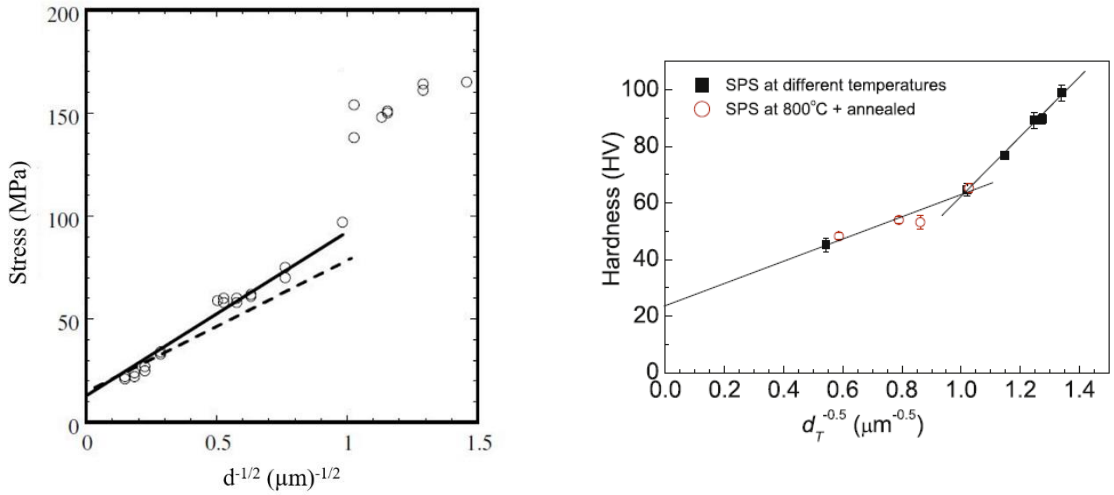

(a) (b)

Fig. I-17 Influence of grain size in the UFG range on strength for Al processed by SPD + annealing [73] (a) and SPS processed Cu (b) [89].

Differences in the microstructures obtained from different processing techniques makes a straightforward hypothesis applicable to all UFG materials impossible. Fig. I-18 collects the results for UFG Ni produced by SPD (N. Krasilnikov *et al.* [66]), ED (C. Xiao *et al.* [90] and F. Ebrahimi *et al.* [91]) and powder metallurgy from nanopowders (Q.H. Bui *et al.* [40,92]). From the HP plot, it is clear that the values obtained for ED processed samples seem to be in accordance with the expected values of yield strength for their corresponding grain size. A shift of the HP relation compared to coarse grained nickel (higher σ_0) might indicate an inherent higher internal stress state in samples in the UFG regime. Specimens obtained from powder metallurgy as well as those prepared by SPD deviate from the behavior

expected from the HP relation. The important presence of oxides on the samples of Q.H. Bui *et al.* was judged accountable for the deviation observed in the samples processed by powder metallurgy. The ED samples would thus represent a microstructure in the UFG range without "artifacts". The additional strengthening found for SPD or powder metallurgy processed samples would be the consequence of the dislocation substructures, deformation modified ("non-equilibrium") grain boundaries and oxides found in such samples.

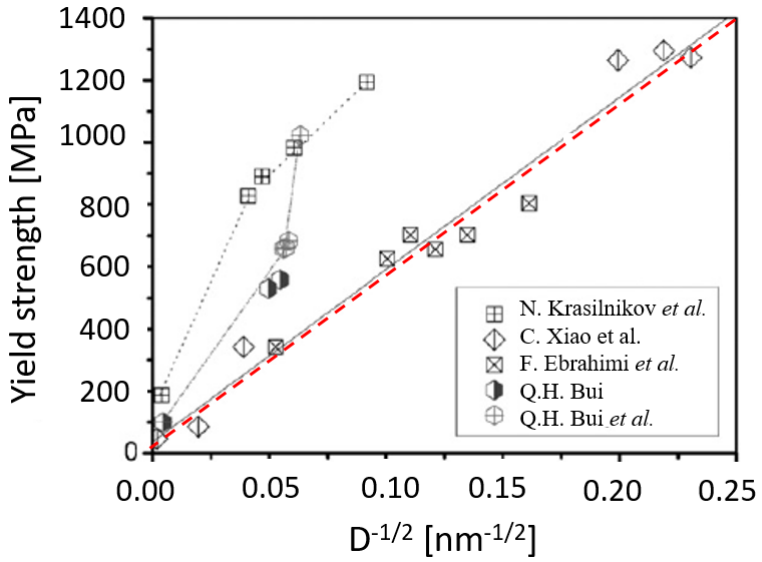

Fig. I-18 Hall-Petch relation for UFG Ni obtained from different processing methods [40]. The solid line represents a linear fit of the data corresponding to ED Ni from F. Ebrahimi *et al.* and C. Xiao *et al.* The dashed red line corresponds to the HP trend for coarse grained Ni [93].

The Hall-Petch relation can be generalized to different levels of deformation, where the values of $\sigma_0(\varepsilon)$ and $k_{HP}(\varepsilon)$ evolve with deformation, and reflect on the different deformation mechanisms that prevail at each deformation level. For instance, X. Feaugas *et al.* [94], studied this evolution for two FCC materials, nickel and austenitic stainless steel, in the coarse grained range. Their results showed an exponential increase of $\sigma_0(\varepsilon)$ with increasing strain, due to the development of high-density dislocation structures. The HP constant on the other hand, increases at low deformation values and becomes stable at higher deformation levels. This indicates a transition from hardening due to the presence of grain boundaries, to hardening induced from dense dislocation structures developed during plastic deformation. This trend can be observed in Fig. I-19 for aluminum and IF steel, in the coarse grained regime. In this work [81], necking began after yielding, thus no values for yield strength in the UFG regime are plotted. The evolution of the HP parameters at different strain levels should be studied for a better comprehension of the deformation mechanisms taking place in the NsM/UFG regimes.

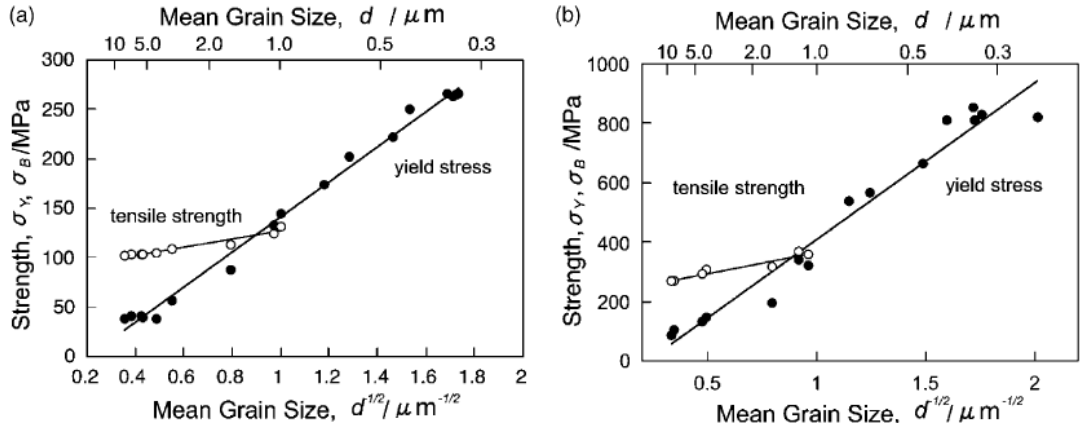

Fig. I-19 Influence of grain size in yield strength (black symbols) and tensile strength (white symbols) for UFG 1100 Al (a) and IF steel (b) [81] processed by SPD + annealing.

Functional properties of UFG metals

Despite the strengthening effect of refining the microstructure, a major concern with UFG metals is a possible degradation of functional properties such as electroconductivity, corrosion, magnetism, etc. Hence, the effect of grain size in the UFG/NsM regime in functional properties is also a major focus of study for many researcher. For instance, A.P. Zhilyaev *et al.* [95], studied the variation of electroconductivity in UFG copper processed by a combination of different SPD techniques. Their results show that no significant decrease is observed in the UFG samples, where the measured relative conductivity (with coarse-grained Cu as reference) was 91.6 %.

Other properties such as thermoelectricity and superconductivity, were discussed by R.Z. Valiev *et al.* [96]. The combination of HPT and annealing treatments enables the synthesis of Bi-Te alloys with excellent thermoelectric properties for low-temperature applications. The quality of thermoelectric properties is described by the "figure of merit",

$$ZT = \frac{TS^2}{\rho_r \lambda_c} \tag{1.3}$$

where T is temperature, S the Seebeck coefficient, ρ_r electrical resistivity and λ_c thermal conductivity. Improved thermoelectric properties are measured by a high value of ZT. Such was the case for Bi-Te alloys in [96] although grain refinement was not the main factor contributing to the improvement of thermoelectricity. The high density of defects introduces by HPT minimized the denominator in Eq. (1.3) and the UFG microstructure does not deteriorated the thermoelectric quality of the material. In the case of superconductivity, small grain size can have a major effect in properties such as the critical temperature (T_c), the critical current density (J_c) and the upper critical magnetic field (H_{c2}), which characterize the range in which the material displays superconductivity. T. Nishizaki *et al.* [97], reported

that reducing grain size in Nb to the UFG regime by HPT, resulted on the increase of all the above-mentioned superconductivity properties (Fig. I-20).

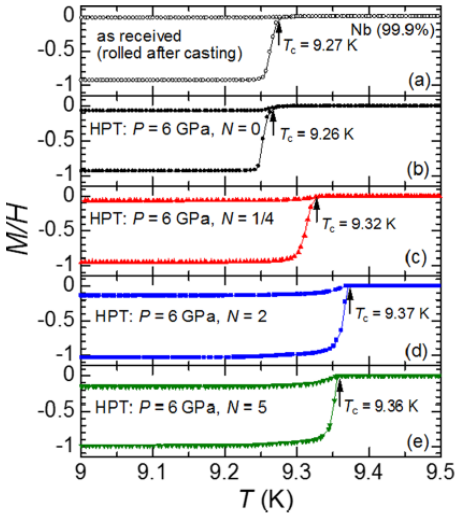

Fig. I-20 Temperature dependence of the magnetization M(T) of Nb for a magnetic field H = 2 Oe in a coarse grained sample (a) and HPT processed samples (b-e) [97].

A last example is corrosion resistance, where a straightforward answer to whether grain refinement in the UFG/nanostructured regime is detrimental is complicated. In the coarse grain range, local corrosion such as pitting or intergranular corrosion decreases with grain size, whereas general corrosion shows the opposite trend [98]. However, K.D. Ralston [99] argued that a more important factor to consider would be the mode of corrosion: active, passive or active/passive. For materials that display active corrosion, corrosion currents increase with finer grains, while the contrary is observed in the passive type of corrosion. In the UFG range, metals display a lower dissolution potential than coarse grained specimens, given their high density of grain boundaries and higher internal energy. Thus, in general, higher tendency to dissolution in aggressive media should be observed [98].

For instance, UFG and nanostructured Ni was investigated by L.Y. Qin *et al.* [100]. They reported a difference in the corrosion behavior dependent on the corrosion media. The high density of grain boundaries contributed positively in media where passivation by the formation of an oxide takes place (10 % NaOH and 3 % NaCl), whereas in 1 % H_2SO_4, the lack of passivation combined with the high density of active sites for preferential attack resulted in accelerated corrosion. Nevertheless, the high sweeping rate (10 mV/s) makes the comparison with other works difficult. In fact, the formation of a passive layer in 1 M H_2SO_4, in nanocrystalline Ni has also been observed by other authors [101], who reported a higher passivity current than for CG Ni. D.B. Bober *et al.* [102] compared the results of L.Y. Qin *et al*. with result for UFG/nanostructured Ni obtained by other authors (Fig. I-21 (a)). Contradictions between the different studies can be observed. These differences arise from different processing techniques used in the synthesis of the samples. Likewise, for UFG/nanostructured copper (Fig. I-21 (b))

a disagreement is still found. According to the authors, variations in the grain boundary character distribution, texture, precipitates, as well as the presence of different defects are responsible for the dispersion of the results found in literature. As a general conclusion, it can be stated that grain refinement to the nano/UFG range is beneficial for corrosion resistance only if a passive layer is formed, as such passive layers are found to be more uniform and durable than the one formed in the coarse grained counterparts [101].

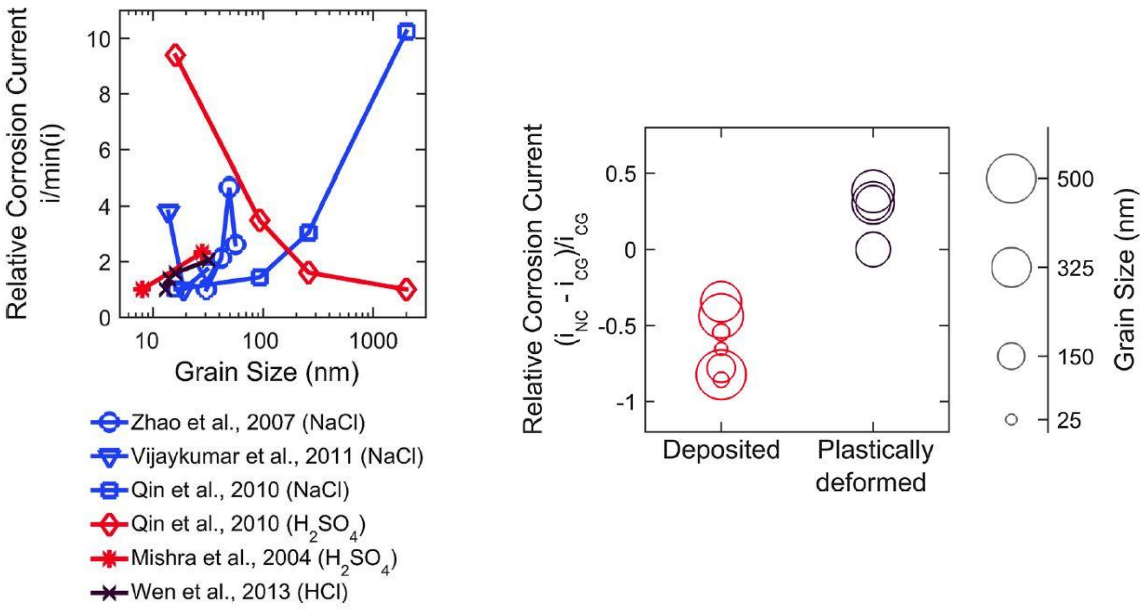

(a) (b)

Fig. I-21 Influence of grain size on corrosion current of UFG/nanostructured Ni (a) and effect of the processing method on UFG/nanostructured copper (b) [102].

3.2. *Microstructural features of UFG metals*

The properties of polycrystalline materials highly depend on their microstructure. As seen in the previous section, discrepancies in the influence of grain size on mechanical and functional properties arise from differences in other microstructural features, which depend on the processing technique. These features highlight grain size, grain boundary character distribution (GBCD), the presence of porosities or precipitates and internal stresses. For a better comparison of the properties of UFG metals processed by different means, a careful description of these characteristics is required.

Grain boundaries: definition and classification

The strong impact of grain boundaries on the properties of polycrystalline materials makes tailoring microstructures during synthesis an important goal for material sciences. Grain boundaries represent the transition area between two neighboring crystals (grains) of same phase but different crystallographic orientation. The geometry of a grain boundary (GB) can be characterize by five independent parameters or macroscopic degrees of freedom (DOF) [103]. Three of them describe the misorientation between grains, which is represented by a rotation that superposes both grains. This misorientation is defined by the rotation axis (**o** in Fig. I-22) which entails two DOF, and the angle θ (one DOF). Then, the orientation of the boundary plane between the misoriented grains is described by its normal direction (**n** in Fig. I-22) (two DOF).

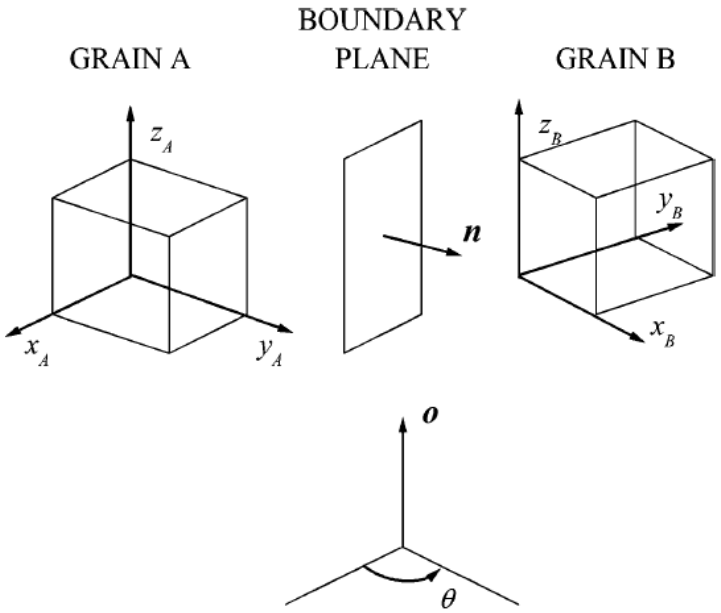

Fig. I-22 Variables needed to describe a grain boundary. Here, x_A, y_A, z_A and x_B, y_B, z_B are the reference axes for grains A and B, respectively. The rotation axis is **o** and θ is the misorientation angle needed to superpose both crystals. Finally, the orientation of the boundary plane is defined by its normal direction **n** [103].

To describe unambiguously a GB the following notation is often used: $\theta°[h_ok_ol_o],(h_{\mathbf{n}A}k_{\mathbf{n}A}l_{\mathbf{n}A})$. The axis of rotation **o** = [$h_ok_ol_o$] is common to both crystals, but the grain boundary plane is described attending to only one of the grains. In addition to the five macroscopic DOF, three other microscopic parameters exist that ensure equilibrium atomic structures in the boundary, and are dependent on temperature, pressure and chemical composition. They concern the translations of the grain in a direction parallel or perpendicular to the boundary plane as well as a change in volume between grains [103].

Due to the existance of an enormous number of distinct grain boundaries, they can be classified in groups according to the relation between the independent parameters [104]. For instance, if we consider

the relation between **o** and **n**, we can classify grain boundaries as tilt (**o**⊥**n**), twist (**o**∥**n**) or mixed (also called random) if they do not belong to one of the two other groups (Fig. I-23).

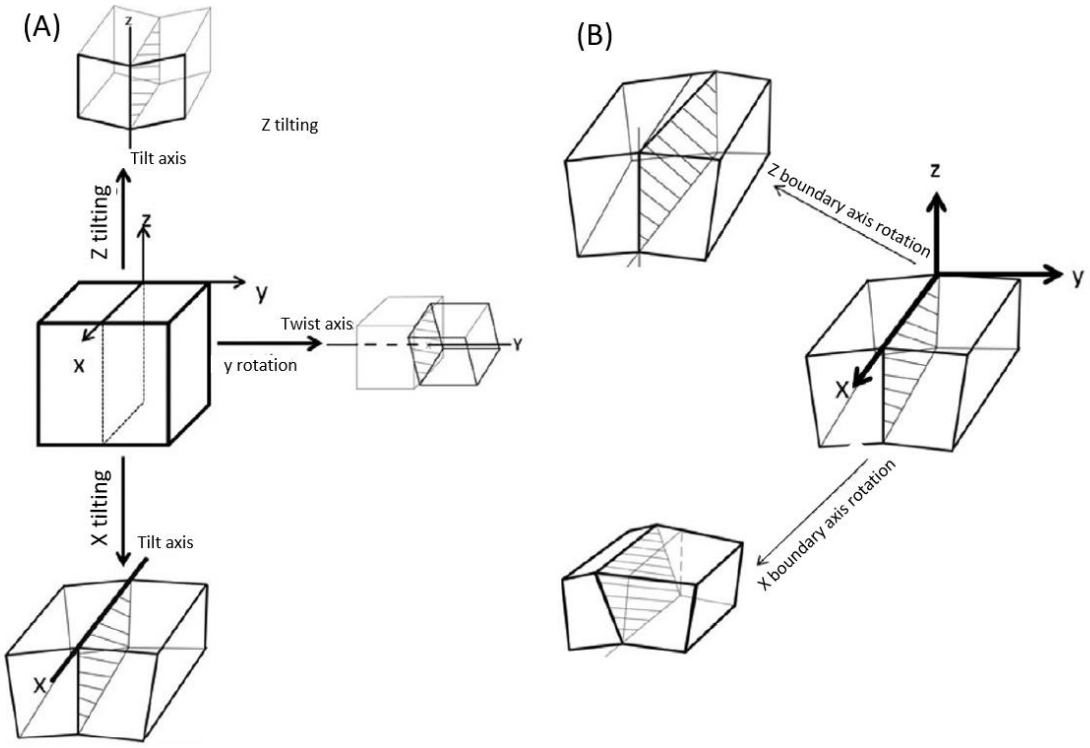

(a) (b)

Fig. I-23 Schematic illustration of the formation of a 5° misorientation grain boundary [104]. Misorientations between lattices to form a tilt or a twist boundary are represented in (a). Two examples of mixed grain boundaries, where **n** is neither parallel nor perpendicular to **o** are displayed in (b).

Because access to information concerning the orientation of the boundary plane is difficult experimentally, it is usually neglected and grain boundaries are classified attending to their misorientation angle. The first type of grain boundaries includes boundaries with misorientation angles between $2° \leq \theta \leq 15°$ (depending on the author the lower limit can be set to 5°) and are called low angle boundaries (LAGB). These boundaries can be described by an array of dislocations, which is easily seen on a symmetrical tilt boundary (Fig. I-24 (a)). The energy per unit area (γ) of the LAGB is related to the misorientation of neighboring grains by Eq. (1), proposed by Read and Shockley [105].

$$\gamma = \gamma_0 \theta(\mathrm{A} - \ln\theta) \tag{1.4}$$

where γ_0 and A are constants, which depend on the material. Despite an initial increase in the energy of a tilt boundary with increasing misorientation, if enough energy is supplied, the arrangement of dislocations into higher angle boundaries decreases the energy of the grain boundary (Fig. I-24 (b)).

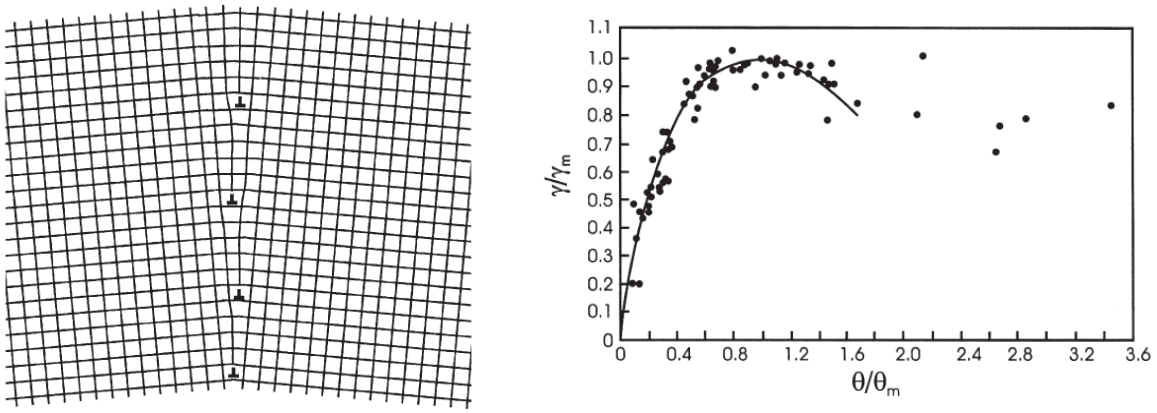

(a) (b)

Fig. I-24 Symetric low angle tilt boundary displaying a wall of edge dislocations that are aligned perpendicular to the slip plane (a). Normalized energy of low angle tilt boundaries as a function of normalized misorientation angle, measured (symbols) and calculated (line) for various metals [84] (b).

The second type of boundaries are high angle boundaries (HAB) and they exhibit a misorientation angle $\theta > 15°$. Unlike LAGBs, high angle boundaries are described as regions of good and bad matching between two grains (Fig. I-25). This hypothesis was first proposed by M. Weins et al. [106] and is still considered valid to date.

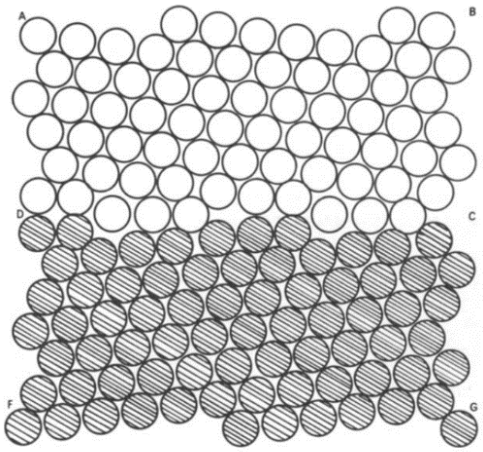

Fig. I-25 Illustration by M. Weins *et al.* [85] representing a symmetric high angle tilt boundary. Atoms of different color correspond to different grains.

The final type of boundaries corresponds to the coincidence site lattice (CSL) boundaries. In this type of boundaries, some atomic sites in the boundary plane are common to the lattices of both grains. They are represented by Σ followed by the reciprocal ratio of CSL sites. An illustrative example can be seen in Fig. I-26, where a rotation of 36.9 ° about an <001> axis generates a Σ5 CSL boundary.

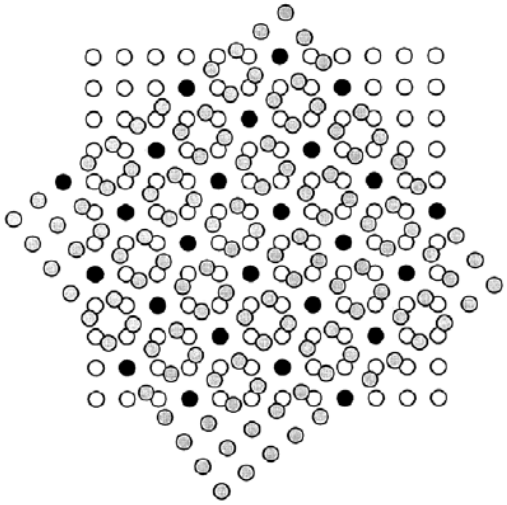

Fig. I-26 Illustration corresponding to a Σ5 boundary formed by rotating two cubic lattices 36.9 ° about an <001> axis. Black circles correspond to atomic sites common to both lattices [107].

The CSL boundaries are considered as an independent type of boundaries due to their special characteristics such as low interfacial energy and low susceptibility to grain boundary corrosion [108,109]. It is thus of interest to use processing techniques that favor the formation of this type of boundaries. In this manuscript, only CSL boundaries Σ3 – Σ30 are considered[2].

Microstructural features highly depend on the characteristics of the material of study such as the crystal structure, the stacking fault energy, number of phases present etc. Thus in the following sections, the microstructure observed in UFG Ni obtained by different processing techniques will be highlighted and discussed.

SPD processed samples

All SPD processed samples present similar general characteristics. Completely dense samples with low or no contamination and a grain size at its optimum (homogeneously distributed microstructure) in the range d = 150-300 nm. Concerning defect density, a high dislocation density is usually reported, which varies with the processing technique. Samples display a grain boundary texture, with a GBCD distant from the random distribution, characterized by a high fraction of LAGB. An important characteristic of SPD processed microstructures is that they possess “non-equilibrium”, or “deformation modified” grain boundaries that are at a high-energy state. They are generated by plastic deformation and display an excessive density of grain boundary dislocations. These dislocations are sometimes called extrinsic grain boundary dislocations and they extend long-range stresses into the grain interior [98].

[2] Low angle grain boundaries can also be defined as Σ1 CSL boundaries.

More specifically, Ni processed by HPT studied by A.P. Zhilyaev *et al.* [29] exhibits a homogeneous microstructure with equiaxed grains if at least five revolutions are performed with an applied pressure of at least 6 GPa. With an approximate grain size at its optimum of ~ 170 nm, the GBCD displays a high fraction of random HAB (65 %) and of LAGB grain boundaries (18.3 %). The fractions measured for Σ3 grain boundaries (3 %) and other coincidence site lattice (CSL) (Σ9- Σ30) boundaries (13.5 %) are fairly close to the values attributed to the random distribution [107] (1.8 % and 9.59 % respectively). As shown in Fig. I-27, differences in the processing parameters (number of rotations and applied pressure) produce samples with notably diverse microstructures, which may account for the disagreement concerning the homogeneity of HPT processed samples.

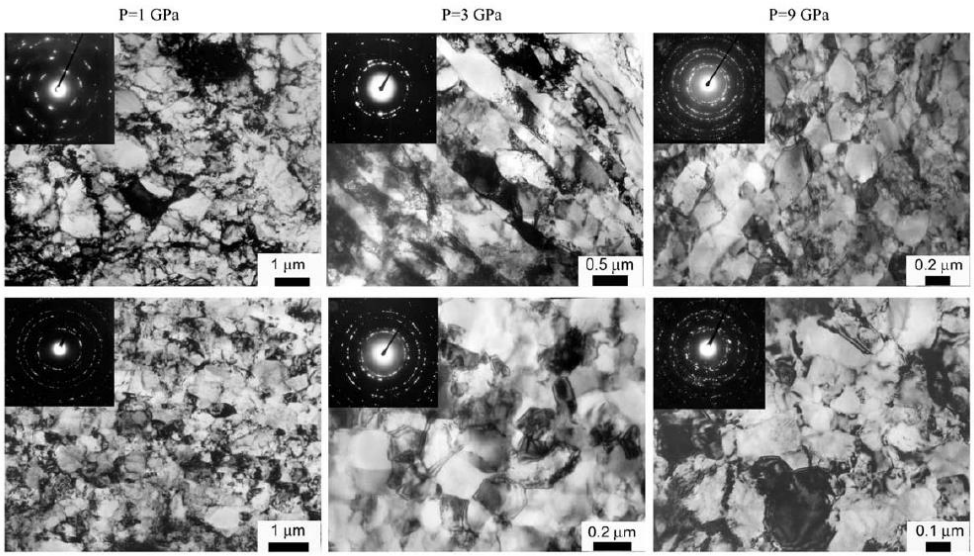

Fig. I-27 UFG Ni processed by HPT after 5 rotation with different applied pressure. The images of the microstructures (and corresponding SAED pattern) obtained by transmission electron microscopy (TEM), show the differences between the center (upper row) and the periphery (lower row) of the specimen [29].

Concerning dislocation density in HPT Ni (5 rotations at 6 GPa), TEM images were used to calculate the dislocation density revealing a value of $0.5 – 1.0 \cdot 10^{15}$ m^{-2} [110]. In this estimation, cell boundaries and dislocations located at the subgrains were included. These value compared to the ones determined by G.K. Williamson *et al.* [111] of $\sim 1 \cdot 10^{12}$ m^{-2} and $\sim 1 \cdot 10^{15}$ m^{-2} respectively for annealed and strain-hardened Al, suggest a high internal stress level in HPT processed Ni. Moreover, in carefully annealed coarse-grain Ni a dislocation density below 10^{10} m^{-2} can be obtained [112].

For ECAP processed Ni [35], a grain size of ~270 nm after 8 passes and ~230 nm after 12 passes is observed, bigger than HPT samples. The fraction of LAGB grain boundaries measured was 23.2 % and 15.6 % respectively. It is important to note that LAGB grain boundaries in [35] are defined with a misorientation of 5° - 15°, if a minimum misorientation of 2° is set the fraction of LAGB boundaries increases to over 30 % for the sample after 12 passes. A similar fraction of HAB is depicted (60 % and

63.07 %) in both samples. This leaves a fraction of CSL of ~20 % at best (12 passes) which includes a fraction of Σ3 grain boundaries of less than 5 %. GBCD for ECAP processed samples is thus similar to that obtained in HPT processed samples [113]. Concerning the geometry of grains, unlike in HPT synthesis, even after homogenization of the microstructure (12 passes) a combination of equiaxed and elongated grains is depicted (Fig. I-28 (a)).

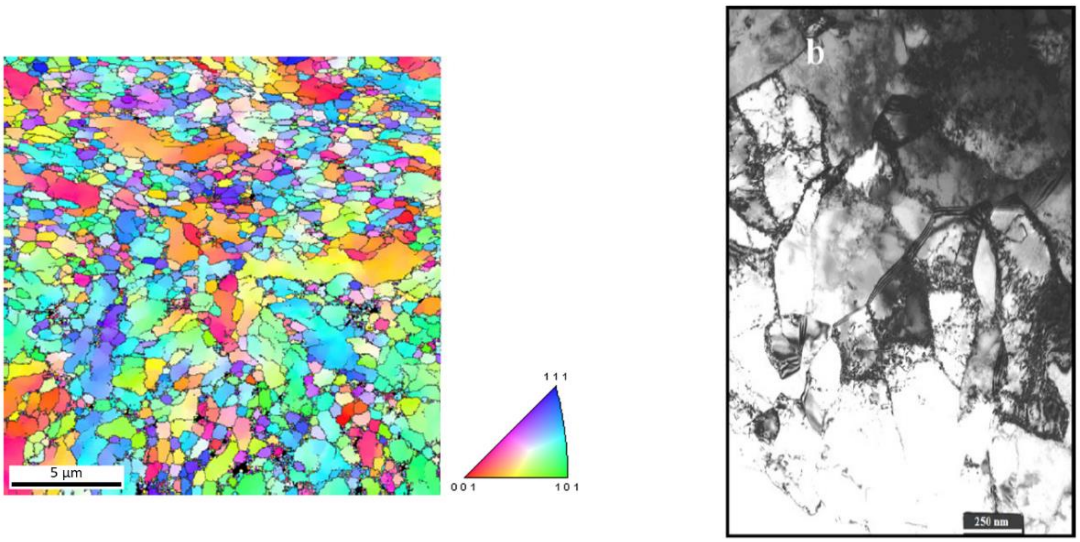

(a) (b)

Fig. I-28 Grain boundary map superposed with orientation cartography (misorientation > 5°) of an ECAP processed Ni sample (12 passes) showing equiaxed as well as elongated grains (a). TEM micrograph of the same sample displaying dark contrasts within grains as a result of high strain and density of dislocations (b) [35].

As for HPT processed samples, a high defect density is observed in ECAP processed samples. Qualitatively, the high amount of strains and density of dislocations inside grains and near grain boundaries is observed in Fig. I-28 (b). Quantitatively, dislocation density computed from XRD data resulted in ~$9 \cdot 10^{14}$ m^{-2} for the sample after 8 passes and ~$1 \cdot 10^{14}$ m^{-2} for the sample after 12 passes. The latter result suggests dynamic recovery of the microstructure after 12 passes.

Samples obtained by PM

The available literature on UFG Ni processed by PM is limited and mostly centered on the use of nanopowders as precursor powders. The use of nanopowders allow for the synthesis of specimens with very small grain sizes (200 – 400 nm). The works of M.A. Bousnina *et al.* [41] and J. Gubicza *et al.* [114] characterize UFG Ni in terms of relative density, grain size, twin boundary fraction and dislocation density (Table I-1).

Table I-1 Processing parameters and microstructural characteristics of Ni samples processed from nanopowders by HIP and SPS.

Processing method	*HIP*[1]	*SPS*[1]	*HIP*[2]	*SPS*[2]
Sintering temperature (K)	973	773	650	600
Sintering pressure (MPa)	140	150	120	53
Dwell time (min)	150	1	60	5
Relative density (%)	95.5 ± 0.1	95.4 ± 0.1	88	86
Average grain size (nm)	403	294	620	200
Twin boundary fraction (%)	19	17	---	---
Dislocation density (10^{14} m^{-2})	5.6 ± 0.5	5.1 ± 0.5	---	---

[1][114], [2][41]

It is noticeable that samples processed by HIP higher sintering temperature and longer sintering times are required comparably to SPS sintering to achieve similar densities after synthesis. A difference in relative density exists between the two studies. The higher density achieved in [114] could be the consequence of using a higher sintering temperature and/or due to a difference in the fraction of NiO present in the final samples. In both investigations, the initial nanopowder displayed a monocrystalline nature of average size of 100 nm (Fig. I-29 (a)). Thus after sintering, an increase in grain size of 4-6 times that of the powder is observed for HIP processing (Fig. I-29 (b)) and 2-3 times for SPS sintering (Fig. I-29 (c)). Grain growth is thus more limited in SPS consolidation compared to HIP processing. A very high fraction of twin boundaries can be depicted, compared to SPD processed UFG Ni. Finally, the dislocation density determined by profile analysis of XRD data exhibits a lower fraction than HPT Ni but surprisingly a higher density than ECAP Ni.

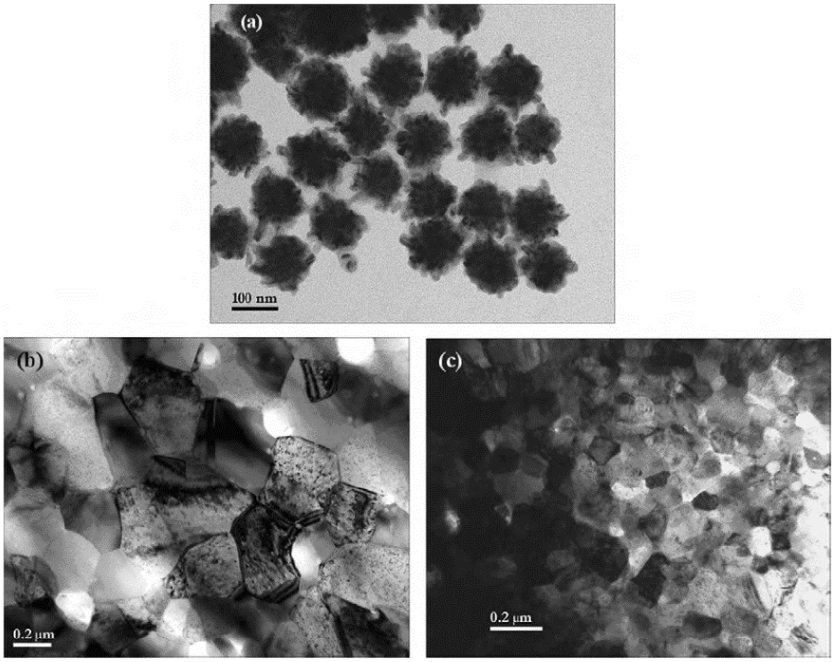

Fig. I-29 Ni nanopowder for UFG processing (a). Microstructure obtained after consolidation of nanopowders by HIP (b) and SPS (c) [41].

Further characterization on the nature of grain boundaries of UFG samples processed from nanopowders was performed by determining the distribution of misorientation angles with similar results between J. Gubicza *et al.* and Q.H. Bui *et al.* [40]. A high fraction of 60° misorientation angles (Fig. I-30) corresponding to Σ3 grain boundaries is depicted, as well as a slightly higher fraction of misorientation angles below 15° than that proposed for random distribution by J.K. Mackenzie [115].

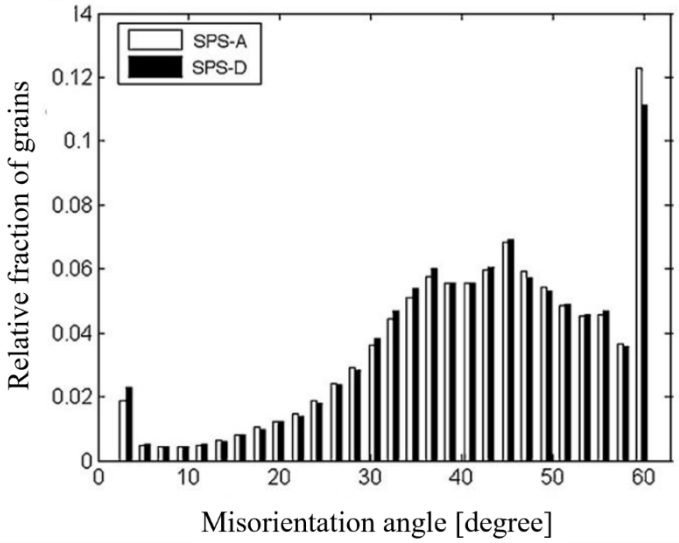

Fig. I-30 Misorientation angle distribution for Ni samples processed by SPS from nanopowders, exhibiting UFG grain sizes of d = 250 nm (SPS-A) and d = 318 nm (SPS-D) [40].

Concerning UFG Ni sintered from BM powder, even less information is available. To our knowledge, a single paper is found in literature [84] of a BM powder sintered by SPS at 750 °C and different uniaxial pressures (holding time of 5 min). Samples exhibit a relative density of 96.0 (5) % and 98.0 (5) % for 100 MPa and 200 MPa pressures, respectively. Unfortunately, the average grain size is only specified for the sample processed at 200 MPa (130 nm, measured by XRD profile fitting) and no other microstructural features are reported.

Thin film Ni samples processed by electrodeposition and sputtering

Microstructures obtained by ED and sputtering exhibit various features depending on the processing parameters. Of all UFG/nanostructuration techniques, they produce samples with the smallest grain sizes. K.S. Kumar *et al.* [64] studied ED Ni with an average grain size of 30 – 40 nm. The samples exhibited equiaxed grains (Fig. I-31) at the surface perpendicular to the deposition axis and columnar grains in the parallel surface. Regarding samples obtained from sputtering, D.B. Bober *et al.* [102] investigated the GBCD in Ni samples, which exhibited a high fraction of Σ3 grain boundaries (~22 %). To account for this observation, authors propose a growth mechanism that promotes the formation of Σ3 type boundaries. This mechanism, would also account for a high fraction of Σ9 and Σ27. As a result, the microstructure displays a fraction of CSL (Σ3 – Σ29) of ~33.5 %. The fraction of low angle grain boundaries of ~7 % is also characteristic of deposited materials (both ED and sputtered), which is still above the fraction found for random distribution (2.9 %).

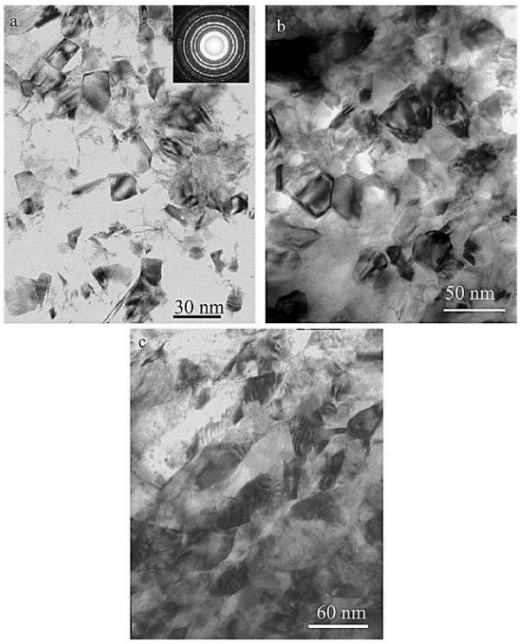

Fig. I-31 Microstructures of Ni samples processed by electrodeposition viewed in the surface perpendicular (a-b) and parallel (c) to the deposition axis. The surface of the sample shows equiaxed grains whereas the cross-section exhibits a columnar grain growth [64].

Dislocation structures are rarely found in NsM materials prepared ED and sputtering, nevertheless, a higher microstrain level than samples prepared by SPD has been reported [110]. Finally, an important difference between ED and sputtered materials with other UFG processing techniques is the presence of crystallographic texture. In the case of ED Ni, the microstructure exhibits a preferential texture along {200} planes and for sputtered Ni, a fiber texture that persists after grain growth.

3.3. *High diffusivity and thermal stability in UFG Ni*

Special high diffusivity paths and low thermal stability have been reported for SPD processed UFG metals [116–119]. Their reduced grain size in the lower range of UFG microstructures combined with the presence of deformation-modified grain boundaries are responsible for these features [78]. Concerning UFG metals processed by other techniques, nanostructured samples obtained by ED also display reduced thermal stability [57,61] and increased diffusivity [120], while studies concerning diffusion or thermal stability of UFG samples prepared by powder metallurgy are not easily found in literature. The following section introduces these aspects for UFG Ni as an important feature to enrich discussions on Chapter V of this manuscript.

High diffusivity in UFG/nanostructured Ni

Diffusion is responsible for major processes such as oxidation, corrosion or thermal stability. Hence, the study of self-diffusion as well as the diffusivity of other species can be the key to understanding unresolved issues concerning the above mentioned and other processes. Solid-state diffusion in crystalline materials takes place through several structurally different paths such as free surfaces, the crystal lattice and microstructural defects (dislocations and grain boundaries). For metals, the jump rates of atoms along free surfaces, dislocations and grain boundaries are much higher than in the lattice [121]. As a result, these regions are called short-circuits or high-diffusivity paths. The slowest path is bulk or lattice diffusion and is characterized by its diffusion length $\sqrt{D_v t}$. Faster diffusion through high-diffusivity paths can be observed in Fig. I-32 (a).

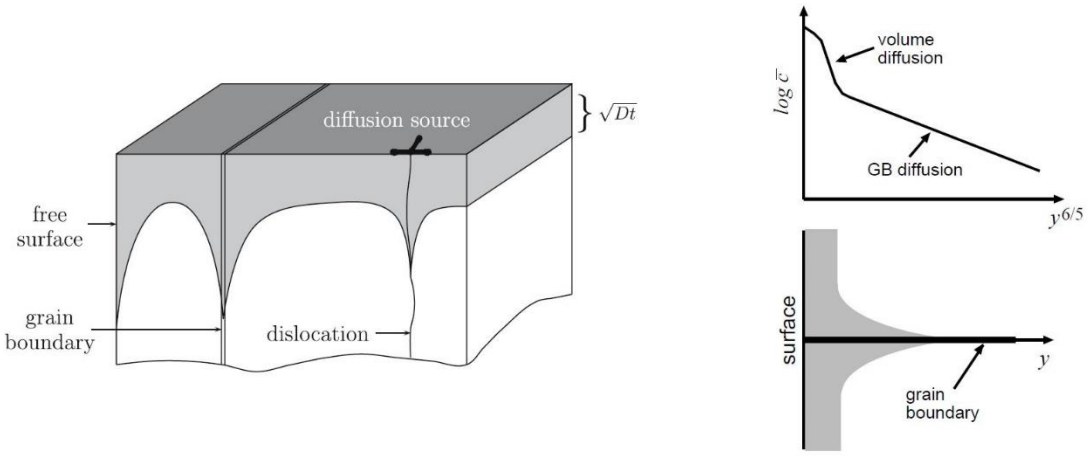

(a) (b)

Fig. I-32 Illustration of high-diffusivity paths in a solid (a) [121]. The gray color area represents the diffusing species. Schematic shape of a penetration profile of grain boundary diffusion (b) [122].

The most studied short-circuits are grain boundaries as they strongly influence major properties in polycrystalline materials. They can be studied experimentally from penetration profiles choosing the appropriate conditions of temperature and time. For instance, Fig. I-32 (b) shows the schematic shape of a penetration profile obtained when investigating grain boundary diffusion. Such penetration profiles can be obtained by the radiotracer method (Fig. I-33), where diffusivity of a radiotracer is evaluated by determining its concentration at different penetration levels after an annealing treatment. Diffusion coefficients can then be calculated considering different diffusion models that will be discussed in more detail in Chapter V.

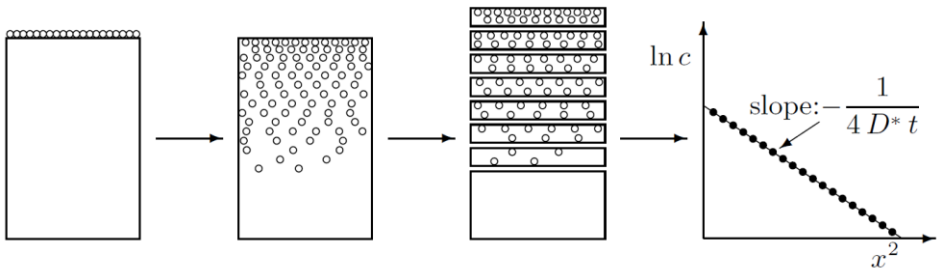

Fig. I-33 Illustration of the major steps of the tracer method: deposition of the tracer, diffusion annealing, serial sectioning and profile construction [122].

Nevertheless, the study of grain boundary diffusion is not trivial as the number of possible paths is elevated. For instance, the distorted structure of dislocation cores entails smaller constraints for atomic motion than lattice diffusion, thus displaying higher diffusivity. Likewise, in free surfaces the motion of diffusion defects is the least constrained, representing the highest diffusivity path. The hierarchy between lattice diffusivity (D_v), dislocation diffusivity (D_d), grain boundary diffusivity (D_{gb}) and surface diffusivity (D_s) can be observed in Fig. I-34 at different temperatures.

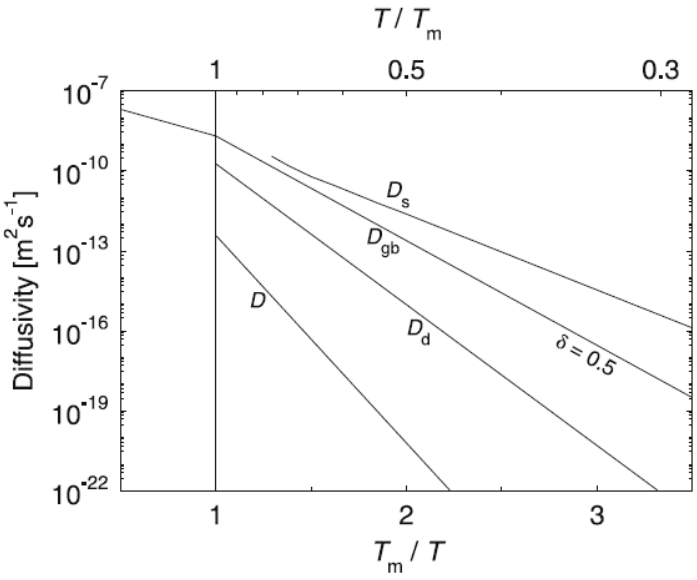

Fig. I-34 Schematic illustration of the evolution of diffusion coefficients with temperature in metals [121].

Grain boundary diffusivity follows an Arrhenius type dependence with temperature:

$$D_{gb} = A_0 \cdot e^{\left(-\frac{E_a}{RT}\right)} \tag{1.5}$$

where A_0 is the pre-exponential factor, E_a the activation enthalpy, R the gas constant and T the absolute temperature. In fact, the smaller activation enthalpy of GB diffusion makes the difference between grain boundary diffusion and lattice diffusion in metals vary with temperature from four to six orders of magnitude, to an even higher value at low temperature [121].

This introduction to high-diffusivity paths is a general view of the problem. Nevertheless, real systems such as SPD microstructures are much more complex. For instance, Fig. I-35 displays four types of grain boundary diffusion paths present in an SPD processed microstructure: deformation modified grain boundaries, random HAB, triple points and twin boundaries (TB). To complete the description of possible short-circuits, dislocation walls are also represented in Fig. I-35, only lacking individual dislocations, LAGB and interconnected porosities.

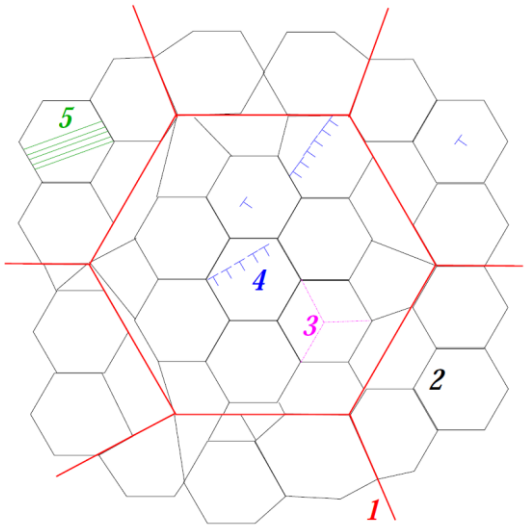

Fig. I-35 Short-circuit diffusion paths present in an SPD microstructure. 1 Deformation modified grain boundaries. 2 Random high angle grain boundaries. 3 Triple points. 4 Dislocation walls. 5 Twin boundaries. [123]

In the review paper by S.V. Divinski [123], an example of the hierarchy of short-circuit paths is stablished from measurements in pure Cu. Coherent twin boundaries, individual dislocations and dislocation walls are the slowest paths, followed correspondingly by LAGB, random HAB and "deformation-modified" boundaries. The fastest path corresponds to interconnected porosities. All of these features can be found on SPD materials and most are found in all metals.

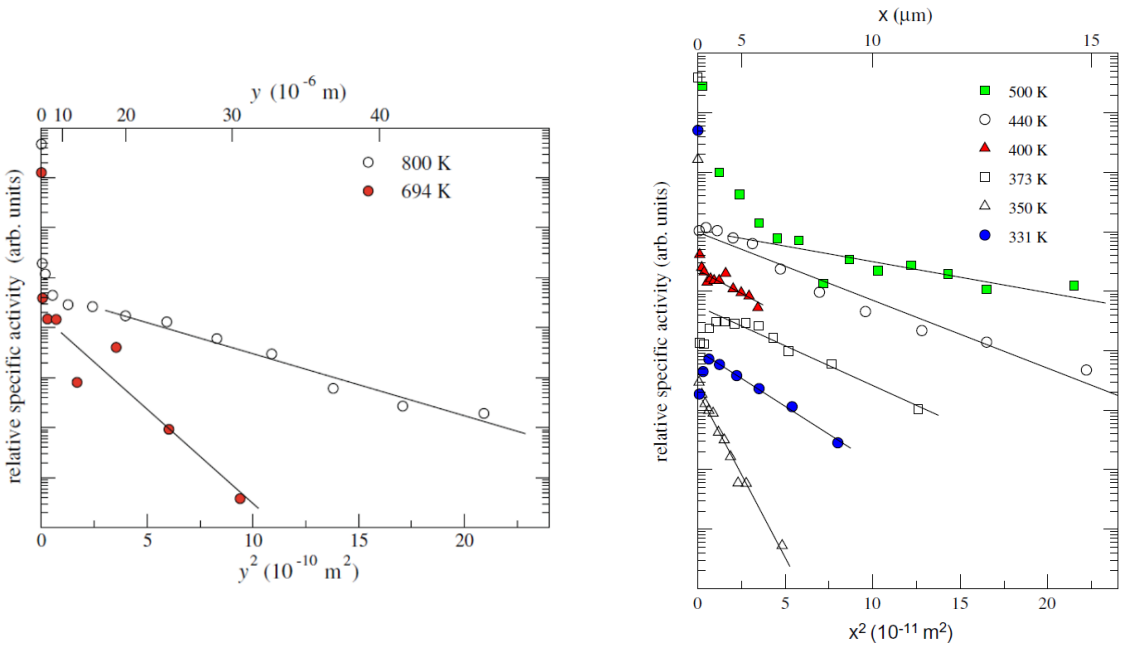

(a) (b)

Fig. I-36 Experimental penetration profiles of CG [124] (a) and UFG [125] (b) Ni of the same purity (2N6) in the C-type kinetic regime. y and x represent the penetration depth.

These short-circuit paths can be discernible from a proper analysis of penetration profiles. Such are the studies performed on UFG Ni processed by ECAP [126], demonstrating the presence of deformation-modified boundaries as well as the formation of percolating porosity after specific heat treatments. In Fig. I-36, experimental penetration profiles for coarse grain (CG) (Fig. I-36 (a)) and UFG Ni (Fig. I-36 (b)) of the same purity are exhibited for comparison. The profile corresponding to T = 694 K in (a) and all profiles in (b) were measured in experimental conditions that reflect only grain boundary diffusion ($\sqrt{D_{gb}t} >> \sqrt{D_v t}$). Concentration is expressed in relative specific activity, as the concentration of radiotracer in each section is determined from the emission of β or γ radiation, which is proportional to the amount of tracer.

A steeper slope corresponds to slower grain boundary diffusion, thus a qualitative comparison can be made between the diffusivity of CG Ni and UFG Ni. The profile corresponding to the lowest temperature (694 K) in Fig. I-36 (a), displays a steeper slope than the profile corresponding to the highest temperature (500 K) in Fig. I-36 (b), which reflects the higher diffusivity measured in the UFG sample. This is confirmed by the calculation of D_{gb} for both cases, $8.34 \cdot 10^{-17}$ m^2/s and $1.74 \cdot 10^{-16}$ m^2/s, respectively. Care must be taken when comparing these two values, as they were determined at different temperatures. Thus, a better outlook is possible from Fig. I-37. Diffusion coefficients in UFG Ni are orders of magnitude above the corresponding values in CG Ni.

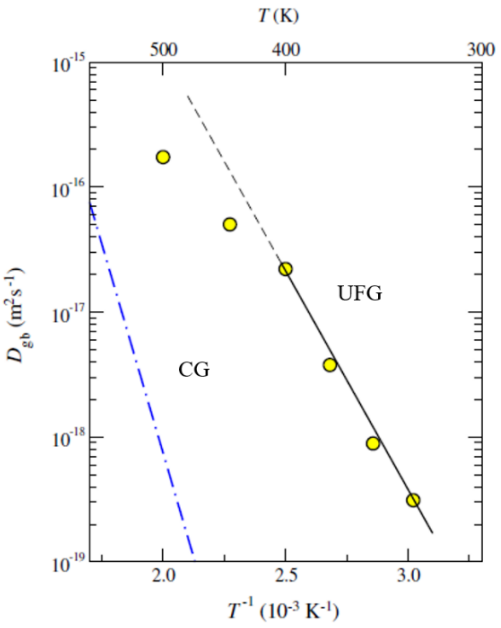

Fig. I-37 Measured diffusion coefficients of ^{63}Ni in ECAP processed Ni (circles) as a function of temperature compared to a CG Ni sample (dashed blue line) [125].

As mentioned above, the high diffusivity is mainly due to the presence of deformation-induced boundaries in UFG specimens compared to random HAB in CG microstructures. The high density of

extrinsic grain boundary dislocations increases the specific energy and the free volume of this type of grain boundaries, which results in higher specific mobility for atomic transport along the boundaries [127]. In fact, to confirm this hypothesis, Y.R. Kolobov *et al.* [120] studied grain boundary diffusion of copper in Ni for three samples, coarse-grained Ni, UFG Ni processed by SPD and nanostructured Ni obtained by ED. Results showed that in both UFG/nanostructured samples (SPD and ED), diffusivity at low temperature was much higher than in the coarse-grained sample. Nevertheless, when comparing the grain boundary diffusion coefficient at 423 K, the value of SPD processed Ni was two orders of magnitude above the one of Ni nanostructured by ED. The non-equilibrium nature of the deformation modified grain boundaries, can be eliminated by "relaxation" of the boundaries by annealing treatments [125]. Nevertheless, the persistence of these ultra-high diffusivity paths after recrystallization, have been observed in SPD processed Ni [117].

Thermal stability

Finally, thermal stability is addressed as an important issue in UFG metals. Their characteristic microstructures display numerous defects and interfaces resulting in low thermal stability. Recovery and recrystallization highly depend on the energy state of the sample. Hence, smaller grain sizes or higher internal stresses contribute positively to lower the temperature at which this processes take place. In fact, homogeneous microstructures with very small grain sizes are the most unstable microstructures as heterogeneities in the microstructure can hinder complete recrystallization. A good example is Ni processed by Dynamic Channel Angular Pressing (DCAP) [128], which is an SPD technique similar to ECAP. For samples prepared by several passes displaying homogeneous microstructures, recovery processes start at 673 K and recrystallization at 773 K. Nevertheless, DCAP processed Ni after only one pass (heterogeneous microstructure) exhibits incomplete recrystallization at 773 K. Interestingly enough, for the optimized UFG microstructure, with d = 0.35 μm, after complete recrystallization (773 K for 1 hour) a high density of defects can still be depicted from TEM observations (Fig. I-38).

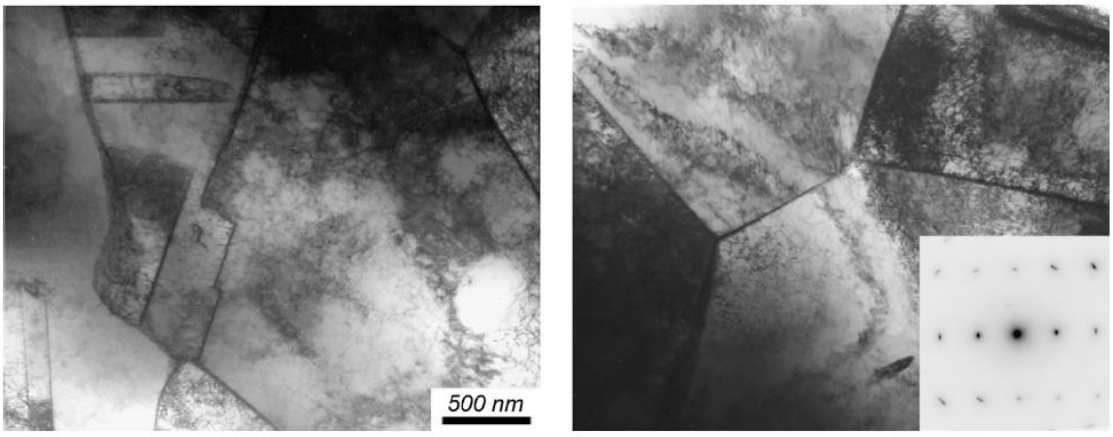

Fig. I-38 TEM micrographs of a DCAP Ni sample after annealing at 500 °C for 1 hour.

K. Sitarama *et al.* investigated Ni processed by ECAP after 12 passes [129]. For this sample, of grain size d ~ 0.17 µm, recovery starts at 423 K although the onset of recrystallization is at 523 K. This temperature is much lower than for DCAP Ni, but grain size is also considerably smaller. Complete recrystallization is achieved at 673 K. No TEM images or dislocation density values are reported in this work for the recrystallized state. Nevertheless, the evolution in the measurement of GOS, from 1.3° at the initial state, to 0.8° in the recrystallized state, confirms a reduction of small crystallographic misorientations that can be related to the presence of dislocation structures (Fig. I-39) [130].

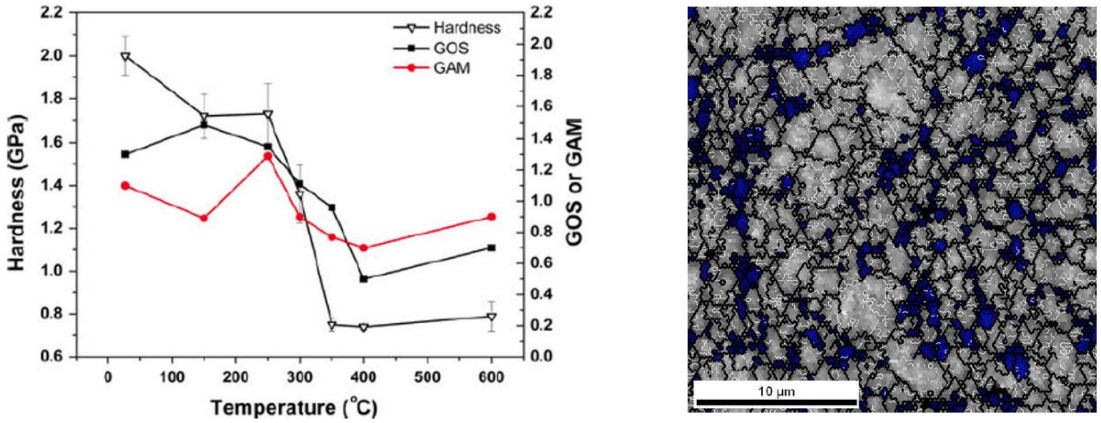

(a) (b)

Fig. I-39 Evolution of GOS, GAM and hardness vaules with isochronal annealing (a). Image quality cartography displaying recrystallized grains, with a GOS ≤ 1° in blue [129].

Let us now consider thermal stability of HPT processed samples. H.W. Zhang *et al*. [118] studied two samples prepared with the same strain level but different purities, 4N and 2N. Both samples display microstructures with elongated grains (some equiaxed grains in sample 4N) and an average boundary spacing of d ~ 100 nm. Recovery starts in the temperature range 413 K-433 K for sample 4N, where at 433 K grain coarsening can be depicted. For the sample 2N, the microstructure is stable up to 623 K and at 773 K full recrystallization is achieved. This suggests boundary pinning by impurities in samples 2N which can considerably increase the stability of the microstructure.

Taking into account the results concerning the thermal stability of SPD processed Ni some conclusions can be drawn. Smaller grain size as well as homogeneous microstructures display the lowest stability, with recovery starting at temperatures below 423 K. Finally, regardless the SPD technique used, full recrystallization is reached at 773 K.

To conclude this section concerning thermal stability, an example of the low stability displayed by ED Ni is shown in Fig. I-40. In this study [61], annealing the nanostructured Ni samples for a short period of time at 523 K is enough to trigger grain growth. This outcome is not surprising considering an

initial grain size of 20 nm. Grain sizes in the present manuscript are in the upper range of UFG sizes and thus expected to display a much higher thermal stability.

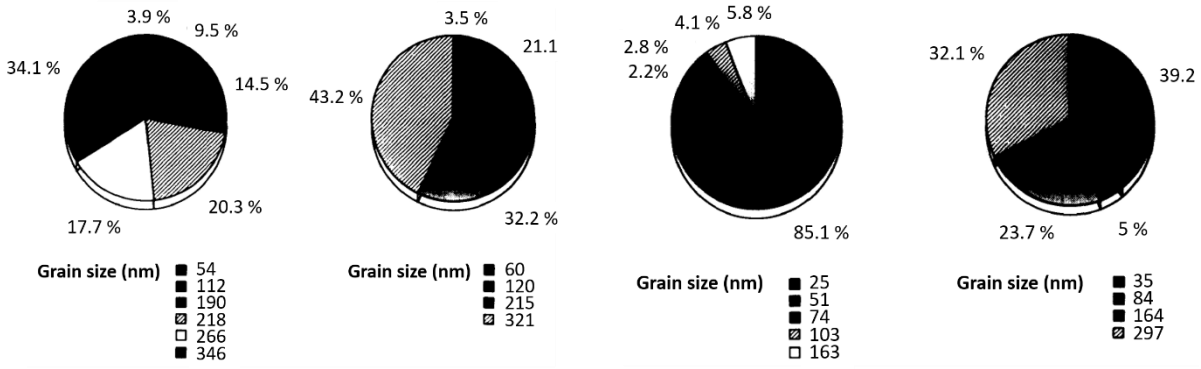

(a) (b)

Fig. I-40 Comparison of the average grain size of 20 nm Ni samples annealed for 15 min (left), 60 min (right) at 523 K (a) and 30 min (left), 60 min (right) at 573 K (b) [61].

4. Conclusions and perspectives

In the present work a mixture of two grain refining processes is contemplated, SPD via ball milling for powder processing and sintering to produce the bulk samples. R.Z. Valiev *et al*. [20] had studied the consolidation of ball-milled Ni powders by straining in torsion under high pressure at room temperature in 1996. Nevertheless, the resulting specimen presented a high density of lattice defects. The use of powder metallurgy allows for sintering and recrystallization of the highly deformed powders, thus producing stable microstructures with a lower density of defects. In addition, the combination of the two methods can withdraw some of the disadvantages of SPD processed specimens such as their limited geometry and size. The development of knowledge concerning powder metallurgy as a tool for processing UFG metals is thus crucial to comprehend the possibilities of these techniques and possibly expand their use for manufacturing high performance pieces. This first chapter stated the context of UFG metals. They represent the middle ground between coarse-grained and nanostructured materials in terms of grain size, yet they display unexpected properties. The different processing methods have been introduced to help construct a global view of the advantages and disadvantages of each technique.

The macroscopic properties of UFG metals were reviewed focusing on mechanical properties, diffusivity and thermal stability as they make the object of study in this manuscript. Concerning mechanical properties, the measured yield strength for UFG Ni prepared by SPD or powder metallurgy displays a deviation from the expected behavior contemplated by the Hall-Petch relation. So far in UFG samples processed by PM the extra strengthening was attributed to an elevated presence of oxides,

nevertheless an investigation concerning non-oxidized samples is lacking. Likewise, studies concerning ductility are scarce and an analysis of the strain-hardening behavior from tensile testing is, to our knowledge, not found in literature for samples prepared by powder metallurgy. Other functional properties were briefly introduced for a better outlook of the effects of refining the microstructure on macroscopic properties.

A summary of the microstructural features in UFG Ni samples showed important differences concerning minimum grain size, GBCD or dislocation densities depending on the synthesis route. For specimens prepared by powder metallurgy, a deeper characterization of the nature of grain boundaries is lacking, which could explain the discrepancies encountered when comparing results concerning some physical or mechanical properties of UFG metals.

Diffusion measurements at low temperature in SPD processed UFG Ni revealed the presence of special ultrafast paths. Deformation modified grain boundaries that are characterized by the presence of extrinsic grain boundary dislocations, which are responsible for the high diffusivity measured in UFG/NsM metals. Nevertheless, relaxation of this type of grain boundaries can be achieved by annealing treatments, decreasing grain boundary diffusion to the level of HAB. Low thermal stability is mostly displayed by UFG Ni samples, where recovery and recrystallization temperatures are dependent on the microstructure (grain size, homogeneity, deformation level) and are usually below 773 K.

Concerning UFG Ni prepared by powder metallurgy from SPD processed powder, many questions remain unanswered. Does the microstructure display a GBCD more similar to that of metals processed by SPD or powder metallurgy? Does yield strength deviate from the HP relation? Does it display good ductility and the same strain hardening mechanisms as CG Ni? Are ultrafast diffusion paths present in this type of samples? Do they exhibit good thermal stability? This manuscript will attempt to answer these questions with the intention of contributing to increase the knowledge on the possibilities of using powder metallurgy to process UFG nickel samples.

CHAPTER II. EXPERIMENTAL TECHNIQUES

As seen in Chapter I the processing technique and parameters for the synthesis (number of passes, pressure, temperature, etc.) have a major impact on the microstructure. Hence, a proper description of the approach used for the synthesis of the samples is essential. Likewise, the preparation of samples prior to measuring properties such as ductility or grain boundary diffusion, as well as the parameters chosen for the measurement itself, gives rise to contradictions in the results obtained by different studies. The aim of this chapter is to present the processing techniques and the methodology used for the characterization and the measurement of the properties displayed by the Ni samples, to enable the reproduction of the experiments performed in this study as well as the comparison with other studies.

1. Starting material: as-received high purity nickel powder

The starting material is a high purity nickel powder provided by Good Fellow©. The powder has a certified purity of 99.8 %, with the main impurities being: Fe 100 ppm, C 200 - 600 ppm, O 1000 ppm and S 10 ppm. The carbonyl process[3] is specified as the synthesis technique.

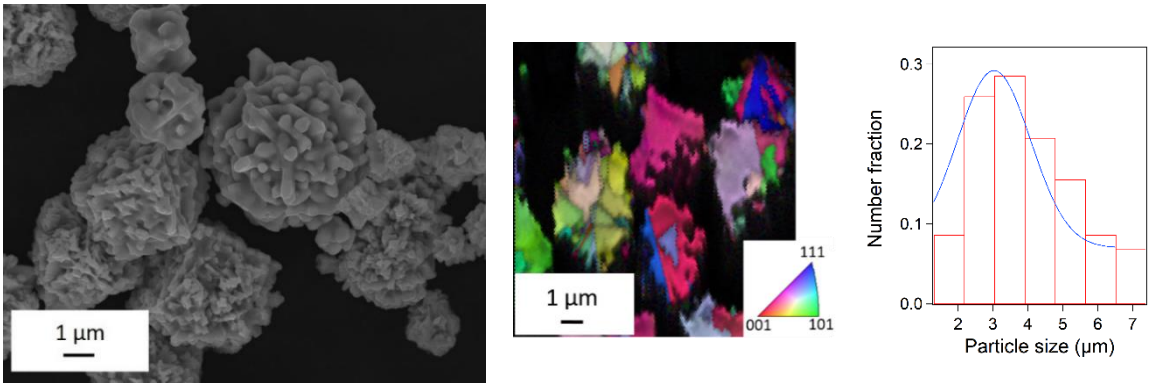

(a) (b) (c)

Fig. II-1 Scanning Electron Microscopy (SEM) image (a), orientation cartography (Inverse Pole Figure) obtained from electron backscatter diffraction (EBSD) (b), and distribution plot of particle size (c) of the as-received Ni powder.

Fig. II-1 (a) shows the morphology of the particles, which is a mixture of spherical and cubic shapes. The "spiky-dendritic" aspect of the surface is present in both shapes and is characteristic of the nickel carbonyl process. Each particle is a polycrystal (Fig. II-1 (b)) with different grain sizes. The mean

[3] Also known as the Mond process [131], in this process the reaction between nickel and carbon monoxide forms nickel carbonyl gas ($Ni(CO)_4$). Decomposition of this compound using thermal shock results in nickel powders with a small particle size.

particle size was determined from digital image processing using the software Igor Pro 6.3, covering over 100 particles. The average particles size is 3.5 µm with a narrow size distribution (Fig. II-1 (c)) and a standard deviation of 1.5 µm.

2. Processing techniques

Processing of bulk UFG Ni samples was accomplished in two steps. First, the as-received powder was nanostructured by means of ball milling. Afterwards, Spark Plasma Sintering was chosen to consolidate the powder into nearly dense samples presenting different microstructures.

2.1. *Powder Nanostructuration by mechanical milling*

Nanostructuration of metallic powders was achieved by means of severe deformation by high-energy ball milling (BM). The process was carried out in a PULVERISETTE 7 premium line using WC grinding vials (80 mL) and balls (diameter of 5 mm). A ball to powder ratio of 10:1 was fixed for all experiments. Per cycle, 12 g ± 0.2 g of powder were milled in each vial. Methanol was chosen as Process Control Agent (PCA) for its low boiling point (338 K) as well as its low reactivity with nickel powders [132,133]. The amount added (variable) was determined by its mass with an uncertainty of 0.1 g. Vials were prepared inside a glove box filled with high purity Ar to avoid oxidation of the powders during milling. For every synthesis, time was divided into cycles of 5 min of milling with 1 minute of pause between cycles to prevent temperature from rising inside the vials creating an overpressure. Both cycles (milling and pause) are considered when detailing milling time. The sense of rotation was systematically reversed between cycles to favor homogenization. In order to eliminate the PCA, MeOH was evaporated at room temperature inside the glove box. No heating of the powder was done prior to the sintering process to preserve the microstructure generated by the milling process.

Three BM parameters were modified to obtain different grain sizes and microstructures: time, speed and the amount PCA. For each set of values, the other parameters were fixed as to have only one variable per group of experiments. The resulting powders were characterized by means of scanning electron microscopy (SEM) imaging and XRD. The SEM (Zeiss Supra 55) was operated at 15 kV, with an aperture size of 30 µm and a secondary electron detector (SE2). XRD with Panalytical X'Pert diffractometer using Cu Kα radiation (λ= 0.1541 nm) was used to verify the absence of contamination peaks and investigate the presence of preferred crystallographic orientation on milled powders.

2.2. *Spark Plasma Sintering*

Conventional sintering is not suited to consolidate highly deformed flattened powders as obtained after ball milling. Spark Plasma Sintering (SPS), combines uniaxial pressure throughout the sintering process with very high heating rate, 50 – 1000 K/min [134] making consolidation of ball milled powders possible with limited grain growth [41].

Principle of SPS

The high heating rate of SPS is achieved through the heat source of the device which consists in the simultaneous application of a low voltage (5.5 V max) and a high current density (20 to 94 kA/cm^2) [44] creating an electric current through the sample. The applied current is believed to generate a spark followed by plasma at the contact point of particles [135–137] under certain conditions. Nevertheless, heating is usually explained as a consequence of Joules effect [46]. In ductile materials, sintering results from the acceleration of dislocation motion and atomic diffusion [49]. Heating powders with different electrical conductivity (resistivity), dislocation density and diffusivity is possible by adjusting the processing current. This is achieved by a feedback mechanism, a thermocouple placed close to the powder measures the actual temperature variation and the program that guides the SPS device uses that information to regulate the voltage and current in order to achieve the heating rate defined in the synthesis program.

The powder is placed inside a graphite structure consisting of a cylindrical die of variable diameter and two punches. The structure is then positioned inside a vacuum chamber between two metallic punches that will serve as electrodes to generate the current and will apply the pressure onto the graphite punches (Fig. II-2).

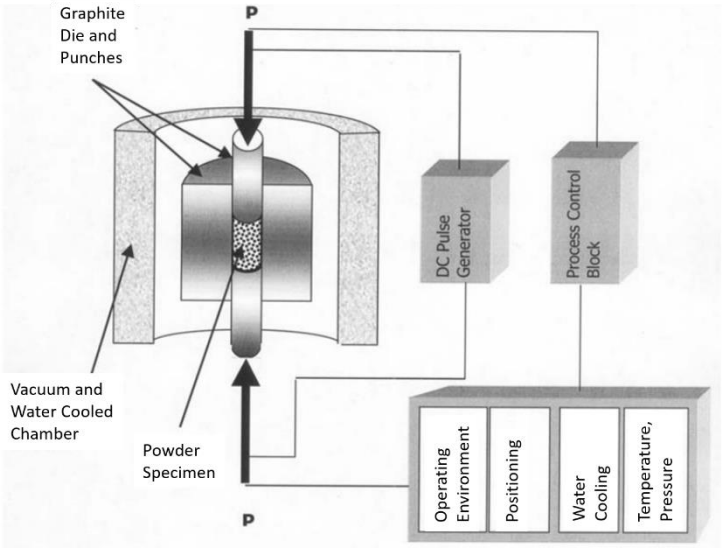

Fig. II-2 Schematic representation of a SPS device [44]

Sample Processing

SPS processing requires defining a sintering program, fixing multiple parameters. In order to limit the control of the microstructure to the BM process, the same SPS program was used independently of the powder. Sintering of the powders was conducted with a dispositive FCT System GmbH, HD 25. The sintering temperature was set to 1023 K and maximum pressure to 75 MPa. The uncertainty of the measurement of temperature by the thermocouple placed 2 mm away from the powder is 0.1 K. Continuous current was used heating at a rate of 100 K/min. Pressure was increased simultaneously to heating achieving the maximum value at 773 K and remaining constant until cooling (Fig. II-3. (a)). Medium dynamic vacuum is maintained throughout the synthesis cycle.

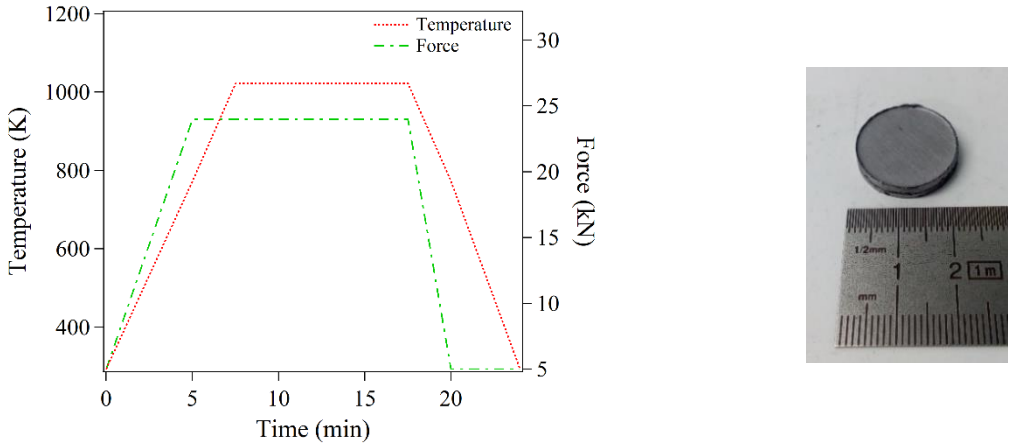

Fig. II-3 Temperature and force cycles during SPS processing of a 20 mm sample (a). Disk-like SPS sample in the raw state (b).

Upon unmolding, the raw specimens are discs with a diameter of 20 mm covered by a graphite paper that prevents the reaction between the powder and the die during sintering (Fig. II-3 (b)). Additionally, samples with diameters of 50 mm and 10 mm were processed for tensile testing and radiotracer self-diffusion measurements, respectively.

3. Specimen characterization

Once the powder is compacted by SPS into dense bulk specimens, an initial preparation of the sample consists in mechanically grinding and polishing the surface to eliminate the graphite foil. A finer preparation by electropolishing[4] or colloidal silica suspension polishing was effectuated for electron backscatter diffraction analyses and radiotracer diffusion measurements respectively.

[4] Electropolishing was performed in a Struers Lectropol device using a solution of perchloric acid, 2-butoxyethanol and ethanol as electrolyte at a voltage of 24 V.

3.1. *Density measurements*

One of the challenges of producing UFG metals by PM is achieving nearly dense samples at sufficiently low sintering temperature to avoid grain growth. Density measurements were performed by averaging four different measurements with an Excellence XP/XS- Mettler Toledo precision balance using absolute ethanol as auxiliary liquid. A method based on the Archimedes principle was used to compute densities using Eq. 2.1:

$$\rho = \frac{A}{A-B}(\rho_L - \rho_0) + \rho_0 \tag{2.1}$$

where A is the weight of the sample in air, B, the weight of the sample in the auxiliary liquid, ρ_L is the density of the auxiliary liquid at the temperature measured and ρ_0 the air density (0.0012 g/cm^3). Likewise, uncertainty for each measurement was determined with Eq. 2.2:

$$\Delta\rho = \left|\frac{-B(\rho_L-\rho_0)}{(A-B)^2}\right|\Delta A + \left|\frac{A(\rho_L-\rho_0)}{(A-B)^2}\right|\Delta B + \left|\frac{A}{A-B}\right|\Delta\rho_L \tag{2.2}$$

where ΔA and ΔB equal to 0.001 g and $\Delta\rho_L$ is 0.00017 g/cm^3 determined with the uncertainty in the measurement of temperature. The air density is considered a constant.

3.2. *Porosity characterization by SEM*

In order to study the size, location and morphology of porosities, two samples were examined by means of SEM imaging. To this aim, the surface parallel to the SPS force axis was prepared by cross-polishing[5]. This technique uses an ion beam to eliminate several layers of the material, to reveal different microstructural features that are hidden or enhanced by other preparation techniques (mechanical polishing and electropolishing). SEM images were taken at a current of 5 kV, an aperture of 30 µm and a working distance (WD) of 3-5 mm. A mixture of detectors of secondary electrons were chosen to obtain an image contrast related to the crystallographic orientation of grains and be able to identify the location of pores: at grain boundaries or inside the grain. A statistical study of the size and location of pores was done for both samples, covering more than 100 pores.

Complementary characterization of the porosities was possible using a Focused Ion Beam (FIB). A surface of 220 µm^2 was inspected for three samples before and after milling at different depths to look for interconnected pores[6].

[5] Preparation done by Muriel Strebel.
[6] Performed by Bernadette Domenges at the CIMAP laboratory.

3.3. *Microstructure analysis by EBSD*

Principle of EBSD

Electron backscatter diffraction (EBSD) is a scanning electron microscopy technique used to determine crystallographic orientations in crystalline materials. The versatility of this tool allows for quantification of different microstructural features including: grain size, phase fraction, grain boundary character distribution (GBCD), microtexture (texture at the microstructure scale) or small misorientations related to internal stresses. The principle of EBSD is the acquisition and analysis of Kikuchi diffraction patterns Fig. II-4 (a) obtained from the surface of the specimen. The sample is placed tilted 70° with respect to the electron gun to maximize the signal of diffracted electrons Fig. II-4 (b).

After setting the acquisition program, the electron beam scans the surface of the sample generating Kikuchi diffraction patterns at points separated by a defined distance (scanning step). Bands are converted to points (Hough transform) and indexed by comparison with a database of interplanar angles. Once the closest fit is chosen, the orientation between the solution and the reference axis system is determined and the result is recorded [138].

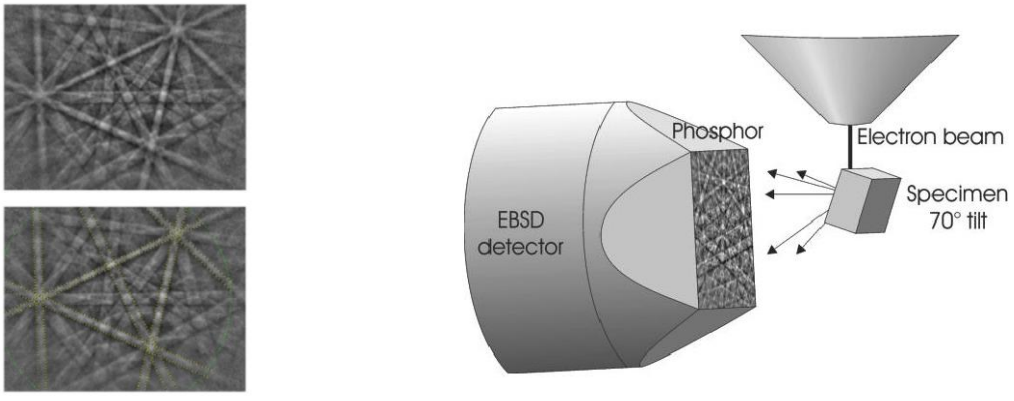

(a) (b)

Fig. II-4 Kikuchi diffraction patterns (upper figure), including simulated bands (lower figure) [139] (a). Schematic EBSD experimental set-up [140] (b).

Once the acquisition is finished, two parameters define the quality of the measured results, the Image Quality (IQ) and the Confidence Index (CI). The IQ is defined by the intensity of peaks in the Hough space, which depends on how clearly the Kikuchi patterns are detected compared to background noise. CI on the other hand provides information on the quality of indexation between the measured patterns and the database options.

Acquisition and post-processing Parameters

For acquisition, an EDAX EBSD analysis system was employed for most of the samples[7]. The conditions for measurements were a voltage of 20 kV, an aperture of 120 µm and a WD of 14 mm. The detector settings where slightly modified (gain, exposure) to optimize the quality of detected patterns and a binning of 8x8 was fixed. Step size was selected as ten times smaller than expected grain size (30 nm – 3 µm) in order to collect enough Kikuchi patterns per grain. For each sample, at least 1000 grains were covered for statistical accuracy.

The measured data was post-processed by means of the commercial TSL OIM® analysis 6x64 software. Basic clean-up was performed by the grain dilation method with a grain tolerance angle of 2° and a minimum grain size of 4 pixels by single iteration to eliminate artifacts. A filter excluding all points with an IQ < 600 was used in selected scans in order to have a more accurate measurement of the GBCD. The following assumptions were made for the microstructural characterization. To define a grain, minimum grain size was set to four times the step size and minimum misorientation to 2°. For grain boundary characterization, low angle grain boundaries (LAGB) were defined in the misorientation range 2°-15° and coincidence site lattice (CSL) boundaries were defined using the Brandon criterion [108,109]. The fraction of different boundaries was determined in a number basis (unless stated otherwise) and considered CSL boundaries are Σ3-Σ30.

Principles of grain orientation spread (GOS), grain average misorientation (GAM) and kernel misorientation

Reconstruction of EBSD data into orientation cartographies provides information on the crystallographic orientation of the sample at an exact point (x,y). Thus, in addition to misorientation between grains, small misorientations within the grains can be determined from EBSD analysis. These misorientations are used by several authors [129,130,141] to investigate the deformation state of polycrystals as the gradient in orientation inside a grain can be directly related to the presence of dislocations. As explained by L.N. Brewer *et al.* [142], the Nye dislocation tensor (α_{ij}):

$$\alpha_{ij} = e_{jkl} g_{jl,k} \tag{2.3}$$

where $g_{ij,k}$ expresses the spatial gradient of orientation and e_{ikl} is the permutation tensor, accounts for the misorientations that can be associated to the lattice curvature, which in turn is related to plastic deformation by:

[7] In November 2018, the system was updated to a QUANTAX EBSD (Bruker). The acquisition conditions: operating voltage of 15 kV, aperture size of 60 µm and WD of 14.5-16.5 mm.

$$\alpha_{ij} = \sum_{k=1}^{K} \rho_d^k b_i^k z_j^k \tag{2.4}$$

where ρ_d is dislocation density and the couple of $b_i^k z_j^k$ specifies a particular dislocation type where b is the norm of the Burgers vector and z is the line direction. In fact, the TSL OIM® analysis software enables the study of the gradient of orientation considering different reference systems for a more complete study of the samples. In this work, three types of misorientation have been selected for a comparative study of the deformation state of samples: GOS, GAM and kernel misorientation.

GOS

Grain orientation spread (GOS) is a parameter that measures the dispersion in orientation inside a grain from comparing the orientation of each pixel with the average orientation of the grain. To this aim, the software determines the average orientation of a grain ($\bar{g}$). Then, the minimum misorientation between the orientation of each pixel (g^A) and $\bar{g}$ is calculated. Finally, the GOS is calculated from the total number of pixels in a grain (N) as the average of all determined misorientations [143]:

$$GOS = \frac{1}{N}\sum_{A=1}^{N}\left\{min\left[\cos^{-1}\left(\frac{trace[\bar{g}(h_i g^A)]-1}{2}\right)\right]\right\} \tag{2.5}$$

where A represents a number given to each pixel and h_i represents a symmetry element that enables the determination of the angle of misorientation between $\bar{g}$ and g^A. An example of GOS cartography for a deformed state and a recrystallized state can be observed in Fig. II-5. The GOS distribution plots show an average value centered at 2.8° for the deformed sample (Fig. II-5 (a)) and at 0.4° for the recrystallized sample (Fig. II-5 (b)).

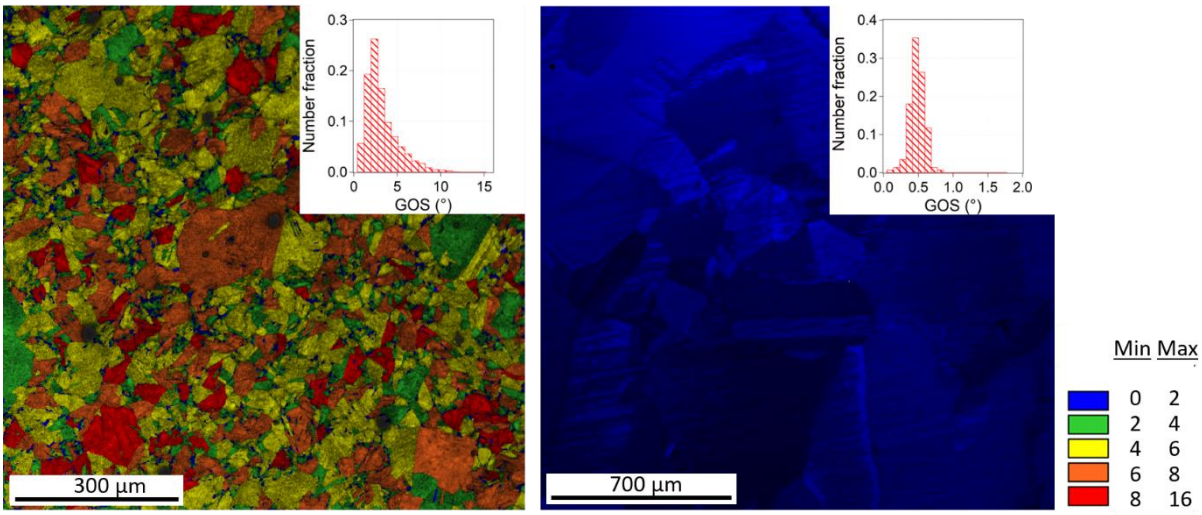

(a) (b)

Fig. II-5 Example of a GOS cartography of a deformed (a) and recrystallized (b) state of a Ni sample. Inset to each sample displays the GOS distribution plot. The color legend represents the GOS in °.

GAM

The grain average misorientation (GAM) represents the average local misorientation in a grain [144] and is calculated in two steps. First, the misorientation between pairs of pixels (Δg_{Ax}) is determined. For instance, the misorientation between pixel A and pixel one would be represented as Δg_{A1} (Fig. II-6). Then the measured Δg_{Ax} values are averaged to obtain a mean value of the misorientation found inside grains between neighboring pixels.

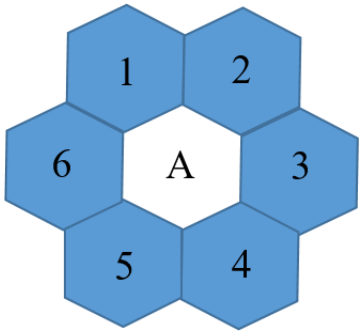

Fig. II-6 Example of hexagonal pixels used to construct grains in TSL OIM®.

GAM is thus a useful tool for an overview of local misorientations present in each grain in deformed samples. An example of a GAM measurement for a deformed Ni sample and an annealed Ni sample are displayed in Fig. II-7 (a) and (b) respectively. From the GAM distribution plots it can be seen that a GAM mean value of 2.6° is obtained for the deformed sample whereas 0.4° is obtained for the recrystallized state.

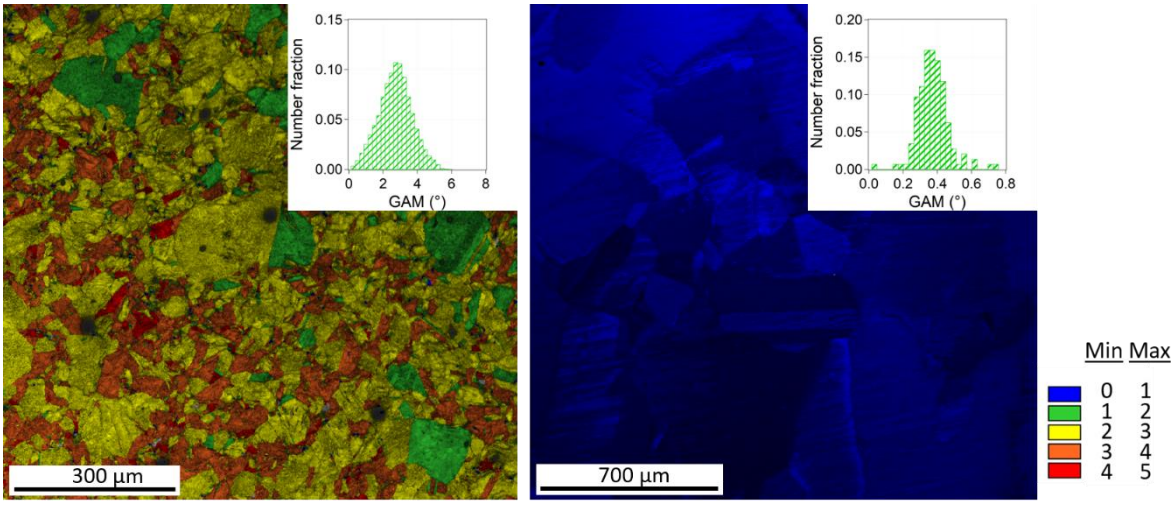

(a) (b)

Fig. II-7 GAM cartography in a deformed Ni sample (a) and an annealed Ni sample (b). The inset to each microstructure displays the GAM distribution plot. The color legend represents the GAM in °.

Kernel misorientation

Finally, the Kernel misorientation is used in addition to GOS and GAM in this work to determine the localization of the local misorientations in samples deformed by uniaxial tensile testing. To calculate the Kernel misorientation, similarly to the first part of GAM determination, Δg_{Ax} is computed for all neighboring points. Then, the average misorientation between A and its six neighbors is computed:

$$\Delta g_A = \frac{1}{6}(\Delta g_{A1} + \Delta g_{A2} + \Delta g_{A3} + \Delta g_{A4} + \Delta g_{A5} + \Delta g_{A6}) \quad (2.6)$$

Once the average misorientation between one pixel and its neighbors is determined, the pixel is colored accordingly to construct a cartography of kernel average misorientation (KAM). In addition to investigating short-range misorientations, the measurement can be performed in reference to pixels situated further from the reference (second neighbor, third neighbor, etc.) to obtain information of correlated misorientations at longer range (Fig. II-8).

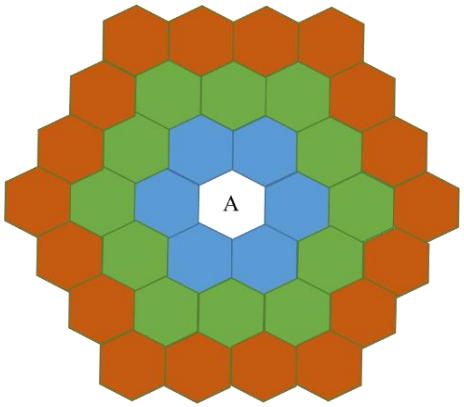

Fig. II-8 Example first neighbor (blue), second neighbor (green) and third neighbor (orange) pixels of pixel A.

Higher values of KAM have been correlated with a higher density of geometrically necessary dislocations (GNDs) [142,145,146]. Therefore, from KAM cartographies the location of higher densities of GNDs can be depicted. Kernel misorientation determination does not take into account grains, as pixels are studied individually, thus a maximum misorientation value has to be set to eliminate misorientations related to grain boundaries. In this work, following other authors [144,147,148], the maximum misorientation was set to 5°.

3.4. *Observation of dislocation structures by TEM*

Transmission electron microscopy (TEM) utilizes the interactions between an electron beam and the sample to render major information concerning the crystal structure, the defects or the composition of a sample at a nanometric scale. In this work, its use is focused on the observation of dislocations structures.

A dislocation is a linear defect characterized by its line direction $\vec{\xi}$ and its Burgers vector $\vec{b}$ (Fig. II-9). These defects are responsible for plastic deformation and their presence causes a distortion within the crystal, which increases the internal energy of the material. By means of TEM, the observation of dislocation structures is possible and provides a qualitative assessment of the energy level of a specimen. Likewise, when studying the deformed state of a sample, dislocation configurations provide key information to understand strain-hardening mechanisms.

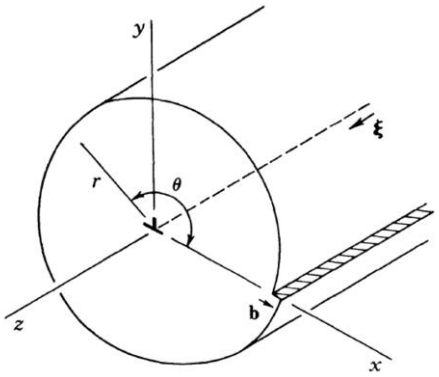

Fig. II-9 Illustration of an edge dislocation [149]**.**

A complete characterization of dislocations requires defining the orientation of the crystal under study in reference to the electron beam (Appendix A). When the sample is conveniently oriented, Bragg diffraction of a specific set of planes can be obtained. Thus by tilting the specimen at a certain angle, we can obtain different diffraction conditions and image contrast [150]. Dislocations in crystals are present and glide in specific planes and directions (slip systems). For face centered cubic (FCC) metals these planes are {111} and gliding occurs in <110> directions. Consequently, images formed from different diffraction conditions are necessary to account for dislocations in different slip systems. Once the crystal orientation reference is set, the specimen is rotated about its X and/or Y axis in order to obtain the information of the desired planes.

Dislocation observation is enabled by a difference in scattering of the electrons in the strained region. The crystal around the dislocation is distorted, planes are bent (Fig. II-10), which generates a perturbation in the interaction with the beam. When the two-beam diffraction condition is used, the direct beam and a diffracted beam are selected and dislocations are observed as black lines for $\vec{g} \cdot \vec{b} \neq 0$ (where $\vec{g}$ is the diffraction vector).

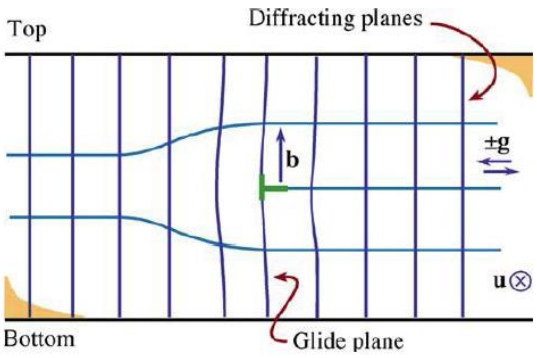

Fig. II-10 Representation of the local distortion of the crystal planes by the presence of an edge dislocation [150]. Here, the line direction of the dislocation is represented by $\vec{\mathbf{u}}$.

Sample preparation and TEM conditions

Regarding the preparation of the specimens for TEM, samples were initially mechanically polished down to a thickness of approximately 100 µm. Afterwards they were cut into 3 mm discs and finally, further reduction of the thickness was performed by electropolishing with a solution of 17 % perchloric acid in ethanol using the twin jet method in a Tenupol 5.

For dislocation observation, samples were mounted in a double tilt stage to enable rotation of the sample in the X and Y axis. A JEOL 2010 operating at a voltage of 200 kV and equipped with a CCD (Charge Coupled Device) camera for image acquisition was used. Small modifications (brightness, contrast and gamma) were performed on images with the software Digital Micrograph (Gatan version 2.32.888.0).

4. Mechanical properties, diffusion and thermal stability

Mechanical properties, diffusion and thermal stability are vast domains of study that cover some of the most crucial properties of materials such as mechanical strength, corrosion or the stability of microstructures with increasing temperature. In this work, the focus concerning mechanical properties is set on uniaxial tensile testing to determine major properties including yield strength, ultimate tensile strength (UTS), homogeneous deformation and work-hardening rates. Concerning thermal stability, self-diffusion at low temperature of selected samples as well as stability of the specimens at high temperature were investigated in order to enrich the understanding of the UFG samples.

4.1. *Mechanical properties*

Tensile specimen preparation

The usage of conventional tensile testing devices in the study of UFG samples requires tensile specimens with the proper dimensions. To this aim, SPS samples with a diameter of 50 mm and a thickness of 6 mm were processed from different powders (commercial and BM). To avoid introducing additional internal stresses into the specimens, electrical discharge machining was employed as the manufacturing method. Three tensile specimens were extracted from each SPS sample (Fig. II-11 (a)). Afterwards, samples with a thickness of one mm were obtained from each individual tensile specimen. The specimen dimensions (Fig. II-11 (b) values in mm) were designed to fulfill the standard specification[8].

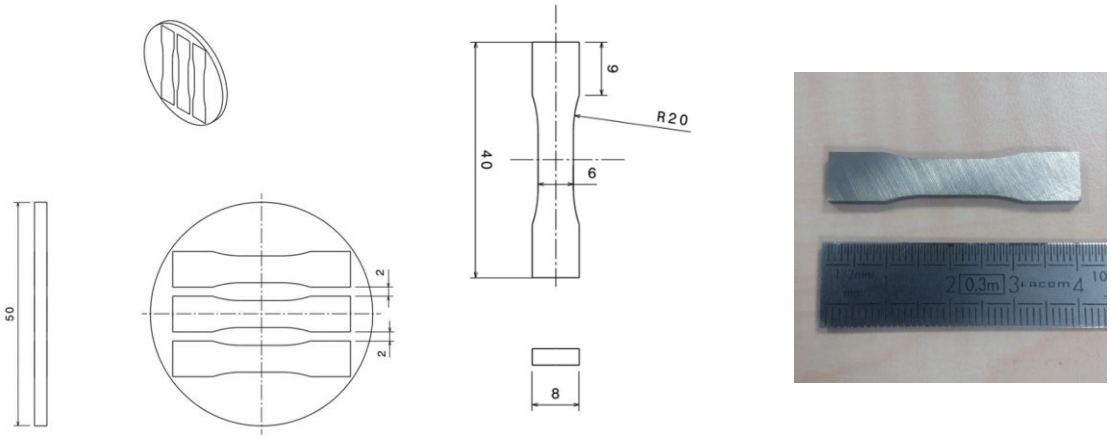

(a) (b) (c)

Fig. II-11 Illustration of the relative placement of tensile test specimens in the SPS processed disc (a), schematic diagram and dimensions of the samples (gauge length 11 mm) (b) and image of the resulting obtained specimen (c).

After processing, the samples (Fig. II-11 (c)) were polished to obtain a mirror like surface. Due to their small dimensions, the grip sections were carefully scratched with SiC grinding paper to guarantee a good grip.

Uniaxial tensile testing

Uniaxial tensile testing was carried out in a Zwick device with a load cell of 50 kN maximum capacity. Strain rate was fixed to 10^{-3} s^{-1} and deformation was recorded by measuring displacement fields using digital image correlation (DIC) through the use of the ARAMIS® software. To this aim, a fine speckle pattern is applied on the surface of the tensile testing specimen. Images of the surface of the

[8] Tensile specimens designed by Antoine Gueydan.

specimen are collected at a certain frame rate with a camera throughout the experiment. The frame rate was adjusted to record at least 250 images depending on the expected ductility of the samples. Three specimens were studied per SPS sample to verify repeatability of the measured properties.

For post-treatment of the images, the zone of interest (gauge length) was defined by facets of sizes 6-11 pixels separated by a step of 4-9 pixels. An extensometer is then created to cover the longitudinal length of the zone of interest and a DIC process determines the shift and distortion of little facet elements with respect to a reference image using a correlation algorithm. As a result, true strain is calculated and associated with the force at that deformation level. The acquisition ARAMIS software is connected to the tensile testing device and records for each image the force (as voltage) exerted at that instant. The maximum force accounted for by the tensile testing apparatus is related to the maximum voltage value determined by ARAMIS to calibrate the measurement. This method was chosen for strain determination due to the small dimensions of the specimens. In addition, deformation cartographies at different strain levels can be obtained (Fig. II-12) which provide information about inhomogeneity or localization of deformation.

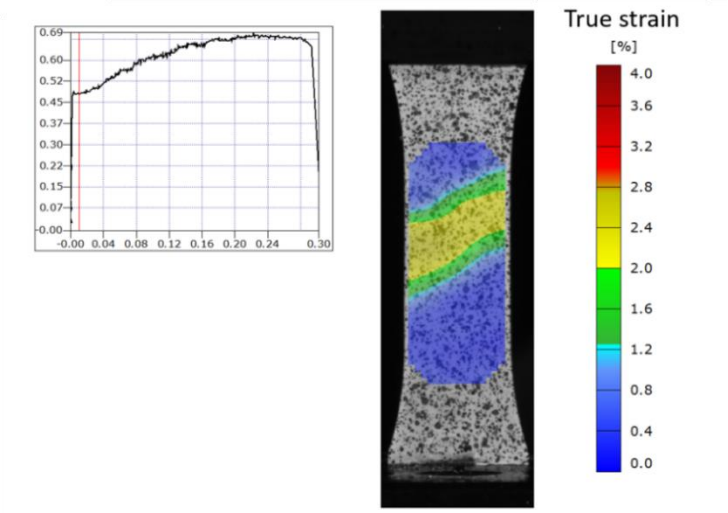

Fig. II-12 Example of a force (V)-true strain plot (left) and deformation cartography (right) of the zone of interest at the level of deformation indicated by the red line in the plot. Results processed by ARAMIS software.

4.2. *Thermal stability*

Radiotracer diffusion measurements at low temperature

Ultrafast diffusion channels have been reported for UFG Ni processed by SPD techniques (Chapter I). In order to evaluate their existence in UFG Ni obtained by SPS, self-diffusion measurements at low temperature were carried out in selected samples.

Radiotracer diffusion measurements were performed at the Institute of Materials Physics (University of Münster) in a doctoral stay of three months under the supervision of PD Dr. Sergiy Divinski. This technique enables the construction of penetration profiles with good accuracy that provide an insight of the diffusivity of a tracer in the system of study. A very small amount of the diffusion species is applied thus the composition of the sample remains constant. Hence, the diffusion coefficient can be determined and is independent of the tracer concentration.

Experimental procedure

To obtain reliable results, samples must be carefully prepared (Fig. II-13). First, mechanical grinding to ensure parallel surfaces was performed, finishing by thoroughly polishing with colloidal silica (OP-S 0.04 µm) one of the surfaces, which was inspected for scratches. Next, 2 µL of the liquid tracer solution was dropped on the mirror like surface. In order to investigate self-diffusion, the isotope ^{63}Ni[9] was chosen as radiotracer, which was available as a chloride solution. To obtain a specific activity of 5 kBq/µL approximately, the chloride solution was diluted with double-distilled water. Once the solution is dry, samples were carefully covered in Ta foil and placed in a sealed silica tube under high purity Ar (4N8).

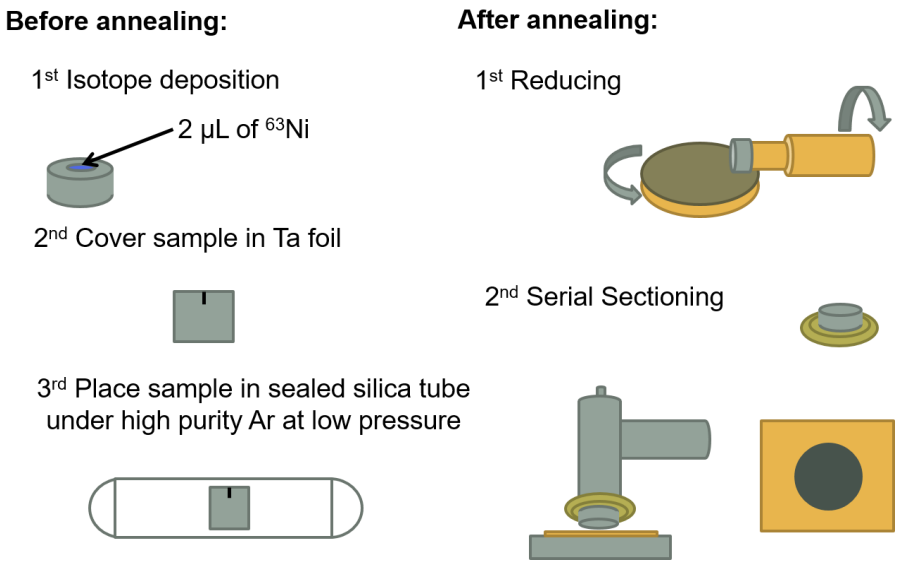

Fig. II-13 Diagram of the major experimental steps for radiotracer diffusion experiments.

Afterwards, the silica tube was introduced inside the furnace where temperature was measured with a Ni-NiCr thermocouple with an uncertainty of ±1 K. The samples were quenched in water at room temperature and the diameters reduced by 0.5 mm approximately to remove the effects of surface diffusion. To do so, samples are glued to a special support that rotates in contact with SiC grinding paper

[9] The isotope ^{63}Ni has a half-life of 100 years and emits β radiation, a neutron decays into a proton releasing a high-speed electron or positron plus an antineutrino.

in an automatic device. Before serial sectioning, the surface of the sample was etched with a solution of 1/3 Acetic acid, 1/3 water and 1/3 nitric acid, to remove the amount of tracer that did not penetrate the sample. A precision parallel grinder with 12 µm special abrasive paper was used to remove layers of different thicknesses from the surface of the sample. The thickness of each section was calculated by measuring the mass of the sample before and after each grinding step in a microbalance (mass accuracy 0.0001 mg). The abrasive paper together with the cotton swabs used to clean the surface of the sample after each section were then placed in a translucent vial for radioactivity measurements.

A liquid scintillation counter (LSC), TRI-CARB 2910 TR PACKARD, Canberra Co, was used to determine the activity of each section. To do so, the radioactive material was suspended in a "cocktail" (Filter Count ®) composed of an organic solvent and scintillators. Photon emissions from the interaction between the β particles and scintillators are counted by the LSC. Each vial was left overnight with 20 mL of the cocktail to allow sufficient contact between the tracer and the scintillators ensuring a more efficient counting. Finally, each vial was measured for 2 hours to have a statistical error of the counting rate of less than 2 counts per minute.

Penetration profiles are built as relative specific activity (proportional to the tracer concentration) plotted against depth. Relative specific activity is obtained from the ratio between the counting rate (in Bq) after background subtraction and the section mass.

Stability at high temperature

The stability of selected sintered samples at high temperature was investigated by means of dilatometry measurements with the device SETSYS 16/18 provided by SETARAM Instrumentation. The apparatus incorporates a stationary plate and a moveable plate parallel to each other. A variation in length of the specimen changes the distance between plates that is recorded as a function of time and temperature with a precision of 0.004 µm. The program consisted in a heating step to 1127 K at a rate of 100 K/min followed by an isotherm of 3 hours and finally cooling to room temperature at a rate of 100 K/min. To avoid the reaction of samples with Pt holders, Al_2O_3 plates were placed between them. The thermal expansion of Al_2O_3 was systematically removed from the displacement values measured for Ni. To avoid pollution or oxidation, an Ar flux of 8 mL/min was applied for 30 minutes prior to the experiment and was maintained throughout the whole process.

CHAPTER III. SYNTHESIS AND CHARACTERIZATION OF UFG NI SAMPLES OBTAINED BY PM

The properties of UFG metals are highly dependable on the processing technique as the resulting specimens display different features other than a refined grain size. Some discrepancies persist to date, concerning mechanisms of plasticity, diffusivity or microstructural evolution at high temperature. Thus, an accurate characterization of samples is crucial to correlate properties to the correct microstructural feature. Highlighting the existing differences will help to understand what all UFG metals have in common, regardless of their synthesis method, as well as their specific characteristics.

In this chapter, the synthesis of the samples from nanostructuring the precursor powder by BM to consolidation by SPS are investigated. Then, the effect of BM parameters on the microstructural characteristics of UFG Ni is reported and discussed. Finally, the internal stress state of selected samples is investigated in terms of weak crystallographic misorientations inside grains combined with the observation of dislocation configurations by TEM.

1. Processing of bulk UFG Ni samples from BM powder by SPS

The combination of BM and SPS enables the synthesis of nearly dense nickel samples with refined grain size in the UFG range. To study the possibilities of these two techniques three BM parameters were varied to produce powder with different characteristics. Consolidation was afterwards accomplished by SPS using the same program for all powders to obtain not only small grain sizes but also specimens with distinct microstructures.

1.1. *Impact of ball-milling parameters on Ni powder*

Evolution of the morphology of powders with milling parameters

The process of BM entails numerous parameters: rotation speed, cycle time, number of cycles, time of pause between cycles, atmosphere, type of process control agent (PCA), amount of PCA, diameter of balls, number of balls, etc., that have an important impact on the resulting powder [36]. In this study, milling time, rotation speed and the amount of PCA were chosen as some of the most influential BM parameters, and were varied to study their impact on microstructures after powder consolidation. First, a systematic study of the effect of these parameters on the morphology of the powder was performed by SEM observations.

The evolution of the powder with milling time was investigated by fixing the rotation speed to 200 rpm and the amount of PCA to 66.7 wt.%. Four different milling times were tested and the resulting morphology variation is shown in Fig. III-1. Particles are plastically deformed and increase in size with increasing milling time. In addition, the homogeneity of the powder evolves from a heterogeneous distribution at shorter milling time (Fig. III-1 (a)-(b)) to a homogeneous powder at longer milling times (Fig. III-1 (c)-(d)). A homogenized particle size is achieved after twelve hours of milling (Fig. III-1 (d)), with a mean diameter of 18 ± 5 μm.

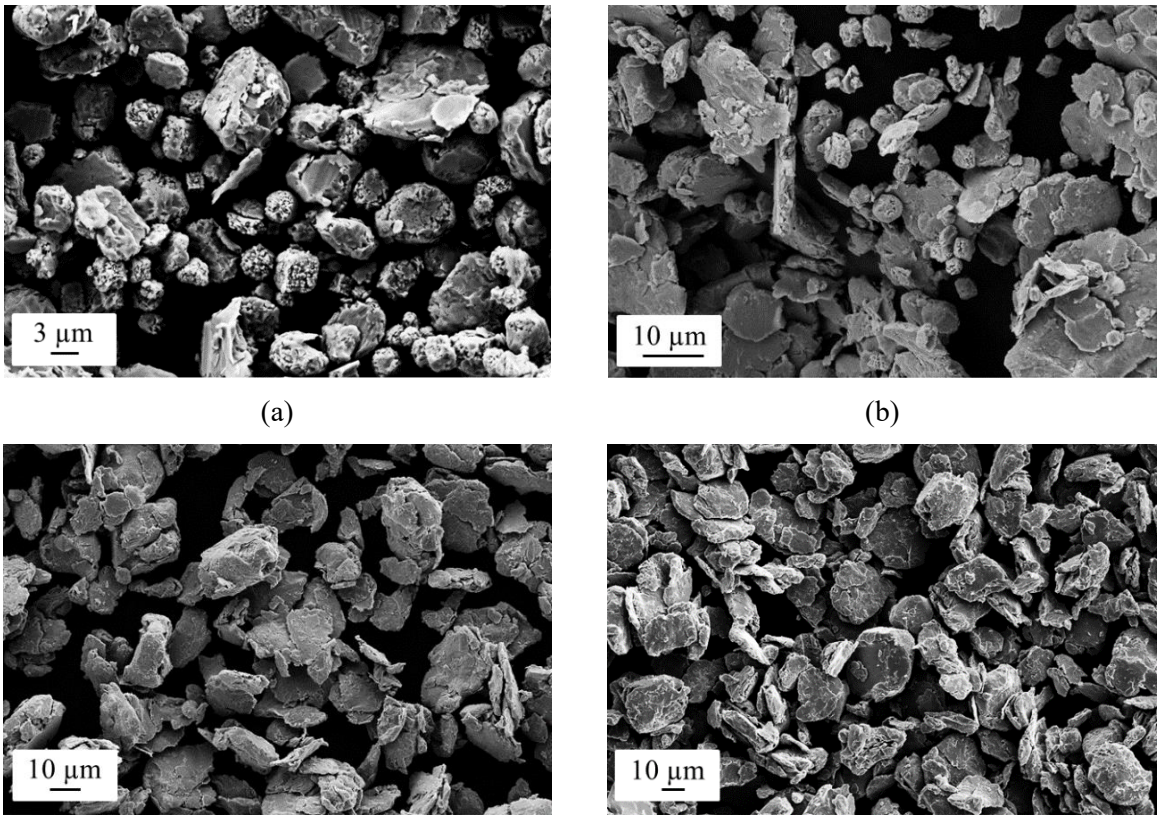

Fig. III-1 SEM images of Ni powders obtained after milling at 200 rpm and 66.7 wt.% of PCA for: 1.5 h (a), 3 h (b), 6 h (c) and 12 h (d).

As expected, highly energetic collisions between the grinding media and the powder result in severe plastic deformation and cold-welding. Slip lines and dimples, representative of ductile fracture mechanisms, can be observed in the surface of the powder. The apparent higher deformation levels achieved with longer milling time correlates well with microhardness measurements performed on Ni powders milled for different times, as show in Fig. III-2 [21]. In fact, the increase in hardness reflects the higher deformation level as well as grain refinement and higher density of defects. Hardness increases rapidly with increasing milling time, once 10 hours of milling is reached a slower evolution of hardness is depicted, and finally the steady state is achieved after 70 hours of milling.

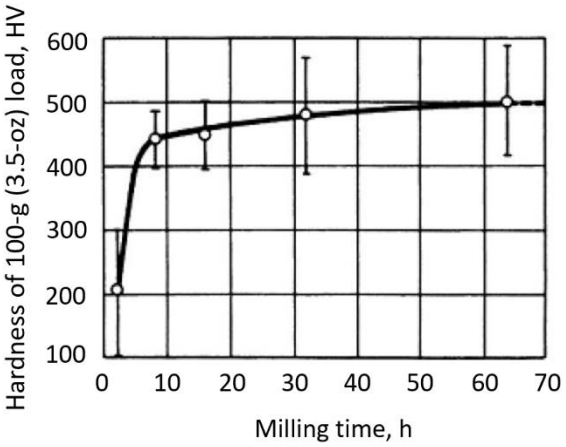

Fig. III-2 Effect of milling time on microhardness measured on particles of high purity (>99.8%) Ni powder [21].

The effect of rotation speed was investigated next, in the range of 200-350 rpm. Milling time was fixed to three hours and the amount of PCA to 66.7 wt.%. Fig. III-3 displays the evolution of the powder with speed. When rotation speed exceeds 200 rpm, a strong flattening of the particles with smoother surfaces is observed. Unlike for 200 rpm, homogenization is reached at 350 rpm after only 3 h of milling. A bigger particle size is obtained at the highest rotation speed, reaching an average diameter of 60 ± 22 μm and a thickness of ~ 1 μm.

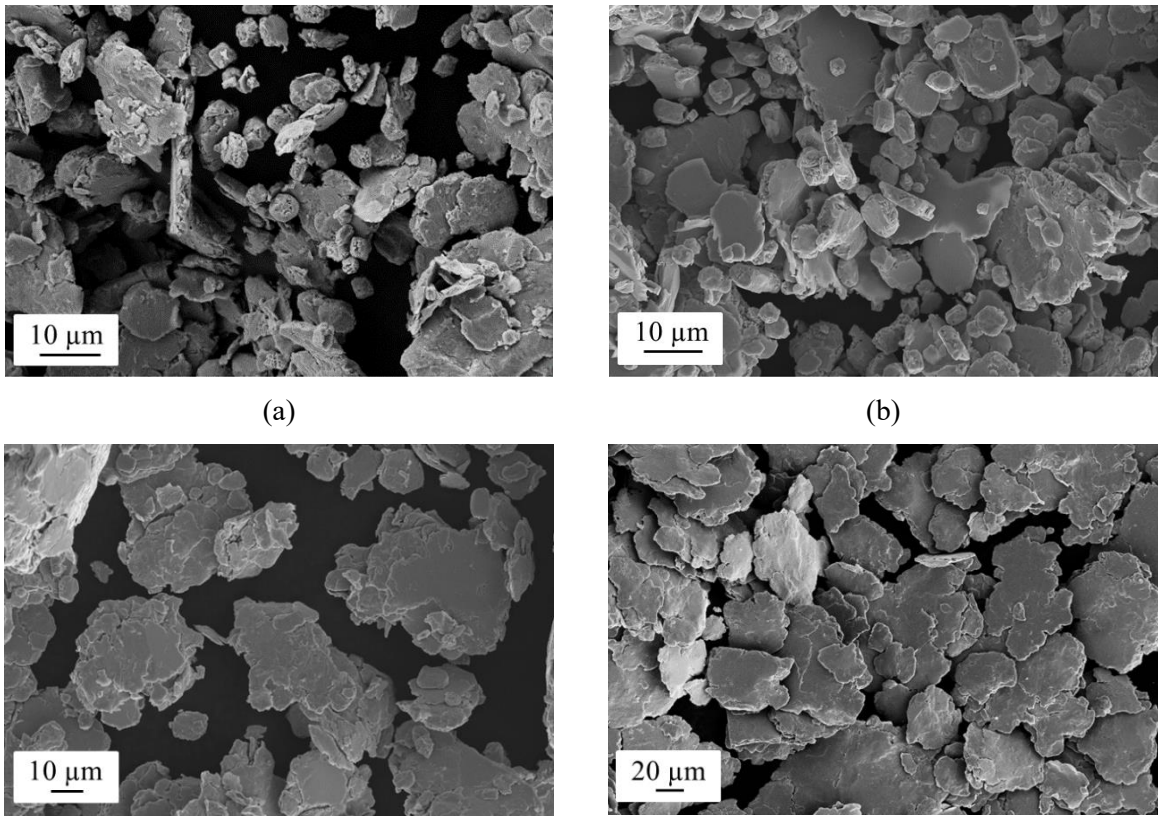

Fig. III-3 SEM images of Ni powders obtained after milling for 3 h and 66.7 wt.% of PCA at a rotation speed of: 200 rpm (a), 250 rpm (b), 300 rpm (c) and 350 rpm (d).

Finally, the amount of PCA was varied to investigate its effect on the resulting powder. The most beneficial amount highly depends on the type of PCA used [151–153] and despite Methanol being reported as PCA solvent [36,133,154], a study on the best quantity to use is not found in literature. In this work, the amount of PCA was varied in the range 66.7 - 8.3 wt.%, milling time was set to three hours and rotation speed to 350 rpm. SEM observation of the powders obtained with various amounts of PCA do not show striking differences (Fig. III-4). Nevertheless, the powder prepared with a higher amount displays less small particles. Considering the nature of MeOH, a small molecule with low boiling point, the effect of a smaller quantity on the milled powder could be compared with the results found for ethyl acetate, which displays similar properties [154]. Indeed, when using ethyl acetate as PCA a bigger amount is beneficiary to avoid excessive welding and only below 2 %, the efficiency of this solvent starts to decrease.

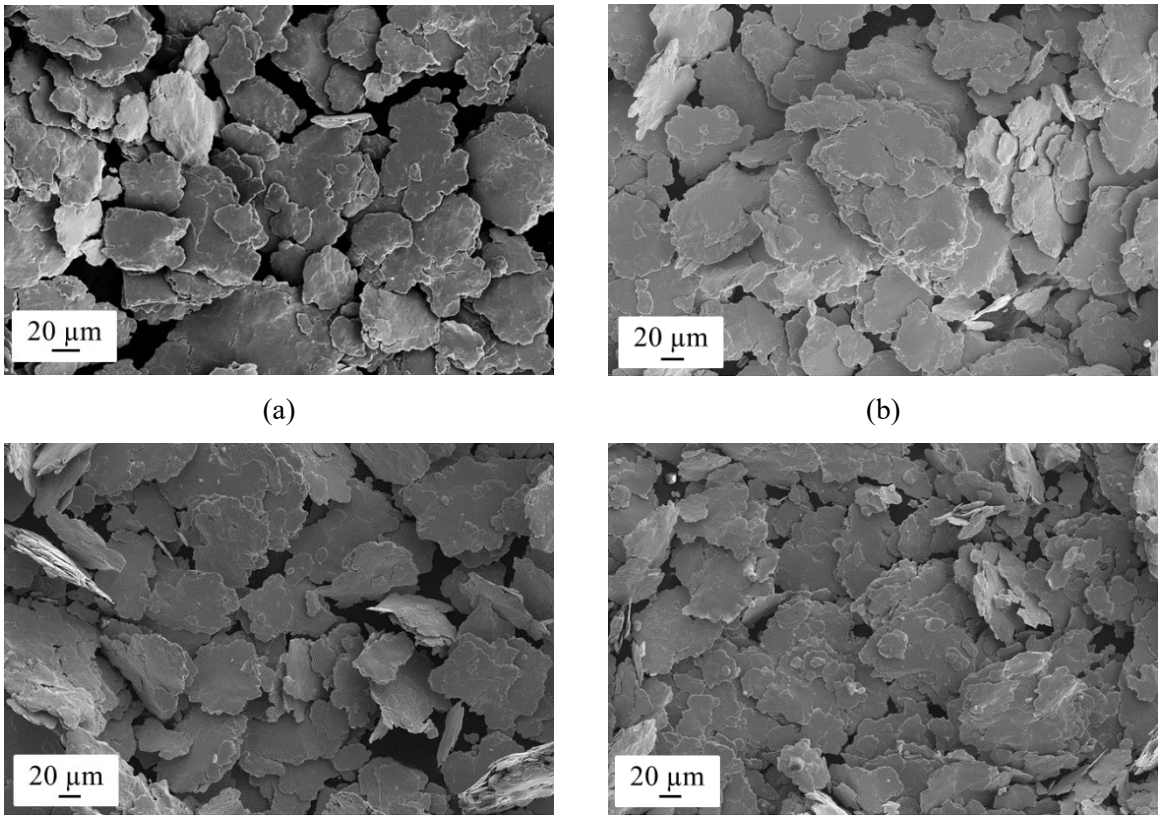

Fig. III-4 SEM images of Ni powder obtained after milling for 3 h at 350 rpm with different amounts of PCA: 66.7 wt.% (a), 33.4 wt.% (b), 16.7 wt.% (c) and 8.35 wt.% (d).

A final powder (P0) was prepared with a milling time of 10 h (to optimize processing time[10]), the most severe milling speed 350 rpm, and the largest amount of PCA, 66.7 wt.%. Such powder displayed

[10] The number of cycles in the BM device is limited to 100 cycles. Two extra hours of milling entail a total process time of over a day.

homogeneously deformed particles (Fig. III-5 (a)) and an average particle size of 38 ± 20 µm (Fig. III-5 (b)).

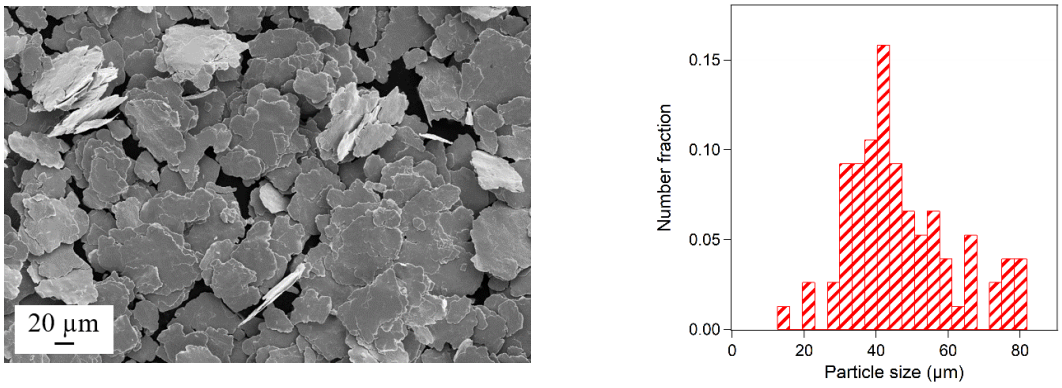

(a) (b)

Fig. III-5 SEM image (a) and particle size distribution (b) of powder P0.

Texture examination of BM powders by XRD

Including the as-received powder, twelve different powders were considered in this study. In order to investigate the presence of peaks corresponding to contamination species such as oxides as well as for texture examination, XRD measurements were performed. Irrespective[11] of the conditions of elaboration, diffractograms display peaks that correspond exclusively to the face centered cubic (FCC) phase of nickel (Fig. III-6 (a)). If the as-received powder and the P0 powder are compared (Fig. III-6 (b)), a difference in intensity and width between the two powders is depicted. These differences are a consequence of higher deformation and grain refinement of the P0 powder [155,156].

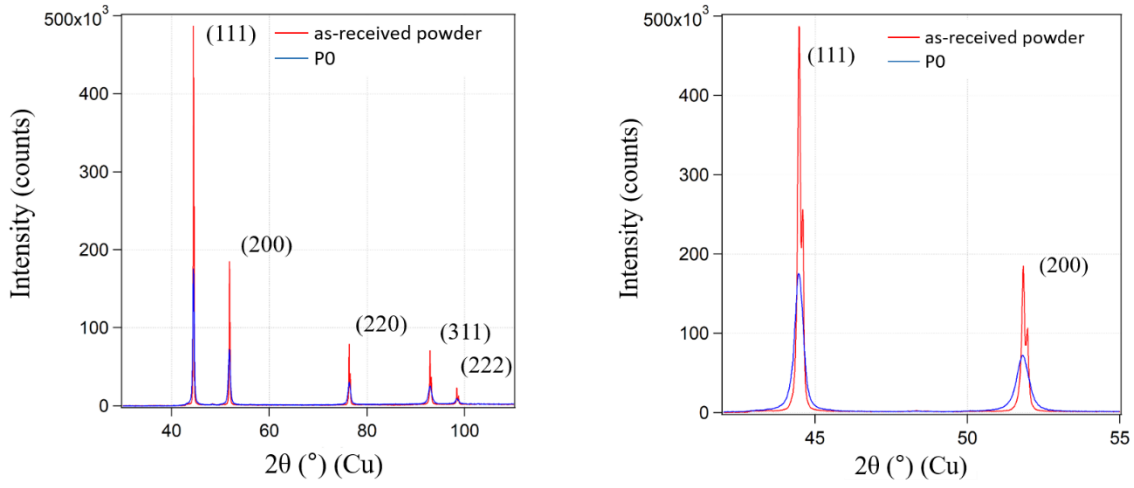

(a) (b)

Fig. III-6 XRD results of the as-received commercial powder (red line) and the ball-milled powder P0 (blue line). The whole diffractogram (a) and a zoom on peaks (111) and (200).

[11] Diffractograms of all powders are collected in Appendix B.

Preferred crystallographic orientation was examined from the ratio of intensities between the diffraction peaks. In Table III-1, the processing characteristics of each powder as well as the ratio I_{200}/I_{111} are collected.

Table III-1 Synthesis characteristics of the different powders processed in this study.

Type of powder	*Name*	*BM time (h)*	*Milling speed (rpm)*	*PCA amount (wt.%)*	I_{200}/I_{111}
As-received	PC	---	---	---	0.41
BM	P1	1.5	200	66.7	0.38
BM	P2	3	200	66.7	0.39
BM	P3	6	200	66.7	0.37
BM	P4	12	200	66.7	0.37
BM	P5	3	250	66.7	0.39
BM	P6	3	300	66.7	0.39
BM	P7	3	350	66.7	0.46
BM	P8	3	350	33.3	0.47
BM	P9	3	350	16.7	0.50
BM	P10	3	350	8.3	0.47
BM	P0	10	350	66.7	0.45

The value of the ratio I_{200}/I_{111} varies between 0.37 and 0.5 depending on the milling condition. These results are close to the value for random orientation in Ni, $I_{200}/I_{111} = 0.42$ as determined from the standard diffractogram for Ni, hence no marked crystallographic texture is observed for any powder. For comparison, nanostructured Ni samples from consolidation of BM powders by SPD displayed a I_{200}/I_{111} of 0.1 [20]. An explanation based on the FCC nature of nickel can account for the results obtained in this study as several slip systems can be activated by the collisions with the milling media producing an overall plastic strain. When a nickel particle is trapped between two balls (or between ball and wall), flattening would occur preferentially along one direction by a first energetic collision. For successive collisions, flattening would most likely continue along the same direction due to an enlarged collision surface. A similar explanation was given by S.S. Razavi-Tousi *et al.*[157] for a ball milled Al powder. Provided the as-received powder is polycrystalline, the processed powder would be flake-like without marked preferred crystallographic orientation.

Investigation of the microstructure exhibited by the powder P0

The powder P0 was embedded in a resin and mechanically polishing down to an OP-S (0.04 µm) suspension for microstructural investigations by EBSD[12]. The orientation cartography (Fig. III-7) exhibits grains in a range of sizes that display different morphologies, smaller equiaxed grains and larger elongated grains. The determined average grain size is 0.26 ± 0.16 (3) µm, with more than 92% of grains displaying a size below 500 nm.

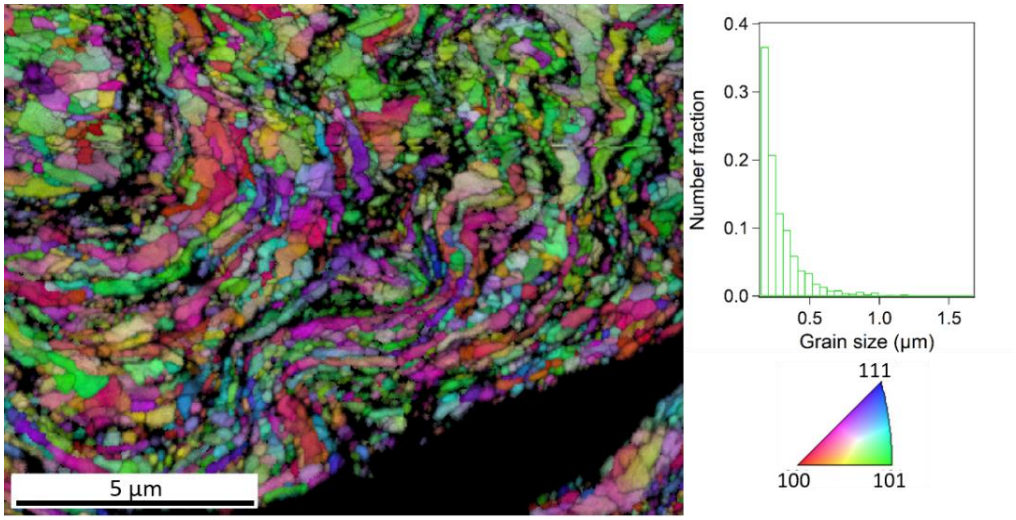

Fig. III-7 Combination of the grain orientation cartography (Inverse Pole Figure) and the image quality (IQ) map of the microstructure displayed by a particle from the powder P0. Grain size distribution plot (upper right).

Concerning the grain boundary character distribution (GBCD), which was determined in a length basis, this particle display a fraction of random high angle boundaries (HAB) and low angle grain boundaries (LAGB) of 66 % and 23.3 % respectively. The fraction of Σ3 grain boundaries was 5 % and other CSL (Σ5-Σ30) boundaries represented 5.6 % of the total grain boundary length. Despite a difference in grain size, the values obtained in this work are in good agreement with those found by D.B. Bober *et al.* [102] for Ni powder obtained by BM with similar milling conditions. An overview of the deformation state of the powder was considered from grain orientation spread (GOS) and Fig. III-8 shows that some grains display values of 4-10°, which indicates the presence of elevated misorientations within the crystals. The average GOS value for this microstructure was 1.5° ± 1.2°, similar to the value measured in ECAP processed nickel [129], which indicates an equivalent internal stress state level, between BM and other SPD techniques.

[12] The step used for orientation measurements was 30 nm, which means that only grains with a grain size of at least 120 nm were taken into consideration.

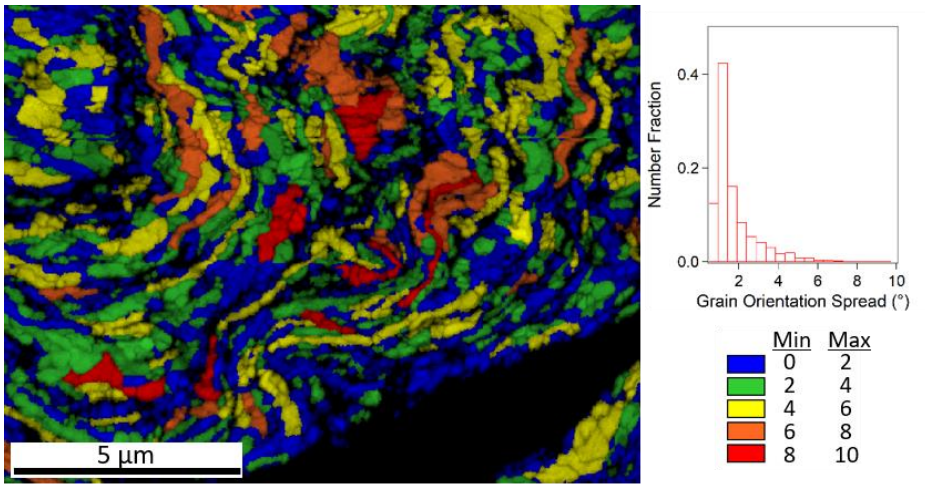

Fig. III-8 Superposition of the GOS cartography and the IQ image for the powder P0 (left). GOS distribution centered around 1.2° (upper right) and color scale of orientation spread (°) (lower right).

An inhomogeneous distribution of GOS, which is dependent on grain size, can be observed in Fig. III-8. The EBSD data can be divided into two partitions where only a part of the microstructure is considered. When grains with sizes below 500 nm are selected, the GOS cartography shown in Fig. III-9 (a) is obtained. The majority of small grains (> 92 %) exhibit GOS values below 4°. On the contrary, for grains with sizes above 500 nm (Fig. III-9 (b)), only 27 % of grains display GOS values of that magnitude. These results enable a partial explanation for the difference in grain size between this study (d = 0.26 µm) and the one published by D.B. Bober *et al.* (d ~ 0.02 µm). Presumably, in their work, complete homogenization of the microstructure was achieved whereas in this work, some bigger grains did not reach the steady state.

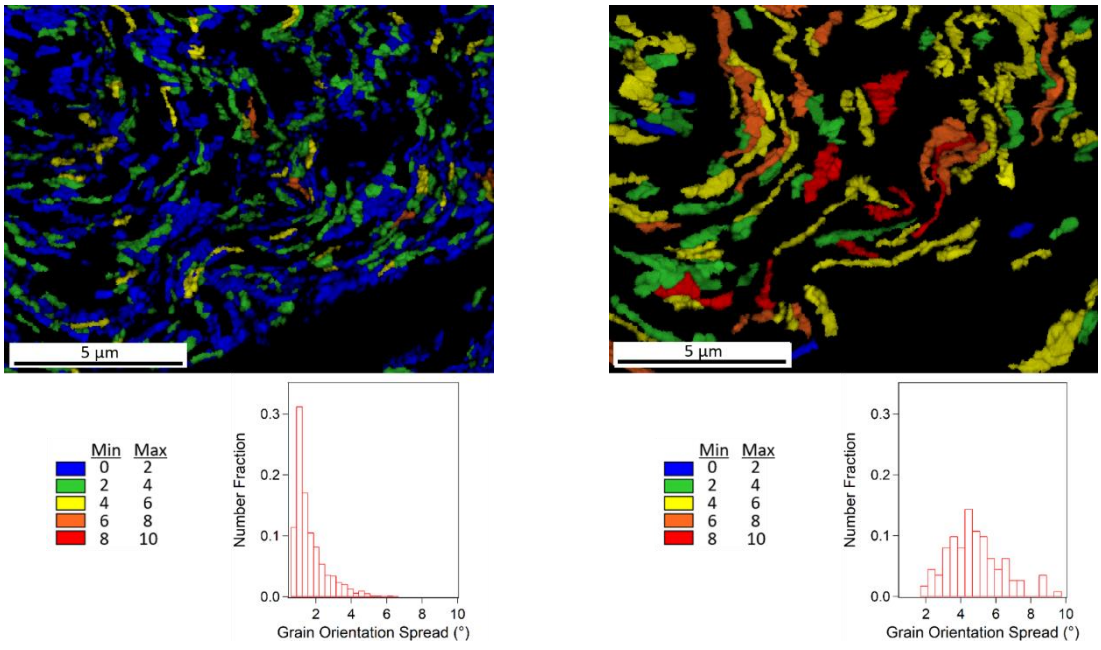

(a) (b)

Fig. III-9 Superposition of the GOS cartography and the IQ image for grains with a size below 500 nm (a) and above 500 nm (b). For each partition, the corresponding GOS distribution is displayed (lower right).

1.2. *Consolidation of BM powders by Spark Plasma Sintering*

The powders obtained with different milling conditions were consolidated by SPS to produce fine grain (FG)/UFG bulk samples. The synthesis of the specimens can be investigated by recording the punch displacement with the increase in temperature[13]. Initially, the motion of the punch is due to compaction of the powder by the increase of the applied force as well as densification. Once the maximum force is achieved (at 773 K), the displacement is mainly due to densification of the powder, accompanied by plastic deformation by compression of the metallic piece at high temperature. The role of the applied force is well evidenced in Fig. III-10, a minimum of 75 % densification is achieved when the maximum force is reached (vertical dotted line at 773 K), regardless of the powder. To reach full densification, powder morphology, homogeneity and deformation have a big impact. Let us consider the sintering process of powders obtained at different milling times. The powder milled for 12 h (P4) displayed a homogeneous aspect (Fig. III-1 (d)) of deformed particles and correspond to the dark blue curve in (Fig. III-10 (a)). It can be observed that the powder is easily compacted and at the maximum temperature of 1023 K (vertical dotted line), the punch displacement tends towards an asymptotic value implying that full densification is already ensured [54]. On the contrary, for the powder milled for 1.5 h (P1), only 91 % of densification occurred when the maximum temperature is reached (green line in Fig. III-10 (b)). This is due to the heterogeneous nature of powder P1 (Fig. III-1 (a)), where the particle distribution is composed of a mixture of particles from the as-received powder (PC) and big flattened particles. Thus for heterogeneous powders, a holding time of 10 min at maximum pressure and temperature is thus crucial for obtaining highly densified samples.

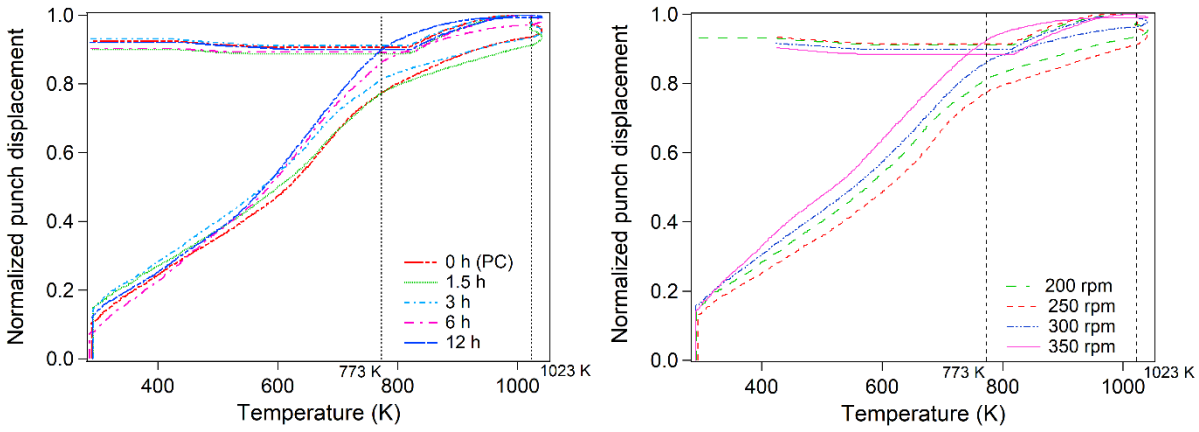

Fig. III-10 Sintering process studied as punch relative displacement vs temperature for the as-received powder and nanostructured powders obtained at longer milling time (P1-P4) (a), and at increasing rotation speeds (P2 and P5-P7) (b).

[13] The plot obtained is not a densification curve but it gives a qualitative view of the shrinkage of the specimens.

The same tendency is observed when comparing sintering curves of powders prepared with increasing rotation speeds (Fig. III-10 (b)). The powder processed at 350 rpm (P7) (Fig. III-3 (d)) is fully compacted at 953 K (pink curve in Fig. III-10 (b)), whereas more heterogeneous powders obtained at lower speed such as P2 and P5 (Fig. III-3 (a)-(b)), reach 93 % and 91 % of densification at 1023 K, and require longer milling time. Concerning sintering curves for powder (P7-P10), no marked differences are found as expected from their similar aspect.

The aforementioned results confirm the high influence of the morphology and homogeneity of the powders in the sintering process. Nevertheless, the influence of the deformation state of the powders has not been addressed. More severe milling conditions (longer milling time or increased rotation speed) entails a higher level of deformation of the particles. Assuming the same sintering mechanisms as the ones proposed for recrystallized Ni powders by Z. Trzaska *et al.* [49], the superior density of dislocations in a BM powder would ensure a vast proportion of diffusion paths, increasing sintering kinetics. This hypothesis agrees with what is observed in Fig. III-10 (a), densification of the as-received powder (red line) takes longer sintering time and higher temperature than the homogeneously deformed powder obtained after 12 h of milling (P4) (dark blue line). Additionally, in the investigation of sintering kinetics of a Ni powder obtained by BM [158], the measured sintering activation energy was 66.2 ± 3 kJ/mol (measured for conventional sintering), which is much lower than the activation energy measured by Z. Trzaska *et al.* for recrystallized Ni powders, 164 ± 30 kJ/mol, [7]. Despite the different sintering technique, these results seem to indicate that deformation of metallic powders is an asset to increase sintering kinetics.

2. Microstructural characterization

2.1. *Density of the consolidated samples and characterization of residual porosity*

One of the characteristics of powder metallurgy is the presence of porosities in the processed samples. This is not necessarily a drawback, as a final porous material can be the goal when looking for lightening the weight of a piece. In the present work, a maximum relative density is sought and as seen in the previous section, the chosen sintering parameters enable a high degree of densification. An increase in temperature or sintering time to obtain fully densified samples was not considered, as these options would notably increase final grain size. B. Flipon *et al.* [159] reported good mechanical properties for AISI 316L stainless steel samples with relative densities between 94.7 %-98.7 %. Thus, with the aim of obtaining the smallest grain size possible, a small percentage of porosities is accepted and is below 5.5 % in all cases.

The two most different samples, sintered from powders PC (S-PC) and P0 (S-P0), were chosen to study the location, size and morphology of porosities. Images of the cross-section of the sample S-PC prepared by cross-polishing, relative density of 96 (1) %, are displayed in Fig. III-11 (a).

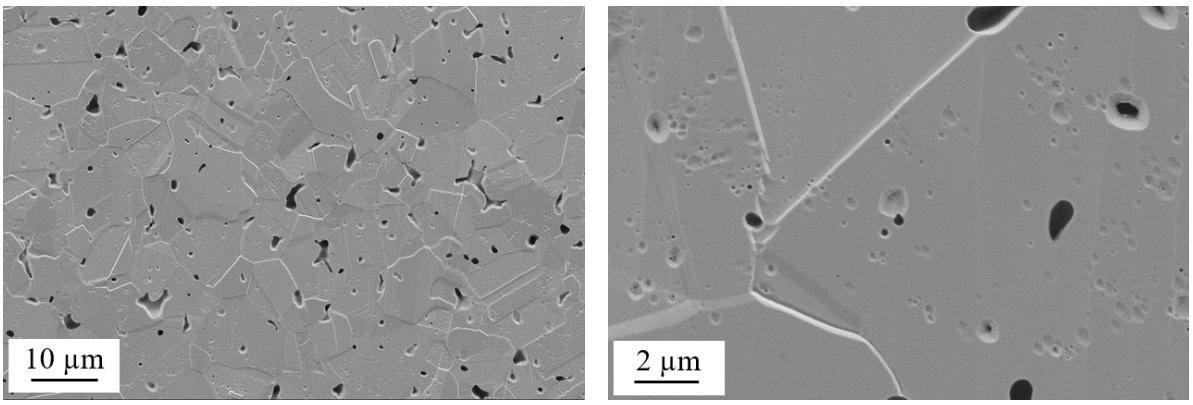

(a) (b)

Fig. III-11 SEM images of sample S-PC prepared by cross-polishing, general overview (a) and enlargement showing pores at grain boundaries as well as in the bulk (b). Surfaces are parallel to the SPS force axis.

Pores were classified with respect to their size, where big pores exhibit a diameter above 1 µm and small pores below 1 µm. Small pores represent 60 % of the total porosities and are mainly located in the bulk of the crystal (65 %). Regarding their geometry, different forms can be depicted (Fig. III-11 (b))[14], although they are mostly circular/oval. Concerning big pores, 40 % of the total, they are predominantly located at grain boundaries (80 %). They do not exhibit geometrical forms but rather irregular shapes. Their geometry is a consequence of the morphology of the initial powder (Chapter II) which exhibits a spiky aspect at the surface preventing a better compaction and contact between particles during sintering.

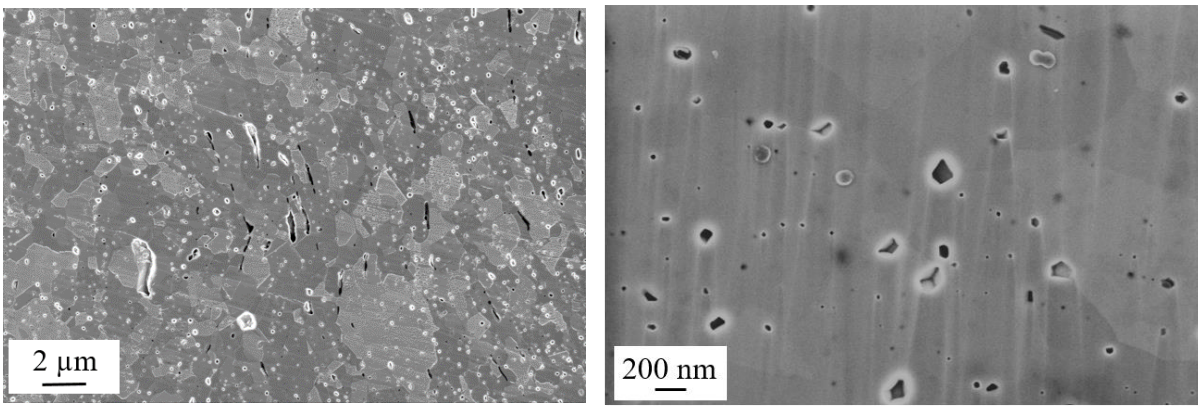

(a) (b)

Fig. III-12 Micrograph of the sample S-P0 showing numerous porosities (a). Difference in the location of pores depending on size (b), bigger porosities are found on grain boundaries and smaller ones in the bulk.

[14] Small imperfections (in light gray) can appear during preparation. Samples prepared by FIB confirm that they do not correspond to porosities.

Sample S-P0 exhibited a relative density of 97 (1) % and porosities of notably smaller size than sample S-PC (Fig. III-12). The pores of this sample were classified in three categories: small ($d \leq 50$ nm), intermediate ($50 \text{ nm} < d \leq 100$ nm) and big ($d > 100$ nm). The majority of the pores correspond to small pores (73.5 %), followed by the intermediate pores (21.3 %). As for sample S-PC, a bigger fraction of small pores (81.1 %) are located in the bulk of the sample whereas, big and intermediate pores (71.4 % and 62.1% respectively) are mostly found at grain boundaries.

Concerning the shape of the pores, in sample S-P0, most of the porosities exhibit geometrical forms typical of the sintering process (Fig. III-13). Elongated pores as displayed in the center of image Fig. III-12 (a) are also randomly found on the microstructure. This results from faulty compaction of the precursor powder, (Fig. III-5 (a)), at certain points of the sample.

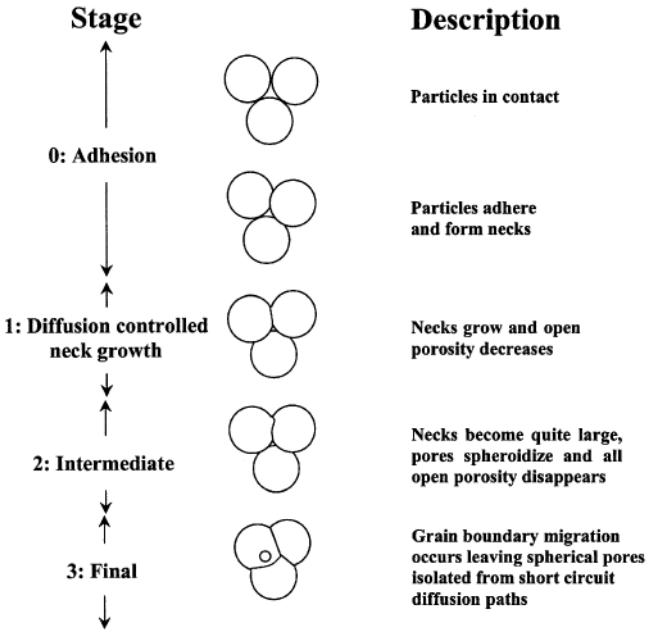

Fig. III-13 Stages of sintering showing the isolation of pores as the final step of the process [42].

2.2. *Influence of powder on microstructural characteristics*

Grain size as a function of BM parameters

The synthesis of samples with the same sintering conditions from different powders, as-received or BM, produces specimens with different microstructural features. Fig. III-14 displays grain orientation cartographies for three samples with average grain size in various ranges: Fine Grain (FG), FG/UFG and UFG. The sample S-PC exhibits a FG microstructure with an average grain size of $d = 3.4 \pm 2.4$ (2) µm. It can be depicted from the grain size distribution (Fig. III-14 (a)) that 93 % of grains have sizes

below d = 7.5 µm, which is in agreement with previous values reported for Ni samples sintered from commercial powders under similar conditions [160,161]. An example of FG/UFG sample is obtained from powder P2 (S-P2) with d = 1.43 ± 1.01 (5) µm (Fig. III-14 (b)), where 92 % of grains present a size below 3 µm, and an example of UFG sample from sintering powder P8 (S-P8), d = 0.78 ± 0.52 (5) µm and 91 % of grains have a size inferior to 1.4 µm (Fig. III-14 (c)).

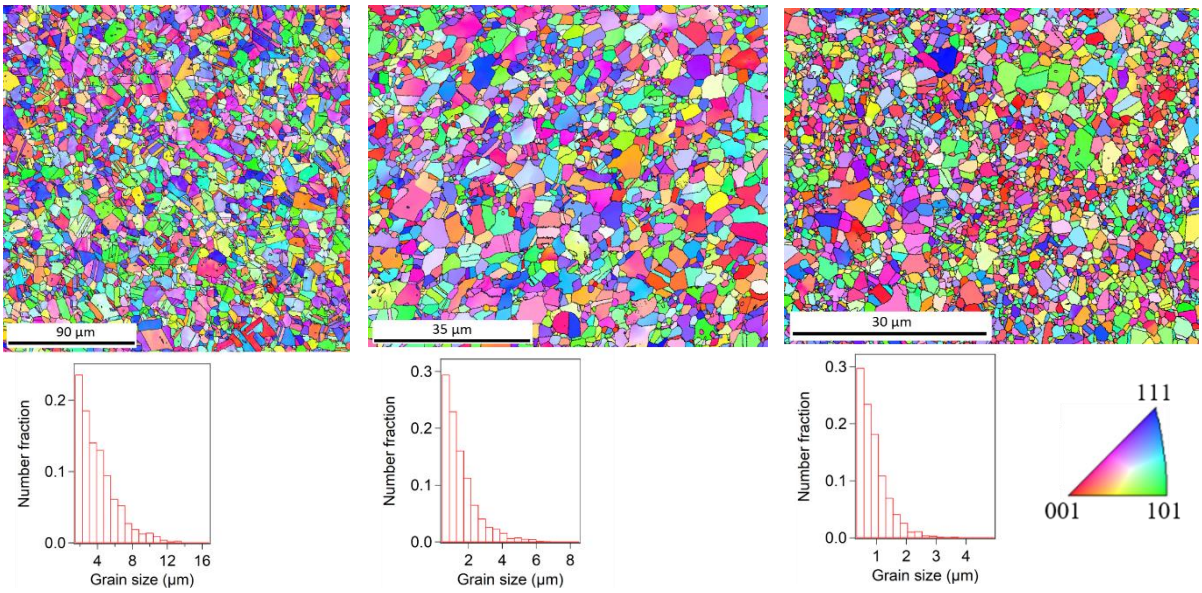

Fig. III-14 Grain orientation cartography (Inverse Pole Figure) and corresponding grain size distribution for SPS processed samples with different grain sizes: sample S-PC (a), sample S-P2 (b) and sample S-P8 (c). The direction normal to the surface of the sample was taken as reference direction for the IPF cartography.

Grain size can thus be adjusted by modifying the milling parameters. Fig. III-15 displays the influence of the three milling parameters investigated in this work on the final grain size. Increasing milling time produces a strong exponential decrease (Fig. III-15 (a), red circles) suggesting a grain refinement steady state after 12 hours, considering a rotation speed of 200 rpm. In BM, time can be considered equivalent to the number of passes in ECAP processing. As exposed in Chapter I, it represents the key parameter in ECAP processing and a certain number of passes, which depends on the material, is required for the microstructure to achieve the steady state. Once the steady state is reached, further passes do not modify the microstructure.

Regarding the effect of the rotation speed on the average grain size of the sintered specimens, an important linear decrease (Fig. III-15 (a) blue squares) is depicted. For instance, the sample processed from the powder obtained after milling for 3 hours at 350 rpm (S-P7) has an average grain size in the same range as the one sintered from the powder milled for 12 hours at 200 rpm (S-P4). Increasing rotation speed translates into more energetic collisions [157,162], thus resulting in higher strain in less time, which makes the process more efficient. The effect of PCA on grain size shown in Fig. III-15 (b),

confirms that the amount of methanol with the conditions used in this study, has little effect in BM nickel. Nevertheless, a weak exponential decrease reveals that a larger amount of is slightly beneficial for grain refinement.

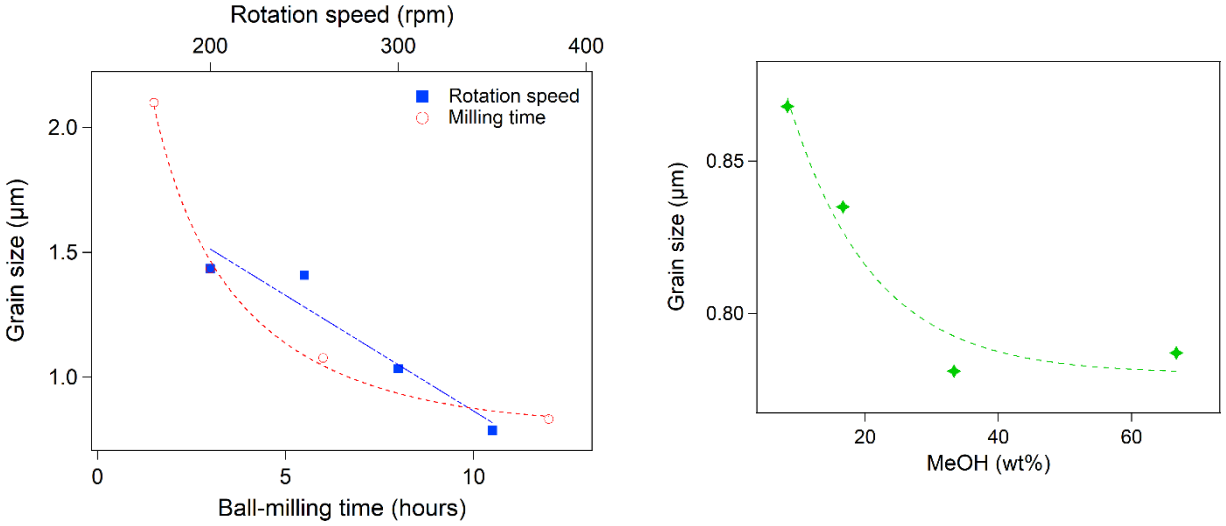

(a) (b)

Fig. III-15 Grain size as a function of milling time (200 rpm, 66.7 wt.% PCA), rotation speed (3h, 66.7 wt.% PCA) (a) and PCA amount (350 rpm, 3h).

Sample S-P0 displayed the smallest grain size in this study d = 0.69 ± 0.44 (3) µm measured in the surface (Fig. III-16 (a)). To verify the homogeneity of the microstructure, EBSD was performed in the surface and cross-sections with regard to the SPS applied force. Indeed, a similar grain size is observed in the cross-section, d = 0.65 ± 0.39 (3) µm and the fractions of GBCD in these two sections show only little differences, less than 4%. Despite the patterns in stereographic projection for the <001> pole, showing a slight preference for a cube texture, values of the maximum density pole, 1.8 in cross and 1.7 in longitudinal sections, combined with the random patterns in stereographic projections for <011> and <111> poles, confirm that the sample has no strong preferential crystallographic orientation.

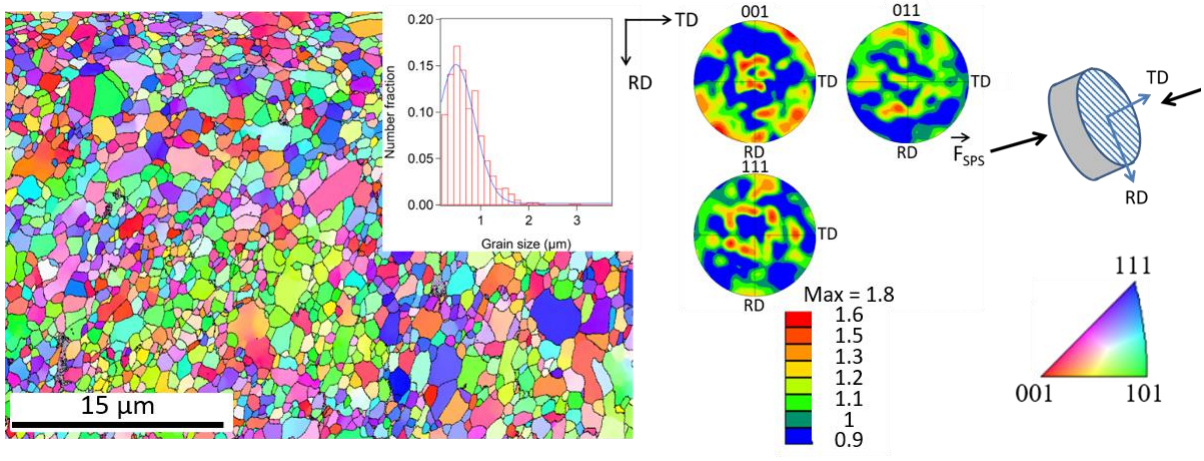

(a)

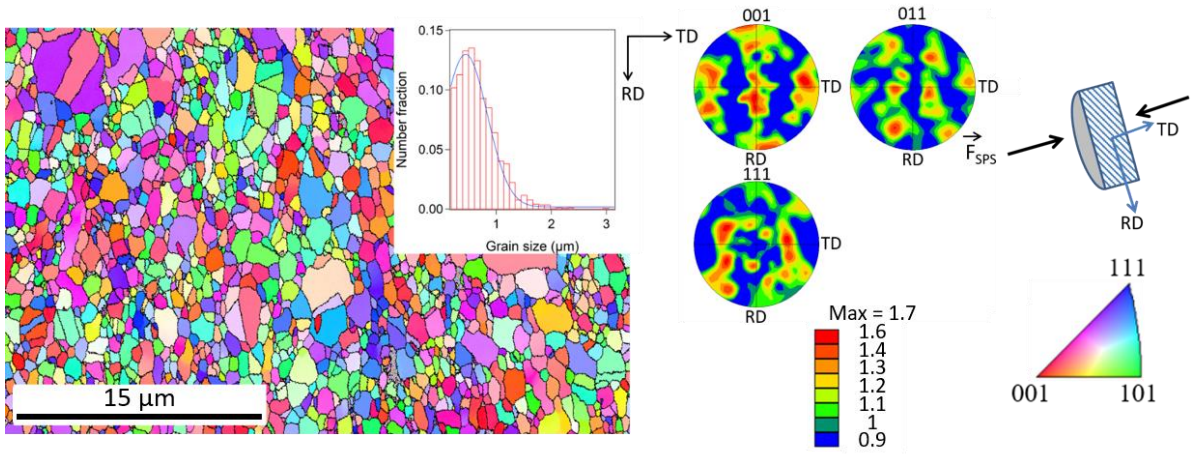

(b)

Fig. III-16 EBSD orientation grain map (left) with grain size distribution (inset), pole figures (middle) and diagram of the acquisition setting (right) of sample S-P0 in the surface (a) and cross-section (b). The direction normal to the surface indicated by blue lines was taken as reference direction for the IPF cartography.

Grain boundary character distribution of UFG samples prepared by BM coupled with SPS

Grain boundary character distribution (GBCD) of the sintered samples was analysed highlighting Σ3 boundaries and LAGB. These types of grain boundaries are characteristic of PM and SPD processed samples, respectively, and can be expected in the samples produced in this study. In fact, when a strained Ni sample is annealed, the formation of Σ3 grain boundaries (specially coherent twin boundaries[15]) is beneficial to decrease the global energy of the system as it evolves to a more stable configuration [163,164]. Thus, the formation of such boundaries during sintering can be anticipated. On the other hand, a high fraction of LAGB in sintered samples such as S-P0 may indicate incomplete recrystallization of their highly deformed precursor powder (P0 in the case of S-P0), which results from the low mobility of this type of boundaries [165].

In Table III-2 the information concerning the precursor powder, the average grain size and the GBCD determined for each sintered sample is collected. An evolution of the GBCD related to the precursor powder can be depicted as well as a dependency between different grain boundary types and the grain size of the sintered sample.

[15] A coherent twin boundary in a FCC structure can be defined as a Σ3 grain boundary (60 ° rotation about a <111> axis), with the boundary plane corresponding to a {111} plane.

Table III-2 GBCD of samples obtained by SPS.

Sample	*Powder*	*Grain size (µm)*	*LAGB*	*Σ3*	*Other CSL (Σ5- Σ29)*	*HAB*
S-PC	PC	3.4 ± 2.4 (2) µm	0.049	0.431	0.067	0.453
S-P1	P1	2.1 ± 1.3 (2) µm	0.034	0.365	0.079	0.522
S-P2	P2	1.43 ± 1.01 (5) µm	0.038	0.359	0.077	0.526
S-P3	P3	1.1 ± 0.7 (1) µm	0.051	0.328	0.084	0.537
S-P4	P4	0.88 ± 0.51 (5) µm	0.111	0.232	0.091	0.566
S-P5	P5	1.41 ± 1.12 (5) µm	0.046	0.363	0.084	0.507
S-P6	P6	1.03 ± 0.77 (5) µm	0.051	0.353	0.081	0.515
S-P7	P7	0.79 ± 0.47 (6) µm	0.071	0.282	0.086	0.561
S-P8	P8	0.78 ± 0.52 (5) µm	0.086	0.274	0.081	0.559
S-P9	P9	0.83 ± 0.54 (5) µm	0.084	0.258	0.087	0.571
S-P10	P10	0.87 ± 0.49 (5) µm	0.087	0.204	0.096	0.613
S-P0	P0	0.69 ± 0.44 (3) µm	0.125	0.147	0.083	0.645

Fig. III-17 represents the evolution of each type of grain boundary as a function of grain size for all processed samples. The fraction of Σ3 grain boundaries decreases with grain size, especially for values below one µm, whereas the fractions of LAGBs and random HABs increase. The fraction of other CSL[16] (Σ5-Σ29) grain boundaries (represented as CSL in Fig. III-17) displays no significant variations.

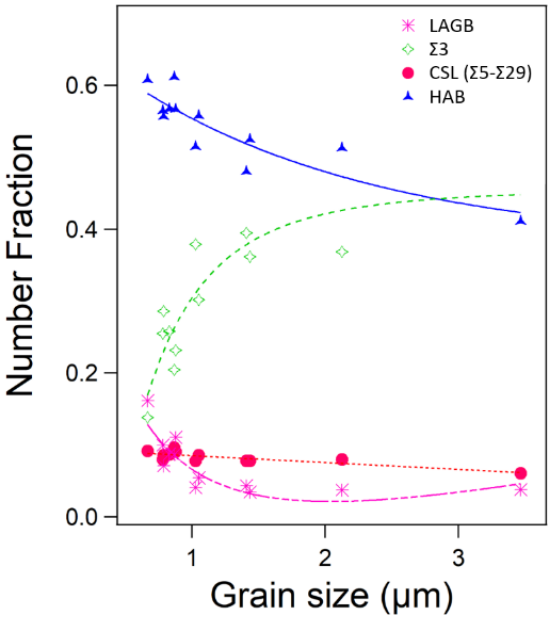

Fig. III-17 Fraction of the different types of GB observed in UFG sintered Ni, as a function of grain size.

[16] For more detail on the distribution of CSL grain boundaries, the reader is referred to Appendix A-3.

Except for the sample with the smallest grain size, in all samples, a fraction 75 - 87 % of the Σ3 grain boundaries correspond to twin boundaries (TB). In fact, deformation and consequent annealing is frequently used by many authors [130,166–169] to increase the density of TB, and it explains the elevated fraction of this type of boundaries in the specimens sintered from BM powders. Concerning the decrease in the density of TB (p) correlated with the refinement of grain size, C.S. Pande *et al.* [170], defined the following relation for FCC metals and alloys:

$$\frac{p}{p_0} = \frac{d_0}{d} log \frac{d}{d_0} \tag{3.1}$$

where p_0 and d_0 are constants.

The increase of the fraction of LAGBs with decreasing grain size, on the other hand is related to the high presence of this type of boundaries in BM powders. For instance, the investigation by EBSD earlier in this chapter of powder P0 showed a fraction of LAGBs of 23.3 %, which is characteristic of SPD processed materials, and the sintered sample S-P0 displayed a fraction of 12.5 %. Thus, during sintering a fraction of the LAGBs evolved to high angle boundaries. Presumably, the less severe milling conditions produce powders with lower fractions of LAGBs as reported by D.B. Bober *et al.* [102]. Then after partial recrystallization during sintering, the density of LAGBs would also be lower. The evolution of LAGBs to HABs with annealing is constrained by the lower mobility of this type of boundaries as reported for Cu [171] and Al [172]. Thus, a relative high fraction is still displayed by the sintered samples.

Complementary information concerning relative orientation of grains in the microstructure can be obtained from the misorientation angle distribution. In this distribution, the minimum misorientation angle between contiguous grains is considered regardless of the rotation axis. The as obtained plots can then be compared to the random distribution determined by J.K. Mackenzie [115]. Fig. III-18 displays the misorientation plots of the sample S-PC (a) and the sample S-P0 (b). For the misorientation plot of all the other samples S-P1-S-P10, the reader is referred to Appendix C. The results of all samples correlate favourably with the measured results of GBCD, as expected. For instance, the most prominent peak at 60° corresponds to Σ3 grain boundaries indicating the high fraction measured on sample S-PC. In addition, the peaks at low misorientation angles represent the LAGB, hence their high fraction on sample S-P0. When comparing with the random distribution computed by Mackenzie (Fig. III-18 (c)), both samples display a similar aspect in the range 20° - 55°. Nevertheless, the deviations exhibited at 60° and low angles suggests the formation of a grain boundary texture in samples processed by SPS.

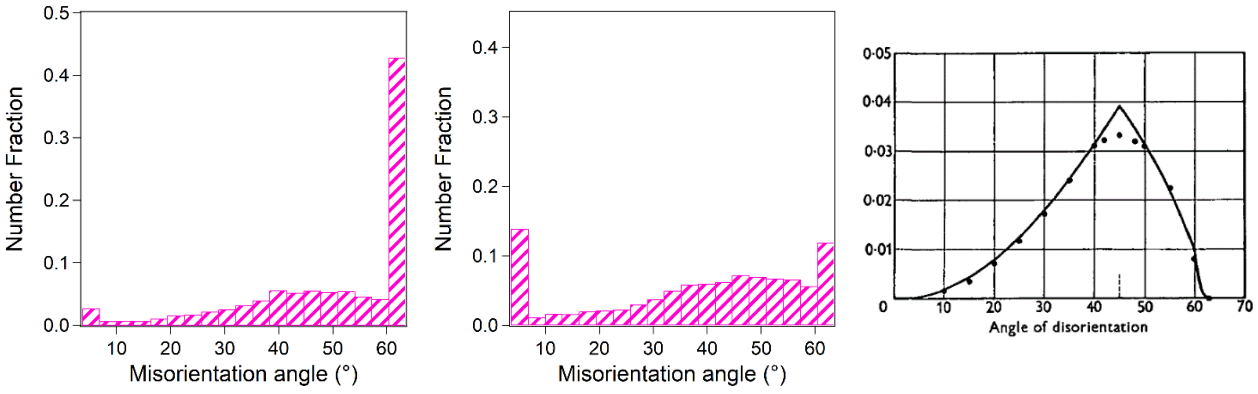

Fig. III-18 Misorientation angle distribution of sample S-PC (a) and sample S-P0 (b). For comparison, the Mackenzie misorientation distribution for cubic structures is shown (c) [115].

2.3. *Analysis of the initial state of the samples by GOS and TEM*

J.P. Hirth and J. Lothe define internal stress as "locked-in stresses present when no external forces act" [149]. Whenever a material exhibits some kind of defect (point, line, planar or bulk), it is accompanied by a certain level of stress (Fig. III-19). These stresses contribute to increasing the elastic energy of the body under study. The high fraction of grain boundaries characteristic of UFG specimens form high-energy systems, where additional defects such as dislocations enhance their "non-equilibrium" nature.

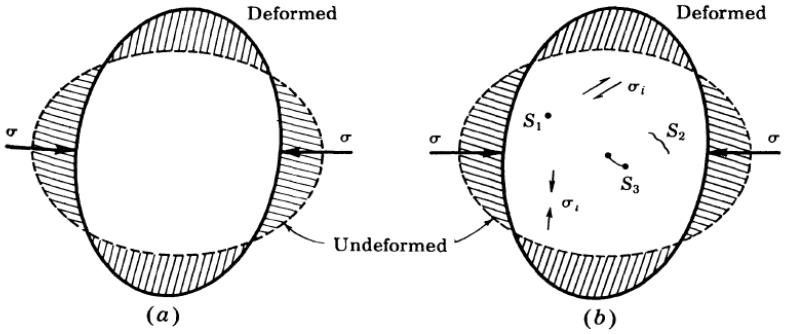

Fig. III-19 Schematic illustration of the deformation, stress free body (a) and body containing diverse internal stress sources labeled S1, S2 and S3 (b). They represent respectively, point, line and surface defect sources [149].

When evaluating internal stresses, we will concentrate on dislocations. Dislocations are generated during strain hardening to enable the continuity of strain across grain boundaries and inside grains. Their presence increases the energy of the system [70], creating long-range internal stresses and short-range internal stresses that can be either intra-granular or inter-granular depending on the deformation state of the sample [94,112]. These internal stresses are related to the presence of different dislocation structures. For instance, an increase on the intra-granular internal stress is related to the presence of dense dislocation structures whereas an increase of geometrically necessary dislocations (GNDs) is related to

inter-granular internal stress [173]. The study of these types of internal stresses is an arduous task that requires an extensive study of dislocations structures by TEM. Thus, in this work, a simplified approach is taken and internal stresses are evaluated from misorientation measurements performed by EBSD. TEM will be use as a complement to verify the analysis made by EBSD.

As reported in Chapter II, misorientations determined from EBSD is a useful tool for a general evaluation of the deformation state of samples. The determination of short-range and long-range misorientations cannot be accountable for short-range and long-range internal stresses. Nevertheless, a comparative study of all samples indicates the relative probability of finding different types of dislocation structures. The GOS cartography superposed to the IQ map of samples S-P1 and S-P5 are displayed in Fig. III-20. A high fraction of grains displaying a GOS below 1° (blue) is depicted. From the distribution plot, it can be seen that a mean value is centered at 0.5° for both samples. The fraction of grains with GOS > 1° are respectively 8 % for S-P1 and 6 % for S-P5.

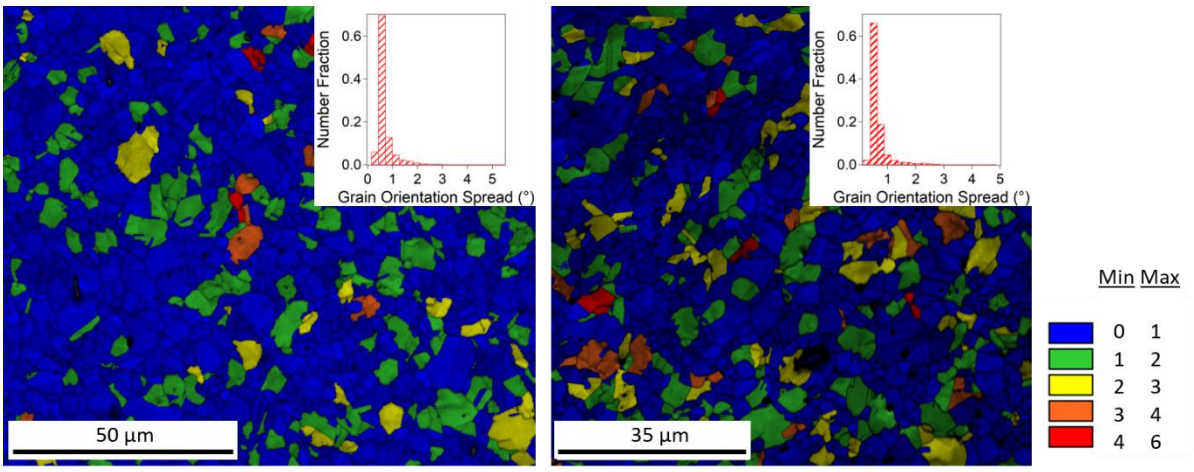

(a) (b)

Fig. III-20 GOS cartographies obtained from EBSD data from the initial state of the samples S-P1 (a) and S-P5 (b). The distribution of GOS values corresponding to each sample are displayed in the inset to each microstructure.

In addition, the corresponding cartographies from the most different samples S-PC and S-P0 are displayed in Fig. III-21. In this case the fraction of grains with GOS > 1°are 12 % for sample S-PC and 26 % for sample S-P0. Despite the higher fraction in sample S-P0, the mean GOS value remains 0.6° ± 0.5° which corresponds to well recrystallized microstructures [129]. These four samples are representative of all samples, which display similar distributions and mean GOS values between 0.5° and 0.8°. The GOS distribution evidences some heterogeneities in the respective microstructures where

grains of higher GOS would display a higher density of dislocations. To corroborate these results TEM observations were made on samples S-PC and S-P0[17].

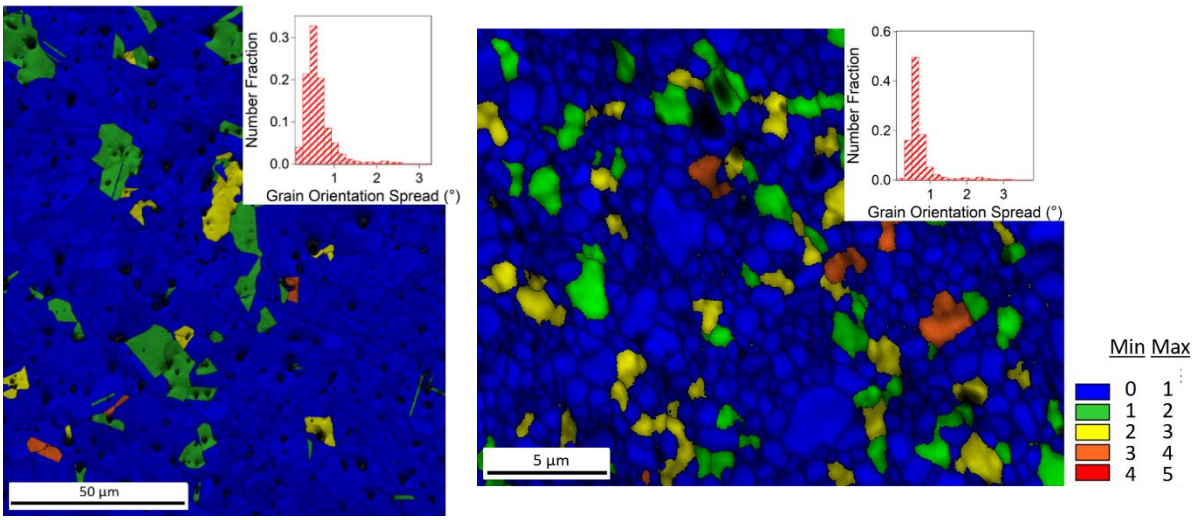

(a) (b)

Fig. III-21 GOS+IQ cartographies obtained from EBSD data from the initial state of the samples S-PC (a) and S-P0 (b). The distribution of GOS values corresponding to each sample are displayed in the inset to each microstructure.

In the case of sample S-PC, grains with a low density of dislocations are generally encountered (Fig. III-22). Mostly rectilinear dislocations are depicted, although the presence of curved dislocations showing higher local stress is also observed.

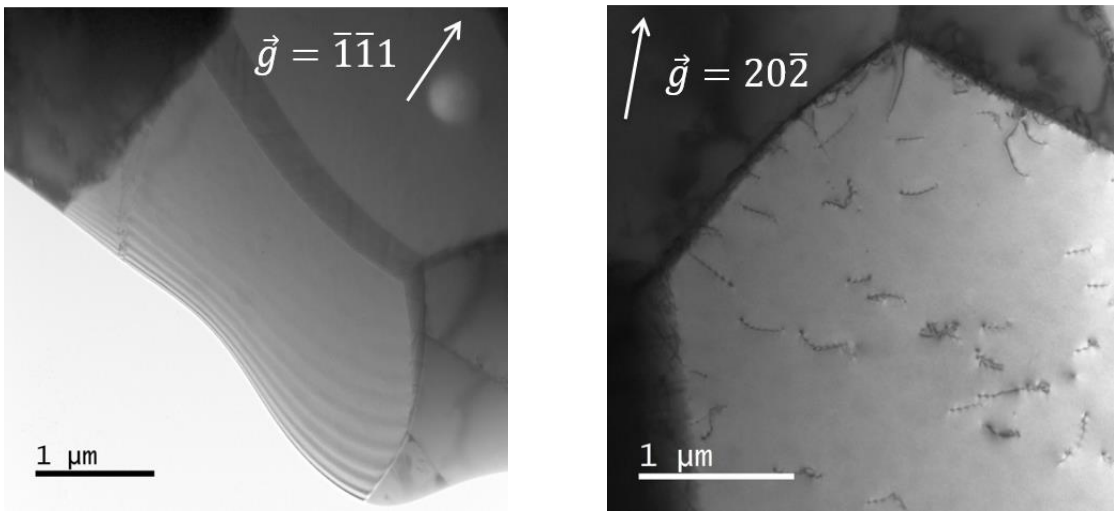

(a) (b)

Fig. III-22 TEM images of sample S-PC displaying a grain free of dislocations (a) and a grain with low dislocation density (b).

[17] Black spots in GOS+IQ cartographies correspond to badly indexed zones due to the presence of pores, which are enlarged by electropolishing.

Longer dislocations and dislocation pileups are occasionally found (Fig. III-23 (a)), as well as dislocations emerging from grain boundaries (Fig. III-23 (b)), which probably formed by the applied force during SPS sintering.

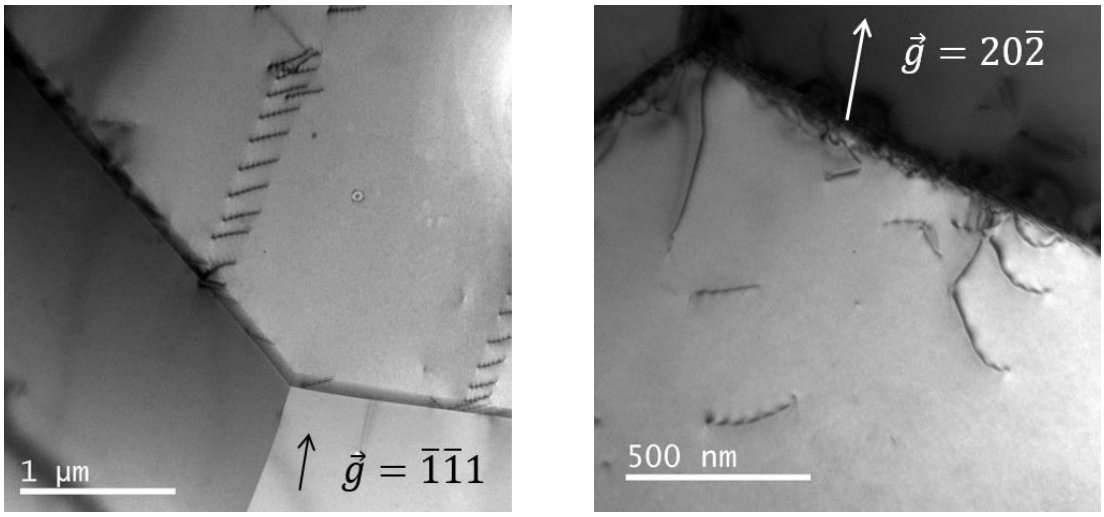

(a) (b)

Fig. III-23 Dislocation pileup crossing a grain close to a triple point (a) and dislocation source (b).

Microstructural observations of sample S-P0 are shown in Fig. III-24. It is noticeable (Fig. III-24 (a)) that the small porosities located specially in the bulk of grains (Fig. III-12 (b)) are enlarged by the preparation of the TEM specimens, and appear as white spots in TEM images. Grains with a diverse dislocation density are shown, which correlates with a higher GOS distribution measured by EBSD. Grains with low dislocation content (Fig. III-24 (b)), as well as dislocation free grains are also observed in this sample.

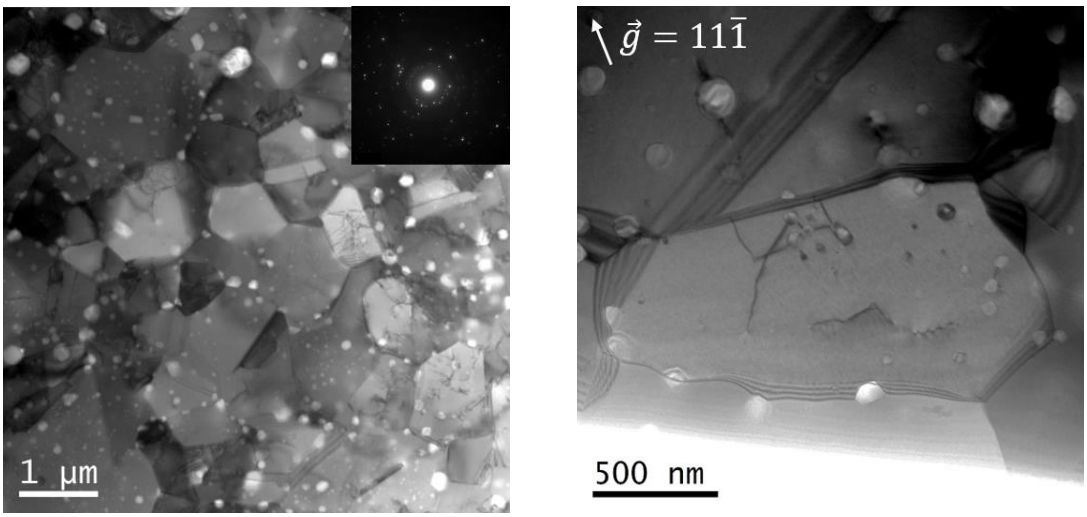

(a) (b)

Fig. III-24 Microstructures of sample BM1 obtained from TEM (a), the inset displays the SADP of the corresponding image. Grain in the UFG range with low dislocation density.

The observations depicted from TEM images, display low dislocation density grains for both samples. Except for some dislocation tangles, no dislocation cells or other dislocation structure representative of a higher stress state were encountered. These results are in agreement with measurements of GOS by EBSD, which confirm that restauration and recrystallization processes of the BM powder takes place during sintering. Likewise, any deformation induced from the applied force during sintering does not produce high internal stresses on the corresponding samples.

3. Summary and conclusions

In this chapter, the possibility of using BM coupled with SPS to process well densified samples with grain sizes in the FG/UFG range was investigated. To this aim, the synthesis of the nanostructured powder as well as consolidation to produce bulk samples was studied. Afterwards, the main microstructural features of the bulk samples were characterized.

The evolution of powder from a spherical to a flattened morphology was evidenced by SEM observations when increasing milling time and rotation speed. XRD investigations showed a preferred crystallographic orientation for all powders close to the random value as well as absence of peaks corresponding to NiO or other contaminants. In addition, EBSD analysis including GOS measurements of P0 confirms the highly deformed nature of the powder. Sintering kinetics as measured from punch displacement, account for the differences in morphology and deformation state of the powder. The produced samples exhibit good density (≥ 96 % relative density) which is higher than the value obtained in specimens made from nanopowder [41,114].

Grain size reduction to the UFG range was achieved with different sets of BM parameters. Distinct GBCDs were produced which correlate with grain size. The high fraction of Σ3 grain boundaries observed in the SPS processed samples decreases with grain size while LAGB and HAB fractions increase. These differences were related to restauration and recrystallization processes taking place during sintering. The anisotropy in the mobility of grain boundaries makes the microstructure of the bulk sample dependent on the microstructure of the powder, thus samples prepared from BM powders displayed higher LAGB fractions. This conclusion can be further corroborated with the comparison of the misorientation angle distribution displayed by sample S-P0 (Fig. III-18 (b)) and that of an UFG Ni sample processed by SPS from nanopowders (Chapter I, Fig. I-30). They both display an important peak at 60° corresponding to Σ3 grain boundaries, characteristic of sintering as processing technique, but they exhibit a difference in the fraction of LAGB, which is a characteristic of BM powders.

Finally, GOS measurements as well as observations by TEM of the dislocation structures for selected samples show an overall low internal stress level for all samples. Nevertheless, a difference in the deformation levels of grains is also observed in the GOS distribution as well as TEM observations.

CHAPTER IV. MECHANICAL PROPERTIES AND PLASTICITY MECHANISMS OF UFG NI SAMPLES OBTAINED BY PM

The results from the previous chapter evidenced that highly dense bulk samples with grain sizes in the FG/UFG range can be obtained from the combination of BM and SPS. In this chapter, the focus is set on the mechanical properties and the mechanisms of plasticity of selected samples. As reported in Chapter I, despite the large body of literature concerning the mechanical properties of NsM/UFG, some questions remain unanswered.

This chapter is divided in three parts. The first part consists on a bibliographic introduction of plastic deformation of polycrystals. In the second part, the mechanical characterization of the samples by uniaxial tensile testing is presented. The microstructure of the samples is studied and the conventional stress strain curves are analyzed. Strain hardening[18] is examined using a power-law mathematical approximation and the influence of grain size on the mechanical properties is discussed. The last part of this chapter concerns the mechanisms of plasticity. The different stages of strain hardening are analyzed and the Mecking-Kocks model is used for a deeper investigation of the mechanisms acting during strain hardening in FG/UFG Ni. The resulting conclusions are then completed with EBSD analysis of the samples after fracture and TEM observations of the dislocation structures in selected samples.

1. Deformation of polycrystals

1.1. *Plasticity in single crystals*

In crystalline materials, plastic deformation usually takes place by slip, which can be visualized as planes of atoms sliding over one another. When stress is applied on a crystal, slip will begin whenever the shear stress on a slip system reaches a critical value called critical resolved shear stress (τ_c), which depends on the material. This yield criterion for slip is known as Schmid's law and can be formulated as follows:

$$\tau_c = \sigma \cos(\lambda) \cos(\varphi) \qquad (4.1)$$

where λ and φ are the angle between the slip direction and the tensile axis and the angle between the tensile axis and the direction normal to the slip plane, respectively (Fig. IV-1). The product

[18] Strain hardening and work hardening are used interchangeably.

$\cos(\lambda)\cos(\varphi)$ is known as Schmid factor and its value varies from 0 to 0.5. This coefficient represents the ease to glide of a crystallographic plane under stress, where an orientation displaying a Schmid factor closer to 0.5 will require less stress to activate slip.

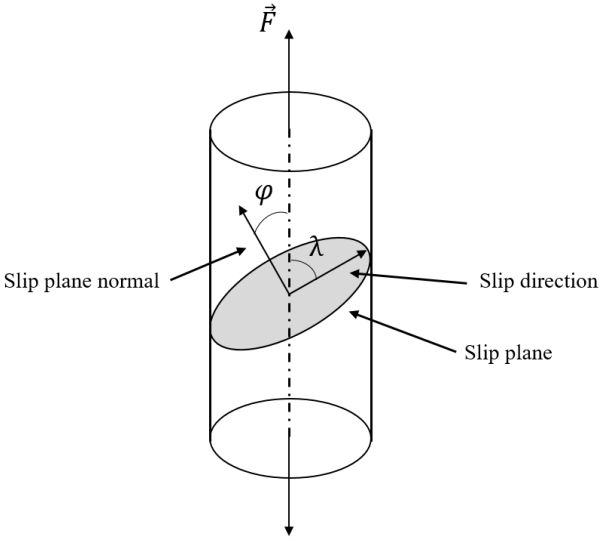

Fig. IV-1 Schematic illustration of Schmid's law.

Once slip is activated, plastic deformation takes place. Schmid's law provides a basic understanding of the mechanisms of plasticity in single crystals and enables the interpretation of a stress strain curve obtained in tensile testing for a crystal oriented for easy glide (only one slip system activates) (Fig. IV-2 (a)).

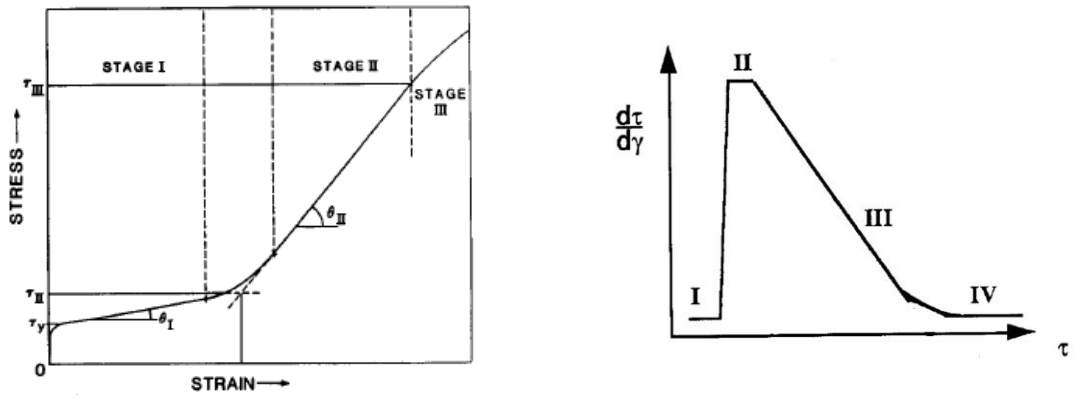

(a) (b)

Fig. IV-2 Tensile stress strain curve of a single crystal oriented for easy glide (a) and corresponding work hardening rate as a function of flow stress (b) [174].

As deformation progresses, the stress necessary to maintain an imposed strain rate changes. This phenomenon is called work hardening (θ_h) and is measured as $\theta_h = \frac{d\tau}{d\gamma}$. In FCC metals, three well-defined work hardening stages can be distinguished during plastic deformation. Stage I corresponds to easy glide and is characterized by a low work hardening rate (Fig. IV-2 (b)). Stage II is characterized by

a high hardening rate due to dislocation interaction and activation of secondary slip. In this stage, dense dislocation structures are formed resulting from the interaction between the primary slip system and secondary slip systems. Finally, in stage III, the strain hardening rate decreases monotonically as cross-slip appears leading to dynamic recovery [174]. These processes make this stage highly influenced by temperature, stacking fault energy and strain rate [175,176]. With increasing strain, the hardening rate decreases until a saturation stress is reached and possibly a stage IV begins. Failure usually takes place during stage III, which is why further stages are not contemplated in this brief introduction.

1.2. *Plasticity in polycrystals*

A polycrystalline material can be considered as an ensemble of single crystals (grains) displaying various orientations, hence deformation by slip remains the essence of the mechanisms of plasticity. The specificity of a polycrystal is that each grain is surrounded by other grains, which means that deformation of each grain must be compatible with its neighbors. G. I. Taylor (1938) resolved this problem by assuming that each grain in a polycrystal undergoes the same shape change (Fig. IV-3) as the whole polycrystal [177]. His assumption, based on observations of the microstructure in the cross-section of a drawn wire, can be fulfilled by the activation of slip in multiple systems within each grain. Thus, unlike single crystals, regardless the orientation of a polycrystal with regard to the force axis, a minimum of five slip systems must be active to enable the imposed strain rate [174].

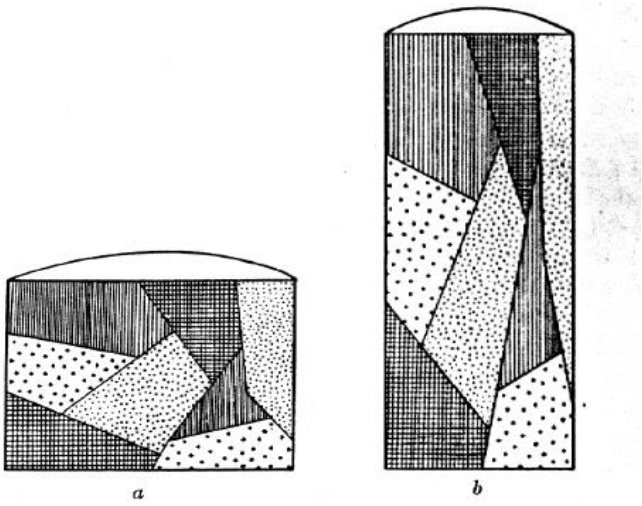

Fig. IV-3 Illustration of a polycrystal unstrained (a) and after tensile deformation (b) [177].

G.I. Taylor proposed a generalization of the Schmid's law for grains in polycrystals as follows [70]:

$$\frac{\sigma_y}{\tau} = M_T \tag{4.2}$$

where σ_y is the yield strength for a grain within the polycrystal, τ is the critical shear for slip and M_T is the Taylor factor. The value of M_T averaged over all orientations for a randomly oriented polycrystal is:

$$\langle M_T \rangle = 3.067 \tag{4.3}$$

Consequently, the activation of multiple slip systems translates into an applied macroscopic strength for polycrystals much higher than for single crystals. For a more microscopic approach of deformation in polycrystals, the work of M.F. Ashby [178] (1970) provides an insight into the physical mechanisms that take place. He investigated polycrystals as plastically inhomogeneous solids where gradients of deformation build up and are resolved by dislocation accumulation (Fig. IV-4). In polycrystals, dislocations accumulate for two reasons, to render deformation compatible or as the outcome of random interactions between them. The first type is known as geometrically necessary dislocations (GNDs) and the second type as statistically stored dislocations (SSDs). M.F. Ashby describes deformation in two steps: general (uniform) deformation, during which accumulation of SSDs take place; and local (non-uniform) deformation, during which GNDs accumulate. The accumulation of both types of dislocations are responsible for strain hardening.

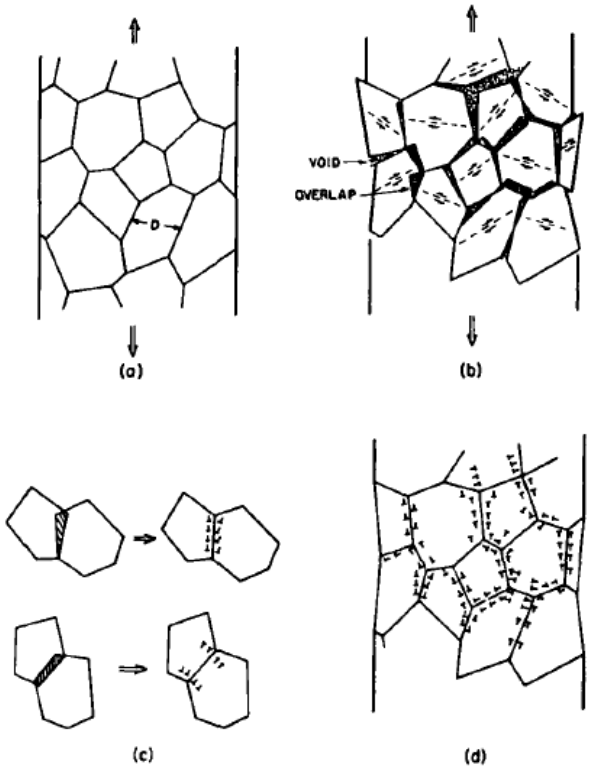

Fig. IV-4 Deformation in a polycrystal as envisioned by M.F. Ashby [178]. Polycrystal at the initial state (a). Grains deform plastically according to Schmid's law creating overlaps and voids (b). GNDs are introduced to ensure continuity (c). The deformed polycrystal with accumulated GNDs around grain boundaries (d).

The case of UFG/NsM materials differs from coarse grain polycrystals. In UFG metals, grain boundaries become exclusively the dislocation sources, whereas in coarse-grain materials dislocation sources can also be found in the grain interior reflecting the internal stress landscape. Moreover, below a certain grain size in NsM, dislocations are no longer responsible for plastic deformation (Fig. IV-5). In the UFG regime, the mean free path of dislocations is limited by the grain boundaries that act as both source and sink of dislocations [75,76]. Hence, dislocations are preferably stored in grains boundaries instead of at the grain interior. For this reason, the increase of strength with grain reduction will depend on whether dislocation annihilation is favored or not. In the case of high dislocation annihilation, hardening is lessened and the effect of grain boundaries in strength would be reduced.

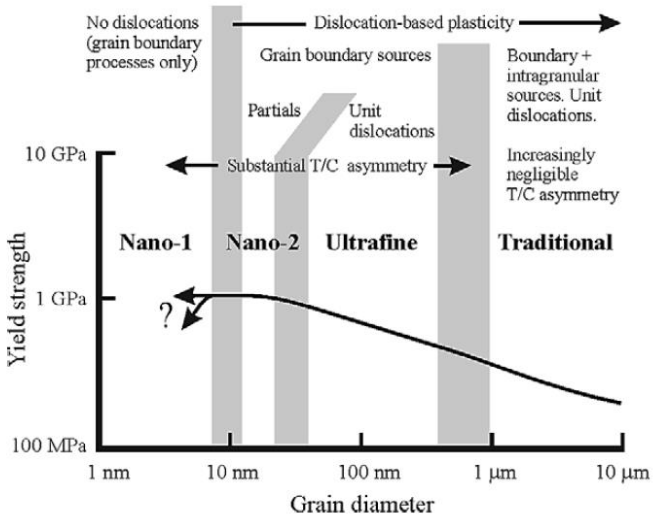

Fig. IV-5 Deformation mechanisms activated depending on the grain size range, suggested by S. Cheng *et al*. [75]. Values of yield strength correspond to Cu as a model material.

1.3. *Strain hardening stages in FCC polycrystals*

Similar to single crystals, in polycrystals strain hardening can be divided into three distinct stages. If work hardening rate is plotted against flow stress, these stages can be easily identified. Fig. IV-6 displays the results obtained for polycrystalline nickel by X. Feaugas *et al.* [94]. The biggest difference between polycrystals and single crystals is stage I. In polycrystals, the strain hardening rate is the highest and decreases with increasing stress. Then, in stage II, a constant hardening rate is depicted and finally in stage III a decrease is observed. Similar to single crystals, work hardening in stage I is related to planar/single slip. Nevertheless, the presence of grain boundaries and deformation incompatibility between grains makes this stage in polycrystals non-linear and of elevated hardening rate [173]. In stage II multiple slip takes place as well as the activation of cross-slip. These mechanisms entail the formation of dense dislocation structures such as tangles, dislocation walls and cells. Finally, in stage III, cross-

slip is generalized as well as the formation of dislocation cells, which is the predominant dislocation arrangement. In this stage, the distribution of dislocations on a microscale is very heterogeneous, with zones of high density of dislocations, such as dislocation walls, and zones of low dislocation density like cell interiors [179].

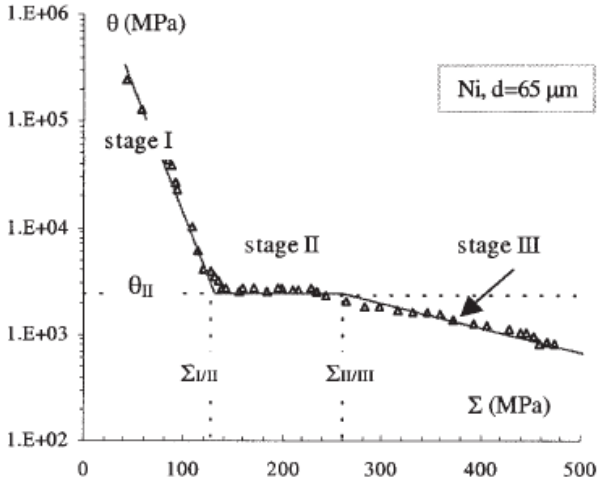

Fig. IV-6 Hardening rate vs flow stress in polycrystalline Ni [94]. The three stages of strain hardening are displayed.

The transition from one stage to another in polycrystals is highly dependable on grain size and temperature. A smaller grain size favors the transition from stage II to stage III due to a higher deformation incompatibility and so does a higher temperature as it facilitates cross-slip.

Concerning samples in nanometric and UFG regimes, F. Dalla Torre *et al.* [110] investigated the strain hardening stages as well as the hardening rate for two Ni samples processed by ED (d = 21 ± 9 nm) and by HPT (d = 105 ± 69 nm).

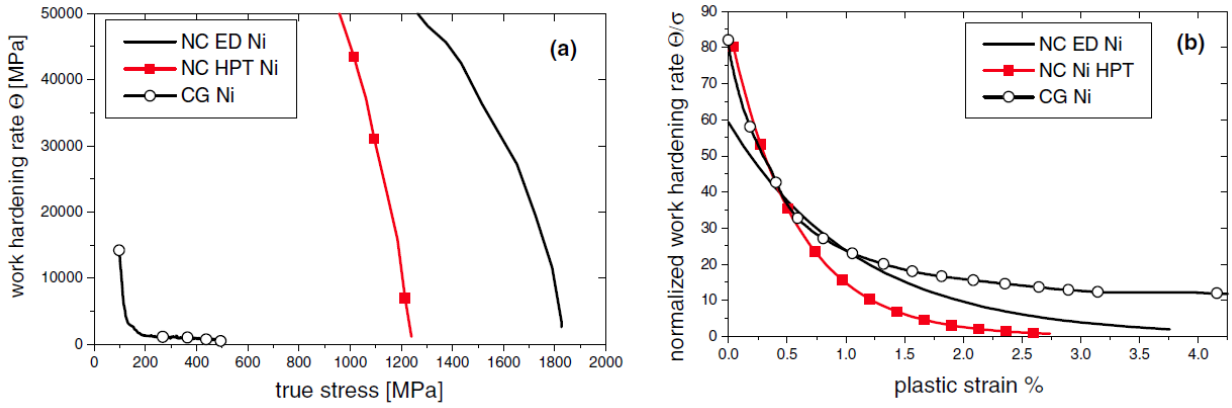

Fig. IV-7 Work hardening rate vs true stress (a) and normalized hardening rate vs plastic strain (b) obtained from uniaxial tensile testing of nanostructured Ni processed by SPD and ED [110].

In Fig. IV-7 (a), the hardening rate of the two nanostructured samples and a coarse grain sample is displayed. A steep decrease of the hardening rate can be depicted for all three samples at the beginning of plastic deformation, whereas the transition from stage I to stage II can only be observed in the coarse-grained sample. If the hardening rate is normalized by true stress (Fig. IV-7 (b)), the three samples can be more easily compared. Both nanocrystalline samples display a lower hardening rate than coarse-grained Ni, which sharpens with strain. These findings are in agreement with the model proposed by S. Cheng *et al*., as the absence of dislocation emission and accumulation in the grain interior eliminates a part of the hardening mechanisms. In view of the continuous decrease in hardening rate for the nanostructured samples, some authors consider that stage III is directly reached whereas others say that no correlation can be made between hardening stages in conventional polycrystals and in NsM/UFG materials [22,110].

2. Mechanical characterization by uniaxial tensile testing of SPS processed samples

2.1. *Sintered samples for tensile testing*

In order to investigate the influence of grain size in the FG/UFG range on the mechanical properties and the mechanisms of plasticity, five samples were synthesized. Three samples were processed from BM powders and two from the as-received commercial powder. In Chapter III, the microstructural characterization of the SPS processed samples displayed a high fraction of Σ3 grain boundaries, which is characteristic of this method of synthesis. The FG/UFG samples obtained from BM powders exhibited different Σ3 GB fractions, which depended on the milling parameters. In fact, this type of boundaries can modify mechanical properties such as the strength or ductility [22,79,80]. Thus, to hinder the influence of GBCD and to evaluate the impact of grain size in tensile properties, BM parameters were chosen to produce specimens with different grain sizes and the most similar fraction of Σ3 grain boundaries. All samples were produced with the same SPS program as presented in Chapter II with the exception of sample 5. In this case, all SPS parameters were kept the same except the maximum temperature, which was fixed to 1273 K, in order to produce a sample with a grain size in the coarse grain range for comparison. Table IV-1 displays the BM parameters of the powders used to produce FG/UFG samples as well as the relative density of the five samples.

Table IV-1 Relative density and synthesis parameters of tensile specimens.

Sample	ρ_{rel} *(%)*	*Type of powder*	*BM time (h)*	*BM speed (rpm)*	*Amount of PCA (%)*
1	98.5 (4)	BM	10	350	66.7
2	99.5 (2)	BM	3	350	16.7
3	99.3 (2)	BM	3	300	66.7
4	97.6 (4)	As-received	---	---	---
5	98.7 (3)	As-received	---	---	---

The good relative density (above 97 %) displayed by the samples indicates that scaling up to obtain larger samples using the same SPS program has a negligible impact on the sintering process. Hardness cartographies were performed on the surface of samples processed with different diameters and results show little difference between them (Appendix D). Microstructural features of the specimens are collected in Table IV-2, where the grain boundary fractions presented were calculated in a length basis.

Table IV-2 Microstructural features of tensile specimens.

Sample	*Grain size (µm)*	*GOS (°)*	*LAGB*	*Σ3*	*CSL*	*HAB*
1	0.82 ± 0.67 (4)	0.7 ± 0.2	0.036	0.495	0.056	0.587
2	1.11 ± 0.84 (7)	0.6 ± 0.3	0.04	0.456	0.044	0.54
3	1.39 ± 1.11 (7)	0.7 ± 0.3	0.023	0.535	0.057	0.385
4	4.0 ± 2.4 (3)	0.6 ± 0.2	0.02	0.526	0.046	0.592
5	25 ± 17 (1.5)	0.7 ± 0.2	0.02	0.616	0.037	0.327

Table IV-2 shows that the grain size range (0.8 µm – 25 µm) covers the UFG/FG spectrum. In addition, the value of GOS below 1° for all samples indicates a low internal stress level as shown in Chapter III and the GBCD shows a high fraction of Σ3 grain boundaries close to 50 % for all samples. Hence, differences depicted in mechanical properties will mainly result from grain refinement.

2.2. *Conventional stress strain curves*

Tensile testing provides key information concerning the mechanical properties as well as strain hardening mechanisms of ductile materials. In this work, uniaxial tensile testing was performed at a

strain rate of 10^{-3} s^{-1} as described in Chapter II and the resulting conventional stress strain curves[19] are plotted in Fig. IV-8.

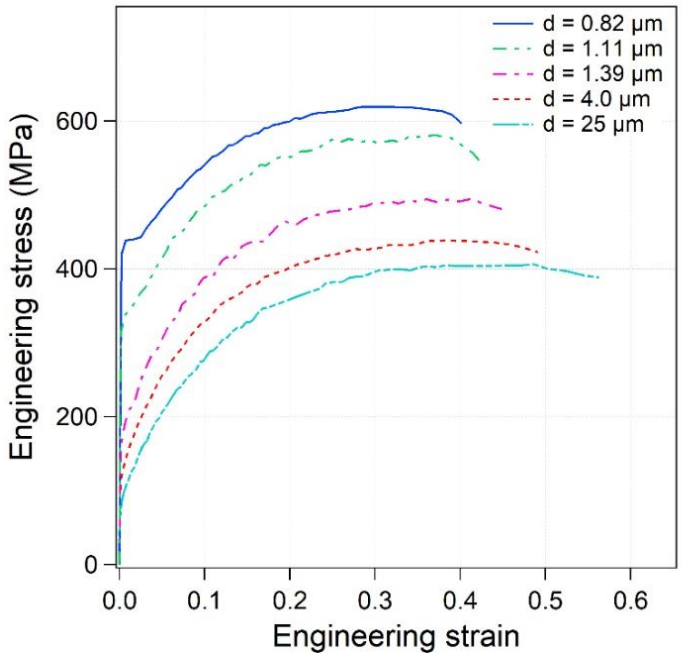

Fig. IV-8 Engineering stress strain curves for samples 1-5 processed by SPS sintering.

At a first glance, the increase in yield strength with grain refinement and high tensile ductility for all samples are the most noticeable features. In addition, the presence of a "Lüders-type" strain is observable for sample 1 and in less importance in sample 2. During tensile testing, in the polished surface of the samples deformation lines in the center of the gauge length were depicted at approximately 45° from the tensile axis at low strain. Since DIC was used to measure the strain evolution, deformation cartographies indicating local distribution of tensile strain were processed (Fig. IV-9). At a true strain (ε) of $\varepsilon = 0.003$ a deformation band appears (Fig. IV-9 (a)), which then propagates throughout the gauge length (Fig. IV-9 (b-c)) to reach a generalized deformation state at $\varepsilon = 0.04$. From that point on, deformation takes place in a uniform way up to the ultimate tensile strength (UTS). This behavior has been reported for other UFG FCC pure metals such as Al [73,81] and Cu [180], as well as for austenitic stainless steel [181]. Lüders-type strain was displayed by samples with grain sizes between $1\ \mu m < d < 4\ \mu m$ in the case of Al and in the range $0.5 < d < 3\ \mu m$ in Cu whereas in this work, only samples with $d < 1.2\ \mu m$ displayed this behavior. This suggests that the transition grain size between coarse grain and UFG might be dependent on the material, as well as the investigated property.

[19] Curves displayed in Fig. IV-8 represent raw data. Only resampling to reduce the number of points per test was performed.

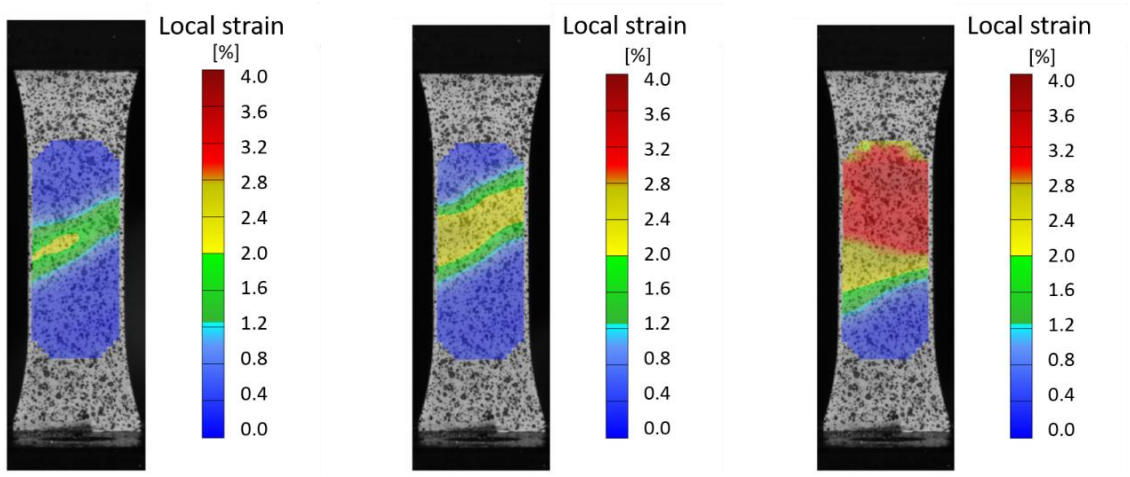

Fig. IV-9 Deformation cartographies obtained from DIC at different strain levels: ε = 0.003 (a), ε = 0.009 (b) and ε = 0.02 (c), for sample 1 (d = 0.82 µm).

Turning to a global outlook of the tensile properties displayed by all samples,

Table **IV-3** presents the measured values of yield strength, UTS, elongation to failure (ε_f), uniform elongation (ε_u) and the product of σ_y x ε_f. It should be noted that the measured values of yield strength and UTS of sample 5 are in agreement with the ones displayed by commercially pure Ni 205, which are 103 MPa and 403 MPa respectively [182]. These results show that the small percentage of porosities in the sintered samples, does not affect the tensile properties.

Table IV-3 Tensile properties of Ni samples.

Sample	σ_y *(MPa)*	*UTS (MPa)*	ε_f *(%)*	ε_u *(%)*	σ_y *x* ε_f
1	441 ± 7	625 ± 4	39 ± 3	30 ± 5	17199 ± 21
2	325 ± 7	582 ± 6	43 ± 1	37 ± 2	13975 ± 7
3	183 ± 9	506 ± 8	46 ± 4	38 ± 4	8418 ± 36
4	130 ± 2	443 ± 2	49 ± 3	41 ± 2	6370 ± 6
5	87 ± 4	408 ± 1	58 ± 3	44 ± 5	5046 ± 12

In addition to a good elongation to failure, a uniform elongation ε_u above 30 % sustains the good ductility of the SPS sintered samples. The product of σ_y x ε_f is included as an indicator of the good toughness. For comparison, the value of this product for a sample produced by SPD and subsequent annealing (to acquire the highest σ_y x ε_f possible) is 10020 [66]. Samples processed by SPS thus display a good combination of strength and ductility, especially specimens with grain sizes in the UFG range.

2.3. *Strain hardening in FG and UFG Ni*

The evolution of stress with deformation i.e. the strain hardening behavior of ductile metals is crucial from a technological point of view, as it provides crucial information about the formability of materials. As a first approach, different mathematical models can be prospected to obtain an explicit expression for the true stress measured by tensile testing as a function of true strain. In this work, the Hollomon approximation was used to obtain an equivalent expression that describes the experimentally obtained curves (Fig. IV-10).

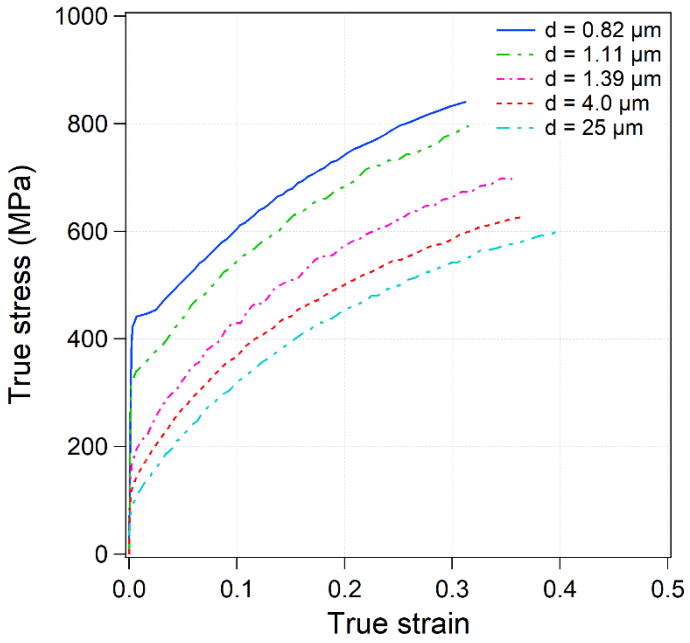

Fig. IV-10 True stress true strain tensile curves for Ni samples 1-5 processed by SPS.

The Hollomon expression (1945) is a simple power law approximation that is adapted to describe the true stress-true strain curves of some metals:

$$\sigma = K_H \cdot \varepsilon^{n_H} \tag{4.4}$$

where K_H and n_H are constants termed respectively Hollomon strain hardening coefficient and strain hardening exponent. If the work hardening behavior of a material can be described by the Hollomon approximation, a linear fit is obtained for ln(σ) plotted against ln(ε) in the plastic domain. The n_H value is obtained from the slope and the intercept at ε = 1 gives the K_H value. These values represent some interesting technological features as from K_H, an approximate measurement of the strength and force required in forming is obtained, whereas n_H provides an indication of the ability of the material to retard the localization of deformation [183].

In fact, because the ultimate tensile strength (UTS) represents the engineering stress at maximum load, it can be determined as [70]:

$$UTS = K_H \left(\frac{n_H}{e}\right)^{n_H} \tag{4.5}$$

Likewise from the definition of n_H:

$$n_H = \frac{d(ln\sigma)}{d(ln\varepsilon)} = \left(\frac{\varepsilon}{\sigma}\right)\frac{d\sigma}{d\varepsilon} \tag{4.6}$$

which implies that $n_H = \varepsilon_u$, for $\frac{d\sigma}{d\varepsilon} = \sigma$ (Considère criterion). The results of fitting ln(σ) vs ln(ε) in the plastic domain for samples 1 and 4 are shown in Fig. IV-11, including the obtained values of K_H, and n_H. A reasonably good fit is obtained for both samples with the biggest deviations found at low strain for sample 1 (Fig. IV-11 (a)) and at high strain for sample 4 (Fig. IV-11 (b)). These deviations have been reported and discussed by several authors [183–185] and usually account for tensile instability which occurs when θ_h decreases to match the flow stress. Hence, the Lüders-type strain depicted in the tensile curve for sample 1 would be responsible for the deviation at low strain in sample 1, whereas in sample 4 the discrepancy could indicate the beginning of necking.

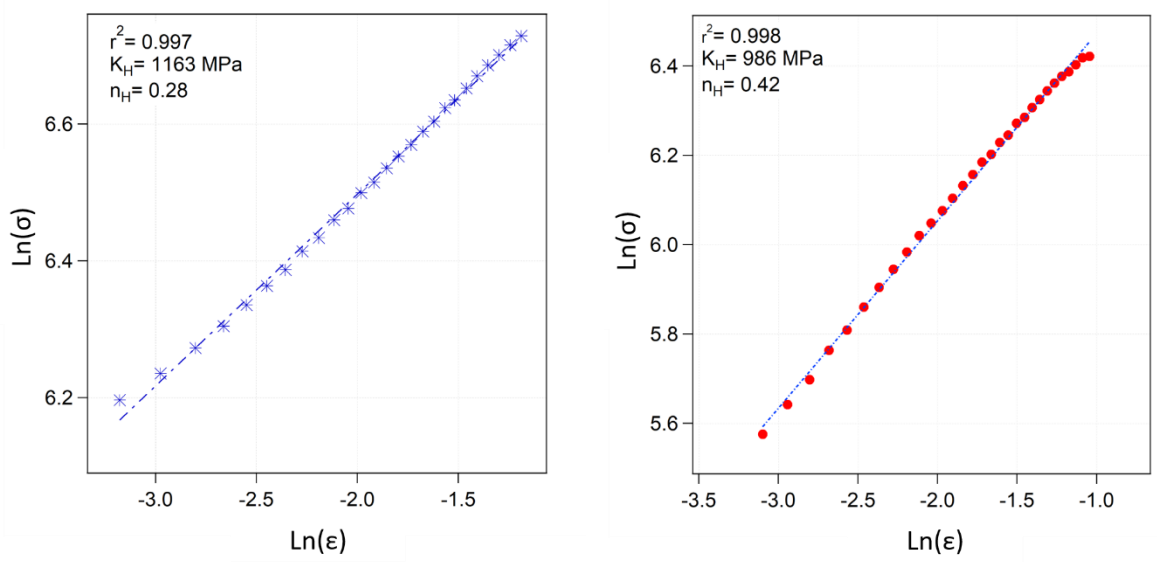

(a) (b)

Fig. IV-11 Linear fit of ln (σ) vs ln (ε) of samples 1 (d = 0.82 µm) (a) and 4 (d = 4 µm) (b).

To verify the accuracy of the mathematical model on describing the deformation behavior in these two samples, the strain hardening parameters can be used to compute an equivalent "Hollomon stress". For sample 1, it can be seen (Fig. IV-12 (a)) that the Hollomon model fails to correctly describe yield

strength as well as stress at low values of ε. Nevertheless, for ε ≥ 0.035, the tensile behavior is well reproduced. In the case of sample 4 (Fig. IV-12 (b)), the computed curve matches precisely the experimental data with the exception of the last points.

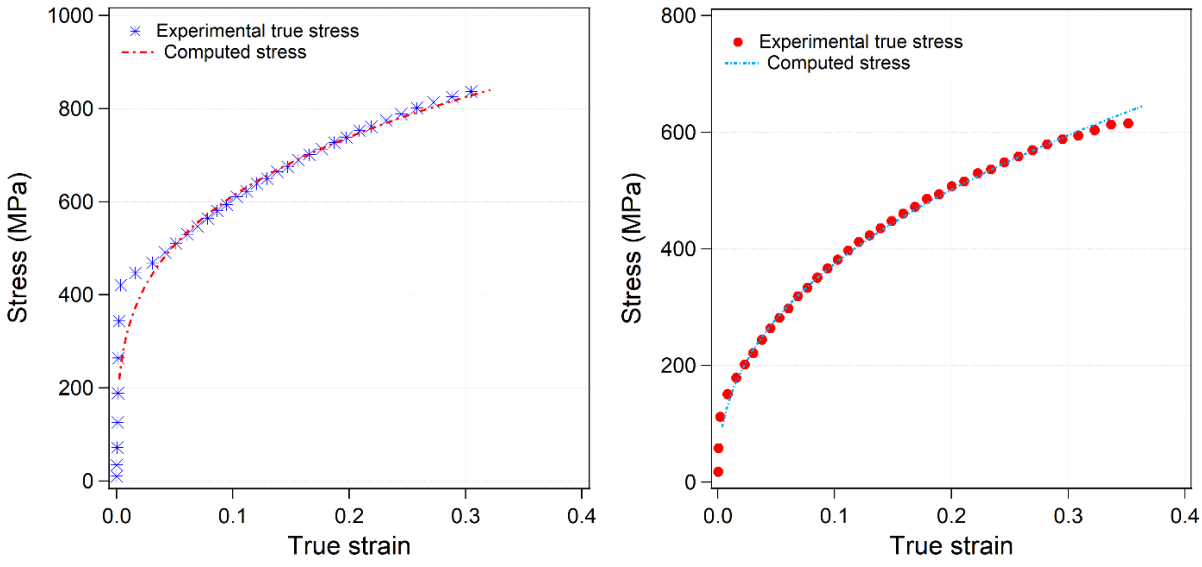

Fig. IV-12 Computed stress superposed to true stress vs true strain curves for samples 1 (d = 0.82 µm) (a) and 4 (d = 4.0 µm) (b).

Similar results were obtained for the other three samples. Samples 3 and 5 are correctly described at all deformation levels, while sample 2 shows a deviation for ε ≤ 0.025. The values obtained for the parameters K_H, and n_H as a function of grain size are plotted in Fig. IV-13.

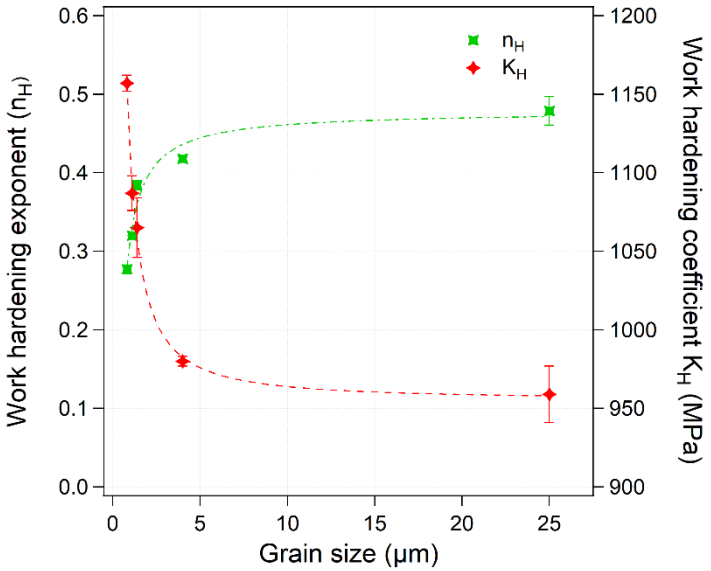

Fig. IV-13 Evolution of work hardening parameters n_H and K_H with grain size.

The value of n_H varies between 0.26 and 0.48 decreasing with grain size. In the coarse-grain size range, a slow reduction is displayed whereas in the UFG range a rapid decrease is observed. For comparison, Fig. IV-14 (a) exhibits the effect of varying n_H at an intermediate value of K_H. A higher value of n_H translates into a higher hardening rate and a larger domain of uniform deformation i.e. necking will start at higher values of deformation [183]. Therefore, this approximation predicts lower strain hardening for smaller grain sizes, especially for d < 1.3 µm, and reduced elongation (Table IV-3).

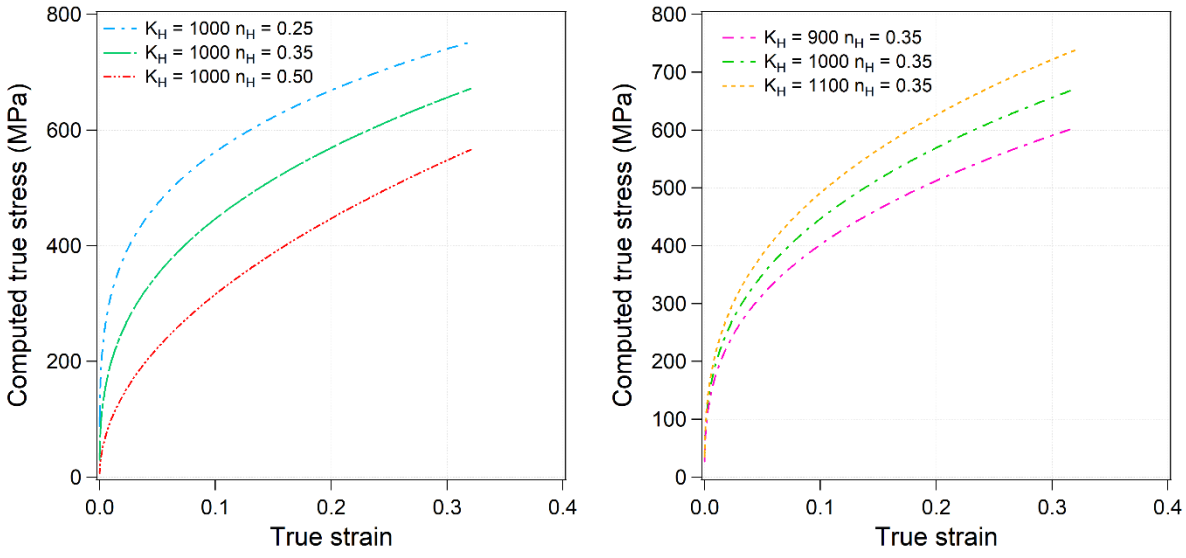

Fig. IV-14 Evolution of the true stress strain curve when n_H (a) and K_H (b) are varied.

In the case of the work hardening coefficient, samples display values between 950 MPa and 1120 MPa and it is inversely related to grain size. In Fig. IV-14 (b), it can be seen that the influence of K_H in the deformation behavior is less pronounced than the influence of n_H. As stated earlier in this section, K_H is related to the strength necessary to deform the material, thus forming the samples of smaller grain size will require the application of higher stress.

2.4. *Influence of grain size on strength and ductility*

Among the microstructural features of a sample, grain size has a major impact on the mechanical properties. An increase in the fraction of grain boundaries (reduction of grain size) entails strengthening, following the HP relation. In Chapter I, the influence of grain size on mechanical properties in the UFG range was introduced. Some deviations from the HP relation were depicted for Ni samples processed by SPD and by powder metallurgy from nanopowders. Thus, in the following section, the effect of grain size on strength and ductility is investigated for samples processed by SPS.

Influence of grain size on strength

First, the influence of grain size on yield strength is evaluated. In Fig. IV-15, the linear HP fit for NsM/UFG Ni samples processed by ED is included as a reference [40], with a friction stress (σ_0) of 37 MPa and a HP constant (k_{HP}) of 175 MPa/µm$^{1/2}$. As reported in Chapter I, these values are very close to those determined by C. Keller et *al.* [93] for coarse-grained Ni, σ_0 = 14.23 MPa and k_{HP} = 180 MPa/µm$^{1/2}$.

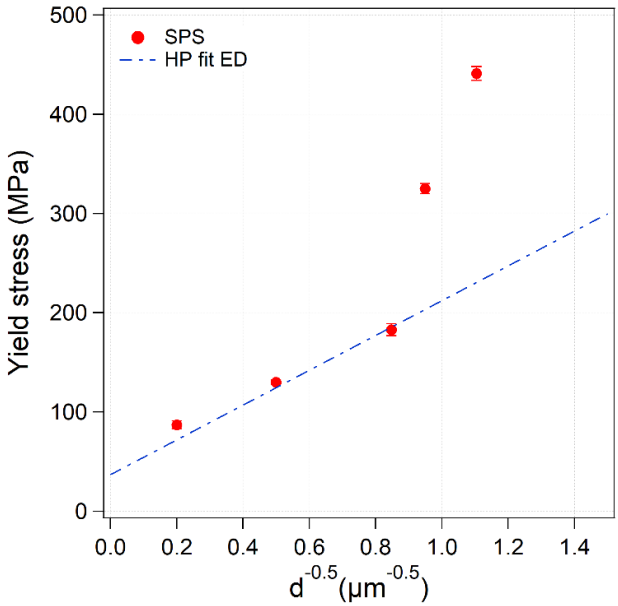

Fig. IV-15 Influence of grain size on yield strength for Ni samples processed by SPS. A deviation from the HP relation can be depicted for samples with grain sizes in the UFG range.

Samples 3-5 display a yield strength in agreement with the value expected from the HP relation, whereas samples 1-2 deviate to higher values. In Chapter III, the absence of diffraction peaks corresponding to oxides or other contaminants by XRD was reported, which means that contamination is not the main cause of the supplementary strengthening. A hypothesis from C.Y. Yu *et al.* [73] for a similar behavior observed in UFG Al obtained from SPD and consequent annealing seems like a more plausible explanation. They investigated a larger range of UFG samples and obtained the results displayed in Fig. IV-16.

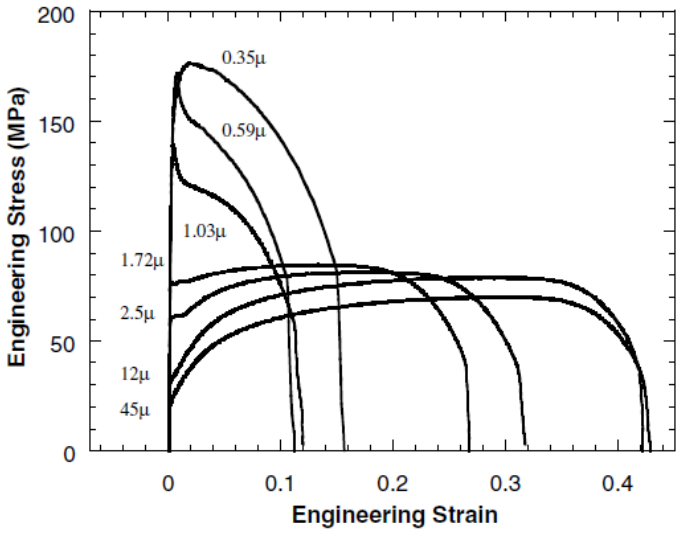

Fig. IV-16 Tensile stress strain curves obtained for Al processed by ECAE + annealing at different temperatures [73].

The curve corresponding to the smallest grain size presents the same shape observed for UFG Ni samples prepared by SPD (Chapter I). A second behavior is observed for 0.4 µm < d < 1.5 µm, exhibiting a yield drop at the beginning followed by necking, which was discussed in Chapter I. The third behavior (1.5 µm < d < 3 µm) is the one displayed by the samples in this study, a Lüders-type strain after yielding, followed by strain hardening. Finally, the behavior expected for coarse-grained materials is observed. The authors suggest that the origin of the different behaviors results from inhomogeneous yielding due to of the presence of very small grains. The difference in size makes yielding easier in some grains, thus undergoing a pre-yielding microstrain that then percolates to generate a general yielding. To do so, the hardening rate has to be high enough to allow the spreading of deformation to the surrounding grains. The lower strain hardening displayed by small size grains delays the homogenization of deformation, which results in the presence of a Lüders-type deformation. Once strain hardening is generalized, uniform deformation begins. If grains are too small, necking occurs before uniform deformation is reached.

If inhomogeneous yielding takes place, the average strain measured across the gauge length is not representative of the strain in the deformed zone. To eliminate the "inhomogeneous yielding factor", C.Y. Yu *et al.* suggested extrapolating the stress at 0.2 % deformation using a work hardening model capable of describing the deformation behavior of the investigated samples. The extrapolation of the yield strength using the modeled curves from the Hollomon model provides values for samples 1 and 2 that correspond to the ones expected by the HP relation (Fig. IV-17).

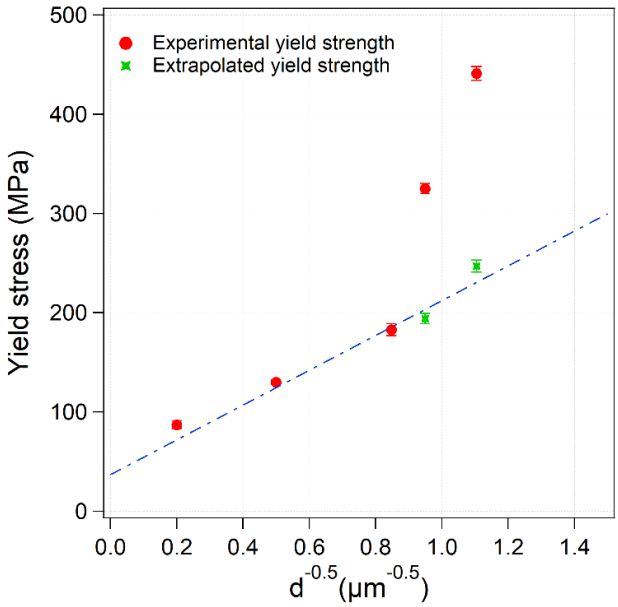

Fig. IV-17 Grain size vs measured yield strength (red circles) and extrapolated yield strength (green stars).

Despite the small difference in average grain size between samples 2 and 3, the difference in the fraction of grains in the UFG regime can account for the presence of the Lüders-type strain in sample 2 and not in sample 3 (Fig. IV-18). For instance, the fraction of grains that display a grain size of $d < 1$ µm is 10.6 % in sample 2 and 6.5 % in sample 3. This difference is not very important, nevertheless, the results obtained for UFG Al by C.Y. Yu *et al.* show that the transition to the UFG regime, is not fixed at 1 µm. If the transition takes place for $d < 2$ µm, the corresponding fractions are 42.4 % for sample 2 and 26.5 % for sample 3.

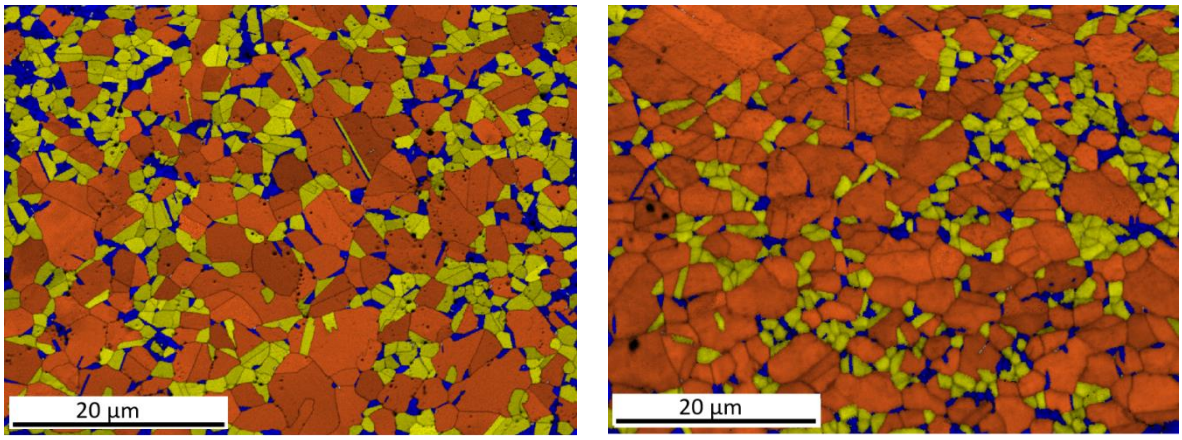

(a) (b)

Fig. IV-18 Grain size cartography superposed over the IQ cartography of samples 2 (a) and 3 (b). Blue grains display a grain size $d < 1$ µm, yellow grains 1 µm $< d < 2$ µm and orange grains $d > 2$ µm.

The hypothesis of C.Y. Yu *et al.* seems coherent with the results obtained in this study for yield strength. To verify if this effect persists at higher deformation levels, the effect of grain size on stress at

different strain levels is displayed in Fig. IV-19. A deviation is still found at higher deformation levels, despite a smaller difference in k_{HP} at higher deformation. The linear fit in the UFG and coarse grain regimes has to be considered roughly, as only three points were used for this purpose. Nevertheless, as an estimation, k_{HP} determined for $\varepsilon = 0.002$ is 6.6 times higher in the UFG regime than the coarse-grained regime, whereas for $\varepsilon = 0.2$ it is 3.3 times higher.

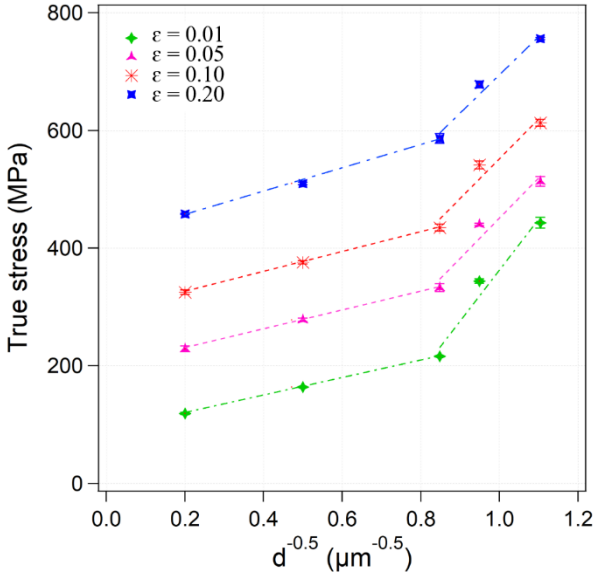

Fig. IV-19 Effect of grain size on stress at different deformation levels.

Finally, concerning the UTS, Fig. IV-20 shows that the experimental values are in good agreement with the computed values using K_H (Eq. (4.5)), where two distinct linear sections are still observed.

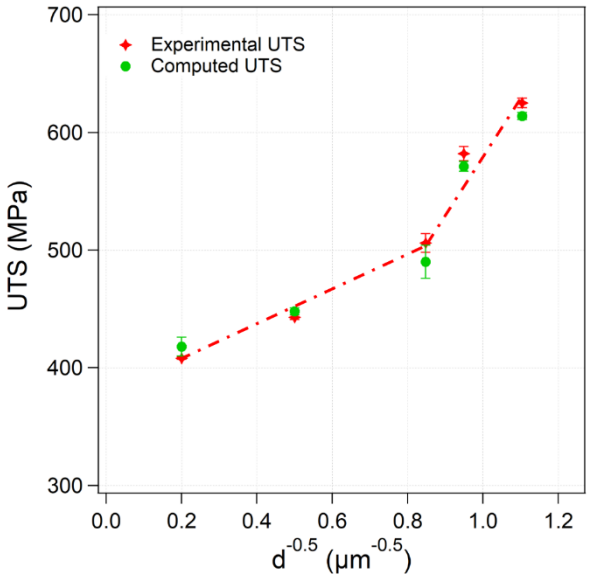

Fig. IV-20 Effect of grain size on UTS.

Influence of grain size on ductility

Concerning the influence of grain size on ductility, uniform elongation and elongation to failure plotted against $d^{-1/2}$ are displayed on Fig. IV-21 (a). A reduction of ductility with decreasing grain size is observed. It is important to acknowledge that even if elongation is reduced for smaller grain sizes, the smallest grain size (sample 1) displays a uniform elongation of ~30 %. This high ductility in UFG samples, can result from the high presence of Σ3 grain boundaries induced by the SPS process, as reported for Cu [22,79,80]. The values of uniform deformation obtained experimentally are in good agreement with the values of n_H computed using the Hollomon approximation Fig. IV-21 (b).

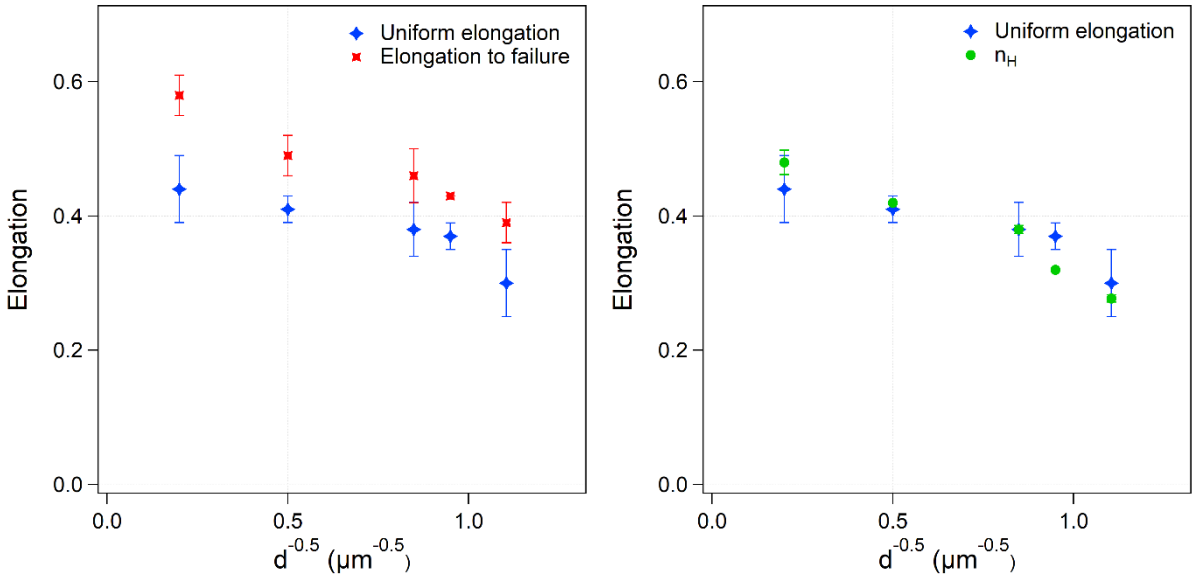

Fig. IV-21 Grain size dependence of elongation to failure and uniform elongation (a) and comparison of ε_u with n_H (b).

As explained in Chapter I, this reduction of ductility is expected, because of the reduced hardening rate in UFG samples, compared to their coarse-grained counterparts. Considering elongation to failure, a bigger difference between samples 1 and 5 can be depicted, which evolves from a 15 % difference in uniform elongation, to a 20 % difference in elongation to failure. Hence, once necking occurs samples with smaller grain size are less resistant to fracture. In this work, all samples display fracture surfaces with dimples, which are characteristic of ductile failure. This is in agreement with the literature, as it has been shown [22], that the fracture morphology in UFG FCC metals such as copper or nickel are similar to the coarse-grained specimens.

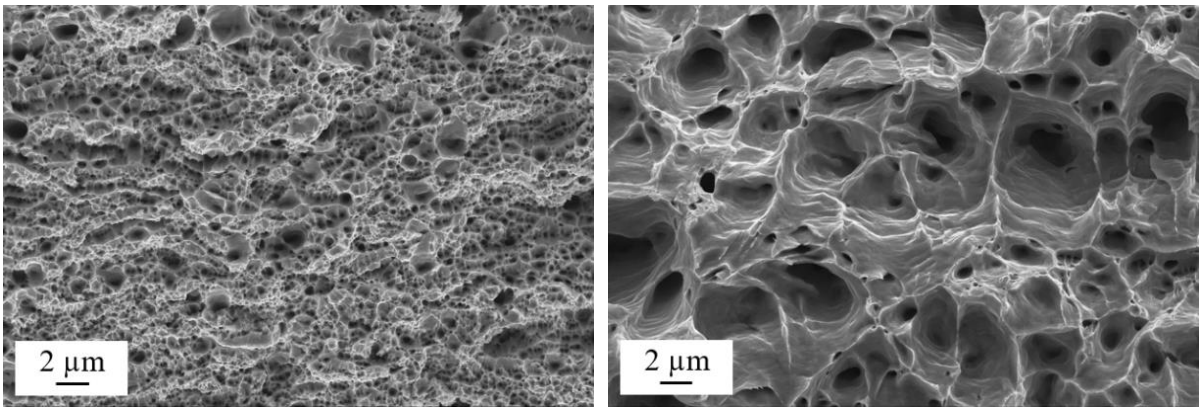

(a) (b)

Fig. IV-22 SEM images of the fracture surface of samples 1 (d = 0.82 µm) (a) and 4 (d = 4 µm) (b).

Nevertheless, a difference in dimple size can be depicted depending on the sample (Fig. IV-22). The presence of pores, as the main defects in all samples, are probably at the origin of fracture as they represent regions of high stress [70]. In Chapter III the porosities in samples similar to samples 1 and 4 were examined showing a difference in the size and location of the pores. Even if relative density was similar, the sample with smaller grain size displayed a higher number of spherical pores situated preferably in the volume, whereas big pores situated at grain boundaries were observed in the sample with bigger grain size. The lower resistance to fracture of sample 1 might result from the bigger amount of pores situated closer to each other, thus allowing for a faster pore coalescence resulting in failure (Fig. IV-23).

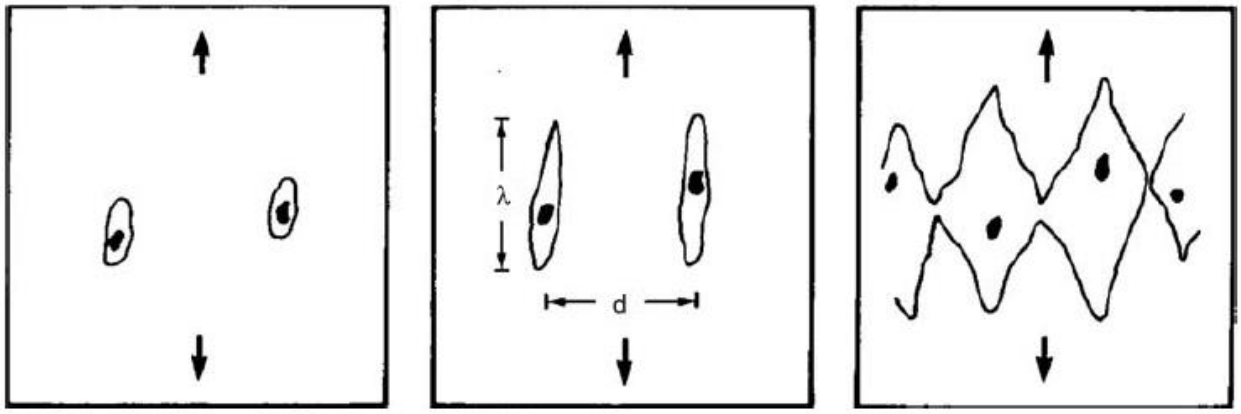

Fig. IV-23 Schematic drawing displaying the formation, growth and coalescence of voids during tension [70].

3. Mechanisms of plasticity

So far, results have shown that UFG Ni samples prepared by SPS display some deviations from classical FCC coarse-grained mechanical behaviors such as the presence of a Lüders-type strain or a higher strength than that expected from the HP relation. Nevertheless, a deeper investigation on the

mechanisms of plasticity leading deformation for these samples is still lacking. To this aim, the dislocation based model of Mecking-Kocks was employed for a quantitative study of strain hardening, the classical stages of hardening were evaluated and microstructures after fracture investigated by means of EBSD and TEM.

3.1. *The Mecking-Kocks model*

The study of strain hardening in metals has entailed the development of different models, aiming to describe the evolution of flow stress with increasing deformation. Phenomenological models such as the Hollomon approximation do not provide information about the physical mechanisms related to strain hardening. Hence, physical models based on the dislocation theory of plasticity were developed.

According to the Mecking-Kocks model, the relation between flow stress in terms of resolved shear stress and total dislocation density (ρ_d) can be expressed as [175,186,187]:

$$\tau = \alpha_d \mu b \sqrt{\rho_d} \tag{4.7}$$

where α_d is an interaction coefficient that depends on the type of interaction between dislocations as well as their configuration and can be taken as 0.35 [188], μ is the shear modulus (81000 MPa for Ni [173]) and b is the norm of the Burgers vector, 0.25 nm for Ni [189]. In terms of externally applied stress, through equation (4.2), equation (4.7) can be rewritten as follows:

$$\sigma = \alpha_d \mu b M_T \sqrt{\rho_d} \tag{4.8}$$

Furthermore, the evolution of ρ_d with deformation can be described by the following equation [173,186,190]:

$$\frac{d\rho_d}{d\varepsilon} = \frac{M_T \sqrt{\rho_d}}{\beta_d b} + \frac{k_g M_T}{bd} - \frac{2 M_T P y_a \rho_d}{b} \tag{4.9}$$

This equation takes into account three dislocation related phenomena: accumulation of dislocations, generation of GNDs at grain boundaries and dislocation annihilation. The first term in the right side of the equation represents the accumulation of mobile dislocations, where β_d represents the ratio between the dislocations mean free path (Λ) and the near neighbor dislocation spacing (l_d): $\beta_d = \frac{\Lambda}{l_d}$, and the other parameters have their usual meaning. The dislocations mean free path is the distance traveled by a dislocation before interacting with the microstructure (*i.e.* other dislocations, precipitates, grain

boundaries) and become stored [191]. On the other hand, the near neighbor dislocation spacing provides information on the total density of dislocations as they as related as: $l_d = \frac{1}{\sqrt{\rho_d}}$ [187]. The second term accounts for the presence of GNDs at grain boundaries [173,192], where it is noticeable that the density of GNDs is inversely proportional to grain size [178]. In this term, the parameter k_g represents a geometric factor that depends on the morphology of grains. Finally, the last term corresponds to dislocation annihilation that results from generalized cross-slip. The probability of annihilation is represented by P and y_a symbolizes the distance of annihilation of two dislocations by cross-slip [173,192]. Because of the low probability of dislocation annihilation at the beginning of strain hardening, this last term is negligible throughout stages I and II. Equations (4.8) and (4.9) can be combined as follows:

$$\frac{d}{d\varepsilon}\left(\frac{\sigma}{\alpha_d \mu b M_T}\right)^2 = \frac{\sigma}{\alpha_d \mu b^2 \beta_d} + \frac{k_g M_T}{bd} - \frac{2 M_T P y_a}{b}\left(\frac{\sigma}{\alpha_d \mu b M_T}\right)^2 \tag{4.10}$$

rearranging terms and using the chain rule, the following expression is obtained:

$$\sigma \cdot \theta_h = \sigma \frac{d\sigma}{d\varepsilon} = \frac{\alpha_d \mu M_T^2}{2\beta_d}\sigma + \frac{\alpha_d^2 \mu^2 b M_T^3 k_g}{2d} - \frac{\alpha_d \mu M_T P y_a \sigma^2}{b} \tag{4.11}$$

The product $\sigma \cdot \theta_h$ can be used to study the transition between strain hardening stages as well as to obtain information of the β_d and k_g parameters. An example of the evolution of $\sigma \cdot \theta_h$ with stress for Cu at different temperatures and coarse-grained Ni with different grain sizes are displayed in Fig. IV-24. In these curves, stage I represents the steep decrease in $\sigma \cdot \theta_h$ and stage II the linear part of increasing $\sigma \cdot \theta$ (dashed line in Fig. IV-24 (a)). The study of the evolution of $\sigma \cdot \theta_h$ as a function of σ in stage II enables the determination of parameters β_d and kg, as the term concerning dislocation annihilation is negligible. Once linearity is lost, stage III of strain hardening begins.

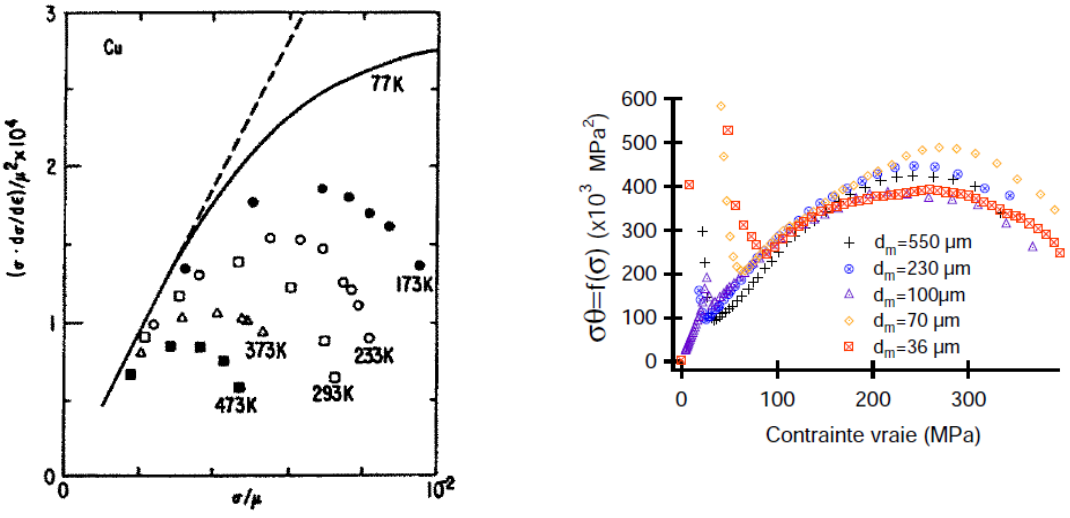

(a) (b)

Fig. IV-24 Example of the evolution of $\sigma \cdot \theta_h$ as a function of σ for Cu polycrystals at different temperatures [175] (a) and for Ni polycrystals with different grain sizes [173] (b).

3.2. *Stages of strain hardening in FG/UFG Ni*

The evolution of the strain hardening rate with flow stress is plotted in Fig. IV-25 (a) for all five sintered samples. It can be observed that all samples display a strong decrease in hardening rate at low flow stress that evolves to a more stabilized hardening rate. Despite the shift of the curves to higher flow stress with decreasing grain size, which is a consequence of the difference in yield strength, the aspect of the curves is very similar. The evolution of the work hardening rate normalized by flow stress (Fig. IV-25 (b)) as a function of strain shows a higher hardening rate for samples with bigger grain size. For instance, at $\varepsilon = 0.1$, the normalized hardening rate of sample 5 is 82 % higher than the normalized hardening rate of sample 1. These results correlate well with the tendency observed by F. Dalla Torre *et al*. [110] on nanocrystalline Ni.

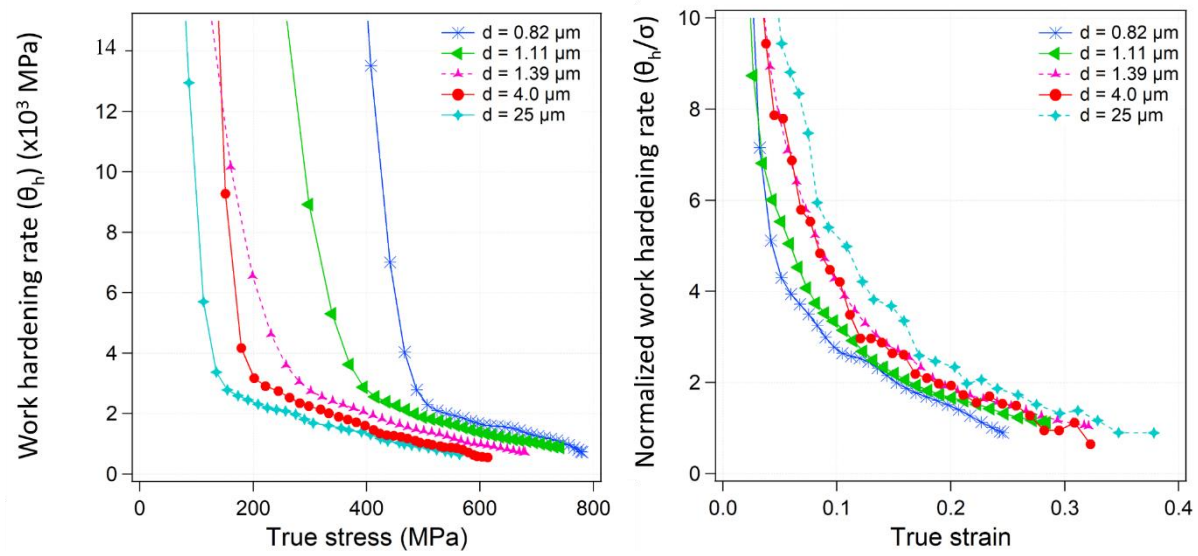

Fig. IV-25 Evolution of the hardening rate with true stress (a) and evolution of normalized hardening rate with true strain (b) for five Ni samples prepared by SPS with different grain sizes.

Let us now investigate the evolution of the $\sigma \cdot \theta_h$ product with stress. From Fig. IV-26 (a), it can be seen that grain size has a big influence in the stress of transition between stages I and II ($\sigma_{I/II}$), which results from the difference in yield strength between samples. Due to the big difference in yield strength between samples, a better comparison can be done if stress is normalized by the yield strength (Fig. IV-26 (b)). In such case, the transition between both stages can be observed at a value of σ/σ_y close to 1.5 for all samples.

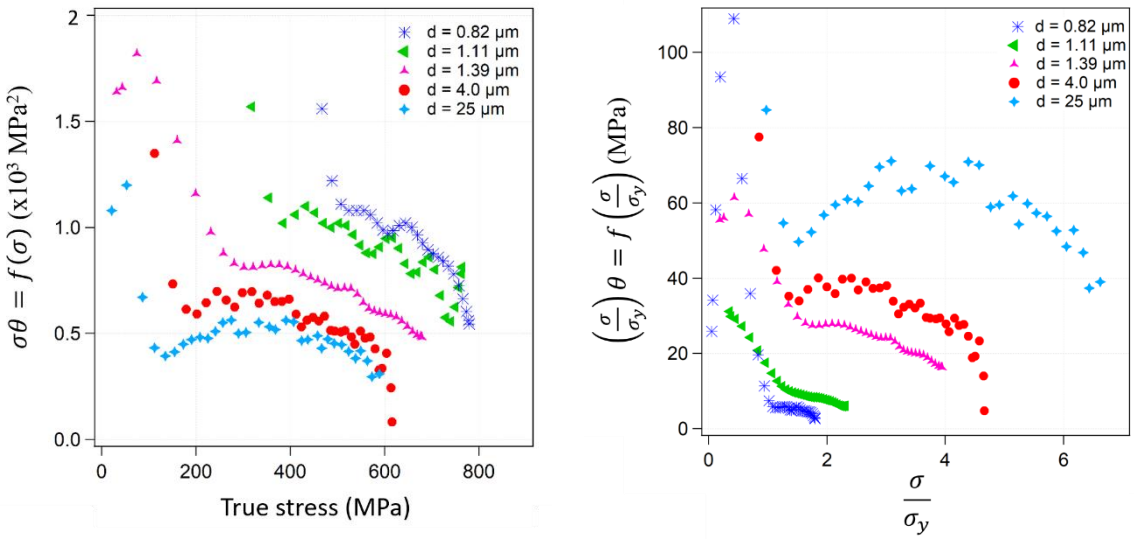

(a) (b)

Fig. IV-26 Evolution of the $\sigma \cdot \theta_h$ product with stress for Ni samples processed by SPS with different grain sizes (a) and the same curves after normalization of stress by yield strength (b).

Concerning the transition stress from stage II to stage III ($\sigma_{II/III}$), it increases with decreasing grain size (Fig. IV-27 (a)). This trend had been reported by X. Feaugas *et al.* [94] for coarse grained nickel. Nevertheless, if normalized by the yield strength (Fig. IV-27 (b)), the contrary trend can be depicted. The stress necessary for the transition to stage III for the coarse-grained nickel sample (sample 5) is ~3.5 times its yield strength, whereas for the two UFG samples (samples 1 and 2) the transition takes place shortly after yielding.

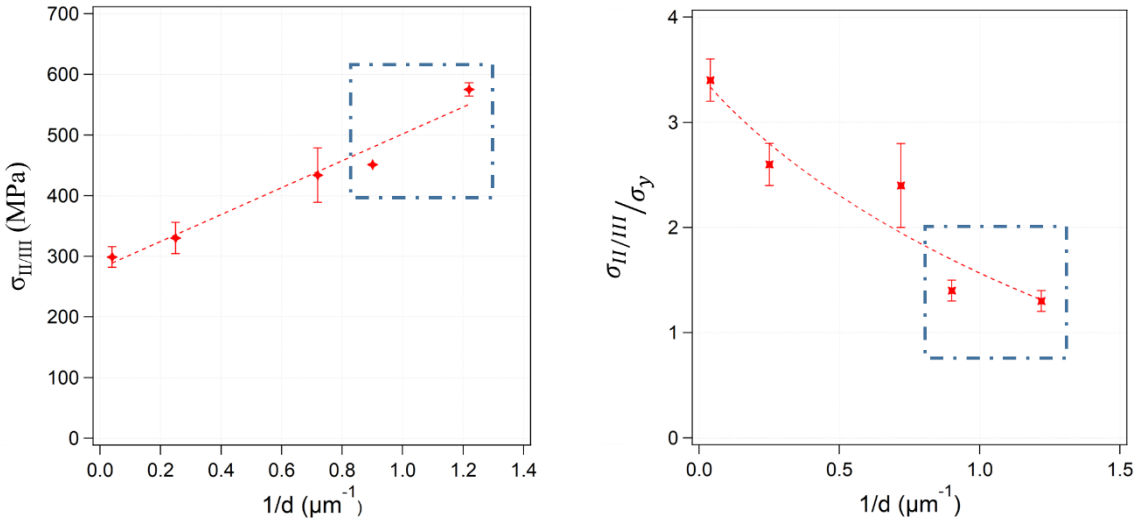

(a) (b)

Fig. IV-27 Evolution of $\sigma_{II/III}$ (a) and $\sigma_{II/III}$ normalized by yield strength (b) as a function of 1/d. The two UFG samples are framed in blue.

As reported above, if the Mecking-Kocks model is assumed Eq. (4.11) can be used to investigate the strain hardening rate in stage II (θ_{II}) as:

$$\theta_{II} = \Delta_{II} + \frac{(\sigma\theta_h)_0}{\sigma} \tag{4.12}$$

where:

$$\Delta_{II} = \frac{\alpha_d \mu M_T^2}{2\beta_d} \tag{4.13}$$

$$(\sigma\theta_h)_0 = \frac{\alpha_d^2 \mu^2 M_T^3 k_g b}{2d} \tag{4.14}$$

Thus, from Eq. (4.12) it can deduced that hardening in stage II depends on two terms, a first one related to the interaction between dislocations (Eq. (4.13)) known as latent hardening rate [173] and a second one, inversely proportional to stress. The second term corresponds, for a polycrystal of a pure single-phase metal, to the contribution of grain boundaries, through GNDs, to strain hardening. The dependency of $(\sigma\theta_h)_0$ with grain size (Eq. (4.14)) implies an increase of the second term of Eq. (4.12), when refining the microstructure. Nevertheless, with increasing stress, the contribution of this term decreases until becoming negligible. These two terms can be obtained from the fraction of the plots of $\sigma\cdot\theta_h$ as a function of stress situated between $\sigma_{I/II}$ and $\sigma_{II/III}$ (Fig. IV-28). A linear fit of this section gives Δ_{II} as the slope and $(\sigma\theta_h)_0$ as the origin intercept[20].

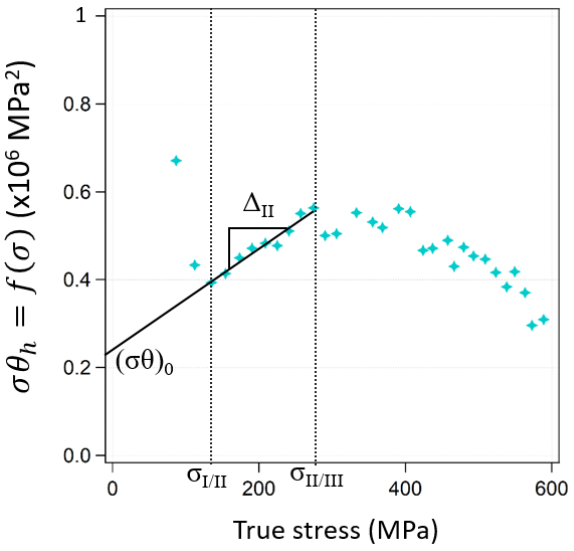

Fig. IV-28 Evolution of the $\sigma\cdot\theta_h$ product with stress for sample 5 (d = 25 µm), displaying transition stresses $\sigma_{I/II}$ and $\sigma_{II/III}$ as well as terms Δ_{II} and $(\sigma\theta_h)_0$.

[20] Smoothing of the stress-strain curves was performed for samples 1-3 to visualize correctly the strain hardening behavior.

The evolution of the latent hardening rate as a function of grain size is plotted in Fig. IV-29. An important decrease of Δ_{II} with grain size can be depicted, with samples of smaller grain sizes in the UFG range displaying a negative value.

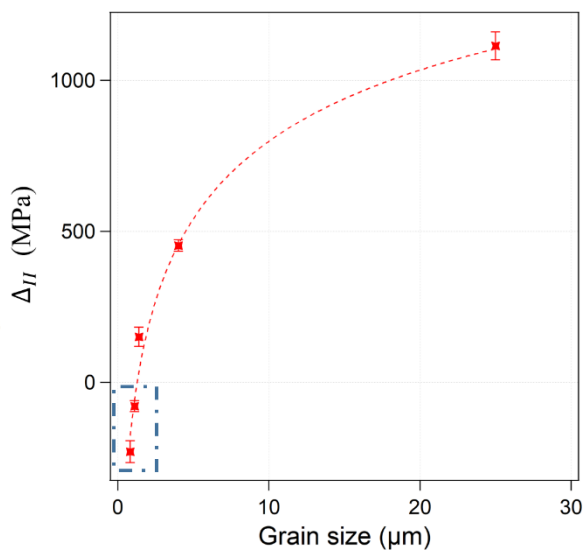

Fig. IV-29 Evolution of the latent hardening rate, Δ_{II}, in stage II of strain hardening as a function of grain size. The two UFG samples are framed in blue.

From Eq. (4.13) and using the values of α, M_T and μ reported earlier, the values of β_d can be determined. For sample 5, β_d = 120 which is in agreement with the order of magnitude reported for coarse grained Ni [173]. On the other hand, samples 4 and 3, display much higher values, β_d = 295 and β_d = 885, respectively, implying a decrease in the near neighbor dislocation spacing (l_d) with smaller grain size if the free mean path is constant. Nevertheless, when the UFG regime is reached a negative value is obtained. Because β_d represents a physical magnitude, a ratio of distances, a negative value is not possible. In order to study the stage II of strain hardening, the assumption of dislocation annihilation being negligible was made. Nevertheless, the high fraction of grains boundaries in the UFG regime that act both as dislocation source and sink [75,76] could enable dislocation annihilation from the beginning of plastic deformation. Thus, the expression of Δ_{II} would have to account for the contribution of the last term of Eq. (4.11). If the probability of dislocation annihilation increases with decreasing grain size, the value of Δ_{II} would become more negative with smaller grain size. On the other hand, given the short length of stage II, the uncertainty when measuring the slope is very high. Thus, possibly for both UFG samples the latent hardening rate is close to zero.

Concerning the second parameter, the evolution of $(\sigma\theta_h)_0$ as a function of the inverse value of grain size is displayed in Fig. IV-30. A linear trend can be depicted, as expected from Eq. (4.14), where the parameter $(\sigma\theta_h)_0$ increases with decreasing grain size. Because $(\sigma\theta_h)_0$ represents the contribution of grain boundaries, if an extrapolation to an infinite grain size is made, the obtained value should ideally

be zero. In the present case the obtained value is 260000 MPa^2, which is ten times higher than the value obtained by C. Keller for carefully recrystallized coarse-grain Ni [173]. The nature of grain boundaries in UFG metals can exhibit a different hardening behavior than conventional CG metals [127], thus using results corresponding to UFG Ni samples for the extrapolation might not be appropriate. If only the CG samples are used for the fit, a decrease in the extrapolated $(\sigma\theta_h)_0$ can already be observed (Fig. IV-30). Nevertheless, the high value probably reflects that additional factors other than grain boundaries, such as impurities or porosities, contribute to hardening in stage II.

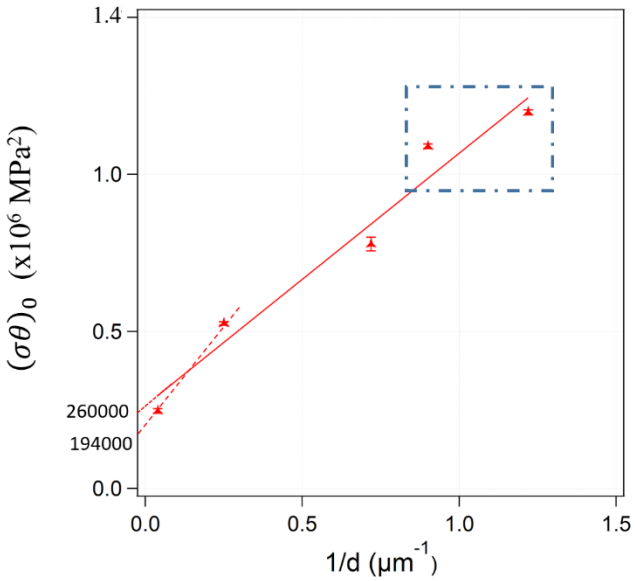

Fig. IV-30 Evolution of $(\sigma\theta_h)_0$ as a function of 1/d. Extrapolation of to an infinite grain size is displayed in the case of using all samples for linear fit and if only CG samples are used. The two UFG samples are framed in blue.

Finally, from the slope of Fig. IV-30, the geometric factor k_g can be calculated using Eq. (4.14) and the values for α_d, μ, M_T and b reported earlier. The obtained value is 0.8, which is in good agreement with the value obtained for coarse-grained nickel k_g = 0.6 [173]. A summary of the results obtained in the study of the strain hardening stage II are collected in Table IV-4.

Table IV-4 Characteristics of strain hardening in stage II of samples processed by SPS.

Sample	*Grain size (μm)*	$\sigma_{I/II}$ *(MPa)*	$\sigma_{II/III}$ *(MPa)*	Δ_{II} *(MPa)*	$(\sigma\theta_h)_0$ *(MPa^2)*
1	0.82 ± 0.67 (4)	535 ± 14	575 ± 11	-229 ± 36	1196800 ± 8200
2	1.11 ± 0.84 (7)	414 ± 2	451 ± 1	-79 ± 18	1088850 ± 7150
3	1.39 ± 1.11 (7)	345 ± 38	434 ± 45	151 ± 32	777890 ± 22030
4	4.0 ± 2.4 (3)	187 ± 6	330 ± 26	453 ± 19	524910 ± 5080
5	25 ± 17 (1.5)	150 ± 29	299 ± 17	1114 ± 46	247040 ± 7420

In this section, it has been shown that a comparative study of strain hardening in the FG/UFG regime is not straightforward due to the difference in yield strength. When normalized by stress, a lower hardening rate is displayed by UFG samples, which is in agreement with the results obtained from the Hollomon approximation. The effect of grain size in the transition from stage I to II is low, whereas the transition from stage II to III is highly influenced by grain size, with samples in the UFG regime transitioning short after yielding. The Mecking-Kocks model seems applicable to the samples in the UFG regime investigated in this study as results follow the expected trend. Nevertheless, the negative values of β_d obtained for the UFG samples suggest that for the UFG regime, the assumption of negligible dislocation annihilation might be incorrect.

3.3. *Investigation of the deformed state at failure by EBSD analysis*

The results obtained in the previous section, indicate that dislocation related mechanisms are responsible for the plasticity in all of the samples investigated in the present study. Nevertheless, some unexpected results indicate that the evolution of dislocation structures might be different in the UFG regime from the coarse-grained regime. To enlighten the discussion, the deformed state at failure was investigated by means of EBSD analysis.

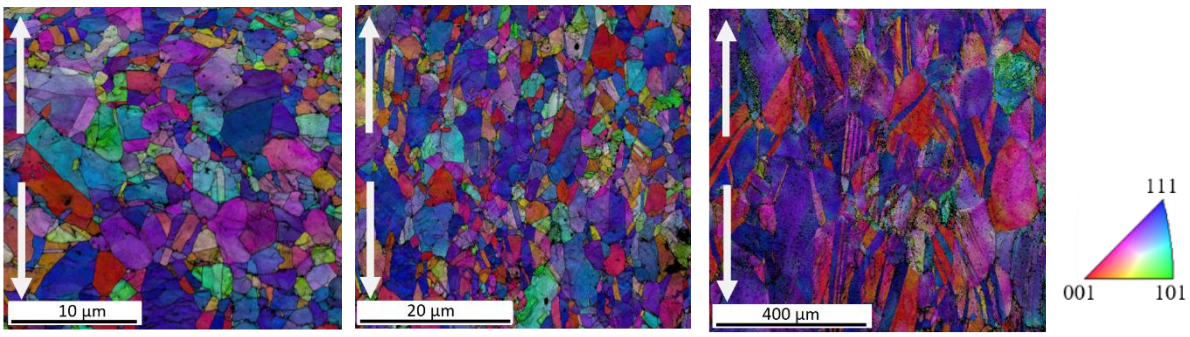

(a) (b) (c)

Fig. IV-31 Superposition of IPF+IQ cartography for samples 1 (d = 0.82 µm) (a), 3 (d = 1.39 µm) (b) and 5 (d = 25 µm) (c) with the tensile stress direction as reference, for the deformation state at failure. White arrows indicate the tensile direction.

First, a global outlook of the deformed microstructure can be obtained from the inverse pole figure (IPF) taking the tensile stress direction as a reference (Fig. IV-31). All samples display a preferred crystallographic orientation where grains have rotated to <111> or <100> orientations in reference to the tensile stress axis, which is the expected behavior for highly deformed FCC metals [177,193]. In addition, elongation of grains following the tensile stress axis can be depicted, which is more severe for sample 5 (Fig. IV-31 (c)) than for sample 1 (Fig. IV-31 (a)), implying an increase of the grain boundary area. The area increase entails a high fraction of dislocations stored, which represent a significant part

of the strain hardening energy [107]. The difference in elongation to failure could explain such difference as $\varepsilon_f = 58 \pm 3$ % for sample 5 and $\varepsilon_f = 39 \pm 3$ % for sample 1. Nevertheless, Q.H. Bui *et al.* [40] reported a more significant change in shape for coarse-grained Ni deformed in compression, than for UFG Ni with the same level of deformation.

An evolution in the GBCD can also be observed for all samples (Table IV-5). An important increase in LAGB accompanied with a decrease in Σ3 grain boundaries (untwining) can be depicted in all samples in comparison to the initial state (Table IV-2). This behavior has been reported by other authors for deformed nickel [40,114] in compression tests. The untwining process is explained in terms of interaction between gliding dislocations and pre-existing twin boundaries, whereas the higher fraction of LAGB would be the consequence of the arrangement of dislocations into subgrain boundaries [142]. The evolution of these two parameters is dependable on grain size, where bigger grain size entails a sharper decrease in Σ3 grain boundaries and an increase of LAGBs. The probability of untwining is thus higher for samples with grain sizes in the coarse-grain regime. This observation was already reported by J. Gubicza *et al.* [114], for UFG Ni prepared by SPS from nanopowders. Concerning the high fraction of LAGB in samples 4 and 5, compared to samples 1-3, it suggests that samples with grain sizes in the UFG regime develop less subgrain boundaries at high strain.

Table IV-5 GBCD of samples deformed at failure.

Sample	*LAGB*	*Σ3*	*CSL (Σ5- Σ29)*	*HAB*
1	0.057	0.388	0.048	0.493
2	0.133	0.246	0.056	0.43
3	0.093	0.336	0.044	0.527
4	0.383	0.202	0.036	0.379
5	0.73	0.088	0.022	0.16

Now, let us consider the deformation state of samples from misorientations determined from EBSD measurements. Fig. IV-32 displays GOS cartographies of samples 1 (a), 3 (b) and 5 (c). The average GOS value[21] increases for all samples from ~0.6° to ~2°, with the smallest value corresponding to sample 1, 1.7 ± 0.9°. Nevertheless, the GOS distribution depends on grain size, for instance, sample 5 exhibits a low fraction of grains with a GOS < 2° (2.9 %), whereas in sample 1 the fraction is 29.8 %. To investigate the correlation between grain size and orientation spread, the EBSD measurements for sample 1 (d = 0.82 µm) were divided into two partitions, grains that display a GOS < 2° and grains with GOS > 2°. The measured average grain sizes of each partition were d = 0.54 ± 0.38 (4) µm and d = 1.39

[21] Distribution plots for GOS, GAM and KAM accompanied by their corresponding cartographies for the initial state as well as the deformed state at failure for all five samples can be found in Appendix E.

± 0.84 (4) µm, respectively. These results seem to indicate that UFG grains are less deformed than FG grains. The same trend was found in samples 2 and 3. The fraction of grains that displayed a GOS < 1° (considered non-deformed grains) was less than 3% for all samples.

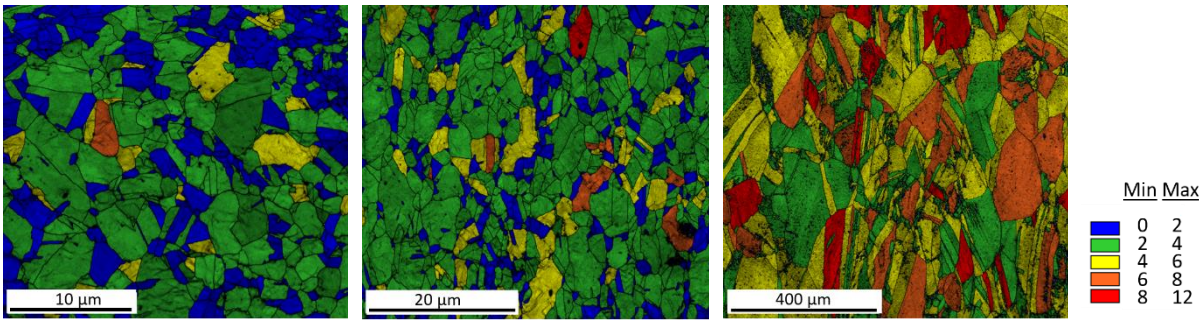

(a) (b) (c)

Fig. IV-32 GOS+IQ map of samples 1 (d = 0.82 µm) (a), 3 (d = 1.39 µm) (b) and 5 (d = 25 µm) (c) deformed at failure. Color legend represents the orientation spread in °.

For a more local measurement, the average misorientation of neighboring pixels given by the GAM can be observed in Fig. IV-33. A higher fraction of grains with higher GAMs are depicted with increasing grain size, where values above 1° are measured in 9.1% of grains in sample 1 (Fig. IV-33 (a)), 61.1% in sample 3 (Fig. IV-33 (b)) and 99.3 % in sample 5 (Fig. IV-33 (c)). The average GAM increases from 0.8° in the initial state to 1.4° and 2.2° respectively in samples 4 and 5, while no noticeable change is depicted for samples 1-3, which could indicate the absence of dislocation cells in the samples of smaller grain size. From these results it can be seen that GOS is more adapted for a global overview of the deformed state as a clear evolution can be depicted from the initial state of the samples to the deformed state in all samples [142].

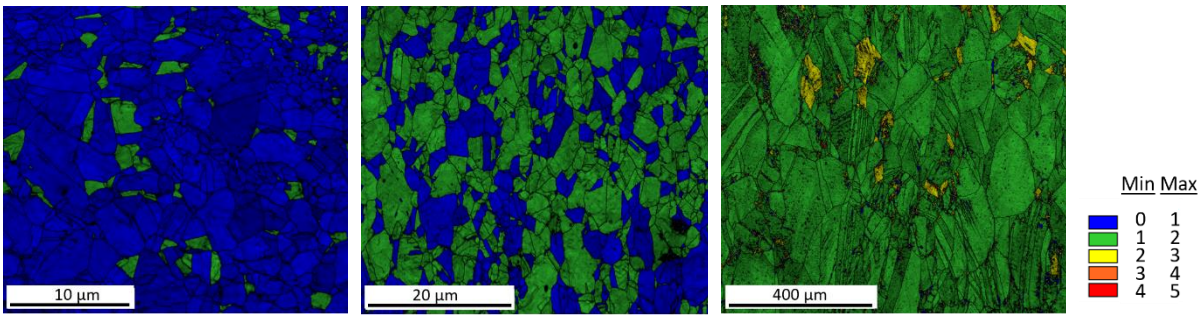

(a) (b) (c)

Fig. IV-33 GAM+IQ cartography of samples 1 (d = 0.82 µm) (a), 3 (d = 1.39 µm) (b) and 5 (d = 25 µm) (c) deformed at failure. Color legend represents the grain average misorientation in °.

GOS and GAM cartographies are good tools for a view of deformation considering averaged values for each grain, nevertheless, different deformation levels are present on a microscale where dislocations are frequently distributed in a heterogeneous matter, alternating regions of high and low local dislocation

density. More precisely, when dislocations organize in cells, the majority of dislocations are located in the dislocation cell walls [179], whereas a low dislocation density is depicted inside the cells. The measurement of such cell walls by EBSD is limited to the accuracy of the techniques as the thickness of the walls is approximately below 100 nm [112]. Nevertheless, KAM cartographies can be employed for a local description of the accumulation of dislocations within a grain. The first neighbor KAM cartographies of samples 1, 3 and 5 are displayed in Fig. IV-34. It is noticeable that in sample 5 (Fig. IV-34 (c)), high misorientations (above 1°) are present at grain boundaries as well as in the interior of grains. In addition, the average KAM value increases from 0.8° in the initial state to 1.7° in this sample. It should be noted that in first neighbor kernel misorientations, the values of misorientations are between 1° and 2° for deformed samples [145]. On the contrary, with grain refinement, generally lower misorientations are observed and are mostly located at grain boundaries (Fig. IV-34 (a) and (b)). As for average GAM, no significant change in the average KAM value between the initial state and the deformed state was obtained for samples 1-3.

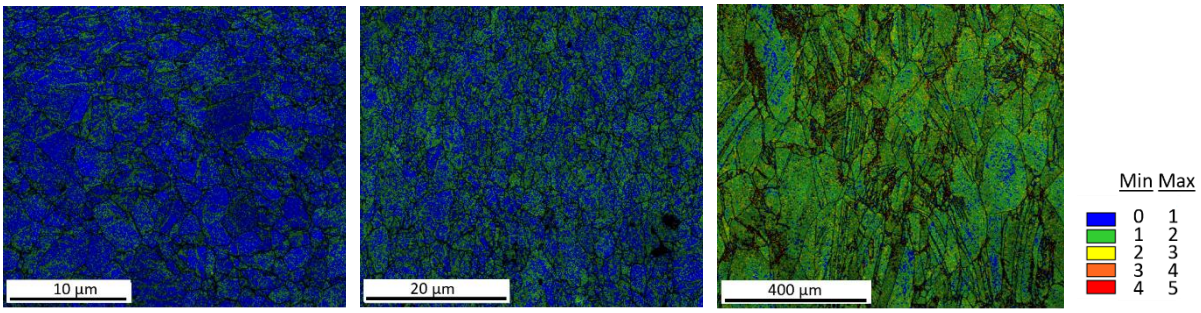

(a) (b) (c)

Fig. IV-34 First neighbor KAM+IQ cartography of samples 1 (d = 0.82 µm) (a), 3 (d = 1.39 µm) (b) and 5 (d = 25 µm) (c) deformed at failure. Color legend represents the kernel average misorientation in °.

Instead of the first neighbor KAM, the third neighbor can be used to obtain information on longer range correlated misorientations [147]. From Fig. IV-35, it can be seen that the conclusions drawn from considering the first neighbor do not change, nevertheless, third neighbor cartographies provide more details. For instance, in sample 5 (Fig. IV-35 (c)), a bigger contrast is depicted between the grain boundaries and the inside of grains. In addition, the evolution in the average value of 3rd neighbor KAM is more noticeable. In the case of samples 4 and 5, it increases from 0.8° in the initial state, to 2.3° and 2.5°, respectively, in the deformed state. In the case of samples 1-3, as expected from their cartographies (Fig. IV-35 (a)-(b)), a smaller increase is observed, 1.2°, 1.7° and 1.5°, respectively.

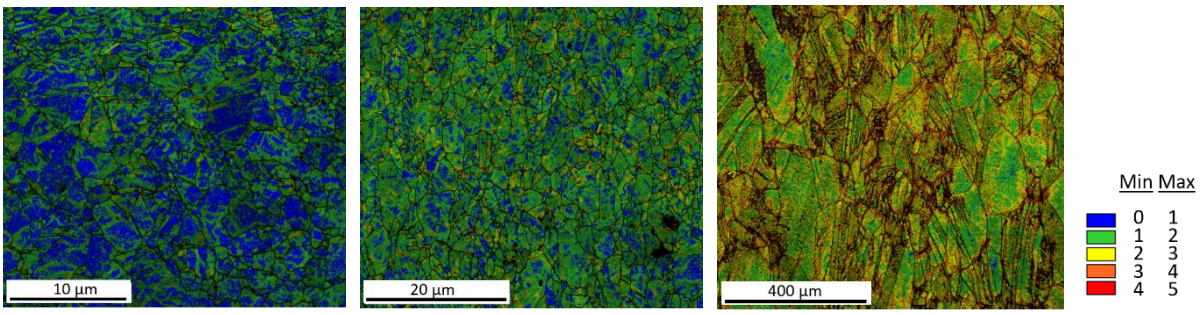

(a) (b) (c)

Fig. IV-35 Third neighbor KAM cartography superposed on IQ map of samples 1 (d = 0.82 µm) (a), 3 (d = 1.39 µm) (b) and 5 (d = 25 µm) (c) deformed at failure. Color legend represents the kernel average misorientation in °.

A generalized higher presence of dislocations at grain boundaries rather than in the grain interior is in agreement with the model developed by Meyers and Ashworth based on a different deformation behavior between the inside of grains and grain boundaries [194]. Deformation incompatibility between grains develops a stress concentration at grain boundaries, which entails the activation of supplementary slip systems as compared to the grain interior [178]. Hence, regions closer to the grain boundaries will strain harden faster. The reduced (or lack) of dislocation sources in the interior of UFG grains, would thus sharpen this effect.

The ensemble of the results obtained by EBSD analysis, show different deformation states between UFG and CG Ni. Misorientation measurements seem to indicate a lower dislocation density accumulated at failure in samples with small grain sizes, especially in the UFG range. Additionally, higher misorientations are found in the areas closer to grain boundaries indicating a preferential accumulation in these regions against accumulation in the grain interior. To complete these results, TEM observations were performed on selected samples.

3.4. *Observation of dislocation structures by TEM*

As reported in the first part of this chapter, in metals with medium or high SFE, dislocation structures evolve with increasing strain from tangled dislocations to dislocation cells or subgrains that start forming in stage II of strain hardening. In addition to these types of structures, heterogeneous structures such as dense dislocation walls, microbands or shear bands are also formed, and depend on several parameters such as grain size, texture, strain rate or deformation mode [195]. In fact, dislocations interact with each other displaying a group behavior that will determine the activation of different glide system combinations, as well as the reduction of the dislocation free energy, by the formation of low-energy dislocation structures (LEDS). Given that they represent centers of internal stresses, the mutual trapping of dislocations will lead to an increase of dislocation density. Through the formation of LEDS,

dislocation accumulation is stabilized from mutual stress-screening of the resolved shear stress components among near-neighbor dislocations [187].

The formation of a given cell configuration is dependent on the applied stress, the available slip systems, the dislocation mobility, the non-dislocation obstacles, etc. First, cell blocks will develop, which require the activation of less slips systems than dislocation cells to form. Then, dislocations will organize within the cell blocks into dislocation cells (Fig. IV-36). At higher deformation levels, the misorientation between cell blocks increases and a higher dislocation density accumulates, creating dense dislocation walls. At even higher deformation levels, the rotation angle across dislocation walls continues to increase, which results in the development of subgrains from the original dislocation cells [196].

Deformation structures refine with increasing applied stress. To achieve this refinement, either dislocation walls dissociate or new dislocation walls are generated within the preexisting cells [195]. Homogenization of dislocation cells or subgrains is accomplished at high deformation levels taking into account that energy per unit length is lowest when cells are similar, roughly equiaxed, of similar size and parallelepiped instead of hexagonal to minimize the wall to volume ratio. Cell blocks shrink faster than dislocations cells, thus at large strains the size of the cell block will decrease until reaching the size of a single dislocation cell.

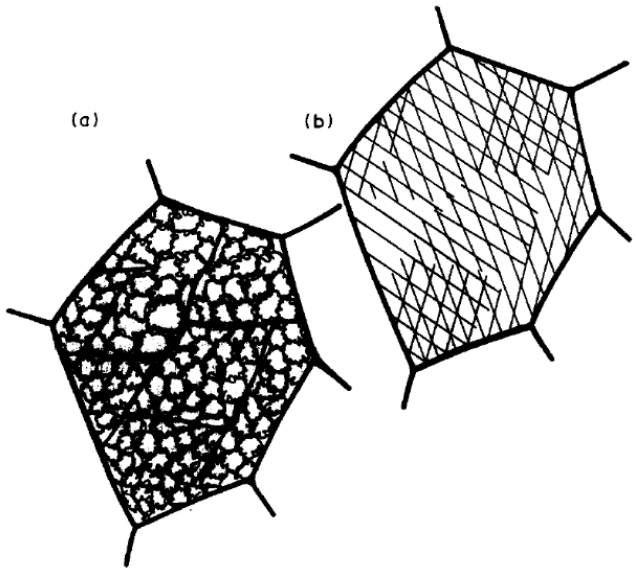

Fig. IV-36 Grain displaying dense dislocation walls representing the limits of cell blocks, which consist on dislocation cells (a). Slip line pattern displayed by the deformed grain in (a) (b) [195].

The presence of these structures have a major impact in strain hardening. Once they are formed, dislocation cells and subgrains act as sources of dislocations (Fig. IV-37) and contribute to flow stress in a Hall-Petch relation type equation [197].

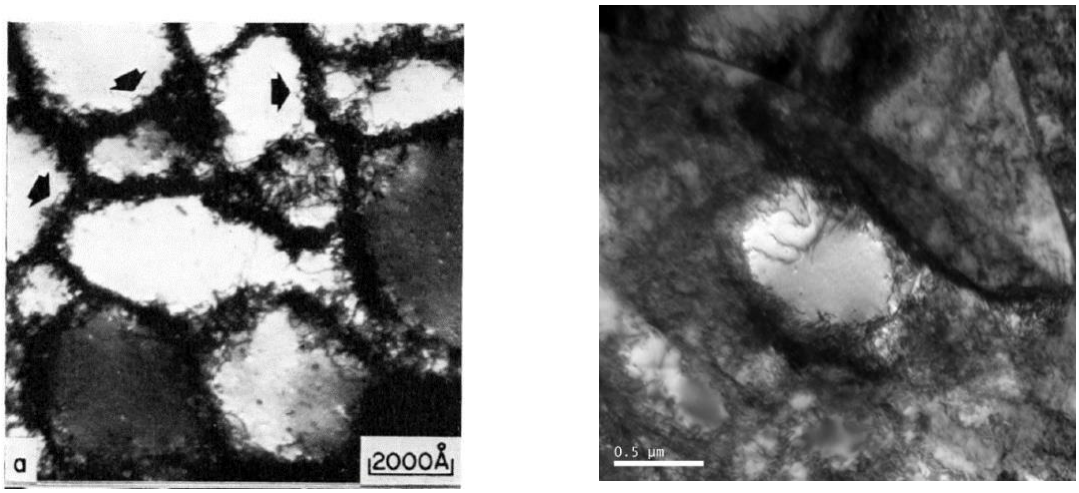

(a) (b)

Fig. IV-37 TEM images of dislocation cells presenting apparent dislocation sources in A.W. Thompson [197] (a) and in sample 4 (d = 4.0 µm) in this work (b).

In this study, dislocation structures were investigated at fracture for two samples, representing the FG and the UFG range, samples 4 and 1, respectively. First, TEM images of the deformed state of sample 4 are shown in Fig. IV-38 (a). Grains divided in dislocation cells (or subgrains) can be observed with different misorientations as depicted from the difference in contrast between them (Fig. IV-38 (b)). The development of dislocation cells in different contiguous grains can be observed in Fig. IV-38 (c), where the grain boundary displayed is edge-on. An estimation of the average size of the dislocation cells[22] (d_c) was determined from 28 cells, obtaining a value of 0.53 ± 0.18 µm. This value is in agreement with the value observed in coarse-grained nickel by X. Feaugas *et al.* [112] for high plastic strain. H. Mughrabi [179] described the deformed structure as composed by a "hard phase" represented by the walls of the cells, and a "soft phase" which corresponds to the interior of cells. Assuming this model, the cell size can be related to the dislocation density in the soft phase (ρ_s) by the expression, $d_c = B_d \cdot \rho_s^{-0.5}$, where B_d is a constant. With $B_d = 4$ for nickel [112], an average density of $\rho_s = 5.7 \cdot 10^{13}$ m^{-2} is found in the present case, which correlates with the results of X. Feaugas *et al.* where $\rho_s \approx 10^{13}$-10^{14} m^{-2}.

[22]Only dislocations cells with well-defined walls were considered in the measurement and were distributed within different grains. No statistical measurement of cells of a single grain were performed.

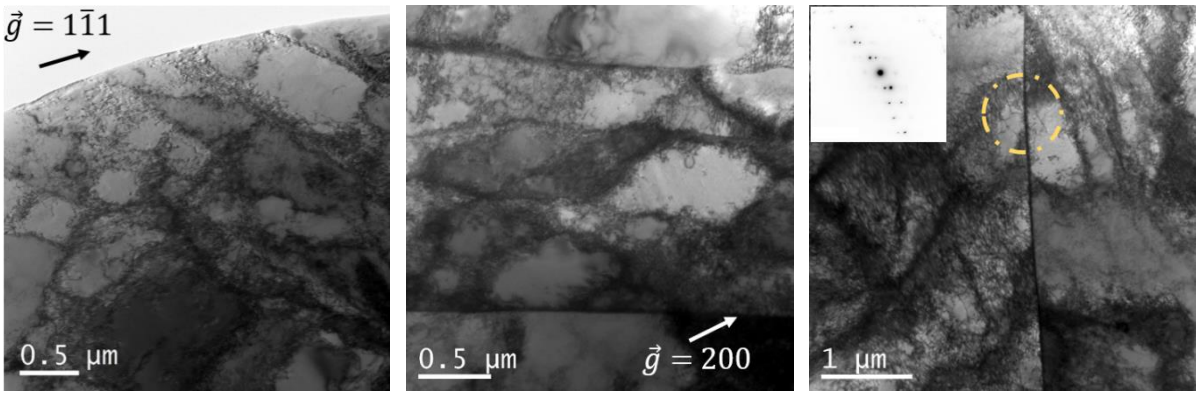

(a) (b) (c)

Fig. IV-38 TEM images of grains of sample 4 (d = 4.0 µm) deformed to failure, containing dislocation cells. Accumulation of geometric dislocation cells of similar size in a single grain (a). Dislocation cells restrained between grain boundaries (b). Contiguous grains displaying dislocation cells with a high density of dislocations.

Concerning the morphology of cells, mostly geometrical shapes are observed such as cubes (Fig. IV-39 (a)), parallelepiped (Fig. IV-39 (b)), or equiaxed (Fig. IV-39 (c)). The thickness of the walls (d_w) varied depending on the dislocation cell d_w ~70 nm (Fig. IV-39 (b)), and d_w ~150 nm (Fig. IV-39 (a) and (c)). From these values, a density of dislocations in the hard phase (ρ_w) can be obtained from, $d_w = A_d \cdot \rho_w^{-0.5}$, where A_d is a constant of the same value as B_d [112]. Hence, a measured dislocation density of $\rho_w = 3.3 \cdot 10^{15}$ m^{-2} and $\rho_w = 7.1 \cdot 10^{14}$ m^{-2}, respectively, is obtained depending on the cell, which are similar to $\rho_w \approx 2 \cdot 10^{14}$-$2 \cdot 10^{15}$ m^{-2}, measured by X. Feaugas *et al* for coarse-grained Ni. A total dislocation density can be obtained with the following expression:

$$\rho_d = f\rho_w + (1-f)\rho_c \tag{4.15}$$

where f denotes the volume fraction of the cell walls, which can be calculated from d_w and d_c as:

$$f = \frac{d_c^3 - (d_c - d_w)^3}{d_c^3} \tag{4.16}$$

in the case of idealized cubic-shaped cells [23]. If an average d_w is considered as ~110 nm, the value of the volume fraction of the cell walls can be obtained from Eq. (4.16), f = 0.502. Considering an average $\rho_w = 2 \cdot 10^{15}$ m^{-2}, an approximate measurement of the total density of dislocations obtained from Eq. (4.15) would be $\rho_d = 1.03 \cdot 10^{15}$ m^{-2}, a typical value for deformed CG metals. Thus, the mechanical behavior of FG Ni displays the expected trend stablished for CG Ni, which means that no modification of deformation mechanisms appears for a grain size of 4 µm.

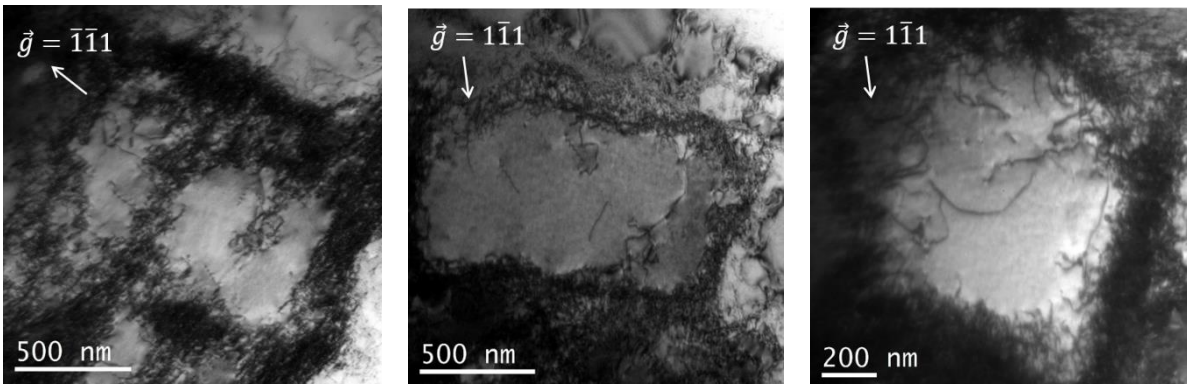

(a) (b) (c)

Fig. IV-39 Bright-field images of dislocation cells of sample 4 (d = 4.0 μm) deformed to failure of different geometries: squared (a), rectangular (b) and equiaxed (c).

Concerning the UFG specimen, sample 1, the deformed state displayed a much different appearance. Due to the small grain size, a global view of the microstructure is possible, which shows (Fig. IV-40 (a)) that grains preserve their equiaxed morphology and size when deformed to failure, correlating with the EBSD measurements presented in the previous section. Concerning dislocation structures, well-defined cells were rarely found (Fig. IV-40 (a) and (b)). Nevertheless, accumulations of dislocations can be depicted from the contrast of images inside grains. Structures such as the one displayed in (Fig. IV-40 (c)), with a diameter of ~ 250 nm, represents the scarce type of dislocation cell encountered.

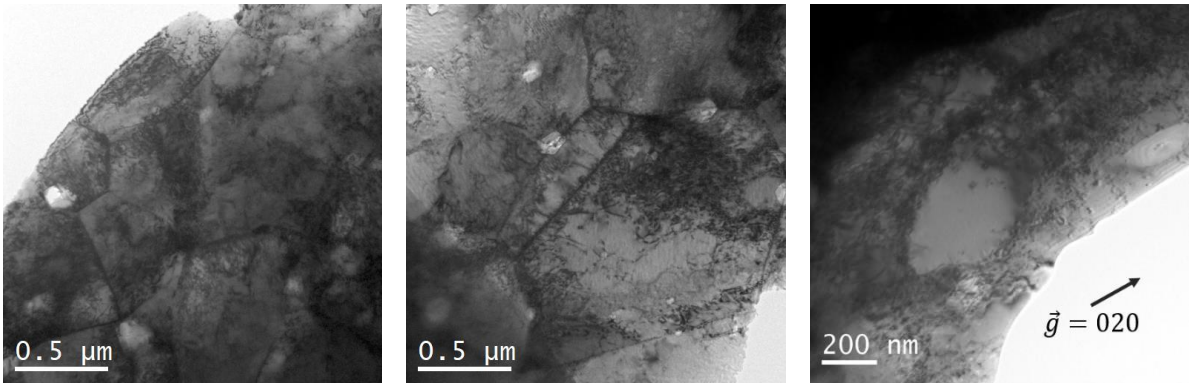

(a) (b) (c)

Fig. IV-40 TEM images of sample 1 (d = 0.82 μm) deformed to failure. Grains with different contrast possibly due to a high density of dislocations ((a)-(b)) and a nanometric dislocation cell (c).

The dislocation cell size at large strain, according to X. Feaugas *et al.* is not very dependent on grain size and for coarse-grained Ni is between d_c = 0.35-0.55 μm. Due to the grain size in sample 1, which approaches the cell size in CG Ni, it is not surprising that the few dislocation cells observed present a smaller size. Nevertheless, the observations by TEM show that dislocation cells are not a characteristic feature of the deformed state of UFG Ni, which correlates to their extremely short second hardening stage. In this stage, dislocation cells form as multiple slip enables the multiplication of dislocations and

the lack of cross-slip forces dislocations to organize in structures such as cells. If cross-slip is generalized soon after yielding (the case of sample 1), the formation of well-organized dislocation structures is hindered.

4. Summary and conclusions

UFG metals have been long studied with the goal of attaining materials with very high strength. Nevertheless, the need for a good compromise between strength and ductility has led to the study of microstructures with grain sizes in the bigger range of UFG as well as marked grain size populations such as bimodal distributions. In this chapter, the mechanical properties of SPS processed Ni samples with grain sizes ranging from 0.8-25 µm were investigated. All samples exhibited a good combination of strength and ductility, especially those in the UFG regime. The relation between yield strength and ductility measured in this study can be plotted next to results of Ni samples obtained with different processing techniques found in literature (Fig. IV-41).

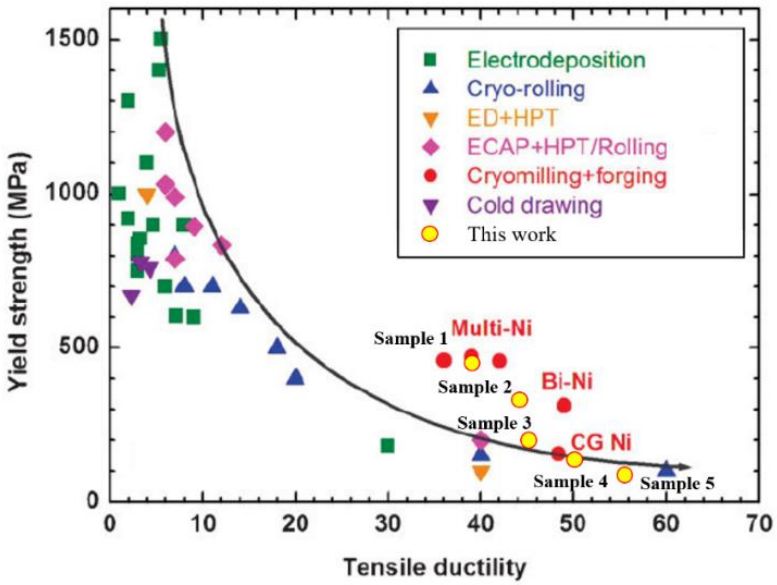

Fig. IV-41 Yield strength plotted against elongation obtained from [198], with yellow and red points displaying a good compromise between strength and ductility. Yellow points correspond to the samples studied in this work.

On the left end of the figure, NsM/UFG samples prepared by ED/SPD techniques are presented, which display high strength and low ductility. On the right end, samples prepared by powder metallurgy are shown in red and yellow. The red points represent samples prepared by cryomilling of powders and compaction by forging, which display grain sizes in the FG range in average (1-3 µm) and microstructures with bimodal or multimodal microstructures. In view of these results, a variation in the grain size distribution represents to date the best way to attain that compromise. Nevertheless, unimodal samples in the FG/UFG range prepared by BM and SPS also display a good strength/ductility ratio.

Lower strain hardening was displayed in UFG samples compared to CG samples, which reflects in several mechanical properties. For instance, heterogeneous yielding was depicted at low deformation levels in UFG samples as well as a higher yield strength than the value expected from the HP relation. In addition, UFG exhibited lower ductility that the CG counterpart, which was more noticeable in elongation to failure.

The application of the Mecking-Kocks model showed the expected trend of dislocation based deformation with reduced grain size. The beginning of the second hardening stage, short after yielding in UFG samples, suggests generalized cross-slip very early in deformation. In addition, the limited length of this stage hinders the possibility of accurately measuring the slope. In UFG samples, low dislocation accumulation and a lack of dislocation cells were depicted, considering misorientations measured by means of EBSD, which presumably results from the early beginning of cross-slip preventing the formation of well-defined dislocation structures. These results were confirmed by TEM observations, where diffuse areas of different contrast were the main feature of the deformed UFG Ni, in contrast to the well-formed dislocation cells observed for FG samples. Additional TEM observation should be performed for a clearer view of the deformation mechanisms that take place in the UFG regime. In addition, the investigation of interrupted tensile testing is necessary to obtain more information concerning the different strain hardening stages in this type of samples.

CHAPTER V. STUDY OF GB DIFFUSION AND THERMAL STABILITY IN UFG NI SAMPLES PROCESSED BY PM

After investigating the mechanical properties and strain hardening mechanisms, the behavior of SPS processed samples during annealing treatments is presented in this chapter in two ranges of temperature. On the one hand, at low temperature (400 K), grain boundary (GB) diffusion was studied to examine the possible presence of ultrahigh diffusivity paths. These paths are a highlighted feature in UFG metals processed by SPD and could be present in the UFG samples of this study due to the highly deformed nature of the BM powders. On the other hand, at high temperature (up to 1123 K), the stability of the samples is analyzed by means of dilatometry measurements.

1. Grain boundary diffusion

Grain boundary (GB) diffusion is a key parameter in many processes that concern engineering materials, including Coble creep, sintering, oxidation, recrystallization and grain growth. These processes take place at high temperature but grain diffusion at low temperature or even room temperature can also modify the properties of some materials and limit, for instance, the service life of metals used in different microelectronic devices [122]. Despite indirect observations of the high diffusivity of grain boundaries in the 1920-1930s, direct proof was obtained in 1950s from autoradiography [199]. The darker color along GBs in autoradiography indicated higher penetration of the radiotracer into the GBs in comparison to the lattice. The development of the radiotracer serial sectioning technique soon after, enabled the construction of accurate penetration profiles revealing long penetration “tails” in profiles measured in polycrystals that were attributed to grain boundary diffusion [121]. At this time, F.C. Fisher [200] developed his theoretical model of grain boundary diffusion, where a quantitative description of the aforementioned profiles was provided, considering the combination of grain boundary and lattice diffusion. In the last decades, GB diffusion has been largely investigated in a wide range of temperatures and materials. The Fisher model has been the base of these studies, extended by different authors to account for new situations encountered experimentally [121,122,201].

1.1. The Fisher model of GB diffusion

Most mathematical approaches used to investigate GB diffusion are developed from the Fisher model. It considers a two-dimensional solid characterized by a high-diffusivity, uniform and isotropic slab (the grain boundary) of constant width (δ), and two semi-infinite low-diffusivity isotropic crystals (Fig. V-1). The GB is oriented perpendicularly to the free surface (y = 0) and is characterized by an

enhanced diffusion coefficient (D_{gb}), compared to lattice diffusivity (D_v), $D_{gb} \gg D_v$. Both diffusion coefficients are considered independent of concentration.

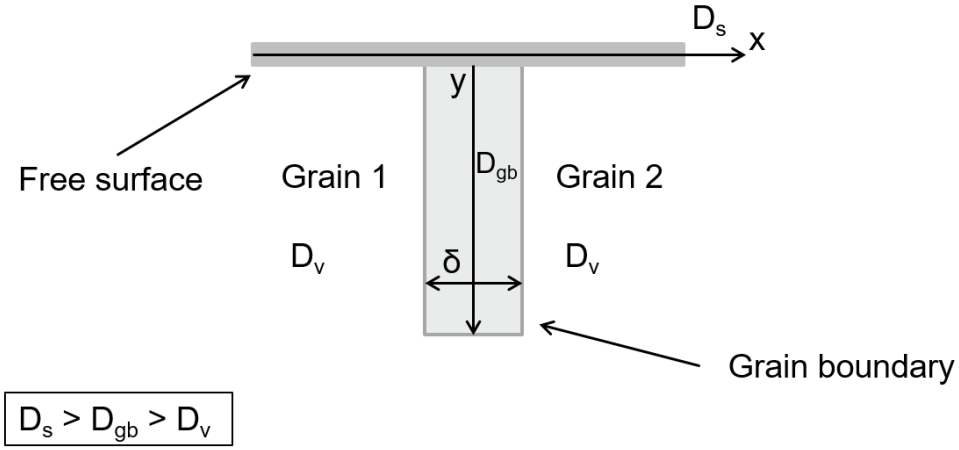

Fig. V-1 Schematic illustration of the geometry of the Fisher model. D_s, D_{gb} and D_v correspond to surface diffusivity, grain boundary diffusivity and lattice diffusivity, respectively. The grain boundary width is represented by δ.

With Fick's second law of diffusion as base, the diffusion problem can be formulated mathematically as [121,201]:

$$\frac{\partial c_v}{\partial t} = D_v\left(\frac{\partial^2 c_v}{\partial x^2} + \frac{\partial^2 c_v}{\partial y^2}\right) \qquad \text{For } |x| > \delta/2 \qquad (5.1)$$

$$\frac{\partial c_{gb}}{\partial t} = D_{gb}\left(\frac{\partial^2 c_{gb}}{\partial x^2} + \frac{\partial^2 c_{gb}}{\partial y^2}\right) \qquad \text{For } |x| < \delta/2 \qquad (5.2)$$

where t represents time, c_v and c_{gb} are the concentration of the diffusing atoms in the volume and grain boundary respectively, and x, y are distances. Direct volume diffusion from the source into the lattice is represented by Eq. (5.1) and diffusion along the grain boundary by Eq. (5.2). Two boundary conditions are necessary to assure continuity of the concentration and diffusion flux across the interfaces separating the grain boundary and the grains:

$$c_v(\pm\delta/2, y, t) = c_{gb}(\pm\delta/2, y, t) \qquad (5.3)$$

$$D_v\left[\frac{\partial c_v(x,y,t)}{\partial x}\right]_{|x|=\delta/2} = D_{gb}\left[\frac{\partial c_{gb}(x,y,t)}{\partial x}\right]_{|x|=\delta/2} \qquad (5.4)$$

The concentration continuity described in Eq. (5.3) is only valid for self-diffusion. Now, assuming that the GB boundary width, δ, is very small and that $D_{gb} \gg D_v$, the problem can be simplified[23] to obtain the following equation:

[23] For the detailed development of the equations see [201].

$$\frac{\partial c_{gb}}{\partial t} = D_{gb}\frac{\partial^2 c_{gb}}{\partial x^2} + \frac{2D_v}{\delta}\left(\frac{\partial c_v}{\partial x}\right)_{|x|=\delta/2} \qquad \text{For } |x| < \delta/2 \qquad (5.5)$$

The diffusion problem is thus described by the final system of equations, Eq. (5.1) and Eq. (5.5). In Eq. (5.5), the first term on the right-hand side represents the change in the concentration of tracer atoms along the grain boundary due to GB diffusion, whereas the concentration change due to tracer leakage into the grains is represented in the second term. An exact solution of this system of equations was obtained by R.T.P. Whipple [202] for the constant source condition and by T. Suzuoka [203] for the instantaneous source condition. Both solutions give very similar values of D_{gb} for measurements performed with the sectioning method, which is important, as the real condition of the surface in a grain boundary experiment is not easily controlled. For this reason, A.D. Le Claire [204] considered these solutions in advantage compared to other authors and provided a generalized simplified expression for application to experimental results.

According to Le Claire's analysis, if concentration profiles are linearized in $ln\bar{c}$ vs $y^{6/5}$, the double product $P = \delta D_{gb}$ can be obtained in self-diffusion experiments, and the triple product $P = s\delta D_{gb}$ in hetero-diffusion. In the triple product, s represents the segregation coefficient, which equals one in self-diffusion. The expression used to determine P will depend on the parameter β [204]:

$$\beta = \frac{s\delta D_{gb}}{2D_v\sqrt{D_v t}} \qquad (5.6)$$

This parameter, also called Le Claire parameter [121], represents a measurement of the enhanced diffusivity along the grain boundary relative to volume diffusion (Fig. V-2).

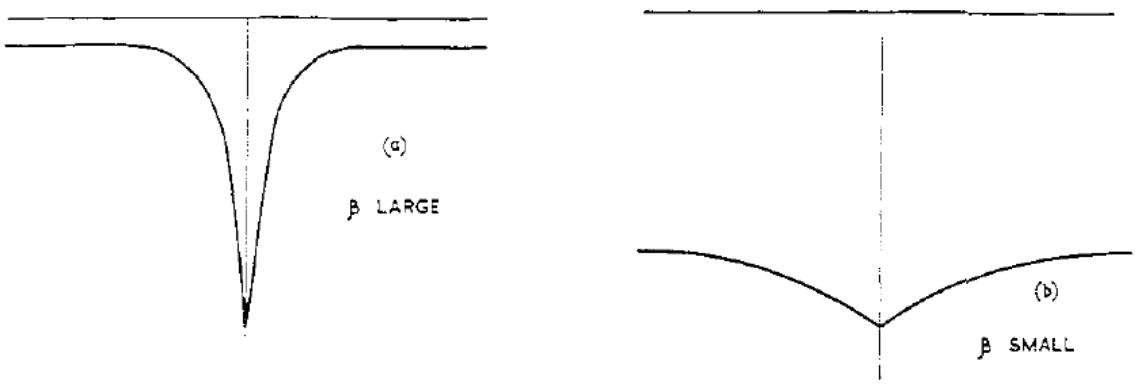

Fig. V-2 Differences in the shape of grain boundary contours for large (a) and small β (b) [204].

The main expressions used to determine the double product P are [201]:

$$P = 1.322\sqrt{\frac{D_v}{t}}\left(-\frac{\partial ln\bar{c}}{\partial y^{6/5}}\right)^{-5/3} \qquad \beta > 10 \qquad (5.7)$$

$$P = 1.308\sqrt{\frac{D_v}{t}}\left(-\frac{\partial ln\bar{c}}{\partial y^{6/5}}\right)^{-5/3} \qquad \beta > 10^4 \qquad (5.8)$$

Thus, the grain boundary diffusion coefficient can be determined from P, for a known δ, using Eq. (5.7) and Eq. (5.8). Nevertheless, because of the approximation of the model, these expressions can only be used under certain experimental conditions. In fact, different diffusion kinetics regimes are observed in GB diffusion, which depend on annealing temperature, time and relative diffusivity between the bulk and the grain boundaries. The most extended classification of diffusion kinetics for a polycrystal is the one proposed by L.G. Harrison [205].

1.2. *Harrison's classification of kinetic regimes of GB diffusion*

As seen in the precedent section, the elementary processes involved in GB diffusion include direct volume diffusion from the surface, GB diffusion and leakage of the diffusing species from the GB to the lattice. Depending on the regime, one or two elementary processes will control the rate of diffusion while others will be negligible [122]. Thus, the analysis of experimental results depends on the kinetic regime. L.G. Harrison classified the different diffusion behaviors in a polycrystal with parallel grain boundaries in three kinetic regimes referred to as type A, type B and type C (Fig. V-3).

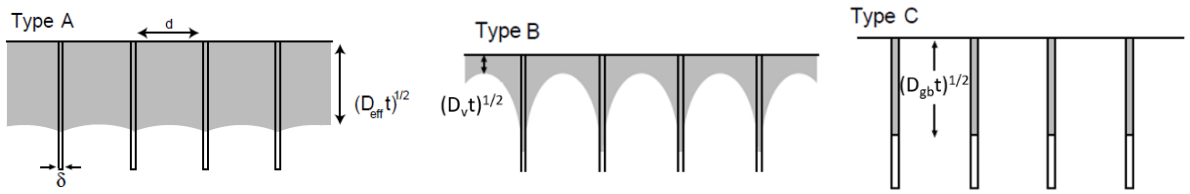

Fig. V-3 Illustration of type A (a), type B (b) and type C (c) kinetic regimes in Harrison's classification [122].

Kinetic regime type A

The A-type regime is observed at high temperature ($T > 0.7\ T_m$) and/or after very long annealing time. In this regime, the diffusion fluxes from neighboring GB overlap (Fig. V-3 (a)) due to a volume diffusion length larger than grain size ($\sqrt{D_v t} \gg d$). Diffusion results in a planar front that follows, in a macroscopic scale, Fick's law with an effective diffusion coefficient D_{eff} defined as [205]:

$$D_{eff} = gD_{gb} + (1-g)D_v \tag{5.9}$$

where g is the volume fraction of GBs in the polycrystal, with $g = q\delta/d$ (q is a numerical factor that depends on grain shape). In this regime, concentration profiles follow a Gaussian or an error function depending on the source condition. Hence, assuming the Gaussian-type solution for tracer diffusion the effective diffusivity can be determined from $ln\bar{c}$ vs y^2 plots, where:

$$D_{eff} = \frac{1}{4t}\left(-\frac{\partial ln\bar{c}}{\partial y^2}\right)^{-1} \tag{5.10}$$

It should be noted that if the grain size is large enough then $g \to 0$ and an estimation of volume diffusivity can be obtained, $D_{eff} \approx D_v$.

Kinetic regime type B

At lower temperature and/or shorter annealing time, the B-type regime emerges. In this regime, the bulk diffusion length is smaller than the space between grain boundaries:

$$\delta \ll \sqrt{D_v t} \ll d \tag{5.11}$$

As for the A-type regime, GB diffusion in the B regime is accompanied by volume diffusion from leaking. Nevertheless, in this case volume diffusion fluxes of neighboring grains do not overlap (Fig. V-3 (b)). This regime is often found in diffusion measurements in polycrystals and L.G. Harrison defined it as the situation where conditions for type A and C were not applicable [205]. Formally, two conditions have to be fulfilled [201]:

$$\alpha = \frac{s\delta}{2\sqrt{D_v t}} < 0.1 \tag{5.12}$$

$$\Lambda^* = \frac{d}{\sqrt{D_v t}} > 3 \tag{5.13}$$

In Eq. (5.12), α represents the GB diffusion parameter which offers a measurement of the leakage of diffusing atoms from GBs into the bulk from the ratio of effective GB diffusion width (sδ) and the diffusion length in the grain interior ($2\sqrt{D_v t}$). On the other hand, Λ^* represents the ratio of the grain size to volume diffusion length. Finally, for proper B-type regime conditions the Le Claire parameter (Eq. 5.6) has to be, $\beta \gg 1$ [122]. In concentration profiles obtained experimentally in this regime, a sharp decrease in concentration is depicted first, a near-surface section that represents the direct volume diffusion from the surface. For GB diffusion investigations, this part is omitted in the fit procedure where

only the linear part of the $ln\bar{c}$ vs $y^{6/5}$ plot is taken into account. Experiments performed in this regime enable the determination of P using equations Eq. (5.7) and Eq. (5.8).

Kinetic regime type C

The last kinetic regime takes place at even lower temperature and/or shorter annealing time. Under such conditions the volume diffusion length is $\sqrt{D_v t} \ll \delta$. Diffusion is thus considered to occur only along GB without any leakage to the grain interior (Fig. V-3 (c)), hence, the volume diffusion becomes negligible. A second condition has to be fulfilled in the C-type regime, the grain boundary diffusion parameter α (Eq. (5.12)) has to be, $\alpha \gg 1$. In this regime, the grain boundary diffusion coefficient can be directly determined from the Gaussian-type solution of tracer diffusion along GB from $ln\bar{c}$ vs y^2 plots [124]:

$$D_{gb} = \frac{1}{4t}\left(-\frac{\partial ln\bar{c}}{\partial y^2}\right)^{-1} \tag{5.14}$$

A complete characterization of grain boundary diffusion thus, can be made by combining diffusion measurements in the C-type and B-type regimes. First, the grain boundary diffusion coefficient is obtained from the measurement in the C-type regime. Then, the grain boundary width can be calculated from the double product P, measured in the B-type regime. In the lack of measurements in both regimes, a δ = 0.5 nm is generally accepted for FCC metals [124].

1.3. *Grain boundary diffusion in CG and UFG/nanostructured metals*

Harrison's classification considers a simplified model of diffusion in polycrystals. Hence, by introducing subregimes an extension of the classification is achieved, which is necessary for a better discussion of diffusion kinetics in polycrystalline materials with different grain sizes. The different regimes and subregimes depend on the relation between the characteristic diffusion length scales in polycrystals and are displayed in Fig. V-4. In his book [121], H. Mehrer classifies polycrystals according to grain size, in three categories: coarse grained, fine grained and ultrafine grained. He made no distinction between UFG and nanostructured materials. Polycrystals of each category display a different set of diffusion regimes, where the critical grain size separating the three types depends on the material [122].

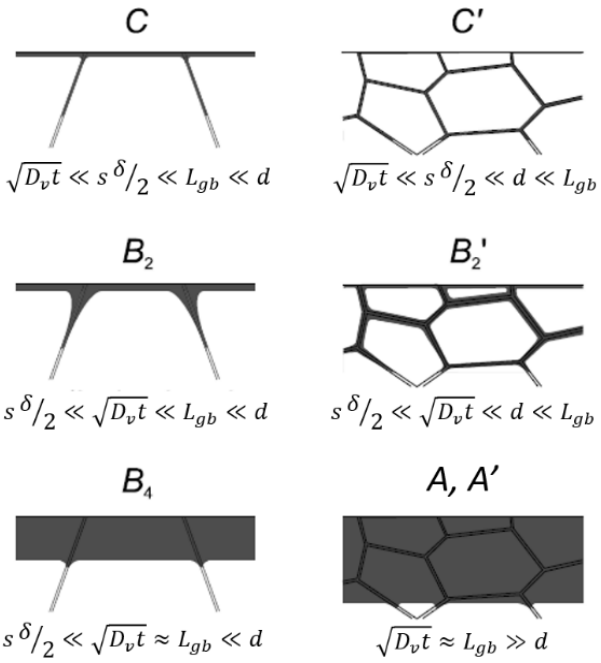

Fig. V-4 Tracer distribution in polycrystals (left) and UFG materials (right) under different kinetic regimes and subregimes [121]. Here L_{gb} represents the diffusion distance along grain boundaries.

Considering a fixed temperature and increasing annealing times, each category of polycrystals exhibits a different sequence of diffusion regimes and subregimes as displayed in Table V-1. A detailed description of the conditions fulfilled by each subregime as well as the transition between them can be found in [121].

Table V-1 Sequence of diffusion regimes and subregimes in different categories of polycrystals [121].

Category of polycrystal	*Sequence of diffusion regime*
Coarse grained	$C \rightarrow B_2 \rightarrow B_4 \rightarrow A$
Fine grained	$C \rightarrow B_2 \rightarrow B_2' \rightarrow A'$
Ultrafine grained	$C \rightarrow C' \rightarrow B_2' \rightarrow A'$

Now, let us consider diffusion in nanocrystalline materials. In the first review by H. Gleiter [206], measurements in different nanocrystalline materials (Pd, Cu, Fe) with different diffusing species (Ag, Au, Bi, Cu, O, B, H) showed a clear trend, grain boundary self-diffusion and hetero-diffusion in nanocrystalline materials are enhanced relative to chemically identical systems of CG microstructures. Nevertheless, the enhancement only applies to solute atoms that are in substitution in the solvent lattice. The low activation enthalpy measured in the nanostructured metals, as well as the ultra-high diffusivity, were explained by H. Gleiter by an excess volume in the grain boundaries. However, other studies of nanostructured metals reported no change in the grain boundary diffusivity [207]. In fact, the existence of a hierarchy of diffusion paths that includes residual porosity, different types of interfaces or the

presence of triple junctions, makes a definitive answer to whether all nanostructured materials display ultra-high diffusivity or not, complicated.

As introduced in Chapter I, nanocrystalline Ni prepared by ED and SPD displays ultra-high diffusivity, although different orders of magnitude are observed between them. Concerning PM, a thorough study on a nanostructured γ-Fe-40wt.%Ni alloy prepared by BM and conventional sintering contains useful information to the present study. In fact, the alloy was produced by BM from oxides, then the powder was reduced to the metallic alloy, to be afterwards consolidated by conventional sintering [208]. The obtained sample, with a relative density of 98 %, displayed a microstructure with two levels of organization that can be observed in Fig. V-5 (a). At a bigger scale, the microstructure exhibits polyhedral large agglomerates or clusters with porosities mostly located in the interfaces. Such agglomerates display a size in the range d_a = 30-50 μm. At a smaller scale, each agglomerate is composed of nanosized grains with a size d = 80-100 nm.

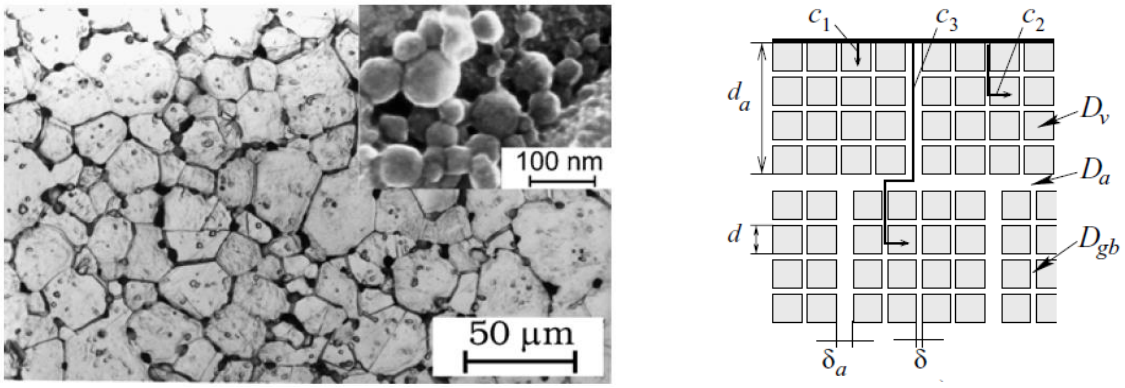

(a) (b)

Fig. V-5 Microstructure of a Fe-40wt.% Ni alloy showing big agglomerates (optical microscope), and enlargement (inset in the upper right) of a small region within an agglomerate displaying nanograins (SEM image) (a). Model of the microstructure, where gray squares represent the nanograins within the agglomerates of diffusivity D_{gb} and D_a represents the diffusion coefficient of the interfaces between agglomerates (b). The agglomerate interface width is represented by δ_a and the agglomerate size by d_a. Different tracer fluxes contributing to diffusion are indicated by c_1, c_2 and c_3 for volume diffusion, grain boundary diffusion of nanograins and interface diffusion between agglomerates [208,209].

The authors performed diffusion measurements in a temperature range T = 625-1013 K and reported four new kinetic regimes C – C, C – B, B – B and A – B, which appear with increasing annealing temperature. They proposed a model (Fig. V-5 (b)) to describe the different diffusion paths in the microstructure and demonstrated that the inter-agglomerate interfaces displayed higher diffusivity than grain boundaries of nanograins. Grain boundaries of nanosized grains within the agglomerates on the other hand, displayed diffusivities similar to relaxed high angle grain boundaries. A similar result had been observed earlier by B.S. Bokstein *et al.* [210], in a sintered nanostructured nickel sample from

nanometric powders, no enhanced diffusivity in nanograins, but ultrafast diffusion through the interface of agglomerates. Despite these results, the presence of GBs with excess volume, which can enhance diffusivity, have been reported for NsMs prepared by powder compaction [211]. Nevertheless, the distribution and strength of such defects may differ from deformation modified grain boundaries.

2. GB self-diffusion investigation on SPS processed Ni by the radiotracer method

In the present manuscript, two types of specimens are investigated, samples processed from commercial as-received powder and samples synthesized from BM powder. High diffusivity has been reported for nanocrystalline samples processed by PM from nanopowders, thus UFG samples synthesized from BM powder might also display unusual ultra-fast diffusivity. In addition, equally to Ni processed by other SPD techniques (ECAP [126] and HPT [212]), it is pertinent to think that BM could also entail the formation of the so-called deformation modified grain boundaries [213]. As introduced in Chapter I, extrinsic GB dislocations characterize the "non-equilibrium" state of such boundaries and relaxation by partial annihilation can be achieved at elevated temperatures by dislocation climb [214]. The relaxation of the deformation modified GBs results in conventional high angle grain boundaries, which display the expected GB diffusivity. An estimation of the relaxation time (τ_{rel}) needed to annihilate an array of random extrinsic GB dislocations is given by [215]:

$$\tau_{rel} = \frac{kTd^3}{A_g \delta D_{gb}^{rel} \mu \Omega} \tag{5.15}$$

where k is the Boltzmann constant, A_g a geometrical factor, Ω the atomic volume, D_{gb}^{rel} the grain boundary self-diffusion coefficient in general HABs, and the other terms have their usual meaning. For Ni of a purity 2N6[24], D_{gb}^{rel} can be determined by [124]:

$$D_{gb}^{rel} = 1.54 \cdot 10^{-4} \cdot e^{\left(-\frac{162\frac{kJ}{mol}}{RT}\right)} (m^2/s) \tag{5.16}$$

Hence, the relaxation time of the deformation modified grain boundaries in BM powders, can be estimated considering the values of A_g, δ, μ and Ω for Ni used by S.V. Divinski *et al.* [125]. For instance, the powder prepared under the most severe BM conditions, P0 (10 h, 350 rpm and 66.7 wt.% of PCA), displayed a d = 0.26 nm, measured by EBSD. At a temperature of 1023 K (the sintering temperature), a

[24] The purity of the as-received powder used in this study is 2N8.

relaxation time of ~1 h (Eq. (5.15)) would be needed for complete relaxation of deformation modified GBs if present in P0. Sintering time in all powders was ten minutes, thus the bulk specimens prepared from BM powders could display ultra-high diffusivity from partially relaxed GBs.

To investigate the presence of ultra-high diffusivity paths in the SPS processed samples, three specimens with different grain sizes were prepared (Table V-2). A sample in the FG range from the as-received powder (S1), and two samples from BM powders: a sample in the FG range (S2) and a sample in the UFG range (S3).

Table V-2 Characteristics of the samples processed for GB diffusion investigations.

Sample	*Precursor powder*	*Relative density (%)*	*Grain size (μm)*
S1	As-received	96.0 (8)	3.2 ± 1.8 (3)
S2	BM powder 3 h, 300 rpm and 8 g of PCA	97.8 (9)	1.69 ± 1.25 (9)
S3	BM powder 10 h, 350 rpm and 8 g of PCA	98.1 (9)	0.86 ± 0.69 (5)

The experimental conditions were chosen to fulfill the criteria necessary for a C-type diffusion regime, a three days annealing at 400 K. These conditions represent a grain boundary diffusion parameter $\alpha = 7{,}2 \cdot 10^{7}$, determined with Eq. (5.12) where the volume diffusion coefficient for Ni was calculated from [216]:

$$D_v = 9.2 \cdot 10^{-5} exp\left(-\frac{278kJ/mol}{RT}\right) \quad (5.17)$$

2.1. *Initial penetration profiles at 400 K for 3 days*

In the study of GB self-diffusion, four different states will be considered for each sample and are summarized in Table V-3. The first diffusion annealing (E2) was performed to investigate the presence of ultra-fast diffusivity paths. Then, a second annealing at 773 K (E3) was chosen to partially relax deformation modified GBs if present in the samples. Finally, a last diffusion annealing (E4) was performed with the same conditions as E2 to investigate the effect of subsequent annealing in the diffusion behavior of the samples.

Table V-3 Characteristics of each annealing state. In bold, states corresponding to diffusion annealing.

State	*Condition*
E1	Initial state after sintering
E2	**400 K for 3 days**
E3	E2 + 773 K overnight
E4	**E3 + 400 K for 3 days**

The diffusion profile of sample S1 for state E2 is shown in Fig. V-6 (a), showing a high penetration of the radiotracer, y > 25 μm. Unexpectedly, a linear relationship of the entire profile with penetration depth (Fig. V-6 (a)) suggests that the anticipated regime might not correctly describe diffusion in S1. This possibility will be considered later on in this chapter. Nevertheless, the condition of $\alpha \gg 1$ is largely fulfilled thus, the C-type regime can be adopted and the diffusion profile divided in two nearly linear parts when plotted against y^2 (Fig. V-6 (b)).

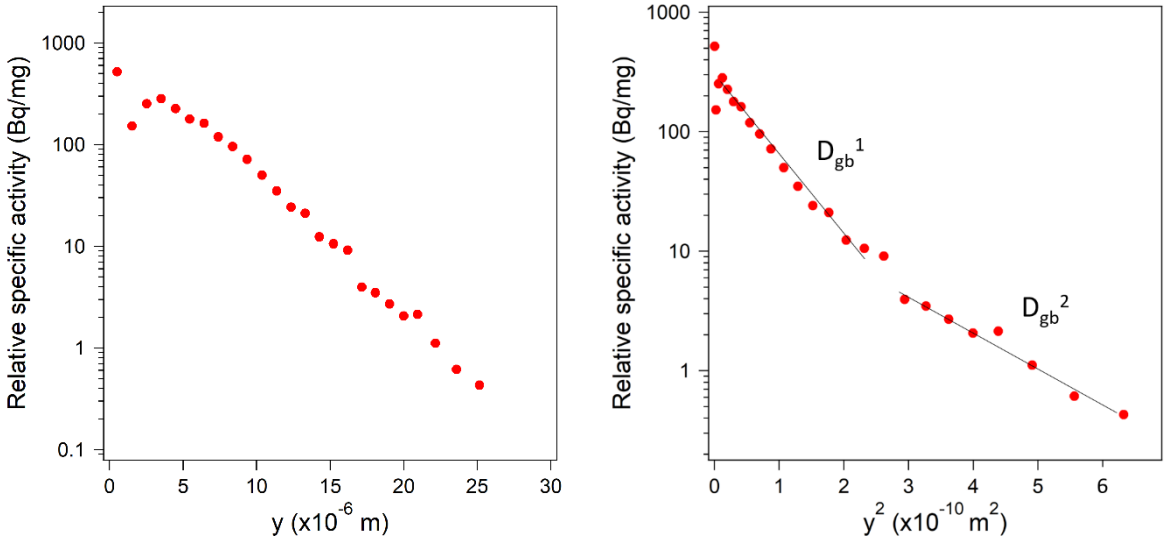

Fig. V-6 Penetration profiles of sample S1 in E2 plotted in relative specific activity against y (a) and y^2 (b).

If the profile is analyzed considering homogeneous interphases in the C-type regime, a grain boundary diffusion coefficient can be calculated for each linear region of the profile using Eq. (5.14). The determined values are $D_{gb}{}^1 = 6.04 \cdot 10^{-17}$ m²/s and $D_{gb}{}^2 = 1.40 \cdot 10^{-16}$ m²/s, respectively for the first and second part of the diffusion profile. Short-circuit diffusion in this sample proceeds faster than along relaxed high angle GBs at 400 K by orders of magnitude, $D_{gb}^{rel} = 1.08 \cdot 10^{-25}$ m²/s (Eq. (5.16)). Furthermore, in comparison to the values displayed by ECAP processed Ni, grain boundary diffusivity in the first part ($D_{gb}{}^1$) is in the same order of magnitude, while in the second part ($D_{gb}{}^2$) it is slightly higher [125]. ECAP processed Ni, exhibits deformation modified GBs and its grain boundary self-

diffusion rate is D_{ECAP} (400 K) = 2.21 · 10^{-17} m^2/s. Although deformation modified GBs are not expected in this specimen (processed from commercial powder), the applied pressure in the sintering process could create "non-equilibrium" GBs.

A similar penetration depth but different profile is observed for sample S2 (Fig. V-7 (a)). An analysis of the profile against y^2, exhibits two distinct sections with a steep and a flat slope (Fig. V-7 (b)). This type of profile which displays a "slow" and a "fast" branch have been reported for Cu-Zr [217], Cu-Pb [218] and ECAP Ni [126] as a result of a hierarchy of diffusion paths in UFG specimens. Diffusivities in S2 are in the same order of magnitude as in S1, D_{gb}^1 = 3.01 · 10^{-17} m^2/s and D_{gb}^2 = 3.33 · 10^{-16} m^2/s, respectively. Nevertheless, it should be noted that a lower GB diffusion coefficient is obtained in sample S2 than in sample S1 for the first section of the profile, while the contrary is observed in the second section.

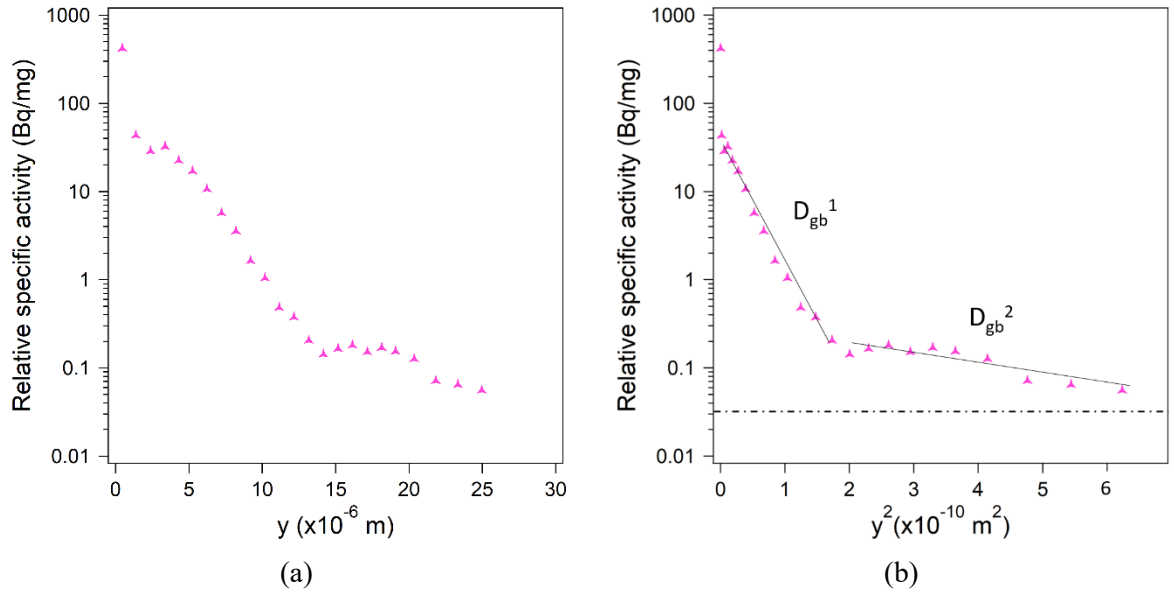

Fig. V-7 Penetration profiles of sample S2 in E2 plotted in relative specific activity against y (a) and y^2 (b). Background level indicated by dashed line.

Finally, the aspect of the diffusion profile of sample S3 is displayed in (Fig. V-8 (a)). In this case the penetration depth is reduced to y ~15 μm and a single section can be observed when plotting against y^2 (Fig. V-8 (b)). Concerning the determined GB diffusion coefficient, D_{gb} = 6.31 · 10^{-17} m^2/s, it is in the order of magnitude of the measured values in samples S1 and S2.

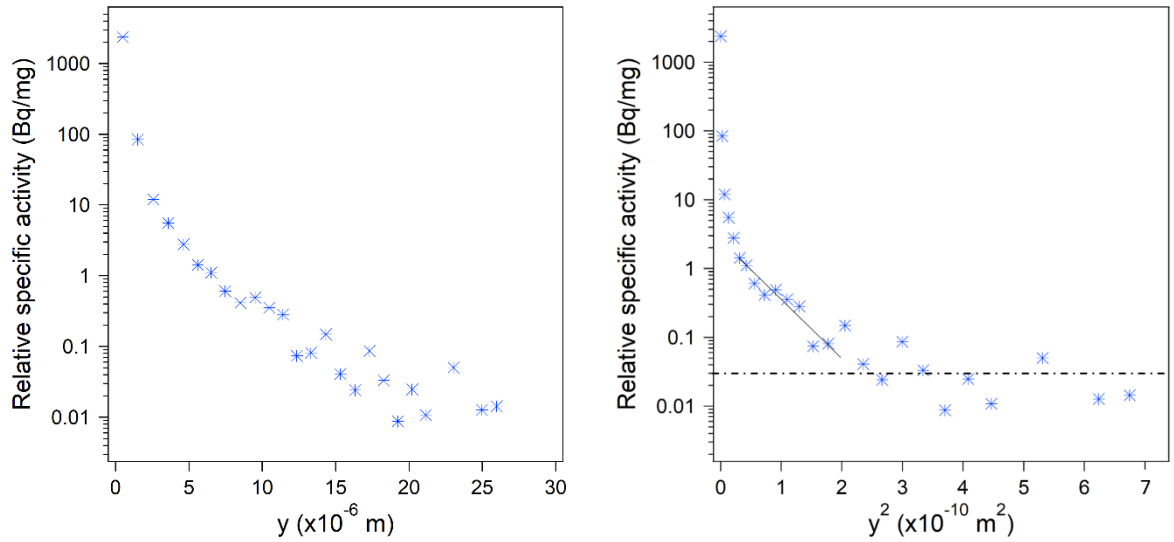

Fig. V-8 Penetration profiles of sample S3 in E2 plotted in relative specific activity against y (a) and y^2 (b). Background level indicated by dashed line.

So far, samples prepared by SPS displayed ultra-fast diffusivity regardless grain size and precursor powder. Within the possible origins of the diffusion enhancement, a hypothetical impurity effect related to contamination during the synthesis of the samples can be discarded. In fact, in FCC metals GB diffusivity decreases with increasing impurity levels [125]. More precisely, for Ni, D. Prokoshkina *et al.* investigated the effect of purity on the GB diffusion rate [219]. A big impact was reported for samples with grain sizes d > 2 µm (Fig. V-9), were the difference in diffusivity exceeded several orders of magnitude. If grain size is reduced below that critical size, grain boundary diffusivity increases approaching the value obtained for pure Ni in the nanometric range.

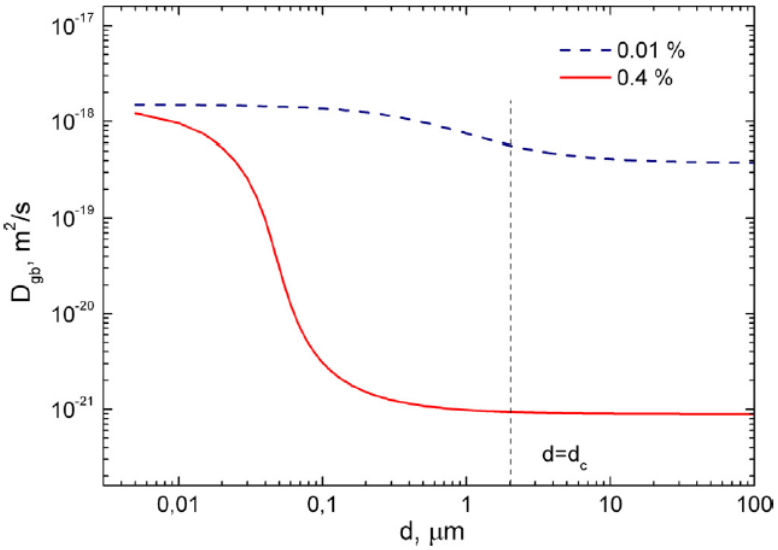

Fig. V-9 Influence of impurities in the GB self-diffusion coefficient of Ni as a function of grain size [219]. Red solid line represent a purity of 2N6 and the blue dashed line a purity of 4N.

Considering no evolution in the microstructure, the other two possible origins for the enhanced diffusivity are the presence of "special" ultra-fast diffusivity grain boundaries and/or percolating porosities.

2.2. *Penetration profiles at 400 K for 3 days after subsequent annealing*

To elucidate the possible presence of "non-equilibrium" grain boundaries in the SPS processed samples, an annealing at 773 K overnight was performed (E3) followed by diffusion annealing in the same conditions as the previous one, 400 K for three days (E4). The annealing time of E3 was chosen for convenience following other studies of GB diffusion in Ni [125]. Since grain size in samples S1, S2 and S3 is bigger than in [125], the relaxation time needed to completely relax deformation modified boundaries (Eq. (5.15)) should be longer for our samples. Nevertheless, Y.R. Kolobov *et al.* [120] reported a decrease in GB diffusivity of four orders of magnitude between non-relaxed and relaxed GBs. Thus, if present, a partial relaxation of the "non-equilibrium" boundaries should still reflect in the diffusion profiles of this study by a less pronounced reduction of the diffusion rate.

The resulting diffusion profile of sample S1 for states E2 and E4 are plotted as a function of y^2 in Fig. V-10. The main difference between the profile of both states is a shift of the curve towards lower values of isotope concentration. A similar feature is observed for sample S2 and is presumably related to sample preparation. Due to the radioactive nature of the samples after the first diffusion annealing (E2), for the second diffusion annealing the surface of the specimens was polished in the parallel grinder. Thus, the outcome of a less neat surface might be responsible for the observed shift towards lower concentration values.

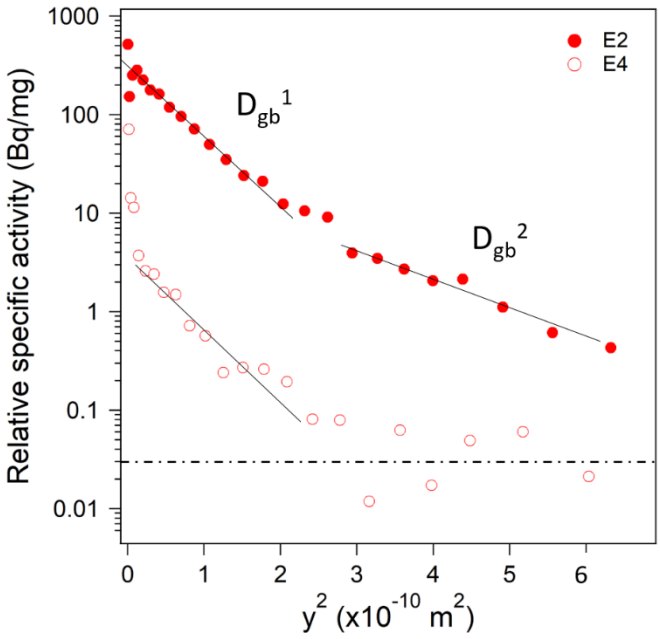

Fig. V-10 Penetration profiles of sample S1 in E2 and E4 plotted in relative specific activity against y^2. Background level indicated by dashed line.

Unlike for state E2, a single slope is depicted for state E4 which displays a GB diffusion coefficient of $D_{gb} = 6.13 \cdot 10^{-17}$ m^2/s. This diffusion rate is practically the same as D_{gb}^1, measured in the first section of E2, thus, the same short-circuits should be accountable for diffusion in both states. To verify the stability of the samples throughout the different states, a systematic study of the microstructure[25] and density of specimens prepared with the same conditions as S1, S2 and S3 was performed. Table V-4 displays the results for sample S1, where no striking differences can be depicted between the states.

Table V-4 Microstructural characteristics of S1 for different annealing states.

State	*Grain size (μm)*	*HAB*	*∑3*	*Other CSL*	*LAGB*	*Density (g/cm^3)*
E1	3.2 ± 1.8 (3)	0.439	0.491	0.053	0.017	8.54 (7)
E2	3.2 ± 1.7 (3)	0.464	0.467	0.050	0.019	8.54 (7)
E3	3.2 ± 1.7 (3)	0.455	0.478	0.048	0.019	8.54 (7)
E4	3.3 ± 1.8 (3)	0.439	0.491	0.050	0.020	8.55 (8)

Concerning diffusion profiles for sample S2, Fig. V-11 displays the results obtained for states E2 and E4 plotted as a function of y^2. Similar to sample S1, a shift towards lower concentration and a single linear section are observed. However, the slope and thus, the GB diffusion coefficient, is different in state E4 than in state E2. In the former state $D_{gb} = 1.84 \cdot 10^{-17}$ m^2/s, compared to $D_{gb}^1 = 3.01 \cdot 10^{-17}$ m^2/s of state E2.

[25] Grain boundary fractions were determined in a length basis and at different zones of the surface of samples.

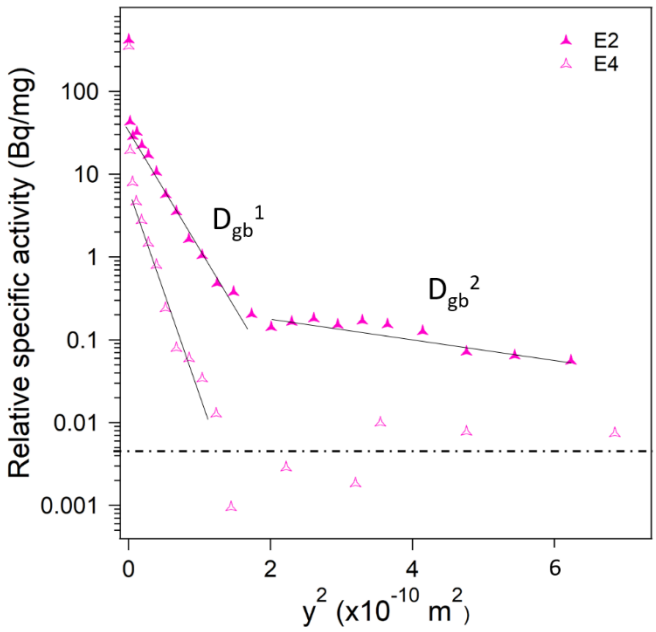

Fig. V-11 Penetration profiles of sample S2 in E2 and E4 plotted in relative specific activity against y^2. Background level indicated by dashed line.

To elucidate the possible causes of the reduced diffusion rate in E4, the microstructure was examined and Table V-5 collects the resulting values. No remarkable changes in grain size or GBCD can be observed besides statistical dispersion. Hence, the evolution in the penetration profile hints towards an intricate structure of ultra-fast paths with possibly a fraction of deformation modified GBs that relaxes upon annealing reducing the effective diffusivity.

Table V-5 Microstructural characteristics of S2 for different annealing states.

State	*Grain size (µm)*	*HAB*	*∑3*	*Other CSL*	*LAGB*	*Density (g/cm³)*
E1	1.69 ± 1.25 (9)	0.474	0.450	0.050	0.026	8.70 (7)
E2	1.56 ± 1.19 (9)	0.457	0.470	0.048	0.021	8.71 (7)
E3	1.75 ± 1.31 (9)	0.446	0.492	0.046	0.016	8.70 (8)
E4	1.92 ± 1.44 (9)	0.443	0.489	0.044	0.024	8.78 (9)

Finally, the results of states E2 and E4 for sample S3 are displayed in Fig. V-12 plotted as a function of y^2. In this case, an unexpected profile is depicted for state E4, an elevated radiotracer concentration at deep penetration combined with a decrease of the slope, which indicates a higher diffusion rate. The corresponding GB diffusion coefficient for E4 is $D_{gb} = 3.99 \cdot 10^{-16}$ m^2/s, an order of magnitude above the D_{gb} of state E2.

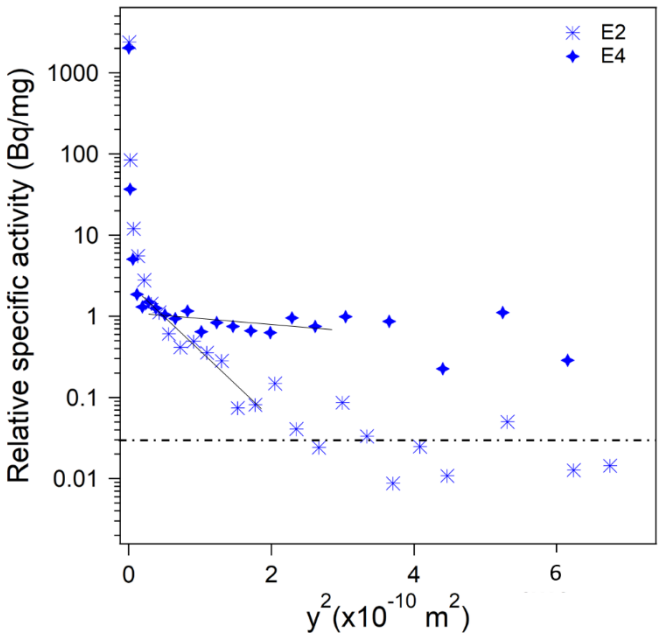

Fig. V-12 Penetration profiles of sample S3 in E2 and E4 plotted in relative specific activity against y^2.

Concerning the microstructural characterization of sample S3, the measured results are displayed in Table V-6. Comparatively to samples S1 and S2, no outstanding variation can be outlined. Thus, the evolution of the diffusion profile cannot be attribute to a modification of the microstructure.

Table V-6 Microstructural characteristics of S3 after different annealing treatments.

State	*Grain size (µm)*	*HAB*	*∑3*	*Other CSL*	*LAGB*	*Density (g/cm³)*
E1	0.86 ± 0.69 (5)	0.476	0.465	0.019	0.040	8.73 (8)
E2	0.79 ± 0.61 (5)	0.494	0.402	0.056	0.048	8.73 (8)
E3	0.90 ± 0.65 (5)	0.415	0.489	0.054	0.042	8.72 (8)
E4	0.78 ± 0.56 (5)	0.482	0.395	0.063	0.060	8.78 (9)

A similar case of increase in the diffusion rate after subsequent annealing treatments at low temperature had been reported for ECAP processed Ni [125]. Presumably, it results from the formation of percolating porosity. In fact, the authors performed a first annealing treatment for GB relaxation that resulted in a decrease of the GB diffusion rate, which was still higher than the diffusivity expected for relaxed GBs, thus a second treatment was performed at higher temperature for complete relaxation. Surprisingly, the determined D_{gb} was higher, even above the initial value. Presumably, the relaxation of residual stresses in SPD processed specimens initiates cracks that widen by vacancy coalescence. This result highlights the contribution of vacancy-like defects to the interface of the "non-equilibrium" GBs. The effect of crack formation on the GB diffusion coefficient at different annealing temperatures is displayed in Fig. V-13.

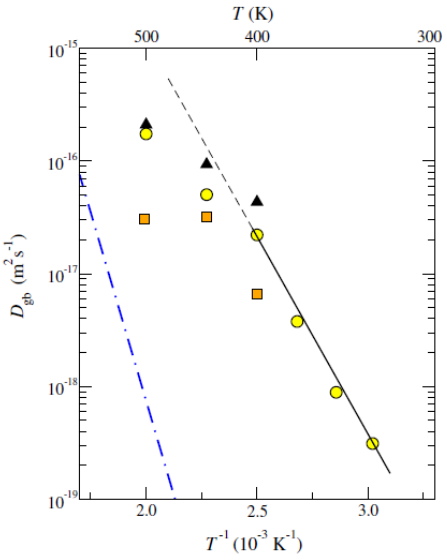

Fig. V-13 Effect of crack formation (black triangles) after subsequent annealing processes on GB diffusion coefficient [125]. The blue dashed line corresponds to annealed coarse-grained Ni with relaxed HAB. Yellow circles represent D_{gb} in the initial state of ECAP Ni and orange squares to D_{gb} of the same samples after the first relaxation annealing.

2.3. *Investigation of the porosity structures*

Finally, the porosity structures as high diffusivity paths is prospected. To do so, the cross-sections of the initial state (E1) of samples S1, S2 and S3 were observed by SEM at different milling depths. The preparation by FIB enables the inspection of porosity geometries as well as possible connections between them. A statistical analysis of the size and location of pores is not performed in this section, but can be found for samples prepared with the same powders as samples S1 and S3 in Chapter III.

Images for sample S1 are shown in Fig. V-14. Big size pores can be observed mostly decorating grain boundaries. In Fig. V-14. (a) two big porosities situated close to each other (indicated by the black arrow), result interconnected when inspected after further milling (Fig. V-14. (b)) creating intricate geometries. This example is not isolated, but rather generalized for this sample (Fig. V-14. (c)).

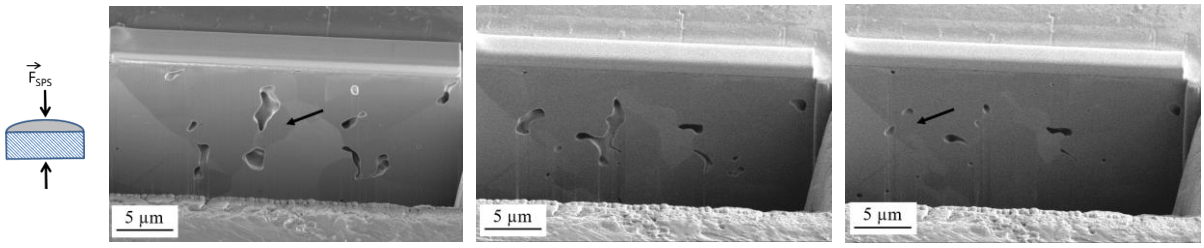

(a) (b) (c)

Fig. V-14 SEM images of sample S1 in state E1 after preparation by FIB at three consecutive depths. Arrows indicate two pores that become interconnected.

On the contrary, in sample S2, no sign of percolating porosity was observed. In Fig. V-15 it can be seen that porosities display smaller size, mostly spherical and are located at grain boundaries as well as grain interiors. After milling ~0.5 µm in depth, the pores in Fig. V-15 (a) disappear with the exception of the pore indicated by the arrow in Fig. V-15 (b).

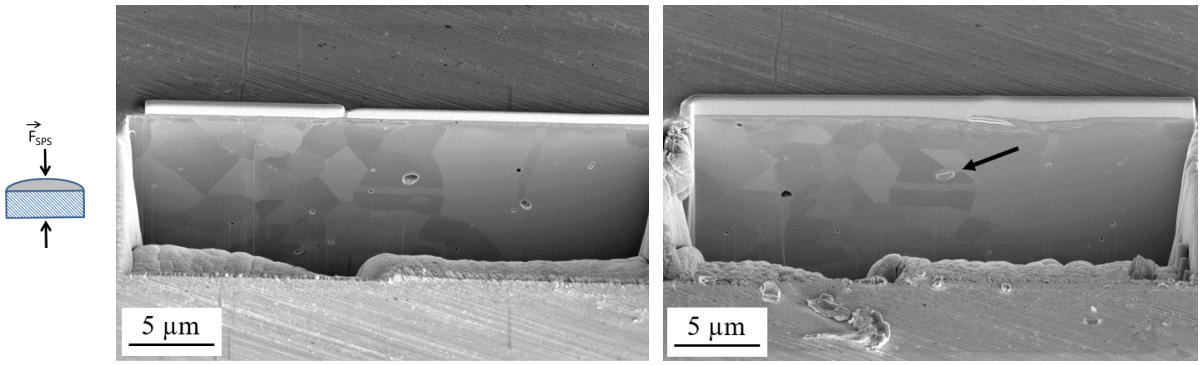

(a) (b)

Fig. V-15 SEM images of sample S2 in state E1 after preparation by FIB at two consecutive depths. The arrow indicates a pore visible at both depths.

Likewise, in the case of sample S3, isolated pores of even smaller size are observed. Fig. V-16 displays the corresponding images at two different milling depths, where only two pores are depicted in both images (Fig. V-16 (b)).

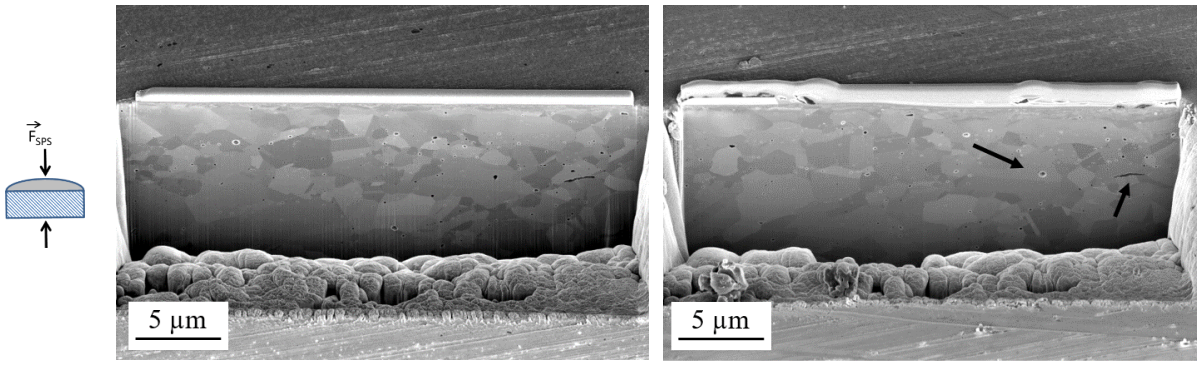

(a) (b)

Fig. V-16 SEM images of sample S3 in state E1 after preparation by FIB at two consecutive depths. Arrows display two pores visible at both depths.

Finally, to complete the inquiries concerning the implication of porosity structures in the evolution of diffusion behavior after subsequent annealing in sample S3, the state E4 was investigated. Indeed, the formation of continuous porosity paths can be observed in this state (Fig. V-17). This result indicates that the increase in diffusivity depicted for state E4 is related to the formation of interconnected porosities during annealing. Moreover, the flat-like aspect of the channel shown in Fig. V-17 (c), suggest

an important diffusion in the direction perpendicular to the surface considered in the Fisher model of GB diffusion, which would explain the elevated radiotracer concentration measured at deep penetration.

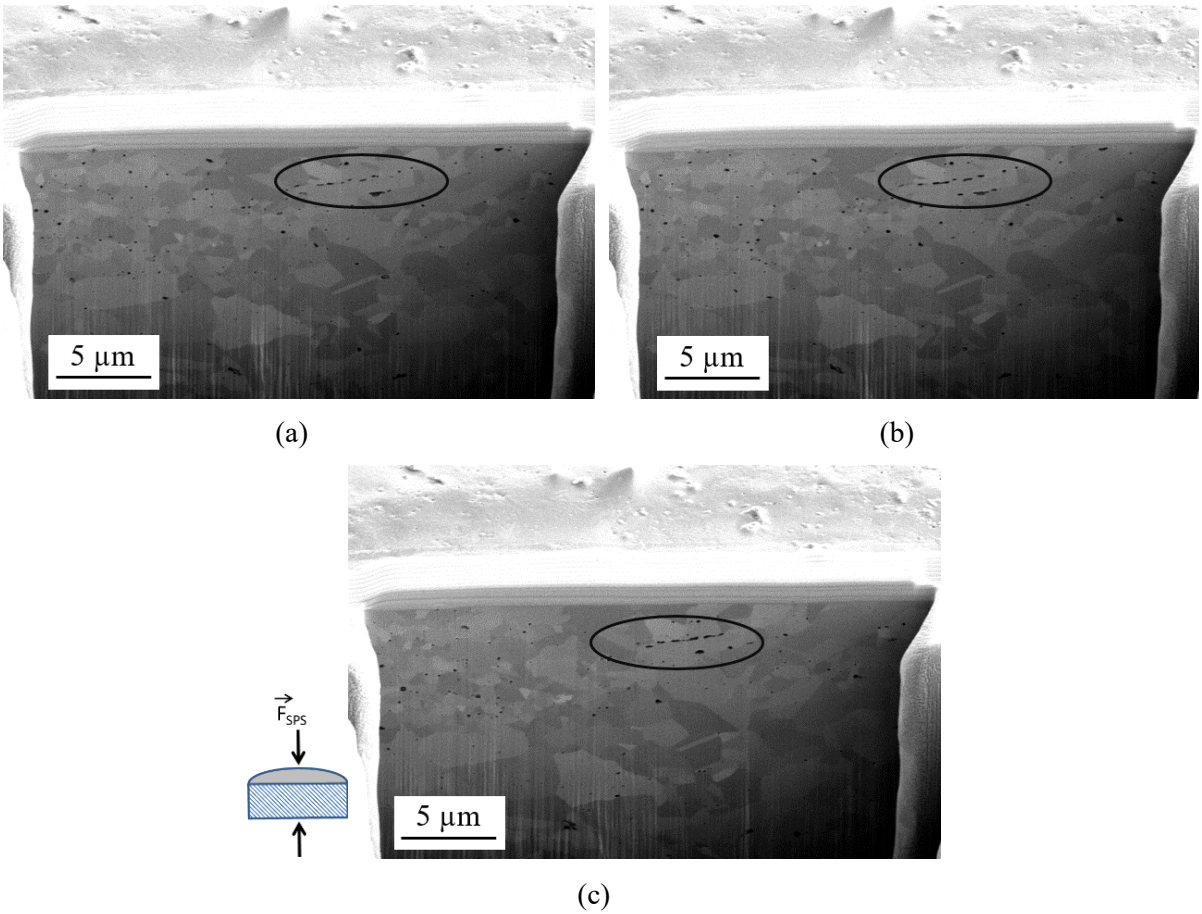

Fig. V-17 SEM images of sample S3 in state E4 after preparation by FIB at three consecutive depths. Indicated in black, the formation of a continuous porous path.

The observation of the porosity structures of specimens S1, S2 and S3 in state E1 enables the distinction between samples with interconnected porosities (S1) and with isolated pores (S2 and S3). Thus, a different analysis concerning the measured diffusion profiles discussed in the previous sections has to be employed between them. A complex structure of ultrafast paths including isolated pores located at grain boundaries and perhaps the presence of remnant deformation modified grain boundaries from the BM process makes a deeper analysis of the diffusion behavior of samples S2 and S3 complicated without further measurements. Nevertheless, for sample S1 a different approach can be taken.

The lack of change between the GB diffusion coefficients measured in state E2 and E4 suggests no relaxation of “non-equilibrium” GBs, thus, the main diffusion paths in this sample would be conventional HABs and porous channels. The high linearity displayed by the diffusion profile of sample S1 referred to penetration depth (Fig. V-6 (a)) suggests a “modified” B-type kinetic regime, where the

diffusion profile becomes linear against $y^{6/5}$. In the case of S1, the diffusing system would be composed of porous channels (Fig. V-14 (a)) as the principal high diffusivity path and leakage would occur into relaxed high-angle GBs. Thus, adopting a model that considers leaking at points where the porous channel meets a GB, a "surface" diffusion coefficient (D_p) through the pores could be estimated. To this aim, the model proposed by S.V. Divinski *et al.* for sintered γ-FeNi introduced in section one of this chapter (Fig. V-5 (b)) could be adapted to our system. They proposed a double product for inter-agglomerate interfaces (P_a) determined as follows:

$$P_a = \frac{\delta_a \cdot D_a}{\lambda_a} = 0.661 \left(\frac{4D_{gb}}{t}\right)^{1/2} \left(-\frac{\partial ln\bar{c}}{\partial y^{6/5}}\right)^{-5/3} \tag{5.18}$$

where the factor λ_a is added to take into account the outdiffusion to the GBs exclusively at crossing points between the inter-agglomerate interfaces and GBs. For polyhedral grains:

$$\lambda_a = \frac{\pi\delta}{2d} \tag{5.19}$$

Thus, if the grain boundary diffusion coefficient is known, using Eq. (5.18) and (5.19), D_a can be estimated assuming an arbitrary agglomerate interface width (δ_a). For the present case, we can assume $D_{gb} = D_{gb}^{rel}$ (calculated from Eq. (5.16)), $\delta \sim 0.5$ nm and $\delta_a \sim 1$ nm (similarly to [209]) to obtain an approximate value of D_a, where $D_a = D_p$. The diffusion profile of S1 plotted against $y^{6/5}$ is displayed in Fig. V-18 for states E2 and E4 exhibiting good linearity.

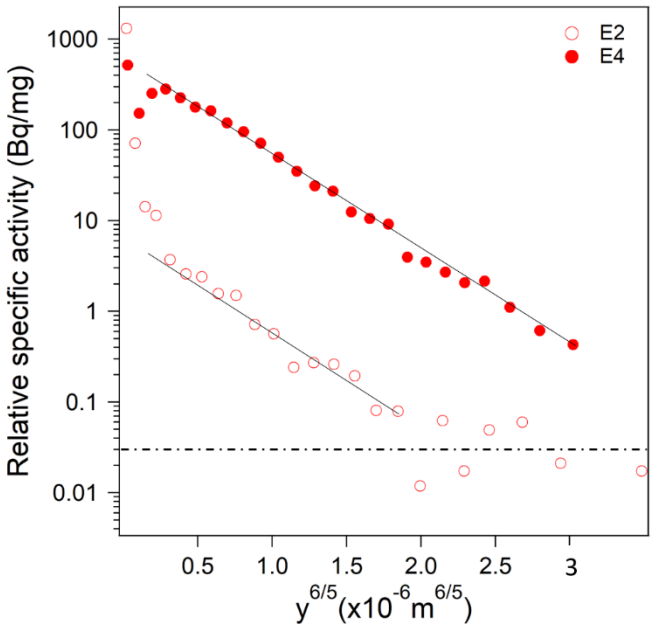

Fig. V-18 Penetration profiles of sample S1 in E2 and E4 plotted in relative specific activity against $y^{6/5}$.

The estimated pore diffusion coefficient is $D_p = 1.40 \cdot 10^{-13}$ m²/s and $D_p = 1.28 \cdot 10^{-13}$ m²/s respectively for states E2 and E4. These values could serve as starting point to develop a model that

takes into account pores as ultra-fast diffusion paths and help develop the current understanding of the relative diffusivity between different short-circuits.

3. Stability of samples processed by SPS at high temperature

As reported in Chapter I, a major concern in UFG samples is their low thermal stability as grain growth or even recrystallization can be observed at rather low temperatures for electrodeposited [58,61] or SPD Ni samples [220]. In the previous section, in addition to the diffusivity study, the systematic characterization of the microstructures after each annealing state showed no noticeable changes in neither grain size nor GBCD of the SPS processed samples. Thus, good stability is displayed by samples S1, S2 and S3 at least up to 773 K. For a further characterization of the stability of the UFG sample processed by PM at high temperature, an annealing treatment at 1173 K for three hours was performed in specimen S3. In fact, in coarse grained nickel, grain growth can be observed, depending on the initial state of samples, at 773 K [173], thus the stability of FG/UFG samples processed by SPS at such relatively high temperature suggests that they might be stable up to the sintering temperature. Hence, a higher temperature (1173 K) was chosen to attempt recrystallization of the sample.

Surprisingly, during annealing of sample S3 grain growth is accompanied by an increase in volume, which represents a decrease in relative density from 97.6 (9) % at the initial state to 71.0 (9) % after heat treatment. The raw surface of the sample examined by SEM displays grains of d ~ 5 µm as well as micrometric pores (Fig. V-19 (a)) and continuous porous paths (Fig. V-19 (b)).

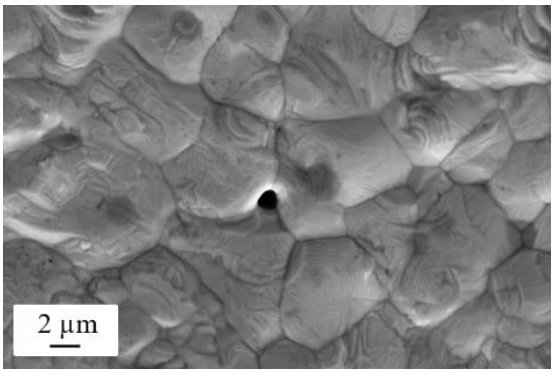

(a)

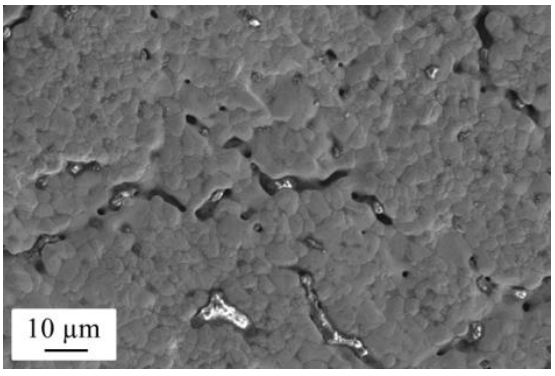

(b)

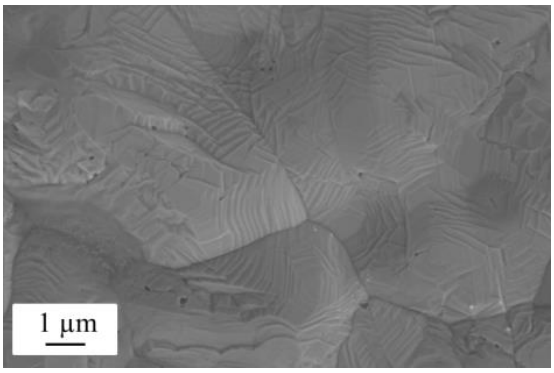

(c)

Fig. V-19 SEM images of the surface of sample S3 after annealing at 1173 K for 3 h displaying a big pore situated at a triple point (a), continuous porous paths (b) and small nanometric porosities located inside the grains (c).

It is noteworthy that sample S3 was synthesized with the powder P0, equally to sample S-P0 presented in Chapter III. Such chapter includes an analysis of the porosities found in sample S-P0, where only 5.2 % of porosities displayed a size above 100 nm and rarely exceeded 200 nm. Thus, during annealing at 1123 K, coalescence of porosities produces bigger pores including porosity channels. The location of the pores, for instance at triple points (Fig. V-19 (a)), suggests that pores travel through grain boundaries to create bigger porosities. In fact, isolated nanometric pores can still be found inside the grains (Fig. V-19 (c)), that do not contribute to the newly formed porosity structures.

Nevertheless, a decrease in relative density of over 25 % cannot be justified by the presence of such micrometric pores. Thus, sample S3 was examined by X-ray computed tomography[26] to obtain volumetric information concerning the porosity structures. Small porosities such as the ones observed by SEM are not visible in the reconstructed sample. However, several big flat voids with a diameter of over one mm can be observed (Fig. V-20).

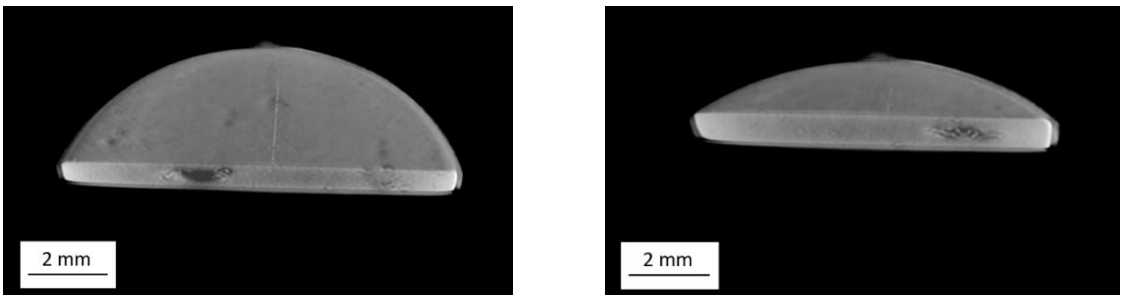

(a) (b)

Fig. V-20 Reconstruction of the sample S3 by X-ray computed tomography displaying flat voids.

[26] These measurements as well as the cross section of sample S3 shown in Fig. V-21, were performed at Presto Engineering Europe.

To confirm these results, the sample was carefully cut to reveal one of the voids (Fig. V-21 (a)). Indeed, a flat-like void of a diameter of 1.46 mm and a thickness of 0.24 mm is depicted, accompanied by a high density of micrometric pores (Fig. V-21 (b)). Likewise, other flat voids can be observed at different distances from the surfaces (Fig. V-21 (c)).

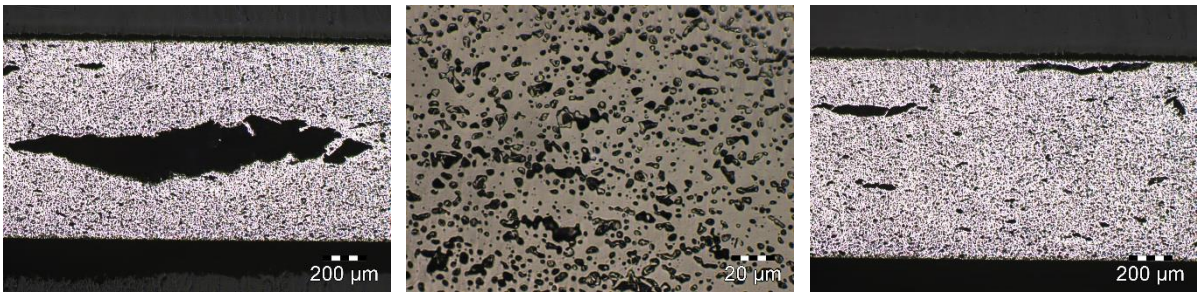

(a) (b) (c)

Fig. V-21 Images of the cross section of sample S3 by optical microscopy, after annealing at 1127 K for 3 h.

To follow the change in volume and obtain more information concerning the temperature and time necessary to observe this behavior, dilatometry was employed with the temperature program specified in Chapter II. The results can be observed in Fig. V-22 (a), as total thickness (h) divided by initial thickness (h_i) (normalized displacement) vs temperature. The same measurement performed in samples S1 and S2 are added for comparison. It is noticeable that only samples sintered from BM powders (S2 and S3) experience swelling. In the case of S1, only thermal expansion is depicted, whereas in samples S2 and S3 a permanent volume change is observed after cooling.

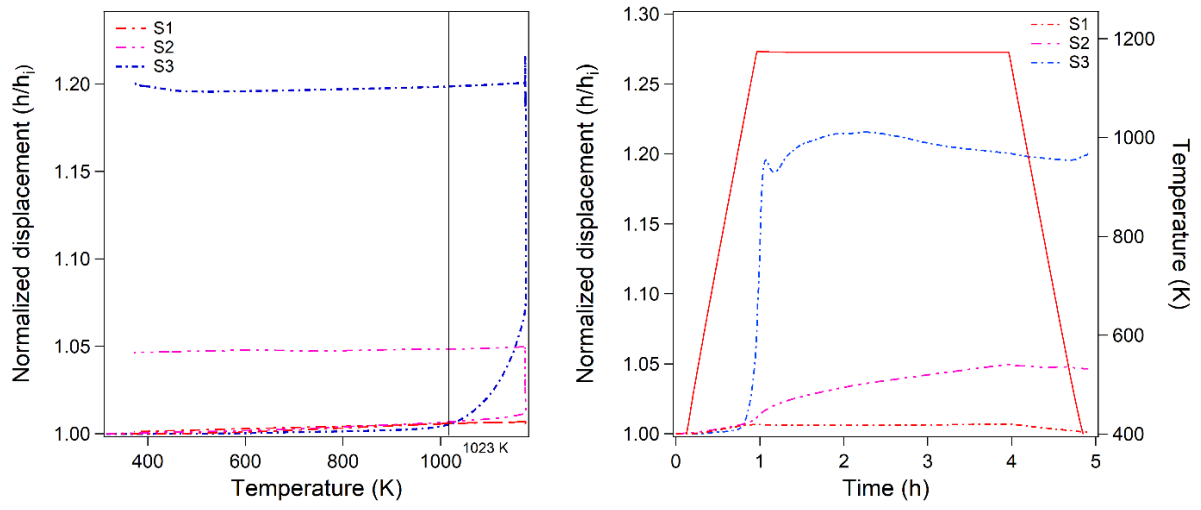

(a) (b)

Fig. V-22 Dilatometry results with displacement normalized by the initial thickness as a function of temperature (a) and time (b). The red solid line in (b) corresponds to the measurement of temperature as a function of time.

More precisely, relative density in S2 decreases from 98.3 (9) % to 94.3 (9) %, whereas S1 presented a relative density of 96.1 (9) % before the measurement and of 96.7 (9) % afterwards (Table V-7). It is noteworthy that no swelling is observed at a temperature below 1023K, the sintering temperature. In fact, for sample S2 most of the volume change takes place at 1123 K, while in S3 it begins at a temperature closer to the sintering temperature. If the normalized displacement is represented against time, it can be seen that the swelling process is not the same for both samples. In the case of sample S3, swelling is almost instantaneous contrary to S2, where once the temperature 1123 K is reached, it gradually changes in volume.

Table V-7 Difference in density of samples after annealing at 1173 K for 3 h.

Sample	*Initial density (g/cm^3)*	*Final density (g/cm^3)*
S1	8.55 (9)	8.61 (9)
S2	8.75 (9)	8.39 (9)
S3	8.66 (9)	6.23 (8)

A decrease in bulk density at temperatures above the sintering temperature or at long sintering times is known as retrograde sintering or retrograde densification. It usually appears during conventional sintering and can be observed in ceramics [221–223] and metallic materials [224–226]. A limited number of mechanism can account for retrograde densification and the most common for metals is the formation of closed porosities that expand at high temperature due to internal gas pressure [222]. Swelling continues until pore opening due to the increase in gas pressure, which results is a small change in the mass of the specimen. For instance, for sample S3 a mass loss of ~0.18 mg is observed after the heat treatment at 1123 K. The presence of open porosities (continuous porous paths) prevents swelling as they enable the removal of the trapped gas, which explains the lack of volume change in sample S1.

Concerning the difference between samples S2 and S3, it is surprising the big difference in density after heat treatment since initial density was very similar. This difference might be due to a difference in pore distribution and/or different GB energy, which could facilitate coalescence of porosities in S3 against S3.

4. Summary and conclusions

In this chapter, GB diffusion at low temperature was investigated for three SPS processed samples in the FG/UFG regime. Each sample displayed ultra-fast diffusivity with singular diffusion profiles that indicate a different hierarchy of fast diffusivity paths in each case. A linear penetration profile plotted against $y^{6/5}$ in sample S1 was observed combined with a stable diffusion behavior after annealing at 773

K overnight. This result suggests that diffusion takes place in a “modified B-type” kinetic regime similar to the C-B kinetic regime proposed by S.V. Divisnki *et al*. FIB preparation and SEM observation of the porosity structures unveiled intricate interconnected porosities, which are presumably the main diffusion channels, with leaking towards relaxed HABs.

In samples S2 and S3, a change in slope in diffusion profiles is depicted between states E2 and E4. In the case of sample S2, the lower diffusion rate measured in E4 hints at GB relaxation. The presence of isolated pores of different size and location makes a customized analysis complicated without further experiments. For sample S3, the increase in GB diffusivity in E4 proved to be the consequence of interconnected pores formed during annealing, which was confirmed by SEM observation of the cross-section. This increase in diffusion, hinders the possibility of evaluating the presence of deformation modified GBs in S3 by these means. In fact, S.V. Divinski [123] discusses in his review that not all SPD processes generate ultrafast diffusivity paths, thus it is not a given for BM. He also exposes the possibility of creating “high-energy” but relaxed grain boundaries when SPD is performed at high temperatures by recrystallization. Thus, it would be interesting to pursue the investigation of GB diffusivity in the samples processed by BM and SPS.

Concerning thermal stability at high temperature, retrograde sintering was depicted by dilatometry measurements in samples prepared from BM powders. The kinetics of the swelling process are clearly different in samples S2 and S3. In the first case, once 1123 K is reached, it gradually increases in volume, while in sample S3 the change takes place very fast and begins short after exceeding the sintering temperature. In the case of our samples, retrograde densification seems to be related to material creeping under stresses caused by the internal gas pressure in pores. Differences in the porosity structures can thus be accountable for the diverse behaviors of samples S1, S2 and S3. However, the results of the GB diffusion investigation for samples S2 and S3, suggest that defects such as deformation modified GBs might be present in this sample and contribute to the instability at high temperature.

Concerning the stability of the microstructure, grain size and GBCD of the three samples are stable up to 773 K. Nevertheless, exhaustive study of thermal stability would be necessary at higher temperatures and different times to complete this investigation.

CONCLUSIONS AND FUTURE RESEARCH

The purpose of the present work can be divided in three parts. A first part that consists on exploring the effect of processing parameters in the synthesis of FG/UFG Ni prepared from SPD processed powder and consolidated by SPS. A second part that aims to analyze the effect of grain size on the mechanical properties and strain hardening mechanisms of the SPS processed samples. Finally, a third part where GB diffusivity is investigated as well as thermal stability at high temperature. In Chapter I, some inquiries were proposed concerning these three axes, and were hopefully clarified throughout this manuscript.

Homogeneous oxide-free UFG Ni samples were processed from BM powders. Keeping milling speed below 350 rpm and milling time below twelve hours, different combinations of milling parameters produced Ni samples with grain sizes between 0.69-2.1 μm with little or no contamination, as depicted from XRD. Such samples displayed relative densities above 95 % and GBCDs dependent on grain size. The porosity structure encountered in samples processed from the as-received powder (S-PC) or BM powders (such as S-P0) differ in size, morphology and location. Big pores of irregular shape are found mostly in GBs in the case of S-PC, and geometric small pores located mainly in the bulk of grains are observed in S-P0. The GBCD of the processed samples is highlighted by a high Σ3 grain boundary fraction, which decreases with grain size, and a low LAGB fraction that increases inversely to grain size. The misorientation angle distribution plot for the sample of smallest grain size (S-P0) displayed in between characteristics as compared to samples processed exclusively by SPD or SPS, with a peak at low misorientation angles and a peak at high misorientation angles. Finally, a low initial internal stress state was reported, regardless the precursor powder (as-received or BM), as depicted from EBSD analyses by GOS and TEM observations.

In an effort to investigate exclusively the effect of grain size in the FG/UFG range on mechanical properties, the synthesis conditions (BM conditions) were selected to produce samples with GBCDs as similar as possible. Despite a small percentage of porosities, the SPS processed samples displayed a uniform elongation that exceeded 30 % in all cases, as well as high strength. The combination of these two characteristics reflects on the good toughness observed specially for the UFG samples, which is far above the values obtained in SPD processed samples.

A deviation of the yield strength from the HP relation was depicted for UFG samples, which is presumably the consequence of heterogeneous yielding, as reported for other FCC UFG metals. Such deviation persists at higher deformation levels, which raises new questions. Does heterogeneous yielding persist throughout the plastic domain? Is the origin of the additional hardening at higher

deformation levels due to other microstructural features? An evolution in strain hardening with decreasing grain size is observed towards lower values of normalized hardening rate, especially in the UFG range, were an almost inexistent second hardening stage is depicted. The investigations concerning the deformed state of the samples confirm the lack of dislocation cells in the UFG samples, which suggest generalized cross-slip as well as dislocation annihilation early in the plastic domain.

Diffusion experiments designed to study GB diffusion shed light on the intricate diffusion paths of the SPS processed Ni samples. Three samples with different microstructural features were investigated. High diffusivity was observed for all samples, which displayed very different penetration profiles indicating a diverse hierarchy of fast diffusivity paths. The feature with the biggest impact on diffusion seems to be the presence of different porosity structures. Contrary to other UFG Ni samples processed by ED or SPD, good microstructural stability was observed in this study up to 773 K. Nevertheless, the evolution of the location and size of pores in the sample with the smallest grain size (S3) at low temperature, suggests an unstable porosity structure. This result correlates with the retrograde sintering phenomenon depicted at high temperature, which is observed exclusively in samples processed from BM powders that display closed porosities. Regardless the small impact of initial porosity on the mechanical properties, the evolution of porosity structures could have a major impact on mechanical strength and ductility.

The ensemble of these results show that nanostructuration of powders by BM and consolidation by SPS represents a promising combination to produce UFG Ni. In comparison with the other techniques used in the synthesis of UFG metals, it displays both advantages, such as good ductility and microstructural stability, and disadvantages, such as lower yield strength and intricate porosity structures. Thus, choosing PM over SPD or ED will depend on the properties sought in our material. Finally, many questions remain open for future research. A study concerning the restauration and recrystallization processes during sintering. A detailed investigation on the strain hardening mechanisms to clarify the results presented in this manuscript. New diffusion studies to verify if UFG Ni produced combining BM and SPS exhibits ultra-fast diffusivity GBs. As well as new studies concerning other metals and alloys or other investigations such as mechanical properties at high temperature, GB diffusion in the B-type regime or the corrosion behavior of UFG materials.

REFERENCES

[1] M. Suarez, A. Fernandez, J.L. Menendez, R. Torrecillas, H. U., J. Hennicke, R. Kirchner, T. Kessel, Challenges and Opportunities for Spark Plasma Sintering: A Key Technology for a New Generation of Materials, in: B. Ertug (Ed.), Sinter. Appl., InTech, 2013.

[2] C. Estournes, C. Maniere, L. Durand, Use of a deformable interface for the production of complex parts, WO2017/077028 A1, n.d.

[3] P. Ramakrishnan, History of powder metallurgy, Indian J. Hist. Sci. 18 (1983) 109–114.

[4] D.A. Levina, L.I. Chernyshev, N.V. Mikhailovskaya, Contemporary powder metallurgy: Achievements and problems, Powder Metall. Met. Ceram. 46 (2007) 202–205.

[5] L.A. Dobrzański, Goals and Contemporary Position of Powder Metallurgy, in: Powder Metall. - Fundam. Case Stud., 2017.

[6] W.B. James, Powder Metallurgy Methods and Applications, ASM Handb. Powder Metall. 7 (2015).

[7] T. Sekiguchi, K. Ono, H. Fujiwara, K. Ameyama, New Microstructure Design for Commercially Pure Titanium with Outstanding Mechanical Properties by Mechanical Milling and Hot Roll Sintering, Mater. Trans. 51 (2010) 39–45.

[8] Z. Zhang, D. Orlov, S.K. Vajpai, B. Tong, K. Ameyama, Importance of Bimodal Structure Topology in the Control of Mechanical Properties of a Stainless Steel, Adv. Eng. Mater. 17 (2015) 791–795.

[9] C. Sawangrat, O. Yamaguchi, S.K. Vajpai, K. Ameyama, Application of Harmonic Structure Design to Biomedical Co-Cr-Mo Alloy for imrpoved Mechanical Properties, Mater. Trans. 55 (2014) 99–105.

[10] J.M. Torralba, 3.11 - Improvement of Mechanical and Physical Properties in Powder Metallurgy, in: Compr. Mater. Process., Elsevier, 2014: pp. 281–293.

[11] H. Gleiter, Materials with ultrafine microstructures: retrospectives and perspectives, Nanostructured Mater. 1 (1992) 1–19.

[12] H. Gleiter, Nanocrystalline materials, Prog. Mater. Sci. 33 (1989) 223–315.

[13] H. Gleiter, Nanostructured materials: state of the art and perspectives, NanoStructured Mater. 6 (1995) 3–14.

[14] H. Gleiter, Nanostructured materials: basic concepts and microstructure, Acta Mater. 48 (2000) 1–29.

[15] P.W. Bridgman, Effects of high shearing stress combined with high hydrostatic pressure, Phys. Rev. 48 (1935) 825.

[16] T.G. Langdon, Twenty-five years of ultrafine-grained materials: Achieving exceptional properties through grain refinement, Acta Mater. 61 (2013) 7035–7059.

[17] J.T. Wang, Historic Retrospection and Present Status of Severe Plastic Deformation in China, Mater. Sci. Forum. 503–504 (2006) 363–370.

[18] R.Z. Valiev, T.G. Langdon, The Art and Science of Tailoring Materials by Nanostructuring for Advanced Properties Using SPD Techniques, Adv. Eng. Mater. 12 (2010) 677–691.

[19] R.Z. Valiev, R.K. Islamgaliev, I.V. Alexandrov, Bulk nanostructured materials from severe plastic deformation, Prog. Mater. Sci. 45 (2000) 103–189.

[20] R.Z. Valiev, R.S. Mishral, J. Grozal, A.K. Mukherjee, Processing of nanostructured nickel by severe plastic deformation consolidation of ball-milled powder, Scr. Mater. 34 (1996) 1443–1448.

[21] ASM International, P.W. Lee, ASM International, eds., Powder metal technologies and applications, [10. ed.], 2. print, ASM International, Materials Park, Ohio, 2002.

[22] M.A. Meyers, A. Mishra, D.J. Benson, Mechanical properties of nanocrystalline materials, Prog. Mater. Sci. 51 (2006) 427–556.

[23] Y. Estrin, A. Vinogradov, Extreme grain refinement by severe plastic deformation: A wealth of challenging science, Acta Mater. 61 (2013) 782–817.

[24] A. Vorhauer, R. Pippan, On the homogeneity of deformation by high pressure torsion, Scr. Mater. 51 (2004) 921–925.

[25] Y. Song, W. Wang, M. Chen, J. Guo, L. Xu, D. Gao, H.S. Kim, Ultrafine-Grained Materials Fabrication with High Pressure Torsion and Simulation of Plastic Deformation Inhomogeneous Characteristics, in: M. Cabibbo (Ed.), Sev. Plast. Deform. Tech., InTech, 2017.

[26] M. Kawasaki, R.B. Figueiredo, Y. Huang, T.G. Langdon, Interpretation of hardness evolution in metals processed by high-pressure torsion, J. Mater. Sci. 49 (2014) 6586–6596.

[27] A.P. Zhilyaev, S. Lee, G.V. Nurislamova, R.Z. Valiev, T.G. Langdon, Microhardness and microstructural evolution in pure nickel during high-pressure torsion, Scr. Mater. 44 (2001) 2753–2758.

[28] C.T. Wang, A.G. Fox, T.G. Langdon, Microstructural evolution in ultrafine-grained titanium processed by high-pressure torsion under different pressures, J. Mater. Sci. 49 (2014) 6558–6564.

[29] A.P. Zhilyaev, G.V. Nurislamova, B.-K. Kim, M.D. Baró, J.A. Szpunar, T.G. Langdon, Experimental parameters influencing grain refinement and microstructural evolution during high-pressure torsion, Acta Mater. 51 (2003) 753–765.

[30] V.M. Segal, Materials processing by simple shear, Mater. Sci. Eng. A. 197 (1995) 157–164.

[31] R.Z. Valiev, T.G. Langdon, Principles of equal-channel angular pressing as a processing tool for grain refinement, Prog. Mater. Sci. 51 (2006) 881–981.

[32] J. Leuthold, G. Reglitz, M. Wegner, G. Wilde, S.V. Divinski, Local texture-microstructure correlation due to deformation localization in ECAP-processed nickel, Mater. Sci. Eng. A. 669 (2016) 196–204.

[33] G. Reglitz, B. Oberdorfer, N. Fleischmann, J.A. Kotzurek, S.V. Divinski, W. Sprengel, G. Wilde, R. Würschum, Combined volumetric, energetic and microstructural defect analysis of ECAP-processed nickel, Acta Mater. 103 (2016) 396–406.

[34] M. Cabibbo, Grain refinement and hardness saturation in pure Nickel subjected to a sequence of ECAP and HPT, Metall. Ital. (2015) 37–48.

[35] K.S. Raju, M.G. Krishna, K.A. Padmanabhan, K. Muraleedharan, N.P. Gurao, G. Wilde, Grain size and grain boundary character distribution in ultra-fine grained (ECAP) nickel, Mater. Sci. Eng. A. 491 (2008) 1–7.

[36] C. Suryanarayana, Mechanical alloying and milling, Prog. Mater. Sci. 46 (2001) 1–184.

[37] T. Prasad Yadav, R. Manohar Yadav, D. Pratap Singh, Mechanical Milling: a Top Down Approach for the Synthesis of Nanomaterials and Nanocomposites, Nanosci. Nanotechnol. 2 (2012) 22–48.

[38] E. Bonetti, E.G. Campari, L. Pasquini, E. Sampaolesi, Microstructure-related anelastic and magnetoelastic behavior of nanocrystalline nickel, J. Appl. Phys. 84 (1998) 4219–4226.

[39] C.C. Koch, Synthesis of nanostructured materials by Mechanical Milling: problems and opportunities, NanoStructured Mater. 9 (1997) 13–22.

[40] Q.H. Bui, G. Dirras, S. Ramtani, J. Gubicza, On the strengthening behavior of ultrafine-grained nickel processed from nanopowders, Mater. Sci. Eng. A. 527 (2010) 3227–3235.

[41] M.A. Bousnina, A. dakhlaoui Omrani, F. Schoenstein, P. Madec, H. Haddadi, L.S. Smiri, N. Jouini, Spark plasma sintering and hot isostatic pressing of nickel nanopowders elaborated by a modified polyol process and their microstructure, magnetic and mechanical characterization, J. Alloys Compd. 504 (2010) S323–S327.

[42] H.V. Atkinson, S. Davies, Fundamental aspects of hot isostatic pressing: an overview, Metall. Mater. Trans. A. 31 (2000) 2981–3000.

[43] S. Billard, J.P. Fondère, B. Bacroix, G.F. Dirras, Macroscopic and microscopic aspects of the deformation and fracture mechanisms of ultrafine-grained aluminum processed by hot isostatic pressing, Acta Mater. 54 (2006) 411–421.

[44] V.A. Mamedov, Spark Plasma Sintering (SPS) as advanced powder metallurgy sintering method, Powder Metall. ProgressSlovak Repub. 2 (2002) 32–43.

[45] N. Chawake, P. Ghosh, L. Raman, A.K. Srivastav, T. Paul, S.P. Harimkar, J. Eckert, R.S. Kottada, Estimation of diffusivity from densification data obtained during spark plasma sintering, Scr. Mater. 161 (2019) 36–39.

[46] N. Chawake, L.D. Pinto, A.K. Srivastav, K. Akkiraju, B.S. Murty, R.S. Kottada, On Joule heating during spark plasma sintering of metal powders, Scr. Mater. 93 (2014) 52–55.

[47] J.M. Frei, U. Anselmi-Tamburini, Z.A. Munir, Current effects on neck growth in the sintering of copper spheres to copper plates by the pulsed electric current method, J. Appl. Phys. 101 (2007) 114914.

[48] E. Olevsky, L. Froyen, Constitutive modeling of spark-plasma sintering of conductive materials, Scr. Mater. 55 (2006) 1175–1178.

[49] Z. Trzaska, R. Cours, J.-P. Monchoux, Densification of Ni and TiAl by SPS: kinetics and microscopic mechanisms, Metall. Mater. Trans. A. 49 (2018) 4849–4859.

[50] A. Al-Qudsi, M. Kammler, A. Bouguecha, C. Bonk, B.-A. Behrens, Comparison between different numerical models of densification during solid-state sintering of pure aluminium powder, Prod. Eng. 9 (2015) 11–24.

[51] G. Dirras, S. Bouvier, J. Gubicza, B. Hasni, T. Szilágyi, Mechanical characteristics under monotonic and cyclic simple shear of spark plasma sintered ultrafine-grained nickel, Mater. Sci. Eng. A. 526 (2009) 201–210.

[52] G. Marnier, C. Keller, J. Noudem, E. Hug, Functional properties of a spark plasma sintered ultrafine-grained 316L steel, Mater. Des. 63 (2014) 633–640.

[53] T. Borkar, R. Banerjee, Influence of spark plasma sintering (SPS) processing parameters on microstructure and mechanical properties of nickel, Mater. Sci. Eng. A. 618 (2014) 176–181.

[54] C. Keller, K. Tabalaiev, G. Marnier, J. Noudem, X. Sauvage, E. Hug, Influence of spark plasma sintering conditions on the sintering and functional properties of an ultra-fine grained 316L stainless steel obtained from ball-milled powder, Mater. Sci. Eng. A. 665 (2016) 125–134.

[55] C. Keller, G. Marnier, K. Tabalaiev, E. Hug, J. Noudem, Spark plasma sintering of ultrafine grained AISI 316L and functional properties characterization, (2015).

[56] Z.H. Zhang, F.C. Wang, S.K. Lee, Y. Liu, J.W. Cheng, Y. Liang, Microstructure characteristic, mechanical properties and sintering mechanism of nanocrystalline copper obtained by SPS process, Mater. Sci. Eng. A. 523 (2009) 134–138.

[57] U. Erb, Electrodeposited nanocrystals: synthesis, properties and industrial applications, NanoStructured Mater. 6 (1995) 533–538.

[58] B. Lü, Z. Hu, X. Wang, B. Xu, Thermal stability of electrodeposited nanocrystalline nickel assisted by flexible friction, Trans. Nonferrous Met. Soc. China. 25 (2015) 3297–3304.

[59] J.-M. Song, J.-S. Lee, Self-assembled nanostructured resistive switching memory devices fabricated by templated bottom-up growth, Sci. Rep. 6 (2016) 18967.

[60] F. Dalla Torre, H. Van Swygenhoven, M. Victoria, Nanocrystalline electrodeposited Ni: microstructure and tensile properties, Acta Mater. 50 (2002) 3957–3970.

[61] U. Klement, U. Erb, A.M. El-Sherik, K.T. Aust, Thermal stability of nanocrystalline Ni, Mater. Sci. Eng. A. 203 (1995) 177–186.

[62] J. Kacher, I.M. Robertson, M. Nowell, J. Knapp, K. Hattar, Study of rapid grain boundary migration in a nanocrystalline Ni thin film, Mater. Sci. Eng. A. 528 (2011) 1628–1635.

[63] K. Hattar, D.M. Follstaedt, J.A. Knapp, I.M. Robertson, Defect structures created during abnormal grain growth in pulsed-laser deposited nickel, Acta Mater. 56 (2008) 794–801.

[64] K.S. Kumar, S. Suresh, M.F. Chisholm, J.A. Horton, P. Wang, Deformation of electrodeposited nanocrystalline nickel, Acta Mater. 51 (2003) 387–405.

[65] C. Gu, J. Lian, Z. Jiang, Q. Jiang, Enhanced tensile ductility in an electrodeposited nanocrystalline Ni, Scr. Mater. 54 (2006) 579–584.

[66] N. Krasilnikov, W. Lojkowski, Z. Pakiela, R. Valiev, Tensile strength and ductility of ultra-fine-grained nickel processed by severe plastic deformation, Mater. Sci. Eng. A. 397 (2005) 330–337.

[67] Y. Wang, M. Chen, F. Zhou, E. Ma, High tensile ductility in a nanostructured metal, Nature. 419 (2002) 912–915.

[68] Y.T. Zhu, X. Liao, Nanostructured metals: retaining ductility, Nat. Mater. 3 (2004) 351.

[69] X. Shen, J. Lian, Z. Jiang, Q. Jiang, The Optimal Grain Sized Nanocrystalline Ni with High Strength and Good Ductility Fabricated by a Direct Current Electrodeposition, Adv. Eng. Mater. 10 (2008) 539–546.

[70] W.F. Hosford, Mechanical behavior of materials, Cambridge University Press, Cambridge; New York, 2010.

[71] Y.T. Zhu, X.L. Wu, Ductility and plasticity of nanostructured metals: differences and issues, Mater. Today Nano. 2 (2018) 15–20.

[72] A. Considère, Mémoire sur l'emploi du fer et de l'acier dans les constructions, Ann. Ponts Chaussées. IX (1885) 574–775.

[73] C.Y. Yu, P.W. Kao, C.P. Chang, Transition of tensile deformation behaviors in ultrafine-grained aluminum, Acta Mater. 53 (2005) 4019–4028.

[74] E. Ma, Instabilities and ductility of nanocrystalline and ultrafine-grained metals, Scr. Mater. 49 (2003) 663–668.

[75] S. Cheng, J.A. Spencer, W.W. Milligan, Strength and tension/compression asymmetry in nanostructured and ultrafine-grain metals, Acta Mater. 51 (2003) 4505–4518.

[76] R.W. Hayes, D. Witkin, F. Zhou, E.J. Lavernia, Deformation and activation volumes of cryomilled ultrafine-grained aluminum, Acta Mater. 52 (2004) 4259–4271.

[77] D. Jia, M. Wang, K.T. Ramesh, E. Ma, Deformation behavior and plastic instabilities of ultrafine-grained titanium, Appl. Phys. Lett. 79 (2001) 611.

[78] A. Hasnaoui, H. Van Swygenhoven, P.M. Derlet, On non-equilibrium grain boundaries and their effect on thermal and mechanical behaviour: a molecular dynamics computer simulation, Acta Mater. 50 (2002) 3927–3939.

[79] L. Lu, S. Yongfeng, X. Chen, L. Qian, K. Lu, Ultrahigh Strength and High Electrical Conductivity in Copper, Science. 304 (2004) 422–426.

[80] L. Lu, R. Schwaiger, Z.W. Shan, M. Dao, K. Lu, S. Suresh, Nano-sized twins induce high rate sensitivity of flow stress in pure copper, Acta Mater. 53 (2005) 2169–2179.

[81] N. Tsuji, Y. Ito, Y. Saito, Y. Minamino, Strength and ductility of ultrafine grained aluminum and iron produced by ARB and annealing, Scr. Mater. 47 (2002) 893–899.

[82] T.G. Langdon, Achieving superplasticity in ultrafine-grained metals, Mech. Mater. 67 (2013) 2–8.

[83] M. Kawasaki, T.G. Langdon, Review: achieving superplastic properties in ultrafine-grained materials at high temperatures, J. Mater. Sci. 51 (2016) 19–32.

[84] F. Naimi, L. Minier, S. Le Gallet, H. Couque, F. Bernard, Dense Nanostructured Nickel Produced by SPS from Mechanically Activated Powders: Enhancement of Mechanical Properties, J. Nanomater. 2013 (2013) 1–11.

[85] E.O. Hall, The deformation and ageing of mild steel: III discussion of results, Proc. Phys. Soc. Sect. B. 64 (1951) 747.

[86] S.S. Quek, Z.H. Chooi, Z. Wu, Y.W. Zhang, D.J. Srolovitz, The inverse hall–petch relation in nanocrystalline metals: A discrete dislocation dynamics analysis, J. Mech. Phys. Solids. 88 (2016) 252–266.

[87] J.R. Weertman, Hall-Petch strengthening in nanocrystalline metals, Mater. Sci. Eng. A. 166 (1993) 161–167.

[88] R.Z. Valiev, Superior strength in ultrafine-grained materials produced by SPD processing, Mater. Trans. 55 (2014) 13–18.

[89] K.N. Zhu, A. Godfrey, N. Hansen, X.D. Zhang, Microstructure and mechanical strength of near- and sub-micrometre grain size copper prepared by spark plasma sintering, Mater. Des. 117 (2017) 95–103.

[90] C. Xiao, R.A. Mirshams, S.H. Whang, W.M. Yin, Tensile behaviour and fracture in nickel and carbon doped nanocrystalline nickel, MaAterials Sci. Eng. A. 301 (2001) 35–43.

[91] F. Ebrahimi, G.R. Bourne, M.S. Kelly, T.E. Matthews, Mechanical properties of nanocrystalline nickel produced by electrodeposition, Nanostructured Mater. 11 (1999) 343–350.

[92] Q.-H. Bui, Polycristaux à grains ultrafins élaborés par métallurgie des poudres: microstructure, propriétés mécaniques et modélisation micromécanique, Paris 13, 2008.

[93] C. Keller, E. Hug, Hall–Petch behaviour of Ni polycrystals with a few grains per thickness, Mater. Lett. 62 (2008) 1718–1720.

[94] X. Feaugas, H. Haddou, Grain-size effects on tensile behavior of nickel and AISI 316L stainless steel, Metall. Mater. Trans. A. 34 (2003) 2329–2340.

[95] A.P. Zhilyaev, I. Shakhova, A. Belyakov, R. Kaibyshev, T.G. Langdon, Wear resistance and electroconductivity in copper processed by severe plastic deformation, Wear. 305 (2013) 89–99.

[96] R.Z. Valiev, Y. Estrin, Z. Horita, T.G. Langdon, M.J. Zehetbauer, Y. Zhu, Producing Bulk Ultrafine-Grained Materials by Severe Plastic Deformation: Ten Years Later, JOM. 68 (2016) 1216–1226.

[97] T. Nishizaki, S. Lee, Z. Horita, T. Sasaki, N. Kobayashi, Superconducting properties in bulk nanostructured niobium prepared by high-pressure torsion, Phys. C. 493 (2013) 132–135.

[98] H. Miyamoto, Corrosion of Ultrafina Grained Materials by Severe Plastic Deformation, Mater. Trans. 57 (2016) 559–572.

[99] K.D. Ralston, N. Birbilis, C.H.J. Davis, Revealing the relationship between grain size and corrosion rate of metals, Scr. Mater. 63 (2010) 1201–1204.

[100] L. Qin, J. Lian, Q. Jiang, Effect of grain size on corrosion behavior of electrodeposited bulk nanocrystalline Ni, Trans. Nonferrous Met. Soc. China. 20 (2010) 82–89.

[101] P. Herrasti, C. Ponce de Léon, F.C. Walsh, The corrosion behaviour of nanograined metals and alloys, Rev. Metal. 48 (2012) 377–394.

[102] D.B. Bober, A. Khalajhedayati, M. Kumar, T.J. Rupert, Grain Boundary Character Distributions in Nanocrystalline Metals Produced by Different Processing Routes, Metall. Mater. Trans. A. 47 (2016) 1389–1403.

[103] P. Lejček, Grain boundaries: description, structure and thermodynamics, in: Grain Bound. Segreg. Met., Springer, 2010: pp. 5–24.

[104] T.-T. Fang, Two-Dimensional (Interfaces) and Three-Dimensional (Second Phases) Imperfections in Solids, in: Elem. Struct. Defects Cryst. Mater., Elsevier, 2018: pp. 169–197.

[105] W.T. Read, W. Shockley, Dislocation models of crystal grain boundaries, Phys. Rev. 78 (1950) 275.

[106] M. Weins, B. Chalmers, H. Gleiter, M. Ashby, Structure of high angle grain boundaries, Scr. Metall. 3 (1969) 601–604.

[107] F.J. Humphreys, M. Hatherly, Recrystallization and related annealing phenomena, 2. ed., 2nd impr, Elsevier, Oxford, 2004.

[108] A.H. King, S. Shekhar, What does it mean to be special? The significance and application of the Brandon criterion, J. Mater. Sci. 41 (2006) 7675–7682.

[109] V. Randle, The coincidence site lattice and the 'sigma enigma,' Mater. Charact. 47 (2001) 411–416.

[110] F. Dalla Torre, P. Spatig, R. Schaublin, M. Victoria, Deformation behaviour and microstructure of nanocrystalline electrodeposited and high pressure torsioned nickel, Acta Mater. 53 (2005) 2337–2349.

[111] G.K. Williamson, R.E. Smallman, III. Dislocation densities in some annealed and cold-worked metals from measurements on the X-ray debye-scherrer spectrum., Philos. Mag. J. Theor. Exp. Appl. Phys. 1 (1956) 34–46.

[112] X. Feaugas, H. Haddou, Effects of grain size on dislocation organization and internal stresses developed under tensile loading in fcc metals, Philos. Mag. 87 (2007) 989–1018.

[113] A.P. Zhilyaev, B.-K. Kim, G.V. Nurislamova, M.D. Baró, J.A. Szpunar, T.G. Langdon, Orientation imaging microscopy of ultrafine-grained nickel, Scr. Mater. 46 (2002) 575–580.

[114] J. Gubicza, H.-Q. Bui, F. Fellah, G.F. Dirras, Microstructure and mechanical behavior of ultrafine-grained Ni processed by different powder metallurgy methods, J. Mater. Res. 24 (2009) 217–226.

[115] J.K. Mackenzie, Second paper on statistics associated with the random disorientation of cubes, Biometrika. 45 (1958) 229–240.

[116] S.V. Divinski, J. Ribbe, G. Reglitz, Y. Estrin, G. Wilde, Percolating network of ultrafast transport channels in severely deformed nanocrystalline metals, J. Appl. Phys. 106 (2009) 063502.

[117] D. Prokoshkina, L. Klinger, A. Moros, G. Wilde, E. Rabkin, S.V. Divinski, Persistence of ultrafast atomic diffusion paths in recrystallizing ultrafine grained Ni, Scr. Mater. 101 (2015) 91–94.

[118] H.W. Zhang, X. Huang, R. Pippan, N. Hansen, Thermal behavior of Ni (99.967% and 99.5% purity) deformed to an ultra-high strain by high pressure torsion, Acta Mater. 58 (2010) 1698–1707.

[119] E. Schafler, R. Pippan, Effect of thermal treatment on microstructure in high pressure torsion (HPT) deformed nickel, Mater. Sci. Eng. A. 387–389 (2004) 799–804.

[120] Y.R. Kolobov, G.P. Grabovetskaya, M.B. Ivanov, A.P. Zhilyaev, R.Z. Valiev, Grain boundary diffusion characteristics of nanostructured nickel, Scr. Mater. 44 (2001) 873–878.

[121] H. Mehrer, Diffusion in solids: fundamentals, methods, materials, diffusion-controlled processes, Springer Science & Business Media, 2007.

[122] P. Heitjans, J. Kärger, eds., Diffusion in Condensed Matter, Springer-Verlag Berlin Heidelberg, 2005.

[123] S.V. Divinski, Grain Boundary Diffusion in Severely Deformed Metals: State of the Art and Unresolved Issues, Diffus. Found. 5 (2015) 57–73.

[124] S.V. Divinski, G. Reglitz, G. Wilde, Grain boundary self-diffusion in polycrystalline nickel of different purity levels, Acta Mater. 58 (2010) 386–395.

[125] S.V. Divinski, G. Reglitz, H. Rösner, Y. Estrin, G. Wilde, Ultra-fast diffusion channels in pure Ni severely deformed by equal-channel angular pressing, Acta Mater. 59 (2011) 1974–1985.

[126] S.V. Divinski, G. Reglitz, I.S. Golovin, M. Peterlechner, R. Lapovok, Y. Estrin, G. Wilde, Effect of heat treatment on diffusion, internal friction, microstructure and mechanical properties of ultra-fine-grained nickel severely deformed by equal-channel angular pressing, Acta Mater. 82 (2015) 11–21.

[127] G. Wilde, J. Ribbe, M. Wegner, H. Rösner, Y. Estrin, M.J. Zehetbauer, D. Setman, S.V. Divinski, Plasticity and Grain Boundary Diffusion at Small Grain Sizes, Adv. Eng. Mater. 12 (2010) 758–764.

[128] V.V. Popov, E.N. Popova, D.D. Kuznetsov, A.V. Stolbovsky, E.V. Shorohov, P.A. Nasonov, K.A. Gaan, G. Reglitz, S.V. Divinski, G. Wilde, Evolution of Ni structure at dynamic channel-angular pressing, Mater. Sci. Eng. A. 585 (2013) 281–291.

[129] K. Sitarama Raju, M. Ghanashyam Krishna, K.A. Padmanabhan, V. Subramanya Sarma, N.P. Gurao, G. Wilde, Microstructure evolution and hardness variation during annealing of equal channel angular pressed ultra-fine grained nickel subjected to 12 passes, J. Mater. Sci. 46 (2011) 2662–2671.

[130] Y. Jin, B. Lin, M. Bernacki, G.S. Rohrer, A.D. Rollett, N. Bozzolo, Annealing twin development during recrystallization and grain growth in pure nickel, Mater. Sci. Eng. A. 597 (2014) 295–303.

[131] L. Mond, C. Langer, F. Quincke, L.—Action of carbon monoxide on nickel, J. Chem. Soc. Trans. 57 (1890) 749–753.

[132] A. Arias, The Role of Chemical Reactions in the Mechanism of Comminution of Ductile Metals into Ultrafine Powders by grinding, NASA Tech. Note. D-4862 (1968).

[133] A. Arias, Chemical reactions of metal powders with organic and inorganic liquids during ball milling, NASA Tech. Note. D-8015 (1975).

[134] W. Chen, U. Anselmi-Tamburini, J.E. Garay, J.R. Groza, Z.A. Munir, Fundamental investigations on the spark plasma sintering/synthesis process, Mater. Sci. Eng. A. 394 (2005) 132–138.

[135] M. Omori, Sintering, consolidation, reaction and crystal growth by the spark plasma system (SPS), Mater. Sci. Eng. A. 287 (2000) 183–188.

[136] R. Marder, C. Estournès, G. Chevallier, R. Chaim, Plasma in spark plasma sintering of ceramic particle compacts, Scr. Mater. 82 (2014) 57–60.

[137] O. Yanagisawa, H. Kuramoto, K. Matsugi, M. Komatsu, Observation of particle behavior in copper powder compact during pulsed electric discharge, Mater. Sci. Eng. A. 350 (2003) 184–189.

[138] T.B. Britton, J. Jiang, Y. Guo, A. Vilalta-Clemente, D. Wallis, L.N. Hansen, A. Winkelmann, A.J. Wilkinson, Tutorial: Crystal orientations and EBSD — Or which way is up?, Mater. Charact. 117 (2016) 113–126.

[139] V. Randle, Electron backscatter diffraction: Strategies for reliable data acquisition and processing, Mater. Charact. 60 (2009) 913–922.

[140] A. Winkelmann, Simulation of Electron Backscatter Diffraction Patterns, Microsc. Microanal. 13 (2007).

[141] Y. Jin, M. Bernacki, G.S. Rohrer, A.D. Rollett, B. Lin, N. Bozzolo, Formation of annealing twins during recrystallization and grain growth in 304L austenitic stainless steel, Mater. Sci. Forum. 753 (2013) 113–116.

[142] L.N. Brewer, D.P. Field, C.C. Merriman, Mapping and Assessing Plastic Deformation Using EBSD, in: Electron Backscatter Diffr. Mater. Sci., Springer Science & Business Media, 2009.

[143] D.P. Field, L.T. Bradford, M. Nowell, T.M. Lillo, The role of annealing twins during recrystallization of Cu, Acta Mater. 55 (2007) 4233–4241.

[144] S.I. Wright, M.M. Nowell, D.P. Field, A Review of Strain Analysis Using Electron Backscatter Diffraction, Microsc. Microanal. 17 (2011) 316–329.

[145] Y. Sakakibara, K. Kubushiro, Stress Evaluation at the Maximum Strained State by EBSD and Several Residual Stress Measurements for Plastic Deformed Austenitic, World J. Mech. 7 (2017) 195–210.

[146] C.D. Landon, B.L. Adams, J. Kacher, High-Resolution Methods for Characterizing Mesoscale Dislocation Structures, J. Eng. Mater. Technol. 130 (2008) 1–5.

[147] W. Wang, Etude des mécanismes de recristallisation de nouveaux alliages à base de Ni, Université Paris-Sud, 2014.

[148] S. Naghdy, P. Verleysen, R. Petrov, L. Kestens, Resolving the geometrically necessary dislocation content in severely deformed aluminum by transmission Kikuchi diffraction, Mater. Charact. 140 (2018) 225–232.

[149] J.P. Hirth, J. Lothe, Theory of dislocations, 2. ed., reprint, Krieger Publishing Company, Malabar, Fla, 1992.

[150] D.B. Williams, C.B. Carter, Transmission electron microscopy: a textbook for materials science, 2. ed, Springer, New York, 2009.

[151] Y.F. Zhang, L. Lu, S.M. Yap, Prediction of the amount of PCA for mechanical milling, J. Mater. Process. Technol. 89 (1999) 260–265.

[152] L. Shaw, J. Villegas, H. Luo, M. Zawrah, D. Miracle, Effects of process-control agents on mechanical alloying of nanostructured aluminum alloys, Metall. Mater. Trans. A. 34 (2003) 159–170.

[153] R.M.L. Neto, R.B. Falcão, E.D.C.C. Dammann, C.J. da Rocha, An Investigation on the High-Energy Ball Milling of Iron-Titanium Powder Mixtures without Process Control Agents, in: Proc. 2010 World Congr. Powder Metall. Part. Mater. Florence, 2010.

[154] L. Lü, M.O. Lai, Mechanical Alloying, Springer Science & Business Media, 1998.

[155] G.K. Williamson, W.H. Hall, X-Ray line broadening from filed aluminum and wolfram, Acta Metall. 1 (1953) 22–31.

[156] W.H. Hall, G.K. Williamson, The diffraction pattern of cold worked metals: II Changes in integrated intensity, Proc. Phys. Soc. Sect. B. 64 (1951) 946–953.

[157] S.S. Razavi-Tousi, J.A. Szpunar, Effect of ball size on steady state of aluminum powder and efficiency of impacts during milling, Powder Technol. 284 (2015) 149–158.

[158] B.B. Panigrahi, Sintering and grain growth kinetics of ball milled nanocrystalline nickel powder, Mater. Sci. Eng. A. 460–461 (2007) 7–13.

[159] B. Flipon, C. Keller, L. Garcia de la Cruz, E. Hug, F. Barbe, Tensile properties of spark plasma sintered AISI 316L stainless steel with unimodal and bimodal grain size distributions, Mater. Sci. Eng. A. 729 (2018) 249–256.

[160] P.P. Bhattacharjee, S.K. Sinha, A. Upadhyaya, Effect of sintering temperature on grain boundary character distribution in pure nickel, Scr. Mater. 56 (2007) 13–16.

[161] G.-D. Dutel, P. Langlois, D. Tingaud, G. Dirras, Room-temperature deformation micro-mechanisms of polycrystalline nickel processed by spark plasma sintering, Mater. Charact. 79 (2013) 76–83.

[162] G.B. Schaffer, P.G. McCormick, On the kinetics of mechanical alloying, Metall. Trans. A. 23 (1992) 1285–1290.

[163] C.B. Thomson, V. Randle, A study of twinning in nickel, Scr. Mater. 35 (1996) 385–390.

[164] J.L. Bair, S.L. Hatch, D.P. Field, Formation of annealing twin boundaries in nickel, Scr. Mater. 81 (2014) 52–55.

[165] R.D. Doherty, D.A. Hughes, F.J. Humphreys, J.J. Jonas, D.J. Jensen, M.E. Kassner, W.E. King, T.R. McNelley, H.J. McQueen, A.D. Rollett, Current issues in recrystallization: A review, Mater. Today. 1 (1998) 14–15.

[166] D. Horton, C.B. Thomson, V. Randle, Aspects of twinning and grain growth in high purity and commercially pure nickel, Mater. Sci. Eng. A. 203 (1995) 408–414.

[167] S. Mahajan, C.S. Pande, M.A. Imam, B.B. Rath, Formation of annealing twins in fcc crystals, Acta Mater. 45 (1997) 2633–2638.

[168] H. Gleiter, The formation of annealing twins, Acta Metall. 17 (1969) 1421–1428.

[169] V. Randle, P.R. Rios, Y. Hu, Grain growth and twinning in nickel, Scr. Mater. 58 (2008) 130–133.

[170] C.S. Pande, M.A. Imam, B.B. Rath, Study of annealing twins in FCC metals and alloys, Metall. Trans. A. 21 (1990) 2891–2896.

[171] N. Liang, Y. Zhao, Y. Li, T. Topping, Y. Zhu, R.Z. Valiev, E.J. Lavernia, Influence of microstructure on thermal stability of ultrafine-grained Cu processed by equal channel angular pressing, J. Mater. Sci. 53 (2018) 13173–13185.

[172] Y. Huang, F.J. Humphreys, Subgrain growth and low angle boundary mobility in aluminium crystals of orientation {110}〈001〉, Acta Mater. 48 (2000) 2017–2030.

[173] C. Keller, Etude expérimentale des transitions volume/surface des propriétés mécaniques du nickel polycristallin de haute pureté, Université de Caen Basse-Normandie, 2009.

[174] A.D. Rollett, F. Kocks, A Review of the Stages of Work Hardening, Solid State Phenom. 36–37 (1993) 1–18.

[175] H. Mecking, U.F. Kocks, Kinetics of flow and strain-hardening, Acta Metall. 29 (1981) 1865–1875.

[176] T. dos Santos, P.A.R. Rosa, S. Maghous, R. Rossi, A simplified approach to high strain rate effects in cold deformation of polycrystalline FCC metals: Constitutive formulation and model calibration, Int. J. Plast. 82 (2016) 76–96.

[177] G.I. Taylor, Plastic strain in metals., (1938).

[178] M.F. Ashby, The deformation of plastically non-homogeneous materials, Philos. Mag. 21 (1970) 399–424.

[179] H. Mughrabi, Dislocation wall and cell structures and long-range internal stresses in deformed metal crystals, Acta Metall. 31 (1983) 1367–1379.

[180] Y.Z. Tian, S. Gao, L.J. Zhao, S. Lu, R. Pippan, Z.F. Zhang, N. Tsuji, Remarkable transitions of yield behavior and Lüders deformation in pure Cu by changing grain sizes, Scr. Mater. 142 (2018) 88–91.

[181] S. Gao, Y. Bai, R. Zheng, Y. Tian, W. Mao, A. Shibata, N. Tsuji, Mechanism of huge Lüders-type deformation in ultrafine grained austenitic stainless steel, Scr. Mater. 159 (2019) 28–32.

[182] J.R. Davis, Properties and Selection: Nonferrous Alloys and Special-Purpose Materials, ASM International, 1990.

[183] K.G. Samuel, Limitations of Hollomon and Ludwigson stress-strain relations in assessing the strain hardening parameters, J. Phys. Appl. Phys. 39 (2006) 203–212.

[184] D.V. Wilson, Relationships between microstructure and behaviour in the uniaxial tensile test, J. Phys. Appl. Phys. 7 (1974) 954.

[185] A.W. Bowen, P.G. Partridge, Limitations of the Hollomon strain-hardening equation, J. Phys. Appl. Phys. 7 (1974) 969.

[186] U.F. Kocks, H. Mecking, Physics and phenomenology of strain hardening: the FCC case, Prog. Mater. Sci. 48 (2003) 171–273.

[187] D. Kuhlmann-Wilsdorf, Theory of plastic deformation:-properties of low energy dislocation structures, Mater. Sci. Eng. A. 113 (1989) 1–41.

[188] L. Kubin, B. Devincre, T. Hoc, Modeling dislocation storage rates and mean free paths in face-centered cubic crystals, Acta Mater. 56 (2008) 6040–6049.

[189] L. Jordan, W.H. Swanger, The properties of pure nickel, Bur. Stand. J Res Doi. 10 (1930) 6028.

[190] T. Narutani, J. Takamura, Grain-size strengthening in terms of dislocation density measured by resistivity, Acta Metall. Mater. 39 (1991) 2037–2049.

[191] B. Devincre, T. Hoc, L. Kubin, Dislocation Mean Free Paths and Strain Hardening of Crystals, Science. 320 (n.d.) 1745–1748.

[192] P.A. Dubos, Influence de la témperature et du trajet de chargement sur les transitions volume/surafec des méteaux cubiques à faces centrées, Université de Caen Basse-Normandie, 2013.

[193] D.J. Jensen, A.W. Thompson, N. Hansen, The role of grain size and strain in work hardening and texture development, Metall. Trans. A. 20 (1989) 2803–2810.

[194] H.-H. Fu, D.J. Benson, M.A. Meyers, Analytical and computational description of effect of grain size on yield stress of metals, Acta Mater. 49 (2001) 2567–2582.

[195] B. Bay, N. Hansen, D.A. Hughes, D. Kuhlmann-Wilsdorf, Overview no. 96 evolution of fcc deformation structures in polyslip, Acta Metall. Mater. 40 (1992) 205–219.

[196] D. Kuhlmann-Wilsdorf, N. Hansen, Geometrically necessary, incidental and subgrain boundaries, Scr. Metall. Mater. 25 (1991) 1557–1562.

[197] A.A.W. Thompson, Yielding in nickel as a function of grain or cell size, Acta Metall. 23 (1975) 1337–1342.

[198] Y. Zhao, T. Topping, J.F. Bingert, J.J. Thornton, A.M. Dangelewicz, Y. Li, W. Liu, Y. Zhu, Y. Zhou, E.J. Lavernia, High Tensile Ductility and Strength in Bulk Nanostructured Nickel, Adv. Mater. 20 (2008) 3028–3033.

[199] R.S. Barnes, Diffusion of copper along the grain boundaries of nickel, Nature. 166 (1950) 1032.

[200] J.C. Fisher, Calculation of Diffusion Penetration Curves for Surface and Grain Boundary Diffusion, J. Appl. Phys. 22 (1951) 74–77.

[201] A. Paul, T. Laurila, V. Vuorinen, S.V. Divinski, Thermodynamics, Diffusion and Kirkendall Effect in Solids, Springer International Publishing Switzerland, 2014.

[202] R.T.P. Whipple, CXXXVIII. Concentration contours in grain boundary diffusion, Philos. Mag. Ser. 7. 45 (1954) 1225–1236.

[203] T. Suzuoka, Exact Solutions of Two Ideal Cases in Grain Boundary Diffusion Problem and the Application to Sectioning Method, J. Phys. Soc. Jpn. 19 (1964) 839–851.

[204] A. Le Claire, The analysis of grain boundary diffusion, Br. J. Appl. Phys. 14 (1963) 351–356.

[205] L.G. Harrison, Influence of dislocations on diffusion kinetics in solids with particular reference to the alkali halides, Trans. Faraday Soc. 57 (1961) 1191–1199.

[206] H. Gleiter, Diffusion in nanostructured metals, Phys. Status Solidi B. 172 (1992) 41–51.

[207] H. Tanimoto, L. Pasquini, R. Prümmer, H. Kronmüller, H.-E. Schaefer, Self-diffusion and magnetic properties in explosion densified nanocrystalline Fe, Scr. Mater. 42 (2000) 961–966.

[208] S.V. Divinski, F. Hisker, Y.S. Kang, J.S. Lee, C. Herzig, Tracer Diffusion of 63Ni in Nano-γ-FeNi Produced by Powder Metallurgical Method Systematic Investigations in the C, B, and A Diffusion Regimes, Interface Sci. 11 (2003) 67–80.

[209] S.V. Divinski, F. Hisker, Y.S. Kang, J.S. Lee, C. Herzig, 59Fe Grain boundary diffusion in nanostructured γ-Fe-Ni, Z Met. 93 (2002) 265–272.

[210] B.S. Bokstein, H.D. Bröse, L.I. Trusov, T.P. Khvostantseva, Diffusion in nanocrystalline nickel, Nanostructured Mater. 6 (1995) 873–876.

[211] W.A. Goddard, ed., Handbook of nanoscience, engineering, and technology, CRC Press, Boca Raton, 2003.

[212] D. Prokoshkina, L. Klinger, A. Moros, G. Wilde, E. Rabkin, S.V. Divinski, Effect of recrystallization on diffusion in ultrafine-grained Ni, Acta Mater. 69 (2014) 314–325.

[213] A.A. Nazarov, A.E. Romanov, R.Z. Valiev, Models of the defect structure and analysis of the mechanical behavior of nanocrystals, Nanostructured Mater. 6 (1995) 775–778.

[214] S. Poulat, B. Décamps, L. Priester, In-situ transmission electron microscopy study of the accomodation in [101] tilt grain boundaries in nickel bicrystals, Philos. Mag. A. 79 (1999) 2655–2680.

[215] A.A. Nazarov, Kinetics of grain boundary recovery in deformed polycrystals, Interface Sci. 8 (2000) 315–322.

[216] K. Maier, H. Mehrer, E. Lessmann, W. Schüle, Self-diffusion in nickel at low temperatures, Phys. Status Solidi B. 78 (1976) 689–698.

[217] Y. Amouyal, S.V. Divinski, Y. Estrin, E. Rabkin, Short-circuit diffusion in an ultrafine-grained copper–zirconium alloy produced by equal channel angular pressing, Acta Mater. 55 (2007) 5968–5979.

[218] J. Ribbe, D. Baither, G. Schmitz, S.V. Divinski, Ultrafast diffusion and internal porosity in ultrafine-grained copper–lead alloy prepared by equal channel angular pressing, Scr. Mater. 2009 (2009) 129–132.

[219] D. Prokoshkina, V.A. Esin, G. Wilde, S.V. Divinski, Grain boundary width, energy and self-diffusion in nickel Effect of material purity, Acta Mater. 61 (2013) 5188–5197.

[220] R. Klemm, E. Thiele, C. Holste, J. Eckert, N. Schell, Thermal stability of grain structure and defects in submicrocrystalline and nanocrystalline nickel, Scr. Mater. 46 (2002) 685–690.

[221] H.M. O'bryan, Sintering and expansion of HTSC ceramics, Thermochim. Acta. 174 (1991) 223–237.

[222] D.W. Johnson Jr, W.W. Rhodes, Retrograde densification in Bi2Sr2CaCu2O8 superconductors, J. Am. Ceram. Soc. 72 (1989) 2346–2350.

[223] R.L. Thayer, S.R. Schmidt, S.E. Dorris, J.W. Bullard, M.T. Lanagan, Reactive sintering and retrograde densification of bulk bismuth-based superconductors, J. Am. Ceram. Soc. 83 (2000) 2365–2368.

[224] E. Biguereau, D. Bouvard, J.M. Chaix, S. Roure, On the swelling of silver powder during sintering, Powder Metall. (2016) 1–7.

[225] C. Manière, E. Saccardo, G. Lee, J. McKittrick, A. Molinari, E.A. Olevsky, Swelling negation during sintering of sterling silver: An experimental and theoretical approach, Results Phys. 11 (2018) 79–84.

[226] Y.-J. Lin, K.-S. Hwang, Swelling of Copper Powders during Sintering of Heat Pipes in Hydrogen-Containing Atmospheres, Mater. Trans. 51 (2010) 2251–2258.

APPENDIX A: DETERMINATION OF STEREOGRAPHIC PROJECTIONS IN TEM

Frequently, investigations carried out with TEM demand the identification of grain orientation. Such is the case of dislocation related studies. To this aim, a stereographic projection of the grain is built, and its determination is presented in this appendix. In the stereographic projection or stereogram a sphere is projected onto a plane. By placing a crystal in the middle of the sphere we can obtain a two dimensional representation of the orientation of such crystal (Fig. A-1 (a)). Crystallographic planes are represented by their normal directions (the poles of the planes), as points in a surface where the angular relationship between them is preserved. The stereogram can be constructed using a special graph paper called Wulff net (Fig. A-1 (b)). It contains ninety great circles as the one shown in green in Fig. A-1 (a) that are 2° apart, with the primitive great circle being the only complete great circle in the net [150]. All distances in the real space correspond exactly to angles. This can be observed from the two poles located in the primitive great circle $0\bar{1}0$ and 010. They represent the normal direction of planes $(0\bar{1}0)$ and (010) and the angle between them is $90 \cdot 2° = 180°$. Thus, once the different poles are placed in the net, the projection will provide the sought information concerning the orientation of our crystal.

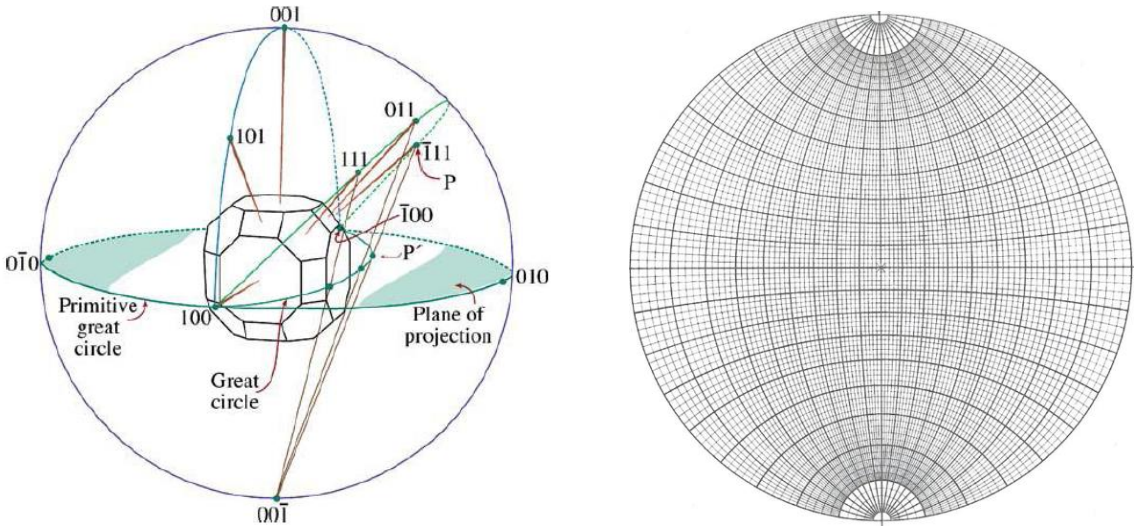

(a) (b)

Fig. A-1 Schematic representation of the principle of the stereographic projection [150] (a). The Wulff net (b).

To construct the stereographic projection at least two-zone axes of a single grain have to be identified. A zone axis is a direction that corresponds to an orientation of the crystal, which is parallel to the intersection of two or more planes. The planes are oriented edge-on and the direction corresponds to the incident direct beam direction [150]. The diffraction patterns of low index such as [001], [011] and [111], are highly symmetrical and easy to identify (Fig. A-2). To have access to different diffraction patterns

the sample has to be tilted in directions X and Y. The reference positions are X = 0 and Y = 0 (here the center of the Wulff net), and once a zone axis is reached the new values of X and Y are recorded.

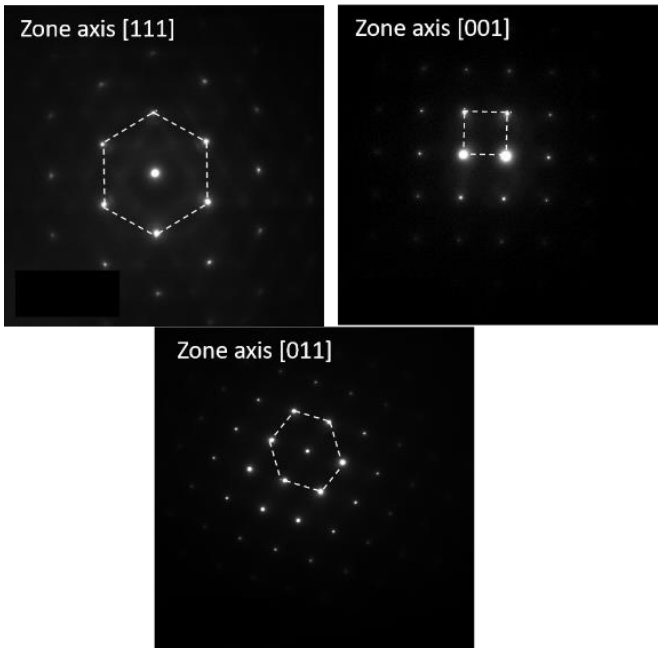

Fig. A-2 Characteristic diffraction pattern of zone axes type [111], [001] and [011] in FCC metals.

Once the diffraction patterns are identified, the pole corresponding to each zone axis can be placed in the Wulff net using the corresponding coordinates in X and Y. Let us consider a crystal of the same orientation as the one in Fig. A-1 (a), where the electron beam would be approximately parallel to [001] when the sample is in X = 0 and Y = 0. In such a case, zone axes [111], [011] and [001] would be placed in the Wulff net as displayed in Fig. A-3 (a). The symbol used to represent each zone axis corresponds to the rotational element of symmetry of the stereographic projections with a normal of [111], [011] and [001], respectively. To verify that a correct identification of the zone axes has been made, the angles between poles are measured using the lines in the net, where each small deformed square represent 2° and each big deformed square represents 10° (Fig. A-3 (a)-(b)).

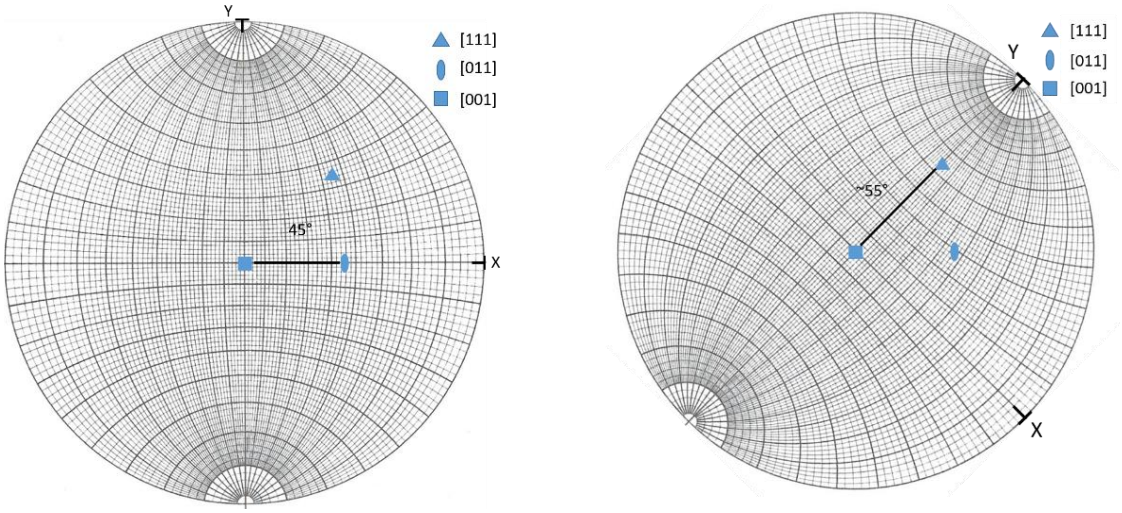

(a) (b)

Fig. A-3 Zone axes type [111], [011] and [001] represented in a Wulff net displaying, [001]^[011] = 45° (a) and [001]^[111] = 55° (b).

Afterwards, other poles are added, which can be inferred from symmetry operations using the initial determined poles and all poles are indexed with respect to a chosen direction (in this example [001]) as displayed in Fig. A-4 (a). Finally, lines connecting different poles are drawn representing the diffracting planes (Fig. A-4 (b)), situated at 90° of their corresponding normal directions. Once the stereographic projection of the grain is built, it can be used to find the best diffraction conditions for the study of dislocations or other defects in the material.

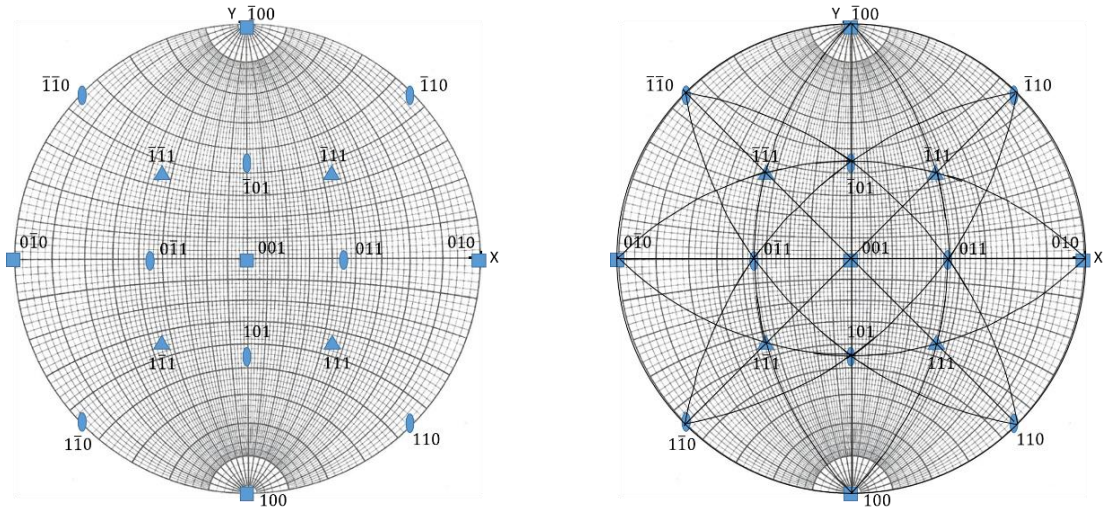

(a) (b)

Fig. A-4 Wulff net with indexed poles (a) and the final stereographic projection 001 (b).

APPENDIX B: X-RAY DIFRACTOGRAMS OF POWDERS

X-ray diffraction was performed systematically on powders to verify the absence of peaks corresponding to contaminants as well as the absence of preferred crystallographic texture. This appendix collects the diffractograms of the different powders used in this work.

- As-received powder (PC) (Fig. B-1).

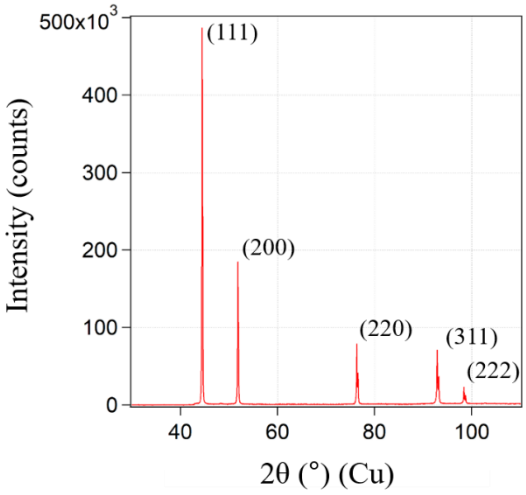

Fig. B-1 Diffractogram corresponding to powder PC.

- Ball-milled powder P1 (200 rpm, 1.5 h and 66.7 wt.% of PCA) (Fig. B-2).

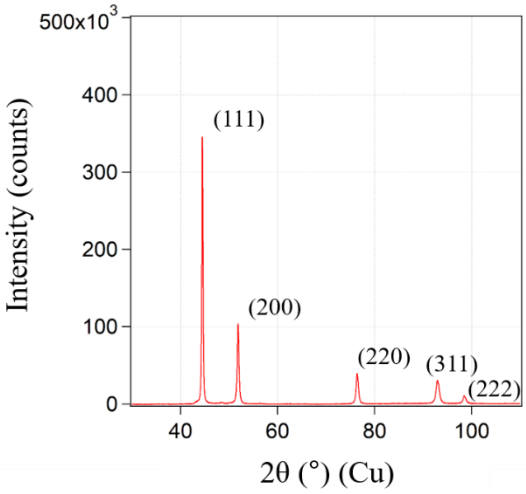

Fig. B-2 Diffractogram corresponding to powder P1.

- Ball-milled powder P2 (200 rpm, 3 h and 66.7 wt.% of PCA) (Fig. B-3).

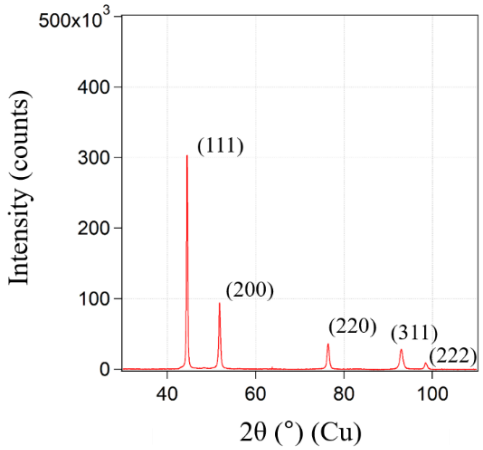

Fig. B-3 Diffractogram corresponding to powder P2.

- Ball-milled powder P3 (200 rpm, 6 h and 66.7 wt.% of PCA) (Fig. B-4).

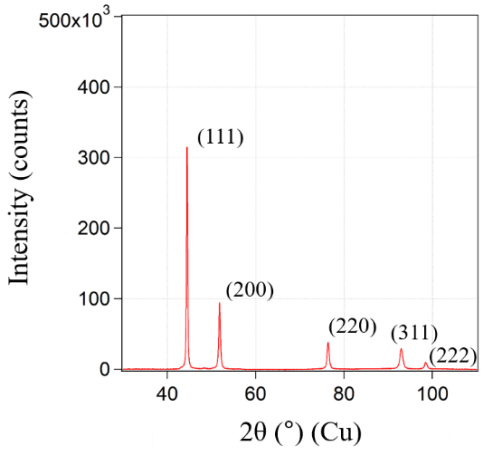

Fig. B-4 Diffractogram corresponding to powder P3.

- Ball-milled powder P4 (200 rpm, 12 h and 66.7 wt.% of PCA) (Fig. B-5).

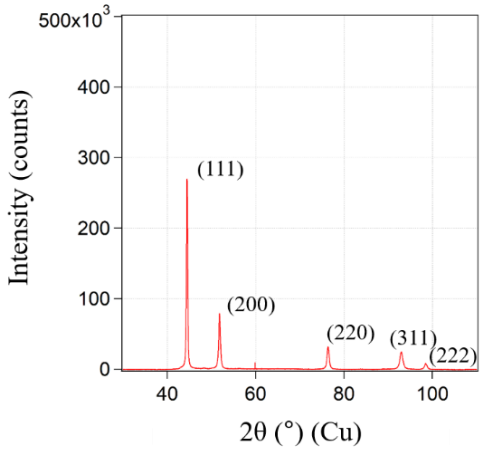

Fig. B-5 Diffractogram corresponding to powder P4.

- Ball-milled powder P5 (250 rpm, 3 h and 66.7 wt.% of PCA) (Fig. B-6).

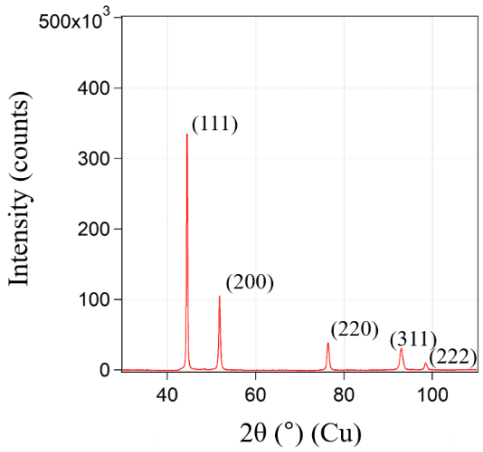

Fig. B-6 Diffractogram corresponding to powder P5.

- Ball-milled powder P6 (300 rpm, 3 h and 66.7 wt.% of PCA) (Fig. B-7).

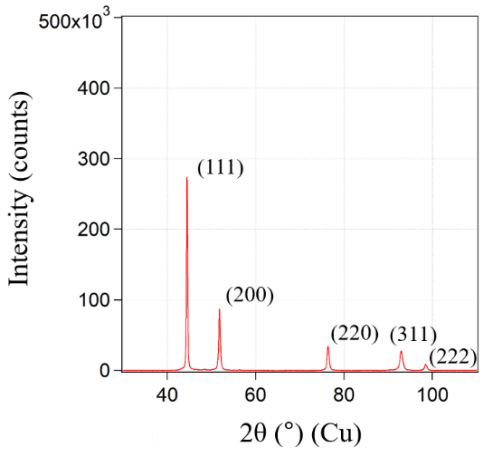

Fig. B-7 Diffractogram corresponding to powder P6.

- Ball-milled powder P7 (350 rpm, 3 h and 66.7 wt.% of PCA) (Fig. B-8).

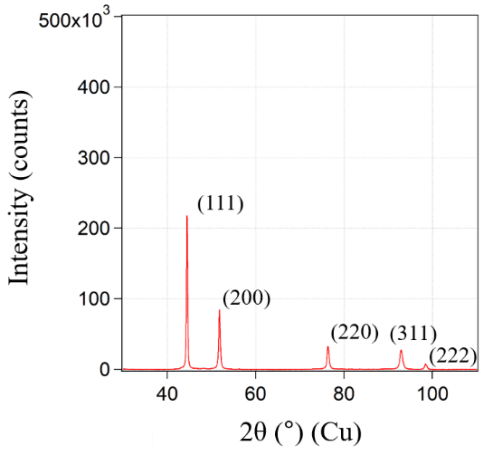

Fig. B-8 Diffractogram corresponding to powder P7.

- Ball-milled powder P8 (350 rpm, 3 h and 33.3 wt.% of PCA) (Fig. B-9).

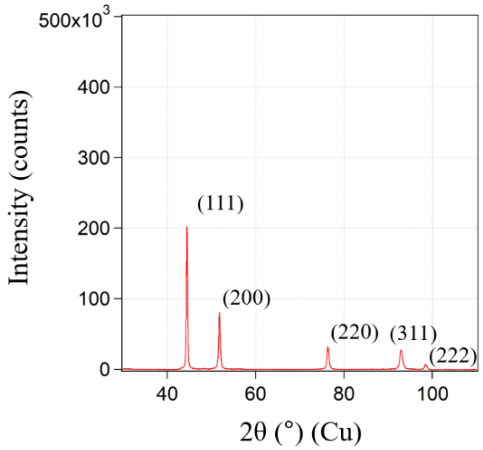

Fig. B-9 Diffractogram corresponding to powder P8.

- Ball-milled powder P9 (350 rpm, 3 h and 16.7 wt.% of PCA) (Fig. B-10).

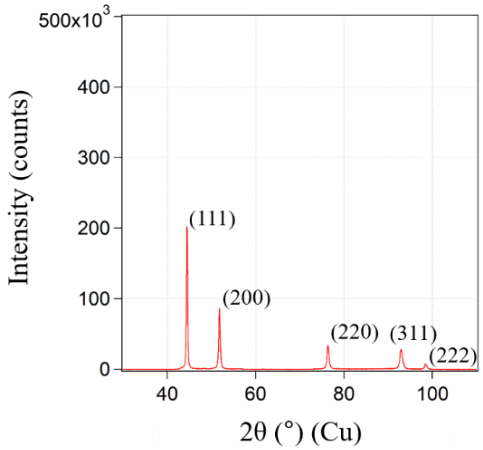

Fig. B-10 Diffractogram corresponding to powder P9.

- Ball-milled powder P10 (350 rpm, 3 h and 8.3 wt.% of PCA) (Fig. B-11).

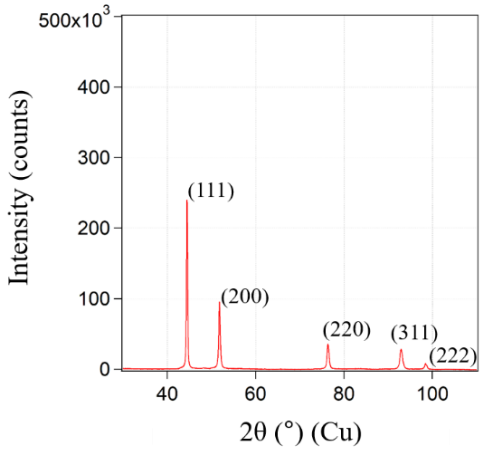

Fig. B-11 Diffractogram corresponding to powder P10.

- Ball-milled powder P0 (350 rpm, 10 h and 66.7 wt.% of PCA) (Fig. B-12).

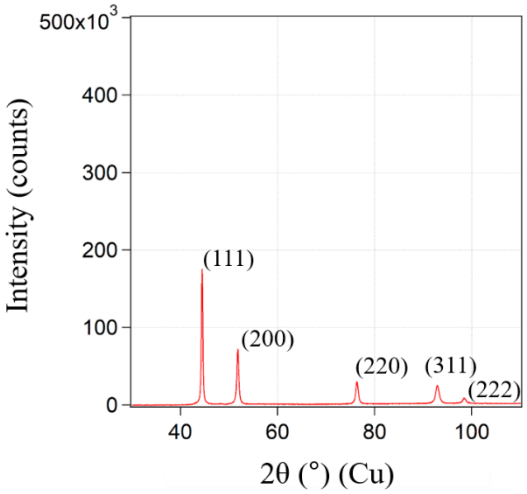

Fig. B-12 Diffractogram corresponding to powder P0.

APPENDIX C: MICROSTRUCTURAL FEATURES OF NICKEL SAMPLES PROCESSED BY SPS

In this appendix, the microstructural characteristics of the twelve samples investigated in Chapter III are collected. It includes for each sample: an orientation cartography in inverse pole figure (IPF) superimposed over the image quality (IQ), the grain size distribution, the CSL boundaries distribution and the misorientation angle distribution. The direction normal to the surface of the sample was taken as reference direction for the IPF cartography.

- Sample S-PC

Sample S-PC, processed from powder PC, has a relative density of 97.3 (5) % and displays equiaxed grains (Fig. C-1 (a)) with an average grain size of d = 3.5 µm ± 2.5 (2) µm (Fig. C-1 (b)). Concerning the CSL boundaries distribution, 88.9 % of the total fraction corresponds to Σ3 grain boundaries (Fig. C-2 (a)), and 84.7 % of these boundaries are TB. The mean misorientation angle is 47.5° (Fig. C-2 (b)).

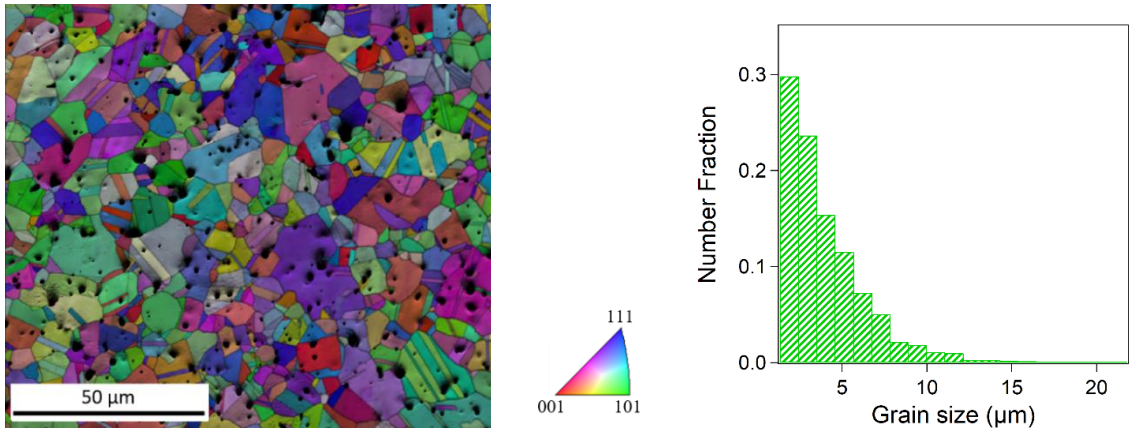

(a) (b)

Fig. C-1 Cartography IPF+IQ of sample S-PC (a) and grain size distribution (b).

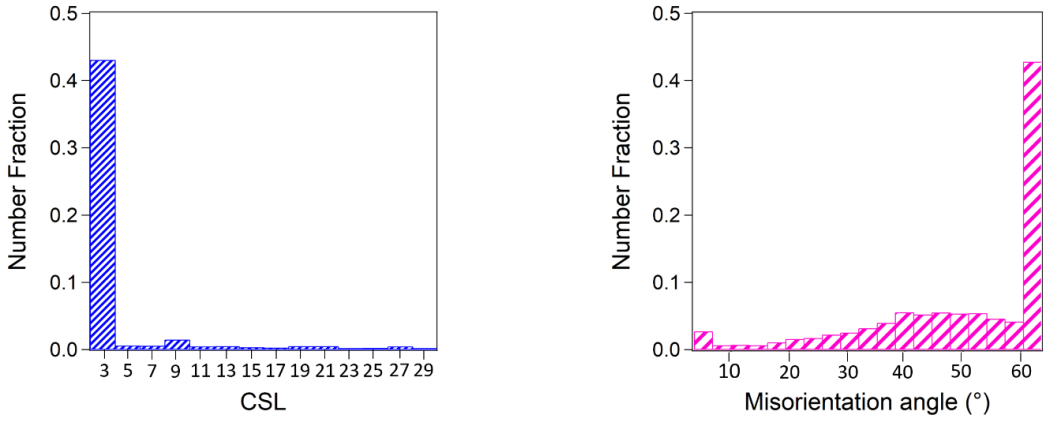

(a) (b)

Fig. C-2 Distribution of CSL type boundaries (a) and misorientation angle (b) for sample S-PC.

- Sample S-P1

Sample S-P1, processed from powder P1, had a relative density of 98.5 (5) % and displays equiaxed grains (Fig. C-3 (a)) with an average grain size of d = 2.1 µm ± 1.3 (2) µm (Fig. C-3 (b)). Concerning the CSL boundaries distribution, 82.2 % of the total fraction corresponds to Σ3 grain boundaries (Fig. C-4 (a)) and 81.6 % of these boundaries are twin boundaries (TB). The mean misorientation angle for this sample is 46.9° (Fig. C-4 (b)).

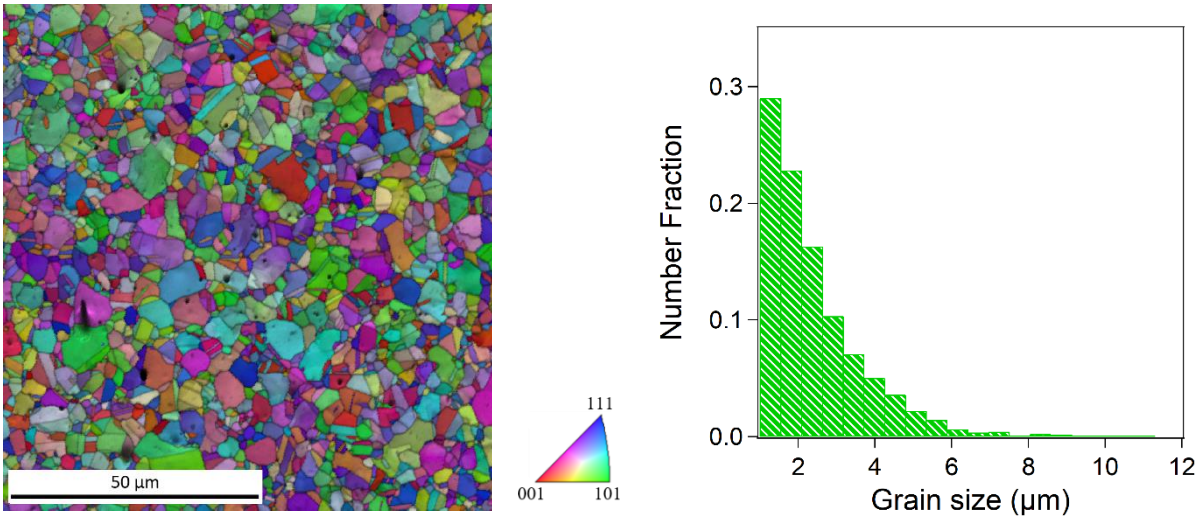

(a) (b)

Fig. C-3 Cartography IPF+IQ of sample S-P1 (a) and grain size distribution (b).

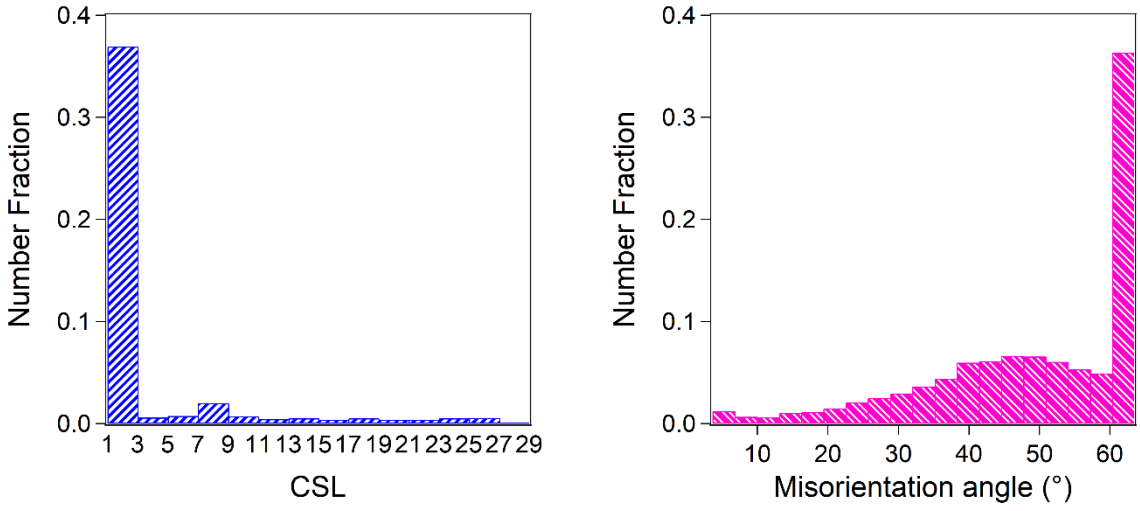

(a) (b)

Fig. C-4 Distribution of CSL type boundaries (a) and misorientation angle (b) for sample S-P1.

- Sample S-P2

Sample S-P2, processed from powder P2, has a relative density of 99.1 (8) % and displays equiaxed grains (Fig. C-5 (a)) with an average grain size of d = 1.43 µm ± 1.01 (5) µm (Fig. C-5 (b)). Concerning the CSL boundaries distribution, 82.3 % of the total fraction corresponds to Σ3 grain boundaries (Fig. C-6 (a)) and 87.0 % of these boundaries are TB. The mean misorientation angle is 47.0° (Fig. C-6 (b)).

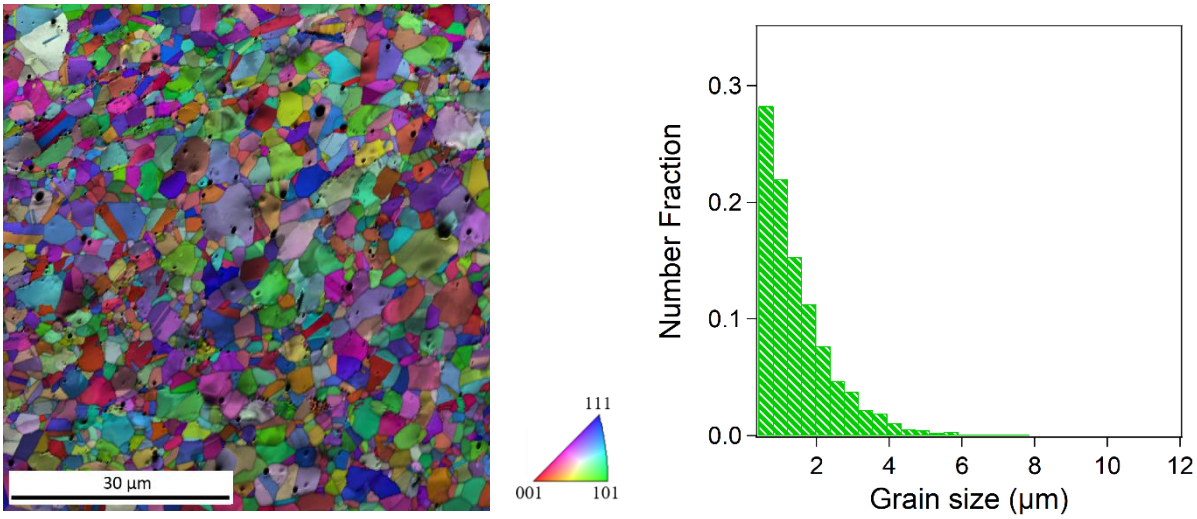

(a) (b)

Fig. C-5 Cartography IPF+IQ of sample S-P2 (a) and grain size distribution (b).

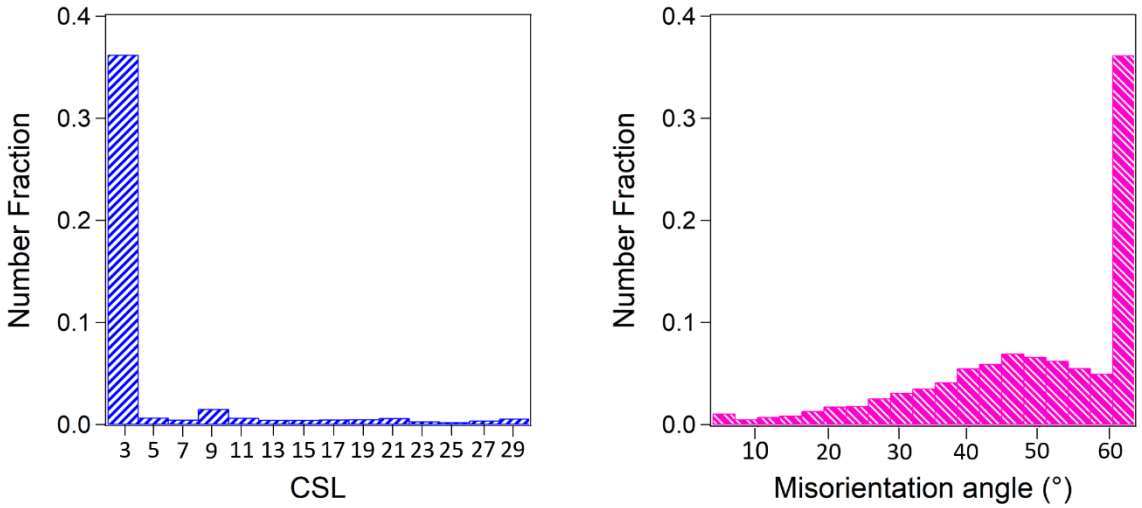

(a) (b)

Fig. C-6 Distribution of CSL type boundaries (a) and misorientation angle (b) for sample S-P2.

- Sample S-P3

Sample S-P3, processed from powder P3, has a relative density of 98.2 (6) % and displays equiaxed grains (Fig. C-7 (a)) with an average grain size of d = 1.1 µm ± 0.7 (1) µm (Fig. C-7 (b)). Concerning the CSL boundaries distribution, 79.4 % of the total fraction corresponds to Σ3 grain boundaries (Fig. C-8 (a)) and 82.8 % of these boundaries are TB. The mean misorientation angle is 45.6° (Fig. C-8 (b)).

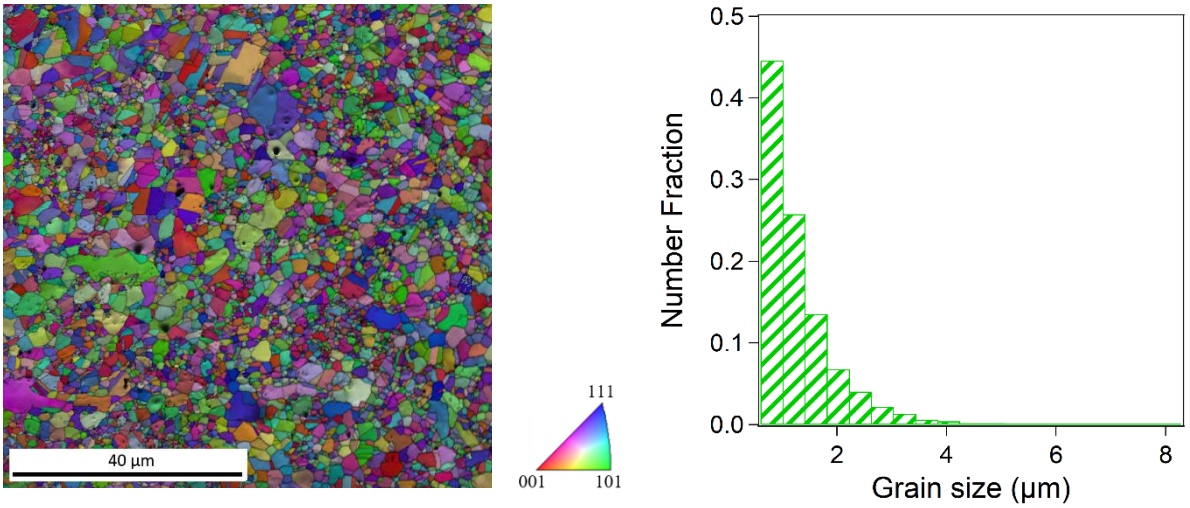

(a) (b)

Fig. C-7 Cartography IPF+IQ of sample S-P3 (a) and grain size distribution (b).

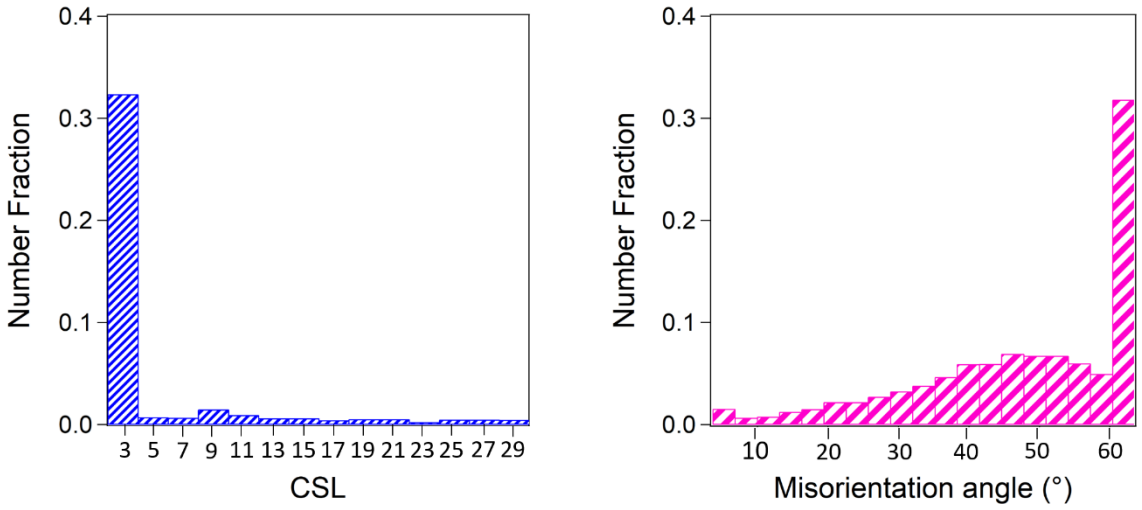

(a) (b)

Fig. C-8 Distribution of CSL type boundaries (a) and misorientation angle (b) for sample S-P3.

- Sample S-P4

Sample S-P4, processed from powder P4, has a relative density of 97.5 (3) % and displays equiaxed grains (Fig. C-9 (a)) with an average grain size of d = 0.88 µm ± 0.51 (5) µm (Fig. C-9 (b)). Concerning the CSL boundaries distribution, 73.2 % of the total fraction corresponds to Σ3 grain boundaries (Fig. C-10 (a)) and 75.4 % of these boundaries are TB. The mean misorientation angle is 41.6° (Fig. C-10 (b)).

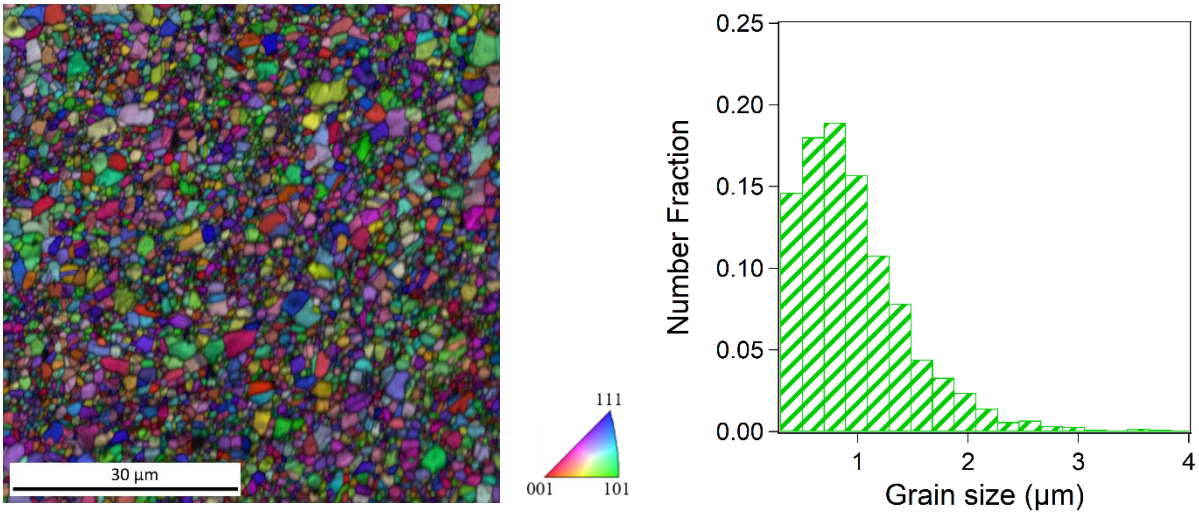

(a) (b)

Fig. C-9 Cartography IPF+IQ of sample S-P4 (a) and grain size distribution (b).

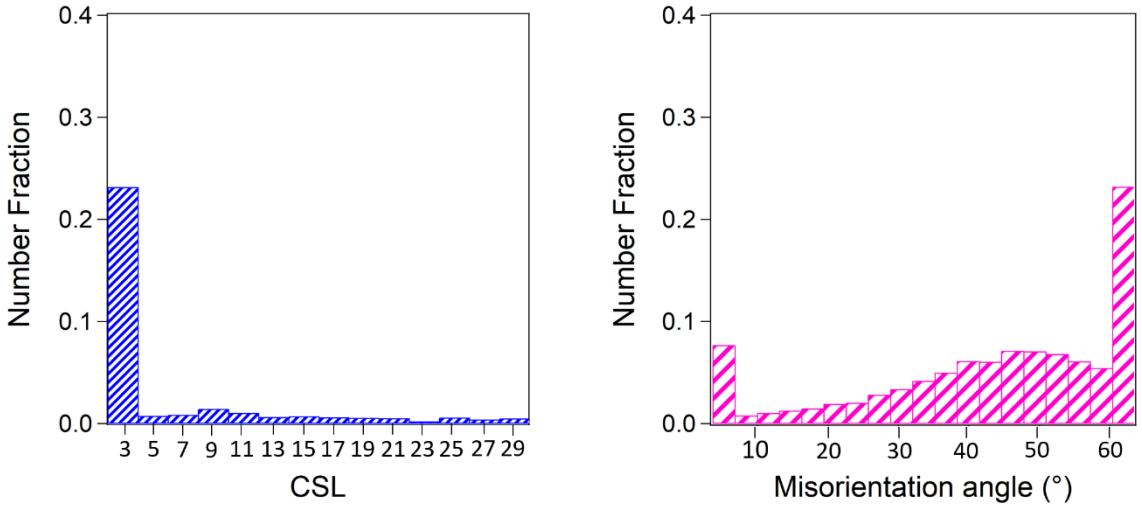

(a) (b)

Fig. C-10 Distribution of CSL type boundaries (a) and misorientation angle (b) for sample S-P4.

- Sample S-P5

Sample S-P5, processed from powder P5, has a relative density of 99.2 (3) % and displays equiaxed grains (Fig. C-11 (a)) with an average grain size of d = 1.41 µm ± 1.12 (5) µm (Fig. C-11 (b)). Concerning the CSL boundaries distribution, 83.0 % of the total fraction corresponds to Σ3 grain boundaries (Fig. C-12 (a)) and 83.5 % of these boundaries are TB. The mean misorientation angle is 47.1° (Fig. C-12 (b)).

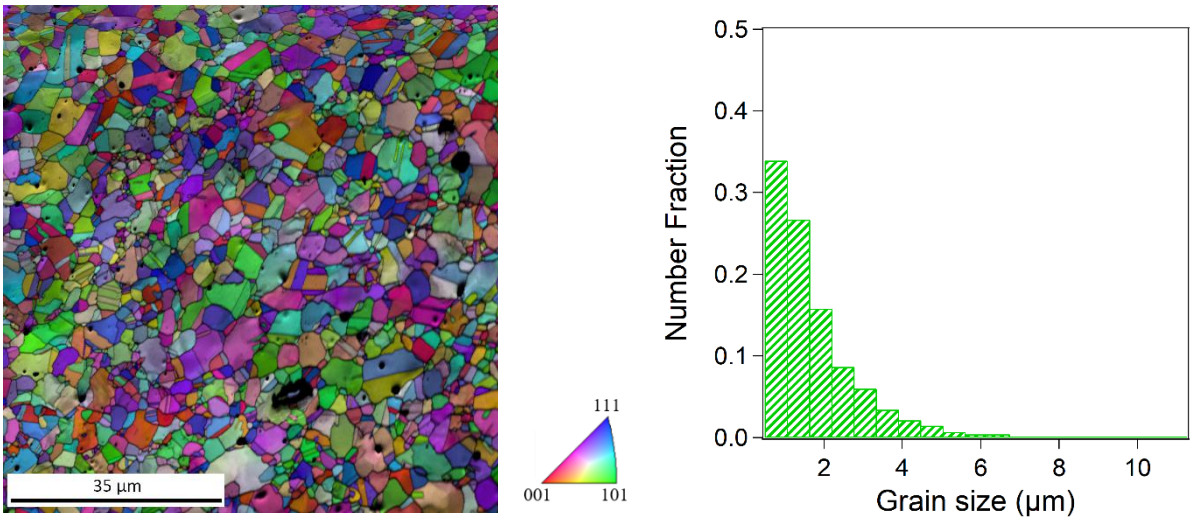

(a) (b)

Fig. C-11 Cartography IPF+IQ of sample S-P5 (a) and grain size distribution (b).

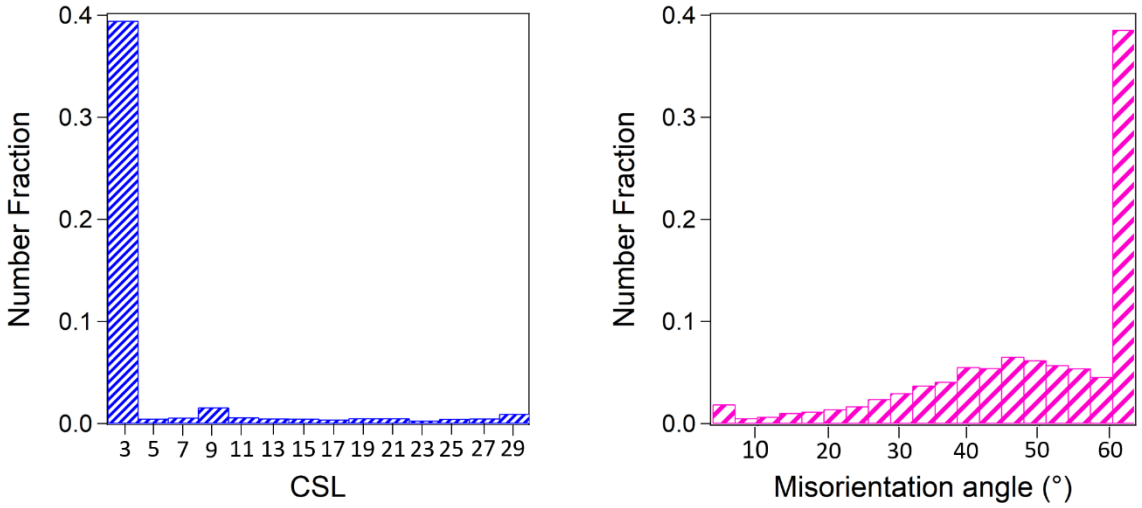

(a) (b)

Fig. C-12 Distribution of CSL type boundaries (a) and misorientation angle (b) for sample S-P5.

- Sample S-P6

Sample S-P6, processed from powder P6, has a relative density of 99.2 (3) % and displays equiaxed grains (Fig. C-13 (a)) with an average grain size of d = 1.03 µm ± 0.77 (5) µm (Fig. C-13 (b)). Concerning the CSL boundaries distribution, 83.0 % of the total fraction corresponds to Σ3 grain boundaries (Fig. C-14 (a)) and 75.7 % of these boundaries are TB. The mean misorientation angle is 47.1° (Fig. C-14 (b)).

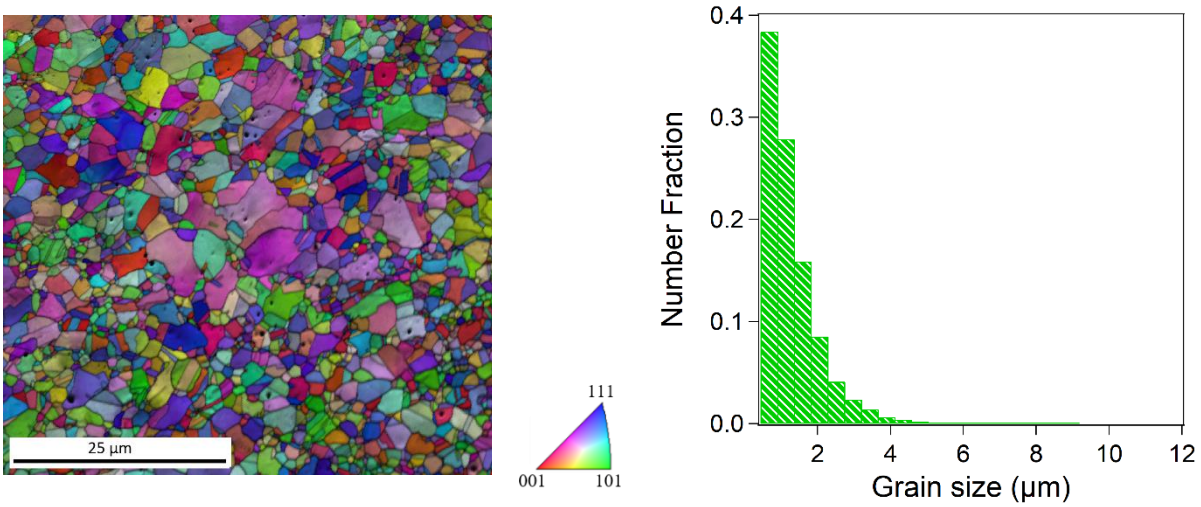

(a) (b)

Fig. C-13 Cartography IPF+IQ of sample S-P6 (a) and grain size distribution (b).

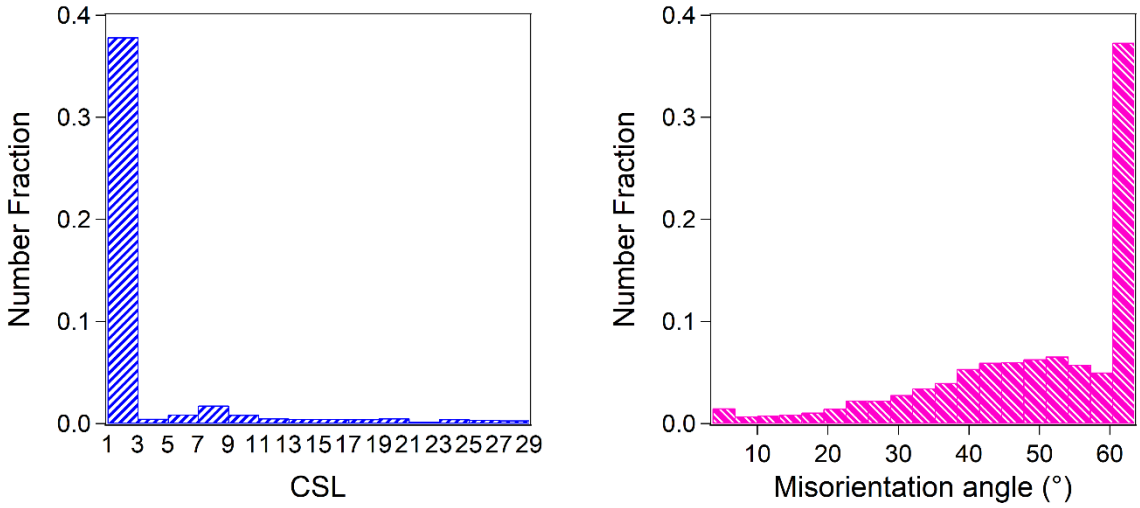

(a) (b)

Fig. C-14 Distribution of CSL type boundaries (a) and misorientation angle (b) for sample S-P6.

- Sample S-P7

Sample S-P7, processed from powder P7, has a relative density of 98.0 (3) % and displays equiaxed grains (Fig. C-15 (a)) with an average grain size of d = 0.79 µm ± 0.47 (6) µm (Fig. C-15 (b)). Concerning the CSL boundaries distribution, 76.6 % of the total fraction corresponds to Σ3 grain boundaries (Fig. C-16 (a)) and 86.4 % of these boundaries are TB. The mean misorientation angle is 44.0° (Fig. C-16 (b)).

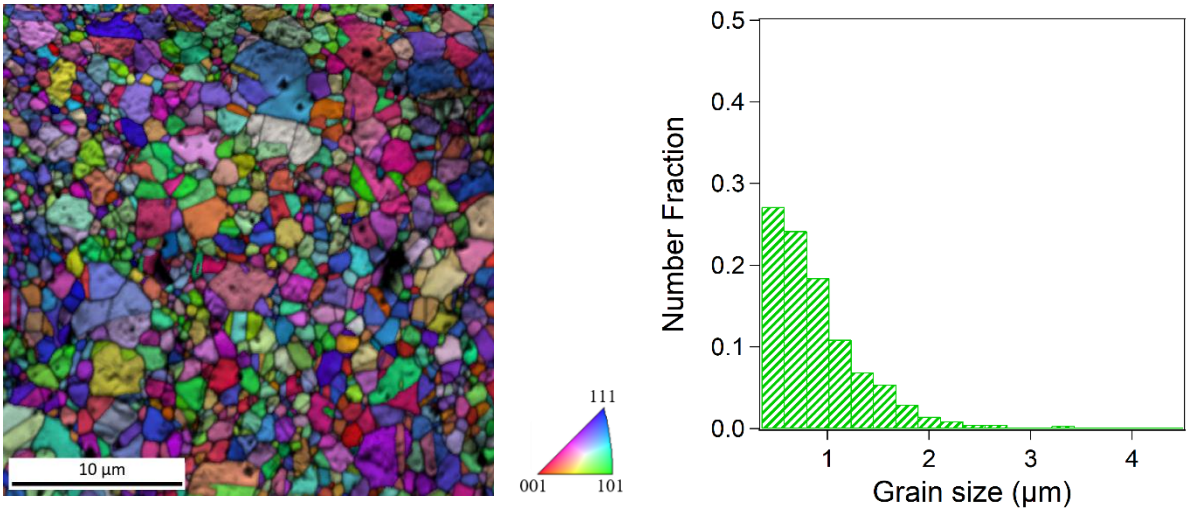

(a) (b)

Fig. C-15 Cartography IPF+IQ of sample S-P7 (a) and grain size distribution (b).

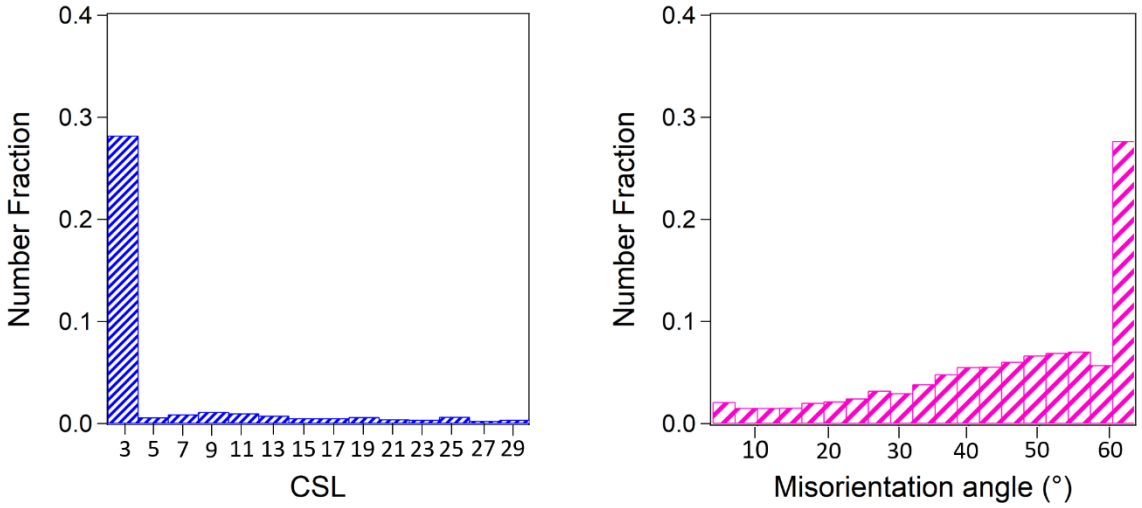

(a) (b)

Fig. C-16 Distribution of CSL type boundaries (a) and misorientation angle (b) for sample S-P7.

- Sample S-P8

Sample S-P8, processed from powder P8, has a relative density of 98.0 (3) % and displays equiaxed grains (Fig. C-17 (a)) with an average grain size of d = 0.78 µm ± 0.52 (6) µm (Fig. C-17 (b)). Concerning the CSL boundaries distribution, 77.2 % of the total fraction corresponds to Σ3 grain boundaries (Fig. C-18 (a)), and 75.2 % of these boundaries are TB. The mean misorientation angle is 43.2° (Fig. C-18 (b)).

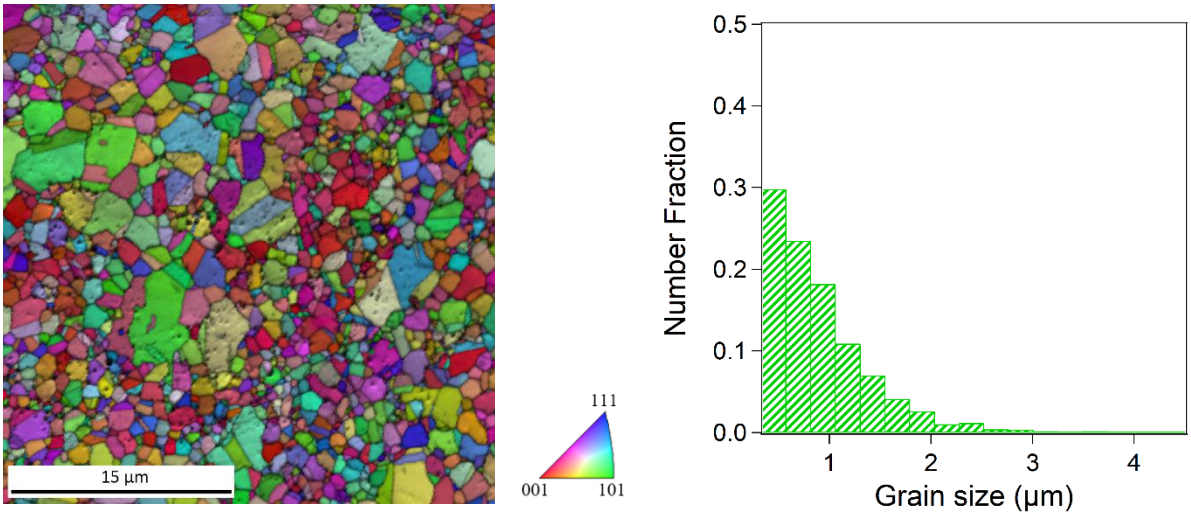

(a) (b)

Fig. C-17 Cartography IPF+IQ of sample S-P8 (a) and grain size distribution (b).

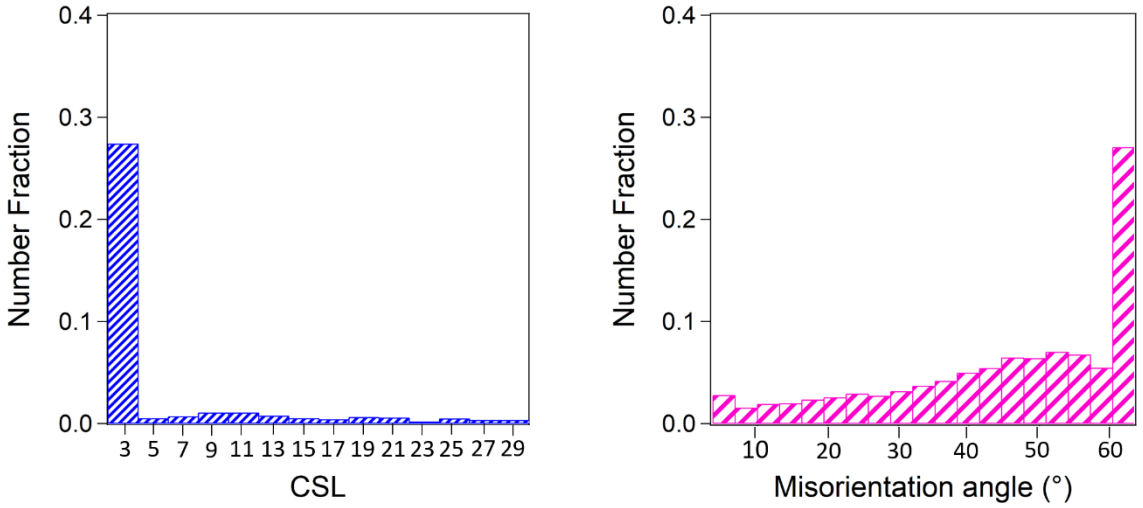

(a) (b)

Fig. C-18 Distribution of CSL type boundaries (a) and misorientation angle (b) for sample S-P8.

- Sample S-P9

Sample S-P9, processed from powder P9, has a relative density of 98.0 (4) % and displays equiaxed grains (Fig. C-19 (a)) with an average grain size of d = 0.83 µm ± 0.54 (5) µm (Fig. C-19 (b)). Concerning the CSL boundaries distribution, 74.8 % of the total fraction corresponds to Σ3 grain boundaries (Fig. C-20 (a)), and 83.7 % of these boundaries are TB. The mean misorientation angle is 43.2° (Fig. C-20 (b)).

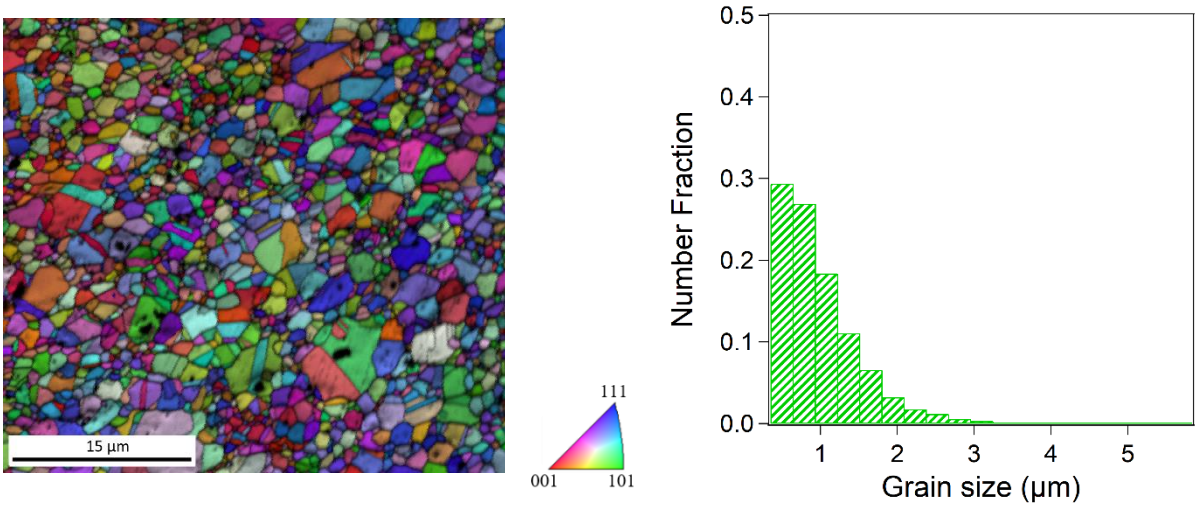

(a) (b)

Fig. C-19 Cartography IPF+IQ of sample S-P9 (a) and grain size distribution (b).

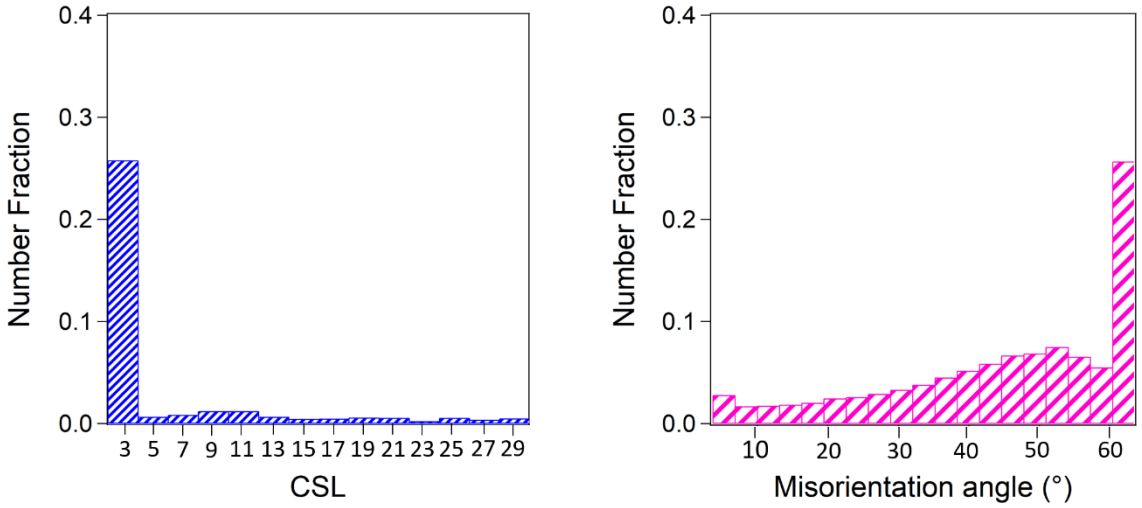

(a) (b)

Fig. C-20 Distribution of CSL type boundaries (a) and misorientation angle (b) for sample S-P9.

- Sample S-P10

Sample S-P10, processed from powder P10, has a relative density of 98.5 (3) % and displays equiaxed grains with an average grain size of d = 0.87 µm ± 0.49 (5) µm (Fig. C-21 Cartography IPF+IQ of sample S-P10 (a) and grain size distribution (b).

Concerning the CSL boundaries distribution, 67.8 % of the total fraction corresponds to Σ3 grain boundaries (Fig. C-22 Distribution of CSL type boundaries (a) and misorientation angle (b) for sample S-P10. (a)), and 81.9 % of these boundaries are TB. The mean misorientation angle is 41.4° (Fig. C-22 Distribution of CSL type boundaries (a) and misorientation angle (b) for sample S-P10. (b)).

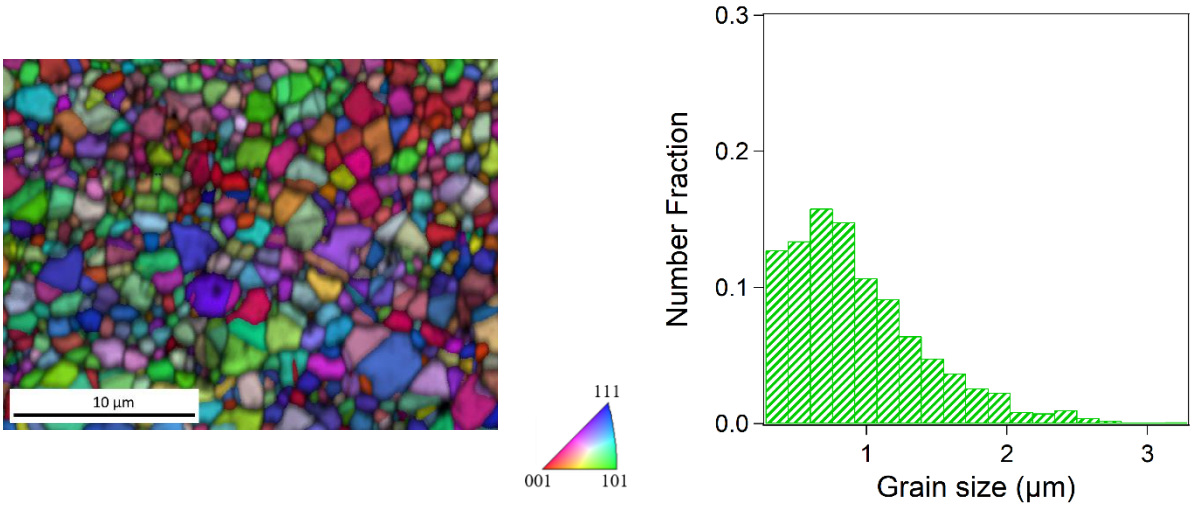

(a) (b)

Fig. C-21 Cartography IPF+IQ of sample S-P10 (a) and grain size distribution (b).

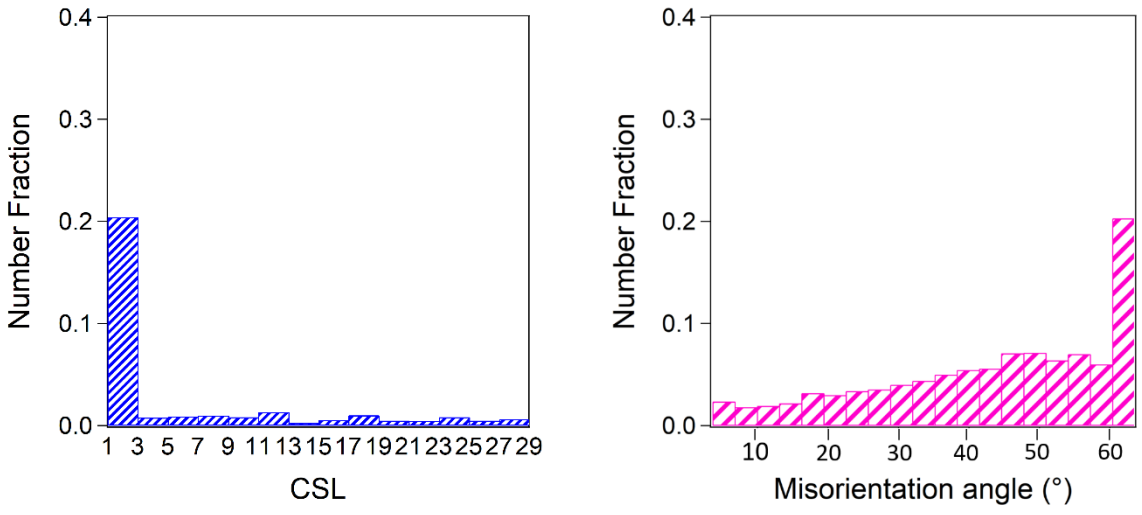

(a) (b)

Fig. C-22 Distribution of CSL type boundaries (a) and misorientation angle (b) for sample S-P10.

- Sample S-P0

Sample S-P0, processed from powder P0, has a relative density of 96.8 (5) % and displays equiaxed grains (Fig. C-23 Cartography IPF+IQ of sample S-P0 (a) and grain size distribution (b). (a)) with an average grain size of d = 0.67 µm ± 0.36 (5) µm (Fig. C-23 Cartography IPF+IQ of sample S-P0 (a) and grain size distribution (b). (b)). Concerning the CSL boundaries distribution, 59.5 % of the total fraction corresponds to Σ3 grain boundaries (Fig. C-24 Distribution of CSL type boundaries (a) and misorientation angle (b) for sample S-P0. (a)), and 61.6 % of these boundaries are TB. The mean misorientation angle is 38.2° (Fig. C-24 Distribution of CSL type boundaries (a) and misorientation angle (b) for sample S-P0. (b)).

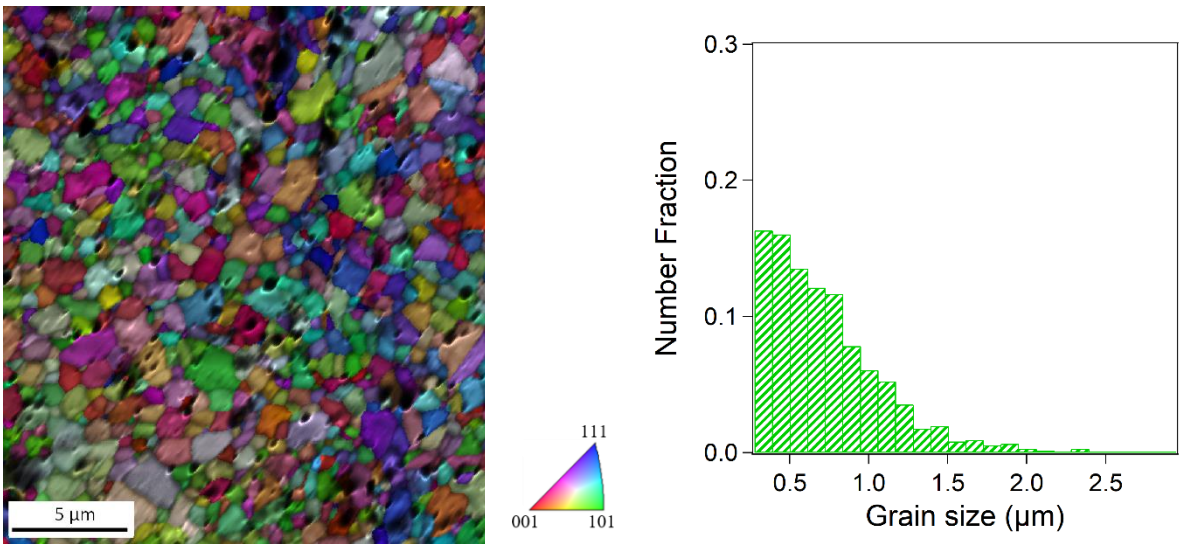

(a) (b)

Fig. C-23 Cartography IPF+IQ of sample S-P0 (a) and grain size distribution (b).

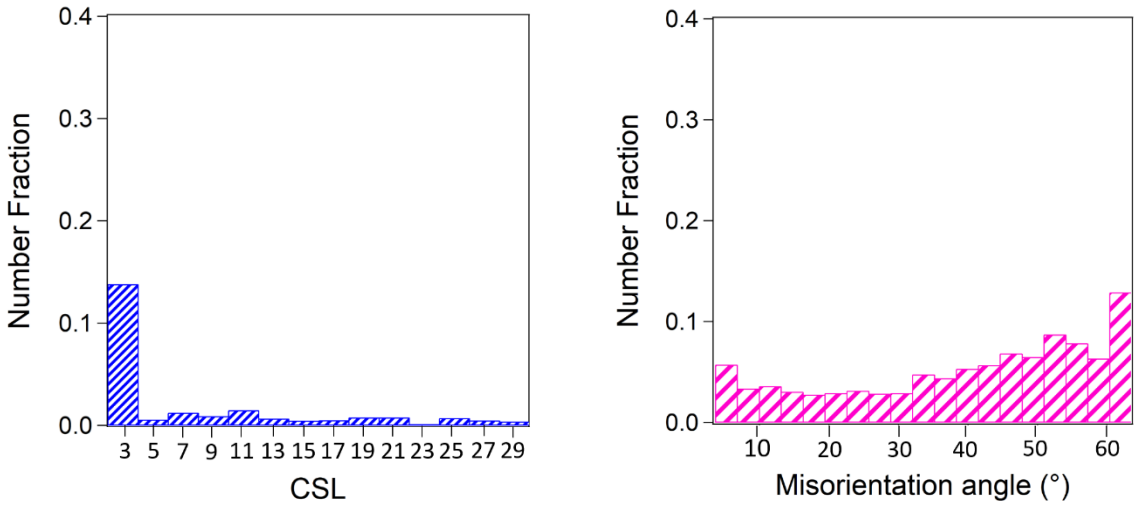

(a) (b)

Fig. C-24 Distribution of CSL type boundaries (a) and misorientation angle (b) for sample S-P0.

APPENDIX D: STUDY OF THE HOMOGENEITY OF SAMPLES BY HARDNESS CARTHOGRAPHIES

Controlling the homogeneity of the specimen is a major concern when processing UFG samples. To investigate this feature on samples obtained from powder metallurgy, hardness cartographies covering the entire surface of samples were performed. Examples of such cartographies are collected in this appendix. Fig. D-1 displays the results obtained for samples S-P1 (Fig. D-1 (a)) and S-P7 (Fig. D-1 (b)). The corresponding average hardness of 149 HV against 197 HV highlights the strengthening impact of grain size, correspondingly d = 2.1 ± 1.3 (2) µm and d= 0.79 ± 0.47 (6) µm. Concerning the dispersion of the measured values, a gradient correlated to the synthesis process is absent but rather a random dispersion of hardness values can be observed. Differences in hardness emerge from grain size distributions, as well as differences in residual deformation or porosity. A slightly higher difference between maximum and minimum values can be depicted for sample S-P1, probably due to a less homogeneous microstructure.

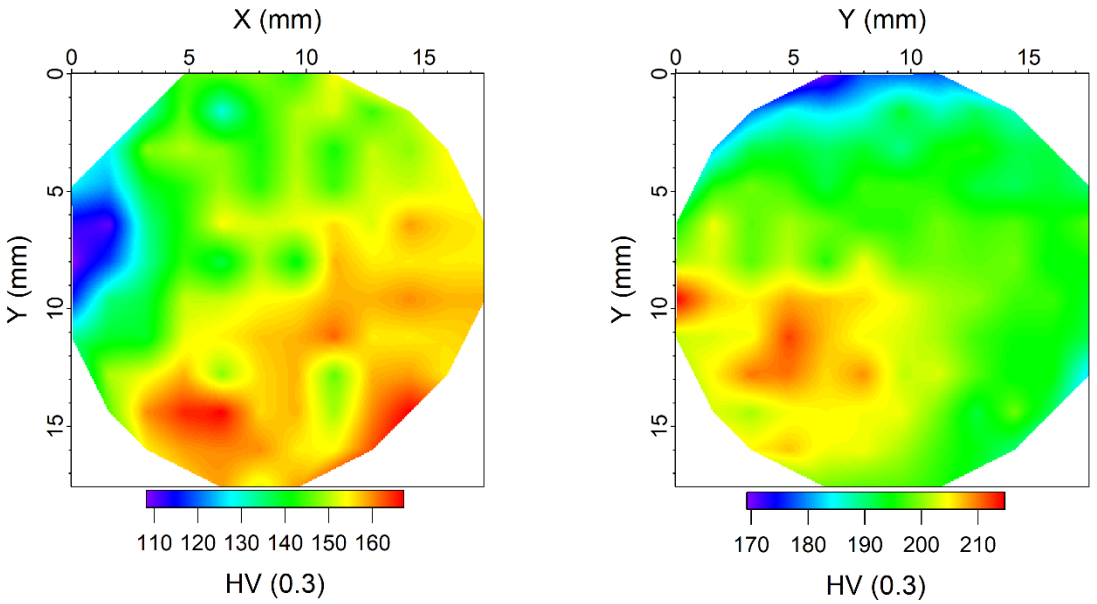

Fig. D-1 Hardness maps for specimens S-P1 (a) and S-P7 (b) of a diameter of 20 mm.

In order to study the reproducibility of the SPS process, samples with diameters of 10 mm, 20 mm and 50 mm were processed using the powder P0. Fig. D-2 displays the corresponding hardness cartographies. All samples present similar values of hardness independently of the diameter. The corresponding dispersion decreases with the sample diameter, from 55 HV for the bigger samples to 20 HV for the smallest one. Standard deviations are however comparable.

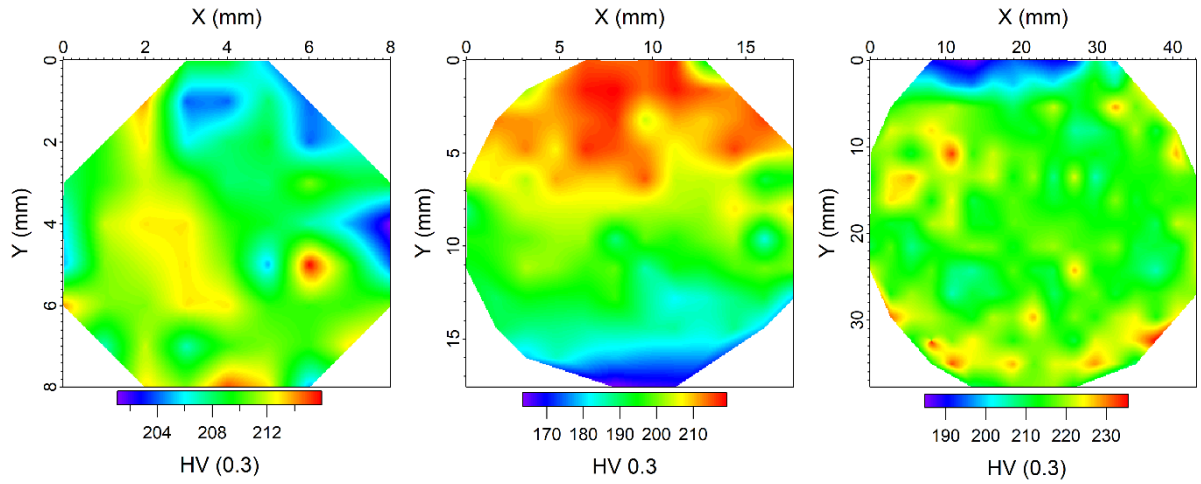

(a) (b) (c)

Fig. D-2 Hardness cartographies of UFG sample S-P0 sintered in sizes: 10 mm (a), 20 mm (b) and 50 mm (c).

APPENDIX E: CARTOGRAPHIES OF TENSILE TESTING SPECIMENS BEFORE AND AFTER DEFORMATION

This appendix collects the orientation and misorientation cartographies, processed from EBSD results, of the samples produced for tensile testing. The initial state (a) and the deformed state to failure (b) are systematically displayed for each sample, including: an orientation cartography in IPF superimposed over the IQ, a GOS map, a GAM map, a first neighbor KAM and a third neighbor KAM. The IPF reference direction is set as the tensile stress direction (white arrows) for the deformed state and as the direction normal to the surface of samples for the initial state. In misorientation maps (GOS, GAM, KAM), insets display the distribution of orientation spread and misorientations. In addition, grain boundaries are added in black to visualized misorientations close to them.

- Sample 1

Processed from powder P0, it displays an initial average grain size of d = 0.82 ± 0.67 (4) µm. The orientation of grains towards the tensile direction can be observed after deformation (Fig. E-1). The increase in average GOS from 0.7 ± 0.2° to 1.7 ± 0.9° between the initial state and the deformed state can be depicted in the corresponding cartographies (Fig. E-2). On the contrary, no variation is observed in the average GAM value, which is 0.8 ± 0.1° in the initial state and 0.9 ± 0.2° in the deformed state (Fig. E-3). Concerning kernel average misorientation (Fig. E-4), when the first neighbor is considered, a similar value is obtained in the initial state and the deformed state, 0.8 ± 0.3° and 0.9 ± 0.3°, respectively. Nevertheless, considering the third neighbor (Fig. E-5) a slight increase is encountered from 0.9 ± 0.3° to 1.2 ± 0.4°.

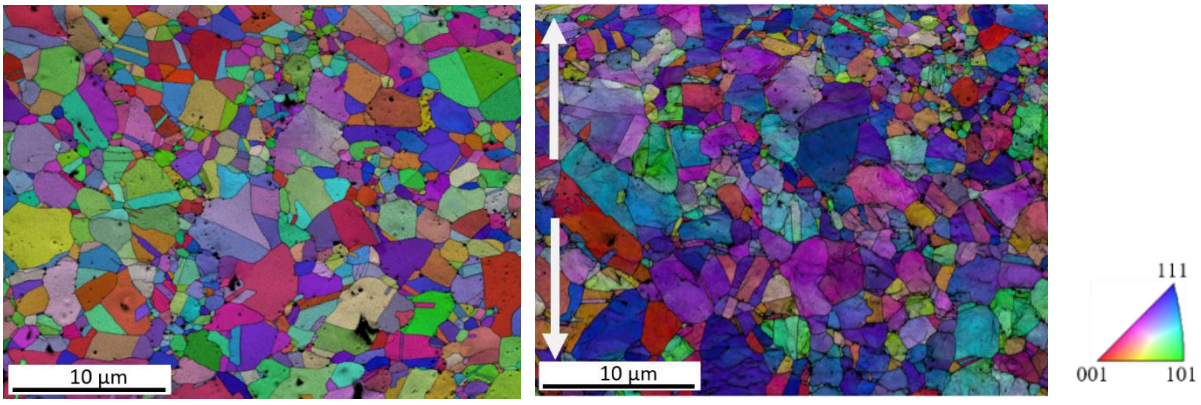

(a) (b)

Fig. E-1 IPF+IQ cartographies of sample 1 at the initial state (a) and after deformation to failure (b).

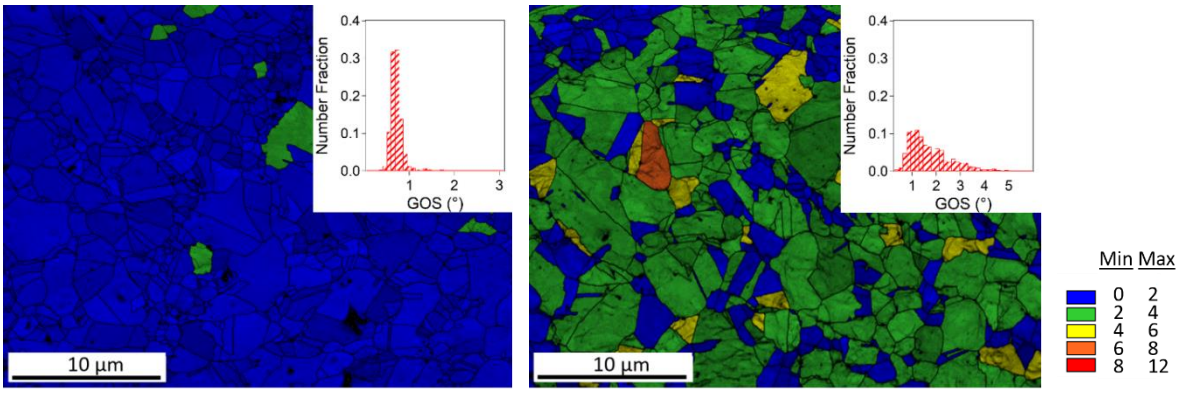

(a) (b)

Fig. E-2 GOS+IQ cartographies of sample 1 at the initial state (a) and after deformation to failure (b). Color legend represents the grain orientation spread in °.

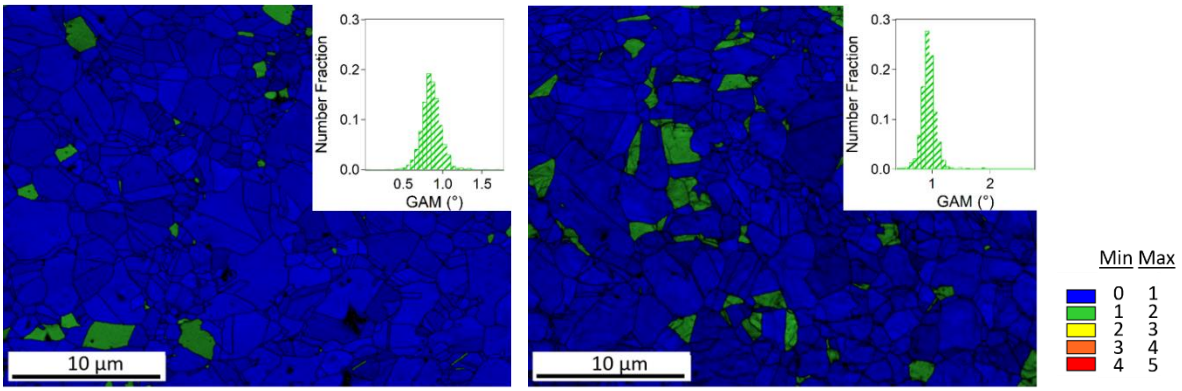

(a) (b)

Fig. E-3 GAM+IQ cartographies of sample 1 at the initial state (a) and after deformation to failure (b). Color legend represents the grain average misorientation in °.

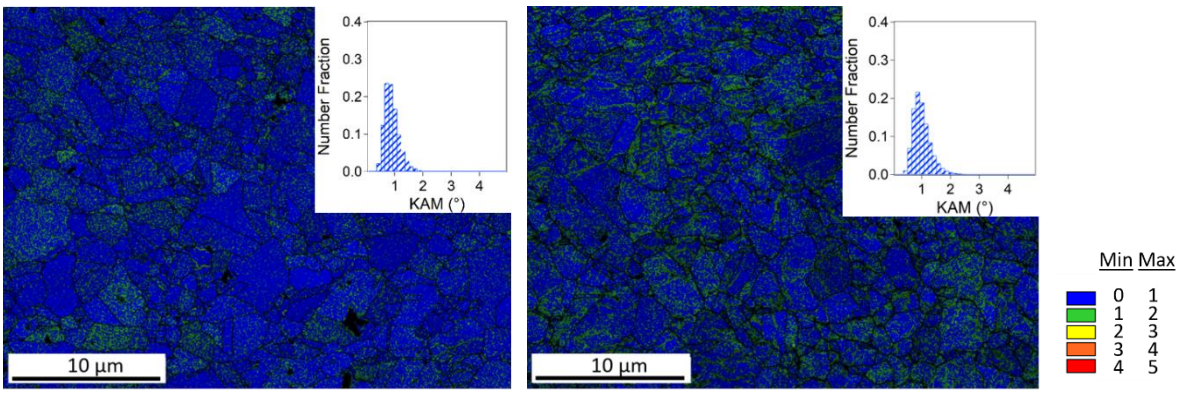

(a) (b)

Fig. E-4 First neighbor KAM+IQ cartographies of sample 1 at the initial state (a) and after deformation to failure (b). Color legend represents the kernel average misorientation in °.

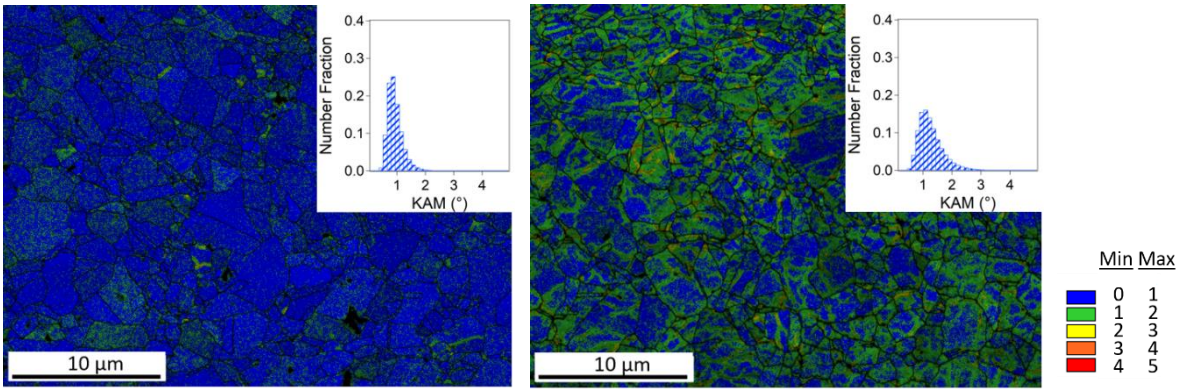

(a) (b)

Fig. E-5 Third neighbor KAM+IQ cartographies of sample 1 at the initial state (a) and after deformation to failure (b). Color legend represents the kernel average misorientation in °.

- Sample 2

Processed from powder P9, it displays an initial average grain size of d = 1.11 ± 0.84 (7) µm. The orientation of grains towards the tensile direction can be observed after deformation (Fig. E-6). The increase in average GOS from 0.6 ± 0.3° to 2.3 ± 1.5° between the initial state and the deformed state can be depicted in the corresponding distribution plot (Fig. E-7). Concerning the average GAM value, it slightly increases from 0.8 ± 0.1° in the initial state to 1.0 ± 0.3° in the deformed state (Fig. E-8). Likewise, a small increase is obtained in kernel average misorientation when the first neighbor is considered, between the initial state and the deformed state (Fig. E-9), from 0.8 ± 0.3° to 1.1 ± 0.4°. If the third neighbor is investigated (Fig. E-10) a clear increase is observed from 0.8 ± 0.3° to 1.7 ± 0.6°.

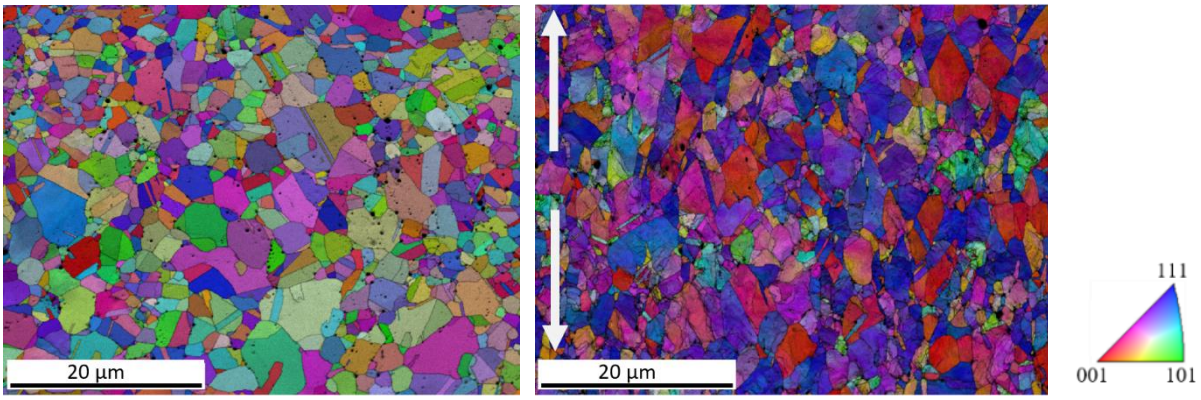

(a) (b)

Fig. E-6 IPF+IQ cartographies of sample 2 at the initial state (a) and after deformation to failure (b).

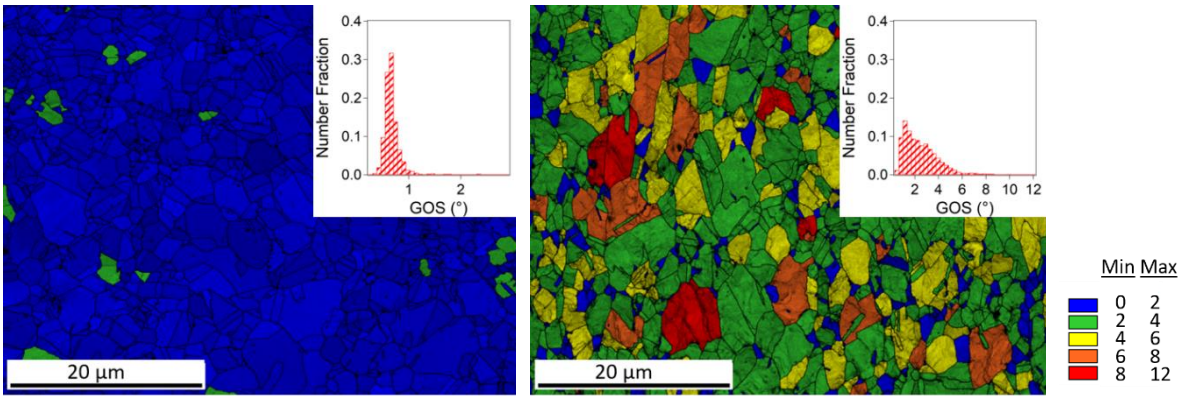

(a) (b)

Fig. E-7 GOS+IQ cartographies of sample 2 at the initial state (a) and after deformation to failure (b). Color legend represents the grain orientation spread in °.

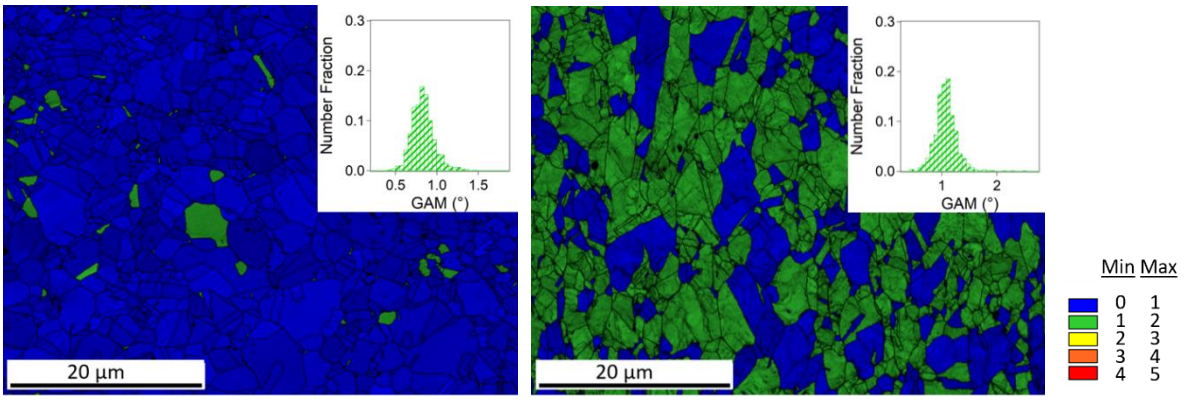

(a) (b)

Fig. E-8 GAM+IQ cartographies of sample 2 at the initial state (a) and after deformation to failure (b). Color legend represents the grain average misorientation in °.

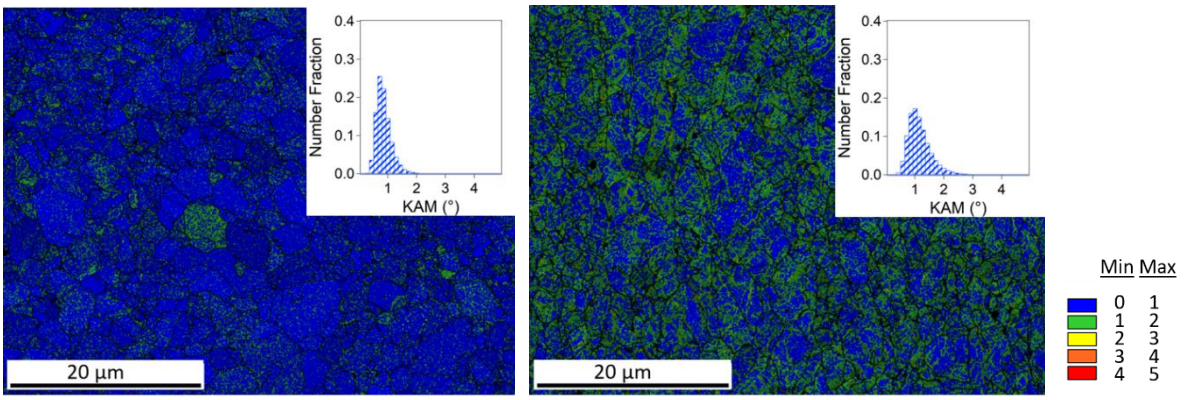

(a) (b)

Fig. E-9 First neighbor KAM+IQ cartographies of sample 2 at the initial state (a) and after deformation to failure (b). Color legend represents the kernel average misorientation in °.

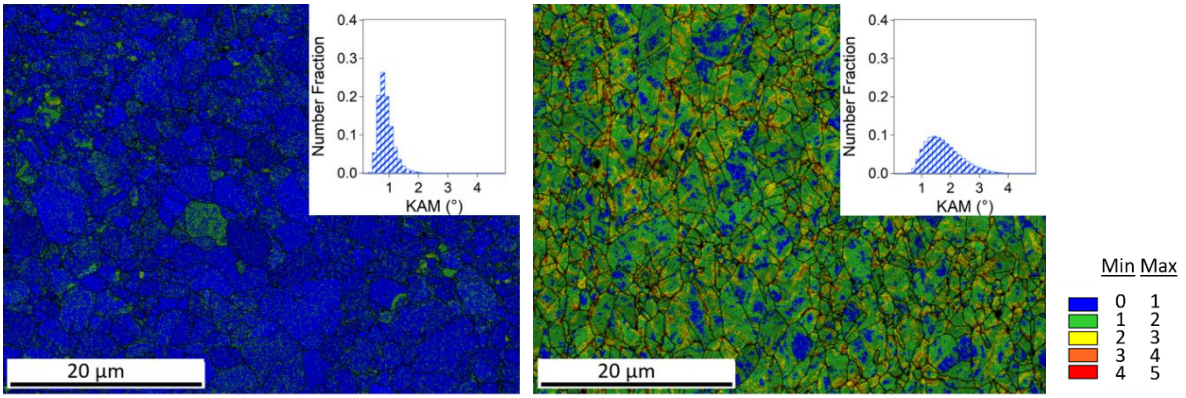

(a) (b)

Fig. E-10 Third neighbor KAM+IQ cartographies of sample 2 at the initial state (a) and after deformation to failure (b). Color legend represents the kernel average misorientation in °.

- Sample 3

Processed from powder P6, it displays an initial average grain size of d = 1.39 ± 1.11 (7) µm. The orientation of grains towards the tensile direction can be observed after deformation (Fig. E-11). From the corresponding distribution plots (Fig. E-12), an increase in average GOS from 0.7 ± 0.2° to 1.9 ± 1.1° between the initial state and the deformed state can be depicted. Concerning the average GAM value, it slightly increases from 0.8 ± 0.2° in the initial state to 1.0 ± 0.2° in the deformed state (Fig. E-13). Likewise, a small increase is obtained in kernel average misorientation when the first neighbor is considered, between the initial state and the deformed state (Fig. E-14), from 0.8 ± 0.3° to 1.1 ± 0.4°. If the third neighbor is investigated (Fig. E-15) a clear increase from 0.8 ± 0.3° to 1.5 ± 0.6° is observed.

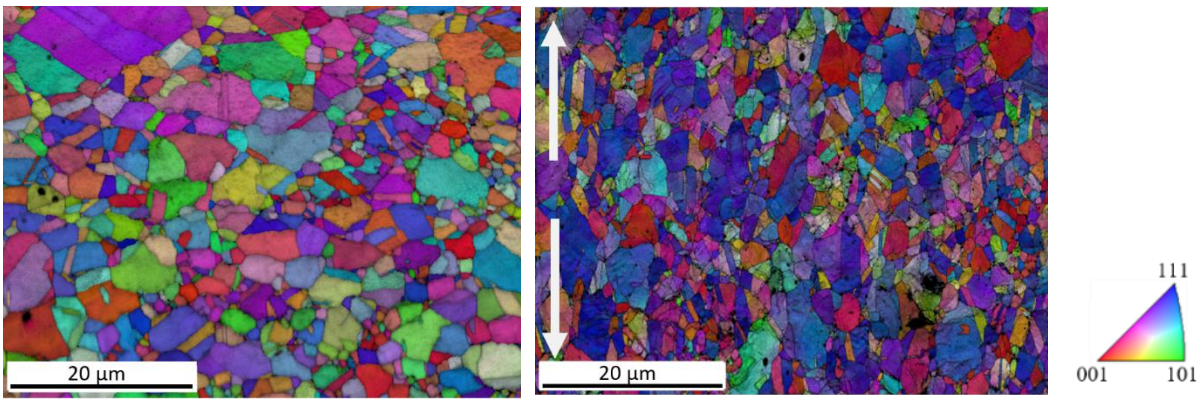

(a) (b)

Fig. E-11 IPF+IQ cartographies of sample 3 at the initial state (a) and after deformation to failure (b).

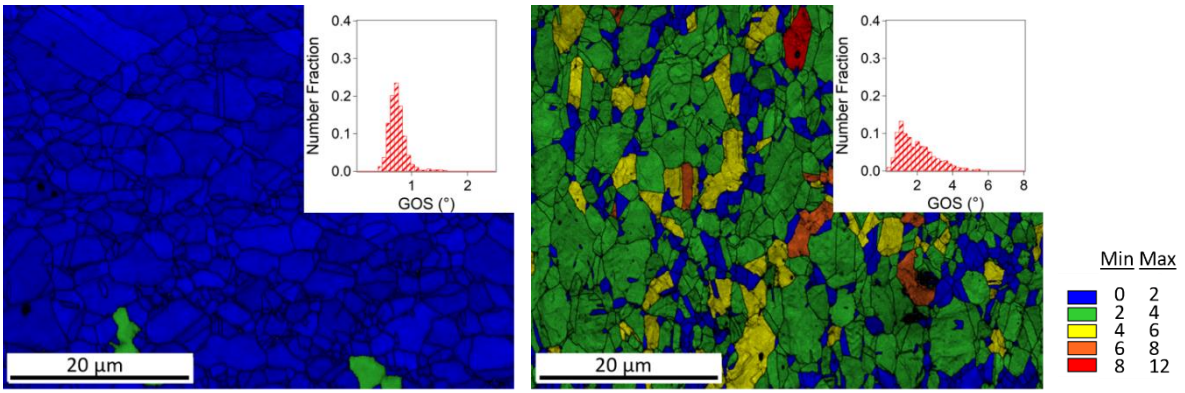

(a) (b)

Fig. E-12 GOS+IQ cartographies of sample 3 at the initial state (a) and after deformation to failure (b). Color legend represents the grain orientation spread in °.

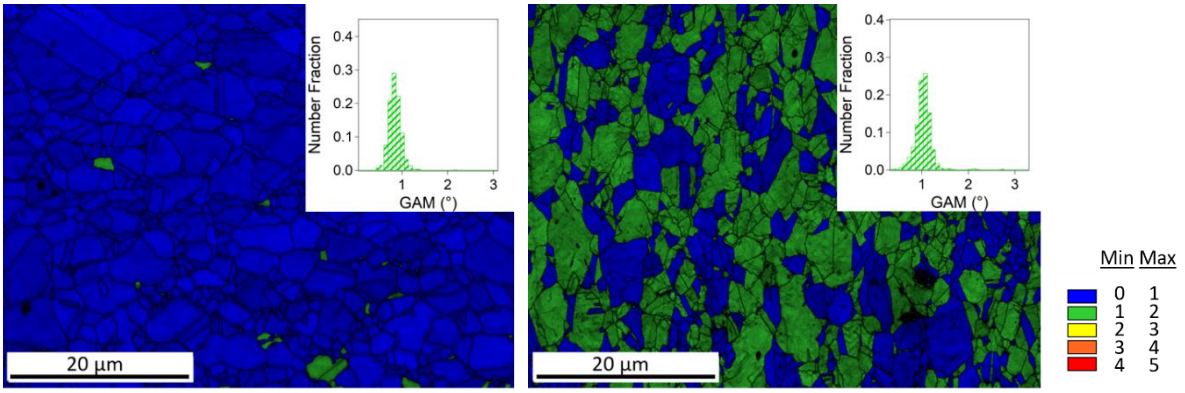

(a) (b)

Fig. E-13 GAM+IQ cartographies of sample 3 at the initial state (a) and after deformation to failure (b). Color legend represents the grain average misorientation in °.

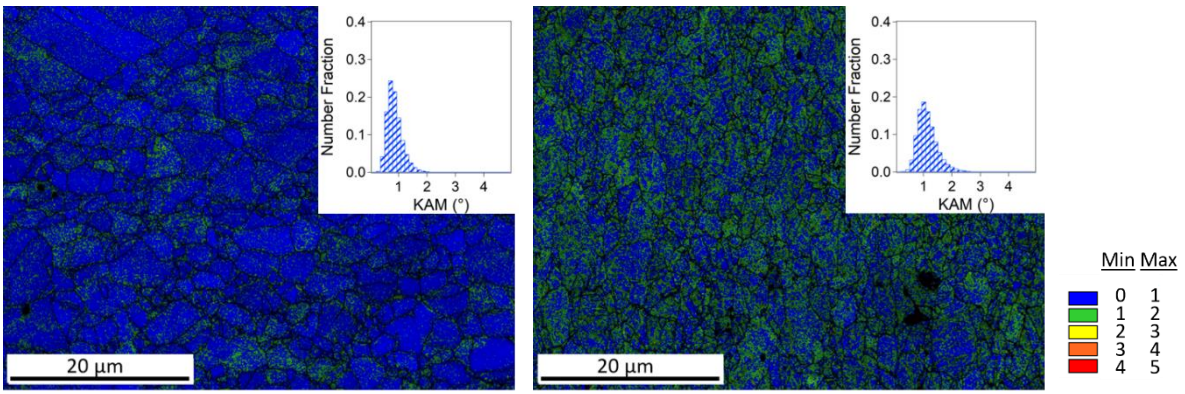

(a) (b)

Fig. E-14 First neighbor KAM+IQ cartographies of sample 3 at the initial state (a) and after deformation to failure (b). Color legend represents the kernel average misorientation in °.

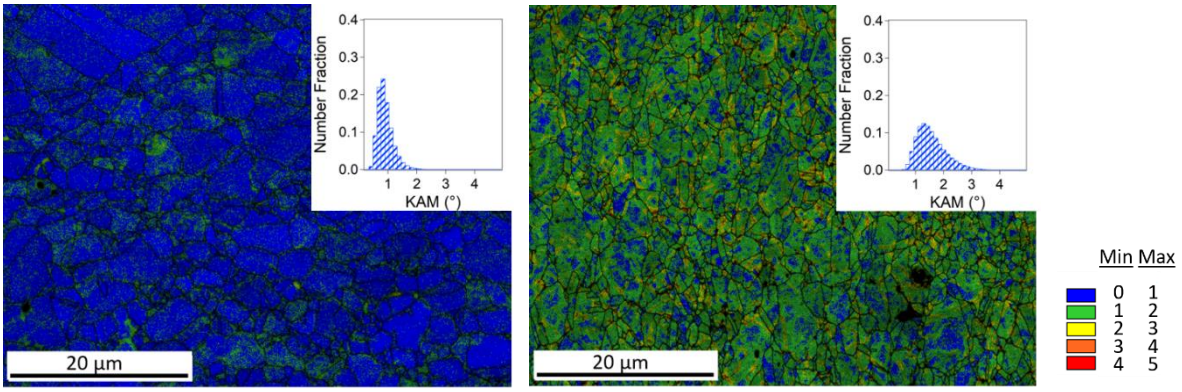

(a) (b)

Fig. E-15 Third neighbor KAM+IQ cartographies of sample 3 at the initial state (a) and after deformation to failure (b). Color legend represents the kernel average misorientation in °.

- Sample 4

Obtained from powder PC, it displays an initial average grain size of d = 4.0 ± 2.4 (3) µm. The orientation of grains towards the tensile direction can be observed after deformation (Fig. E-16). The increase in average GOS from 0.6 ± 0.2° to 2.7 ± 1.7° between the initial state and the deformed state can be depicted in the corresponding distribution plots (Fig. E-17). Concerning the average GAM value, an increase from 0.7 ± 0.2° in the initial state to 1.4 ± 0.6° in the deformed state is observed (Fig. E-18). Likewise, an increase from 0.7 ± 0.3° to 1.4 ± 0.6° is obtained in kernel average misorientation when the first neighbor is considered (Fig. E-19). If the third neighbor is investigated an even higher difference is depicted (Fig. E-20) from 0.7 ± 0.3° to 2.3 ± 0.7°.

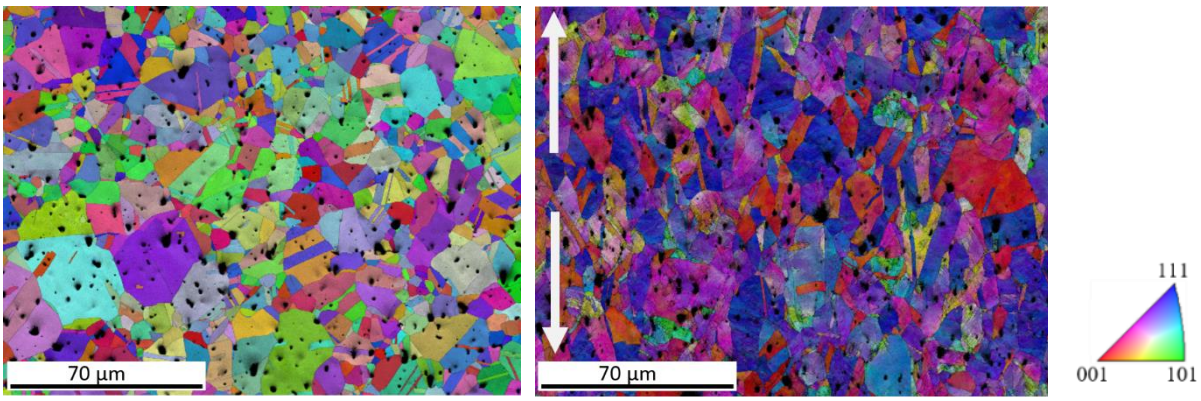

(a) (b)

Fig. E-16 IPF+IQ cartographies of sample 4 at the initial state (a) and after deformation to failure (b).

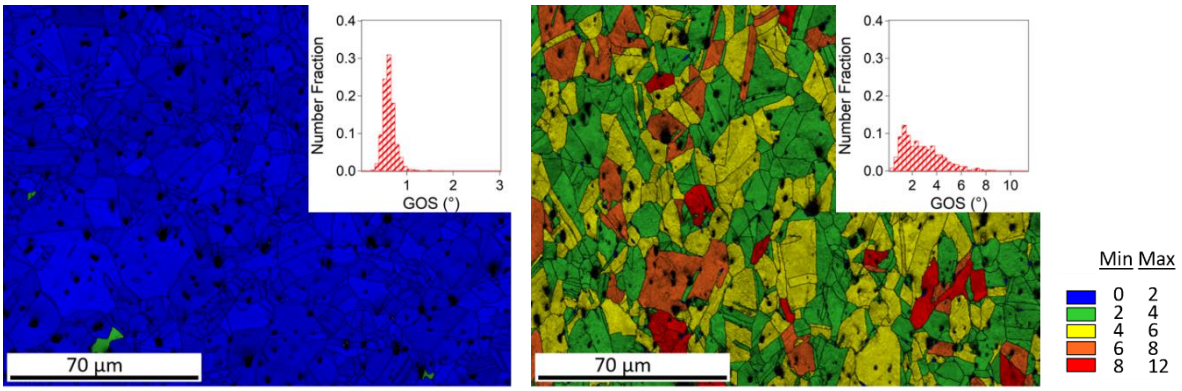

(a) (b)

Fig. E-17 GOS+IQ cartographies of sample 4 at the initial state (a) and after deformation to failure (b). Color legend represents the grain orientation spread in °.

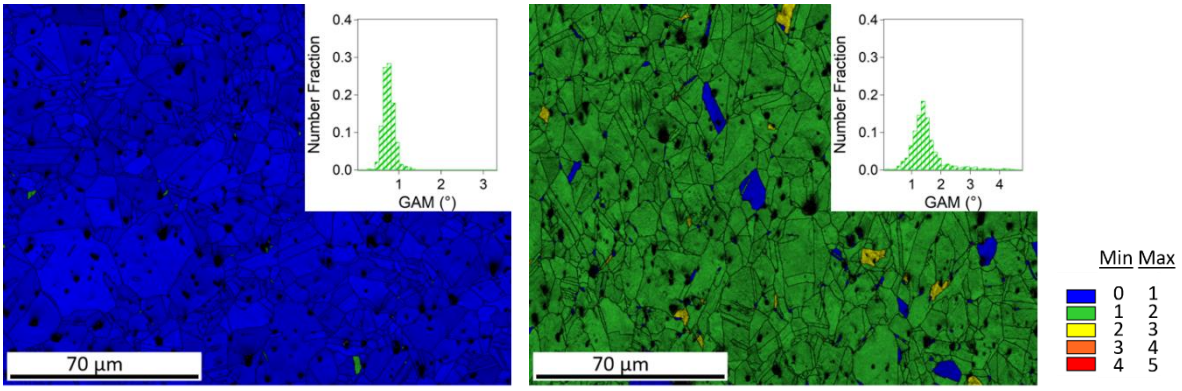

(a) (b)

Fig. E-18 GAM+IQ cartographies of sample 4 at the initial state (a) and after deformation to failure (b). Color legend represents the grain average misorientation in °.

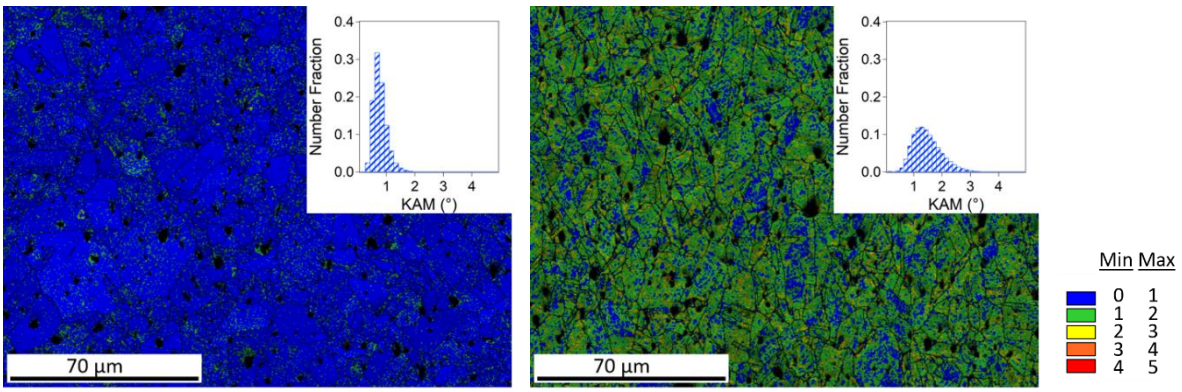

(a) (b)

Fig. E-19 First neighbor KAM+IQ cartographies of sample 4 at the initial state (a) and after deformation to failure (b). Color legend represents the kernel average misorientation in °.

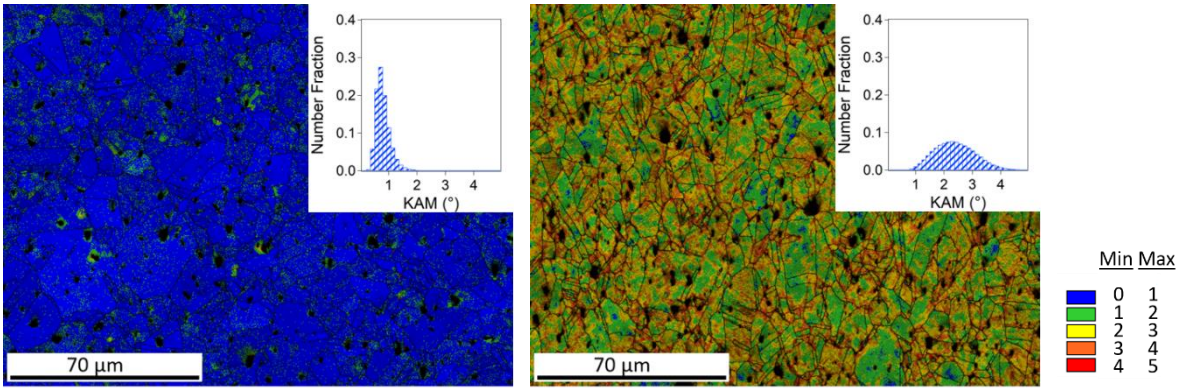

(a) (b)

Fig. E-20 Third neighbor KAM+IQ cartographies of sample 4 at the initial state (a) and after deformation to failure (b). Color legend represents the kernel average misorientation in °.

- Sample 5

This sample was processed using powder PC at a sintering temperature of 1273 K and displays an initial average grain size of d = 25 ± 17 (1.5) µm. The orientation of grains towards the tensile direction can be observed after deformation (Fig. E-21). The increase in average GOS from 0.7 ± 0.2° to 2.1 ± 1.4° between the initial state and the deformed state can be depicted in the corresponding distribution plots (Fig. E-22). Concerning the average GAM value an increase from 0.8 ± 0.2° in the initial state to 2.2 ± 1.0° in the deformed state is observed (Fig. E-23). Likewise, an increase from 0.8 ± 0.3° to 1.7 ± 0.7° is obtained in kernel average misorientation when the first neighbor is considered (Fig. E-24). If the third neighbor is investigated an even higher difference between the initial and the deformed state is depicted from 0.9 ± 0.4° to 2.5 ± 0.8° (Fig. E-25).

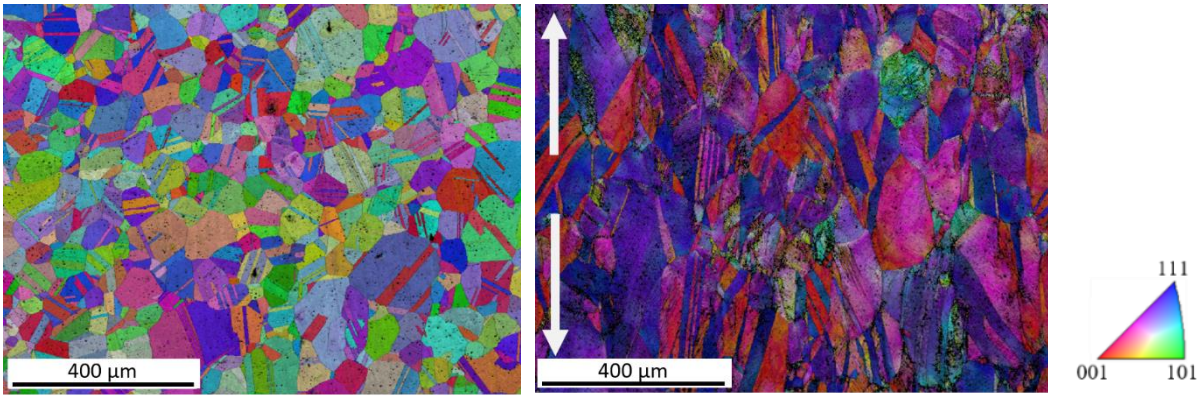

(a) (b)

Fig. E-21 IPF+IQ cartographies of sample 5 at the initial state (a) and after deformation to failure (b).

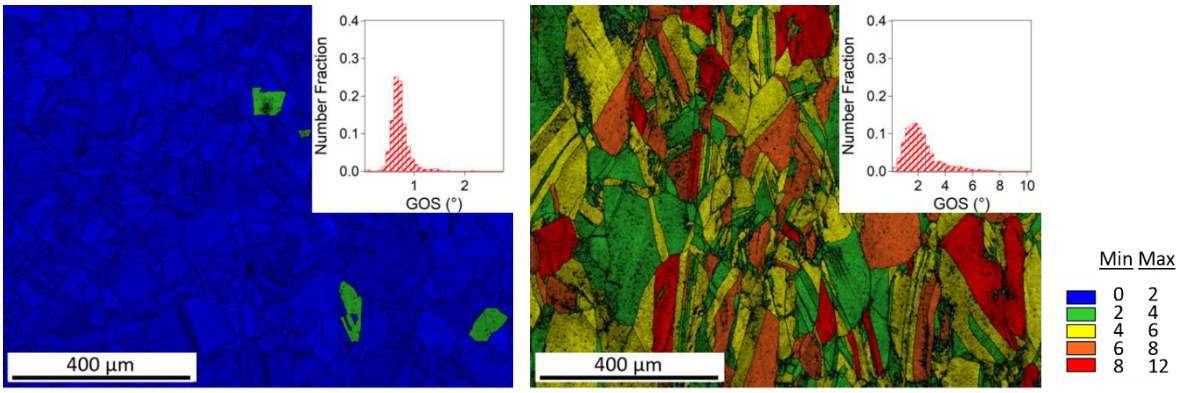

(a) (b)

Fig. E-22 GOS+IQ cartographies of sample 4 at the initial state (a) and after deformation to failure (b). Color legend represents the grain orientation spread in °.

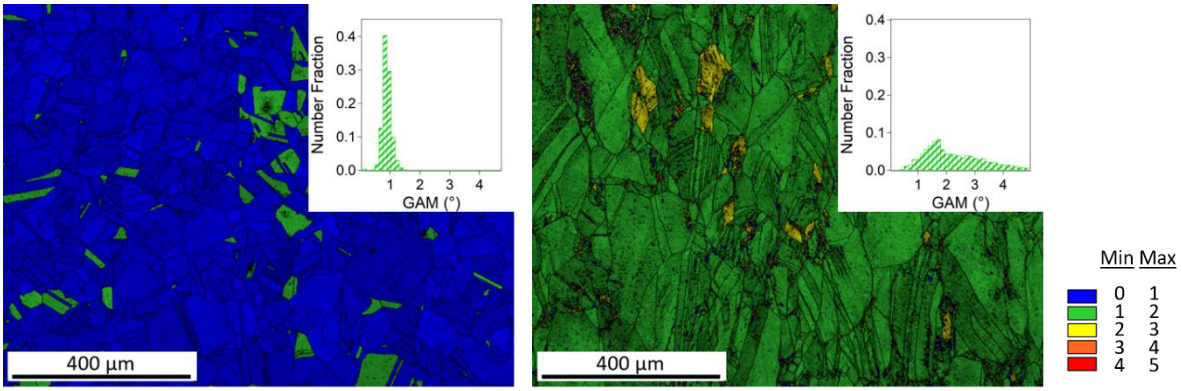

(a) (b)

Fig. E-23 GAM+IQ cartographies of sample 4 at the initial state (a) and after deformation to failure (b). Color legend represents the grain average misorientation in °.

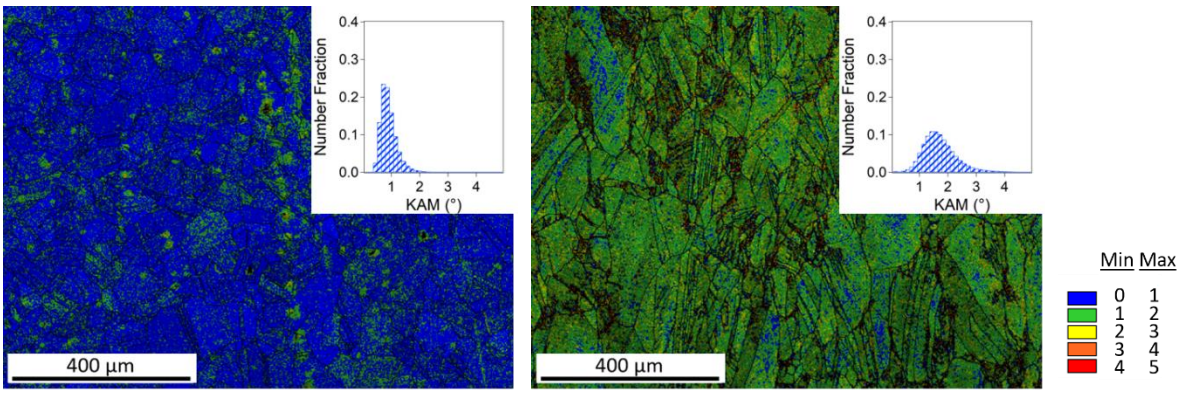

(a) (b)

Fig. E-24 First neighbor KAM+IQ cartographies of sample 4 at the initial state (a) and after deformation to failure (b). Color legend represents the kernel average misorientation in °.

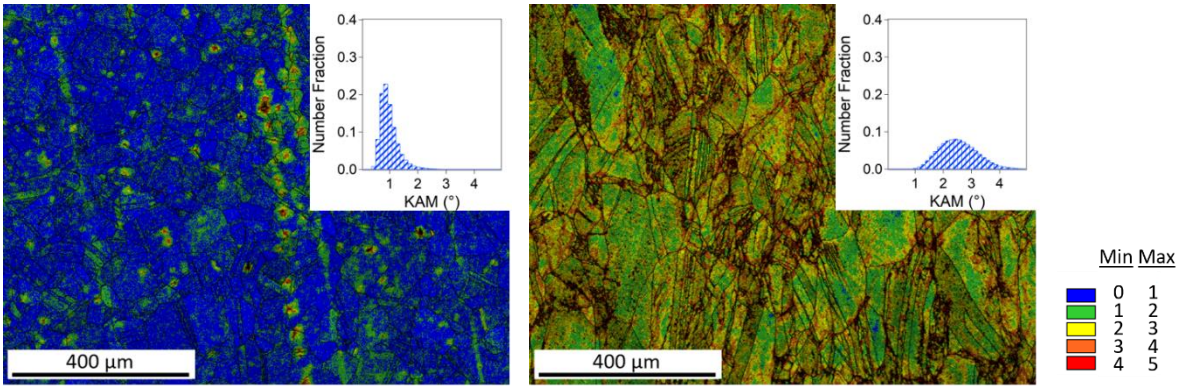

(a) (b)

Fig. E-25 Third neighbor KAM+IQ cartographies of sample 4 at the initial state (a) and after deformation to failure (b). Color legend represents the kernel average misorientation in °.

LIST OF TABLES

LIST OF FIGURES

Résumé en français

Nickel à grains ultrafins : microstructure, propriétés mécaniques et stabilité thermique

Table des matières

1. INTRODUCTION

La métallurgie moderne a besoin de nouvelles méthodes de synthèse pour améliorer les propriétés des matériaux utilisés. Par exemple, le durcissement obtenu en réduisant la taille de grains permet d'alléger les structures en conservant une tenue mécanique équivalente. Les métaux à grains ultrafins (UFG) avec une taille de grains d < 1 µm, permettent une amélioration de la tenue mécanique, mais présentent néanmoins des inconvénients comme une faible ductilité et une faible stabilité thermique.

Une vaste littérature concernant les matériaux UFG ainsi que les matériaux nanostructurés est disponible, mais des contradictions concernant leurs propriétés intrinsèques en ressortent. En effet, la méthode de synthèse a un impact important sur les caractéristiques finales des échantillons, et il est difficile de trouver des études complètes relatives aux effets de la microstructure sur les propriétés mécaniques et physiques mesurées sur de mêmes échantillons.

La synthèse des métaux UFG est principalement réalisée par déformation plastique sévère (SPD) ou par métallurgie des poudres (MP). Les techniques SPD consistent à déformer des échantillons métalliques en appliquant de fortes contraintes afin d'atteindre l'énergie nécessaire pour affiner la microstructure en petits grains à l'échelle UFG. D'autre part, la métallurgie des poudres utilise une température inférieure à la température de fusion pour activer la diffusion à l'état solide afin de compacter des poudres de taille nanométrique ou nanostructurées en échantillons de haute densité.

Les techniques SPD sont les plus étudiées, et permettent la production d'échantillons cylindriques avec une taille de grains d = 150-300 nm sans contamination supplémentaire. Cependant, la réduction de la taille de grains par déformation sévère aboutit à une microstructure métastable avec des contraintes internes élevées. D'un point de vue pratique, le manque d'homogénéité ainsi qu'une limitation de la taille et de la géométrie des échantillons constituent des inconvénients supplémentaires.
Les techniques de MP sont quant à elles adéquates pour la production de métaux UFG homogènes avec des faibles contraintes résiduelles. À cette fin, des techniques de frittage flash, consistant à presser et chauffer simultanément les poudres, sont utilisées. Le Spark Plasma Sintering (SPS) est une bonne option car sa vitesse de chauffage élevée réduit le temps de frittage et limite la croissance de la taille de grains. Avec cette technique et à l'échelle du laboratoire, des échantillons cylindriques d'un diamètre de 10 à 80 mm peuvent être réalisés avec des caractéristiques homogènes dans tout le volume. Le redimensionnement pour répondre aux besoins industriels est réalisable car il consiste à ajuster la quantité nécessaire de poudre pour produire la pièce. Par ailleurs, les premiers produits commerciaux élaborés par ces procédés sont déjà sur le marché [1]. Récemment [2], un brevet concernant la fabrication

des échantillons avec des géométries complexes par SPS a été développé. Cela signifie qu'aucune mise en forme après synthèse n'est nécessaire, ce qui rend encore plus attrayante cette technique.

La métallurgie des poudres est une industrie en plein développement, très utilisée dans différents domaines tels que l'électronique aérospatiale, l'industrie de l'énergie nucléaire, les technologies à usage médical ou dentaire et notamment dans l'industrie automobile [3–5]. La raison principale pour choisir la MP plutôt que d'autres méthodes de fabrication est la combinaison des qualités représentées en Fig. 1-1.

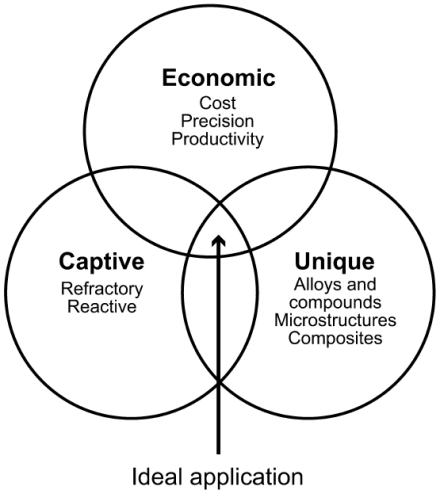

Fig. 1-1 Diagramme de Venn des attributs recherchés lors du choix d'une technique de synthèse. Les techniques de métallurgie des poudres correspondent à l'intersection des trois cercles [6].

Les différents procédés de MP permettent la production de matériaux difficiles voire impossibles à fabriquer par d'autres méthodes tels que le carbure de tungstène, ainsi que des alliages avec des microstructures uniques [7–9]. Egalement, le marché est très concurrentiel car les procédés de fabrication sont économiques d'un point de vue matériaux et énergie par rapport à d'autres technologies de formage des métaux telles que le moulage, le forgeage et le décolletage (Fig. 1-2). De plus, les techniques de MP sont considérées comme des technologies vertes car environ 80 % en poids de la matière première utilisée pour la fabrication provient de déchets recyclés[1].

[1] « Vision 2025 Future Developments for the European PM Industry » The European PM Industry Roadmap, January 2015.

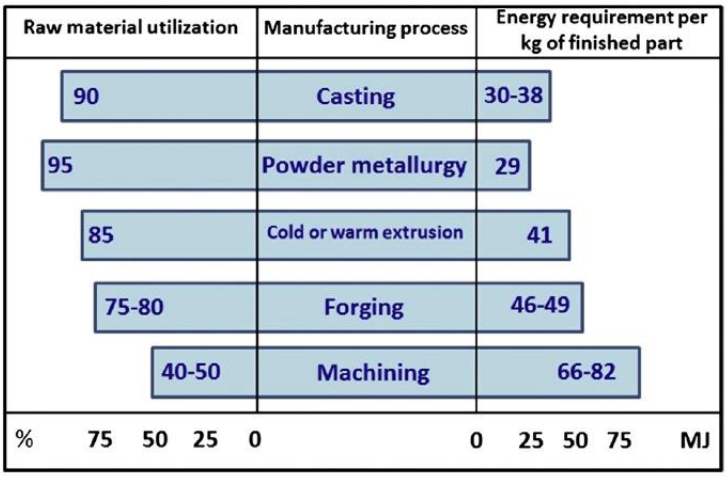

Fig. 1-2 Comparaison de l'utilisation des matières premières et de l'énergie en fonction du procédé de fabrication [10].

Les propriétés des pièces fabriquées par MP peuvent être ajustées en choisissant de manière appropriée le matériau et le processus pour obtenir la microstructure requise [6]. Une large gamme de matériaux utilisés dans l'industrie peut être traitée pour produire des formes très complexes nécessitant peu ou pas d'usinage par la suite (Fig. 1-3). La procédure de synthèse conventionnelle est toujours très utilisée. Elle consiste à presser un mélange de poudres métalliques et de lubrifiant dans une matrice, puis à la pièce est chauffée pour confectionner la pièce métallique. Néanmoins, au cours des deux dernières décennies, d'autres techniques ont été mises au point pour s'adapter aux nouveaux besoins. Ces techniques incluent le moulage par injection, la compression isostatique à chaud et la fabrication additive.

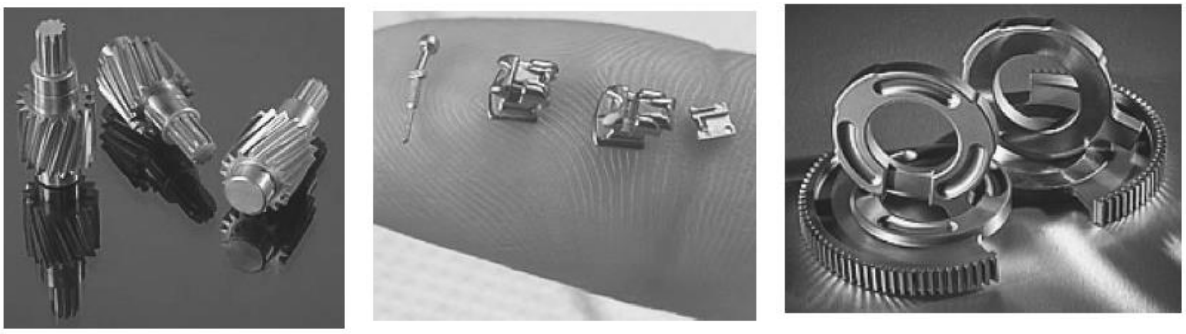

(a) (b) (c)

Fig. 1-3 Pièces présentant des formes complexes fabriquées par MP. Engrenage hélicoïdal et pignon droit (a). Support, glissière et crochet d'un système orthodontique (b). Secteur denté et anneaux fixes (c) [6].

Cette brève introduction à l'industrie de la MP montre l'intérêt d'étudier plus en profondeur les propriétés des matériaux produits par ces moyens. De plus, combiner les avantages de la MP avec des microstructures UFG semble très prometteur et constitue le cadre de cette étude.

Les échantillons UFG peuvent être produits par MP en utilisant des nanopoudres ou des poudres nanostructurées. Les travaux trouvés dans la littérature se concentrent sur l'utilisation de nanopoudres qui présentent malheureusement une quantité importante d'oxydes. Néanmoins, l'utilisation de poudres nanostructurées obtenues par broyage (BM) permet la synthèse d'échantillons avec une taille de grains réduite sans oxydation sous certaines conditions. À ce jour, une étude complète des possibilités de coupler le BM et le SPS pour produire des métaux UFG fait défaut. Le but de cette étude est d'étudier le nickel en tant que matériau modèle, depuis la synthèse de la poudre en passant par la densification jusqu'à l'étude de l'évolution des propriétés mécaniques et physiques d'échantillons avec différentes tailles de grains.

Premièrement, des échantillons avec des tailles de grains dans le domaine UFG ont été élaborés à partir de différentes poudres précurseurs. Pour ce faire, les paramètres de BM ont été modifiés pour produire diverses poudres à partir de la poudre commerciale. Les poudres ont ensuite été consolidées par SPS, technique de frittage choisie pour le temps de traitement court et les bons résultats en termes de densité. Une caractérisation minutieuse des microstructures des échantillons frittés a été réalisée par des analyses de diffraction d'électrons rétrodiffusés (EBSD) pour extraire des informations telles que la taille de grains, la distribution de la nature des joints de grains (GBCD) et les désorientations intragranulaires. D'autre part, les contraintes internes relatives sont discutées à partir des mesures de désorientation à l'intérieur des grains et de l'identification des structures de dislocations par microscopie électronique à transmission (MET) pour des échantillons sélectionnés.

Ensuite, des essais de traction uniaxiale ont été effectués sur des échantillons avec différentes tailles de grains afin de caractériser les propriétés mécaniques suivantes: la limite d'élasticité, la résistance maximale (UTS), la déformation uniforme et la déformation à rupture. De plus, les mécanismes d'écrouissage ont été étudiés pour une meilleure compréhension de l'effet de la réduction de la taille de grains dans la gamme UFG sur la déformation plastique. Les structures de dislocations à la rupture pour des échantillons sélectionnés ont été étudiées pour éclairer les discussions sur le durcissement ainsi que pour rechercher la présence de structures de dislocations spécifiques à l'état déformé.

Enfin, le comportement des microstructures sous énergie thermique (chaleur) a été étudié dans deux domaines. D'une part, à basse température (400 K), la diffusion aux joints de grains (JdGs) a été analysée à l'aide de traceurs radioactifs pour examiner les chemins à forte diffusivité. D'autre part, à haute température (jusqu'à 1123 K), la stabilité de la microstructure ainsi que la densification rétrograde des échantillons produits à partir de poudres BM ont été étudiées. La conclusion de ce rapport combinera les différents résultats obtenus en fournissant une vue d'ensemble de la relation synthèse/microstructure/propriétés, des échantillons UFG obtenus par MP.

2. SYNTHESE ET CARACTERISATION DE NI A GRAINS ULTRAFINS OBTENU PAR MP

Tout d'abord, nous avons étudié la possibilité d'utiliser le BM associé au SPS pour élaborer des échantillons bien densifiés présentant des tailles de grain comprises dans les gammes grains fins (FG) et UFG. À cette fin, la synthèse de la poudre nanostructurée et sa consolidation ont été étudiées. Les principales caractéristiques microstructurales des échantillons frittés ont ensuite été caractérisées.

L'évolution de la poudre d'une morphologie sphérique à une morphologie aplatie lors de l'augmentation du temps de broyage et de la vitesse de rotation a été mise en évidence par des observations en microscopie électronique à balayage (MEB) (Fig. 2-1).

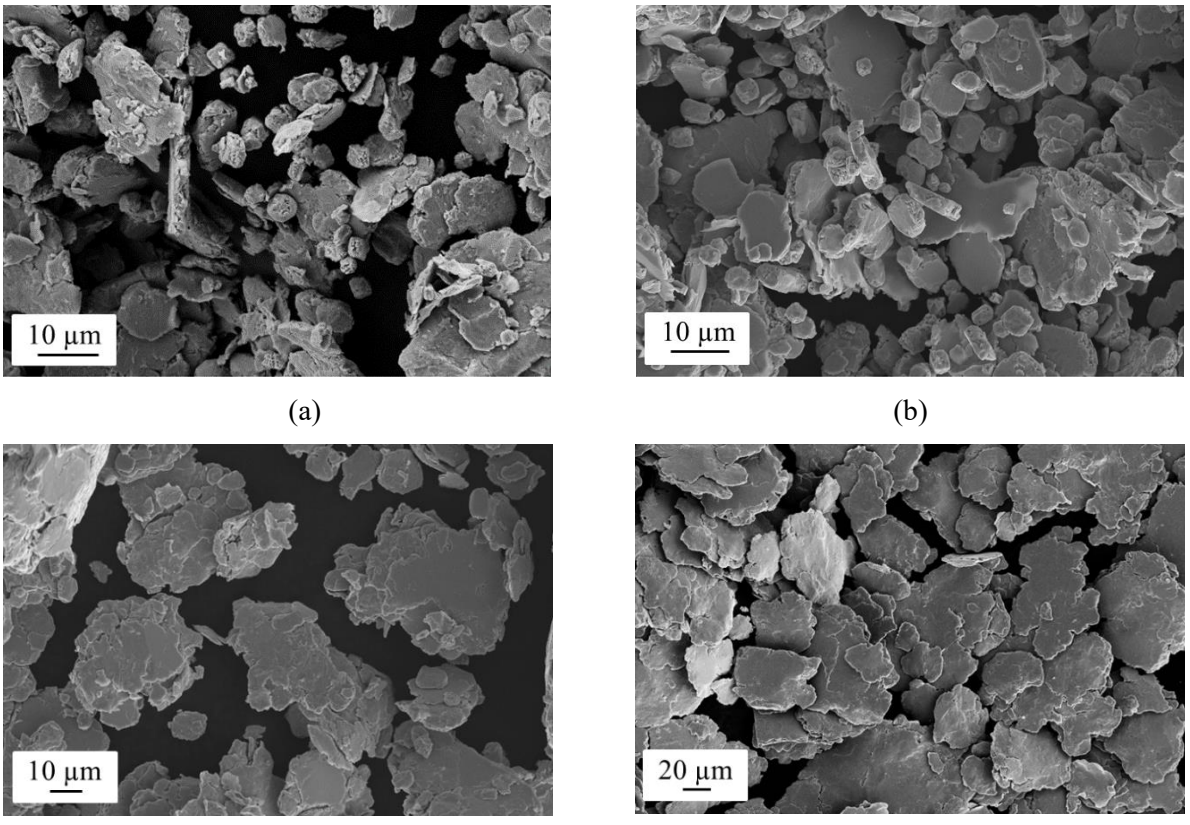

Fig. 2-1 Images MEB de poudres de Ni obtenues après broyage pendant 3 h avec 66.7 wt.% de méthanol à une vitesse de rotation de: 200 rpm (a), 250 rpm (b), 300 rpm (c) et 350 rpm (d).

Les diffractogrammes obtenus par diffraction de rayons X (DRX) ont montré une orientation cristallographique préférentielle proche de la valeur aléatoire pour toutes les poudres, ainsi que l'absence de pics correspondant à NiO ou à d'autres contaminants. D'autre part, l'analyse EBSD effectuée sur la poudre obtenue avec les conditions de broyage les plus sévères confirme la nature fortement déformée

de la poudre. Les différences de morphologie et d'état de déformation de la poudre ont un effet sur la cinétique de frittage, visible sur les courbes de déplacement du piston avec la température (Fig. 2-2). Les poudres plus homogènes montrent une meilleure densification et ont besoin de moins de temps de frittage pour atteindre une bonne densité. Les échantillons produits présentent une densité relative ≥ 96 % , supérieure à la valeur obtenue pour les échantillons fabriqués à partir de poudres nanométriques [11,12].

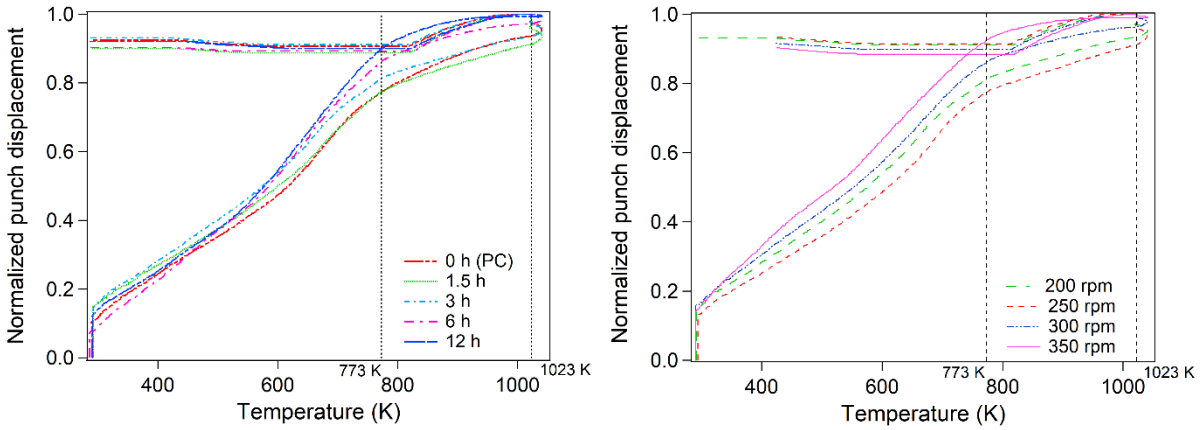

(a) (b)

Fig. 2-2 Procédé de frittage étudié à partir du déplacement relatif du piston en fonction de la température pour la poudre commerciale et les poudres nanostructurées obtenues avec différents temps de broyage (a) et des vitesses de rotation croissantes avec un temps de broyage de 3 h (b).

La réduction de la taille de grains dans la gamme UFG a été obtenue avec différentes associations de paramètres de BM que sont le temps de broyage, la vitesse de rotation et la quantité de méthanol. Il a été montré que la meilleure combinaison pour obtenir un faible taille des grains est 10 h de broyage à 350 rpm avec 66.7 wt.% de MeOH (Fig. 2-3).

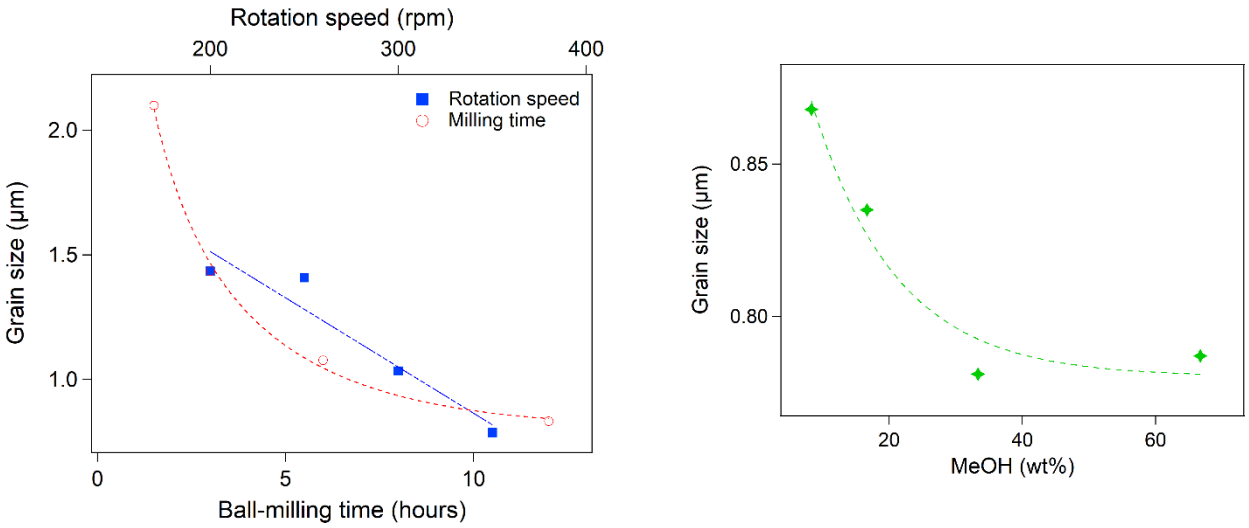

(a) (b)

Fig. 2-3 Taille de grains en fonction du temps de broyage (200 rpm, 66,7 wt.% de méthanol), de la vitesse de rotation (3 h, 66,7 wt.% de MeOH) (a) et de la quantité de MeOH (350 rpm, 3 h) (b).

Des natures distinctes de joints de grains (GBCD) ont été observées selon la poudre utilisée, montrant une corrélation avec la taille des grains (Fig. 2-4). La fraction élevée de joints de grains Σ3 observée dans les échantillons frittés diminue avec la taille de grains tandis que les fractions de JdG de faible désorientation (LAGB) et les JdG de forte désorientation (HAB) augmentent.

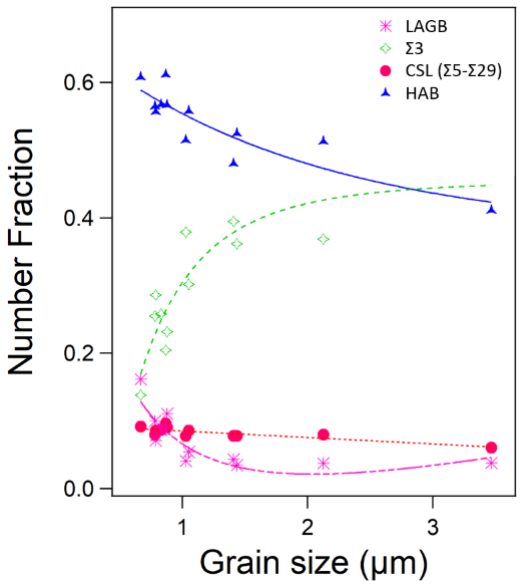

Fig. 2-4 Fraction des différents types de JdG observés dans le Ni UFG fritté en fonction de la taille de grains.

Ces différences sont liées aux processus de restauration et de recristallisation se déroulant pendant le frittage. L'anisotropie de la mobilité des joints de grains rend la microstructure de l'échantillon fritté dépendante de la microstructure de la poudre utilisée. Ainsi, les échantillons préparés à partir de poudres BM présentent des fractions de LAGB plus élevées. Cette conclusion peut être corroborée par la comparaison de la distribution des angles de désorientation, comme il est montré ici pour un échantillon de Ni UFG préparé à partir d'une poudre BM (Fig. 2-5 (a)) confronté à un échantillon obtenu à partir de poudres nanométriques (Fig. 2-5 (b)). Les deux échantillons présentent un pic important à 60° correspondant aux JdG Σ3, caractéristiques de la technique de synthèse par frittage. Néanmoins, il existe une différence dans la fraction de LAGB, qui est caractéristique des poudres BM corrélées à la technique SPD.

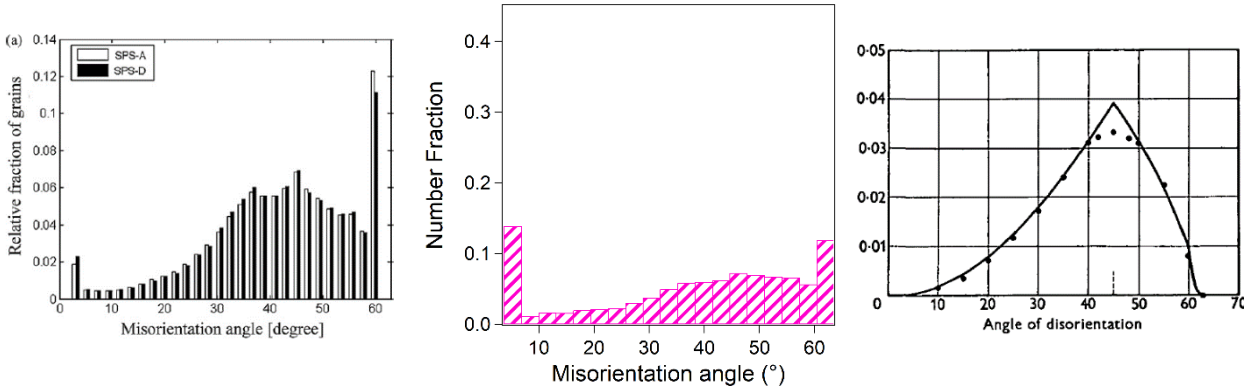

(a) (b) (c)

Fig. 2-5 Distribution des angles de désorientation des échantillons préparés à partir des poudres nanométriques [13] (a) et d'une poudre broyée (b). À titre de comparaison, la distribution de la désorientation aléatoire de Mackenzie pour les structures cubiques est indiquée (c) [14].

Enfin, des mesures de dispersion d'orientation (GOS) ont montré un niveau de contraintes internes faible pour l'état initial des échantillons frittés (Fig. 2-6). La valeur moyenne centrée à 0.5° est proche de la valeur observée dans des échantillons bien recristallisés. Néanmoins, un taux plus important de déformation des grains avec une valeur de GOS sensiblement plus élevée est observée.

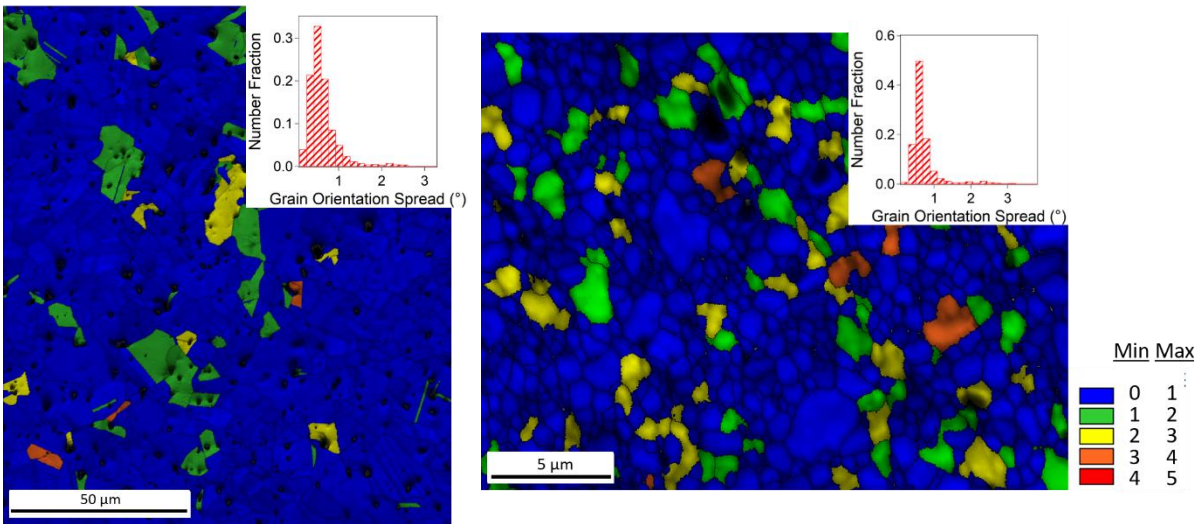

(a) (b)

Fig. 2-6 Cartographies GOS superposées à des cartographies IQ (qualité d'image) obtenues à partir de données EBSD acquises pour l'état initial d'un échantillon UFG (a) et FG (b). La distribution des valeurs GOS pour chaque échantillon est affichée dans l'encart de chaque microstructure.

Les observations par MET des structures de dislocations pour des échantillons sélectionnés montrent une faible densité de dislocations (Fig. 2-7) dans les échantillons FG ainsi que les échantillons UFG. Ces résultats sont en concordance avec les mesures de GOS.

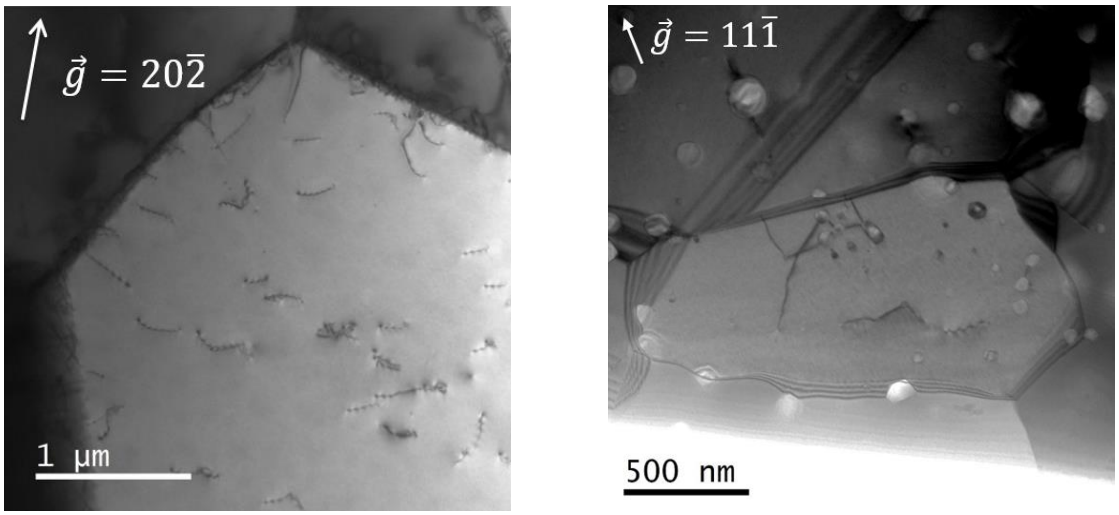

(a) (b)

Fig. 2-7 Images MET d'un échantillon FG (a) et UFG (b) montrant des grains avec une faible densité de dislocations.

3. PROPRIETES MECANIQUES ET MECANISMES DE PLASTICITE DU NI UFG OBTENU PAR MP

Afin d'étudier l'influence de la taille de grains dans la gamme FG/UFG sur les propriétés mécaniques et les mécanismes de plasticité, cinq échantillons ont été synthétisés. Trois échantillons ont été frittés à partir de poudres BM et deux à partir de la poudre commerciale. Ces échantillons présentent des tailles de grains comprises entre 0.82 µm et 25 µm. Des essais de traction uniaxiale ont ensuite été effectués à une vitesse de déformation de 10^{-3} s^{-1}, et les courbes de traction conventionnelles obtenues sont montrées dans la Fig. 3-1. L'augmentation de la limite d'élasticité avec l'affinement de la taille de grains et une ductilité élevée pour tous les échantillons sont les caractéristiques les plus remarquables.

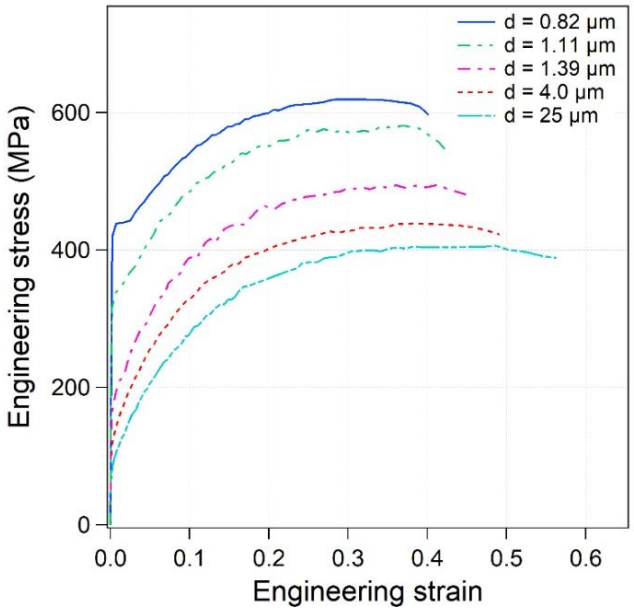

Fig. 3-1 Courbes conventionnelles de traction obtenues pour 5 échantillons frittés par SPS.

L'étude de l'influence de la taille des grains sur la limite d'élasticité montre une déviation (**Fig. 3-2** (a)) du comportement attendu par la loi de Hall-Petch [15]:

$$\sigma_y = \sigma_0 + k_{HP}\frac{1}{\sqrt{d}} \tag{3.1}$$

où σ_0 est la contrainte de friction en l'absence de joints de grains et k_{HP} représente la constante HP, qui donne des informations sur la sensibilité du matériau à la présence de joints de grains. En effet, une capacité d'écrouissage plus faible a été observée pour les échantillons UFG par rapport aux échantillons CG, ce qui entraine une déformation hétérogène à des faibles niveaux de déformation dans les échantillons UFG (Fig. 3-2 (b)).

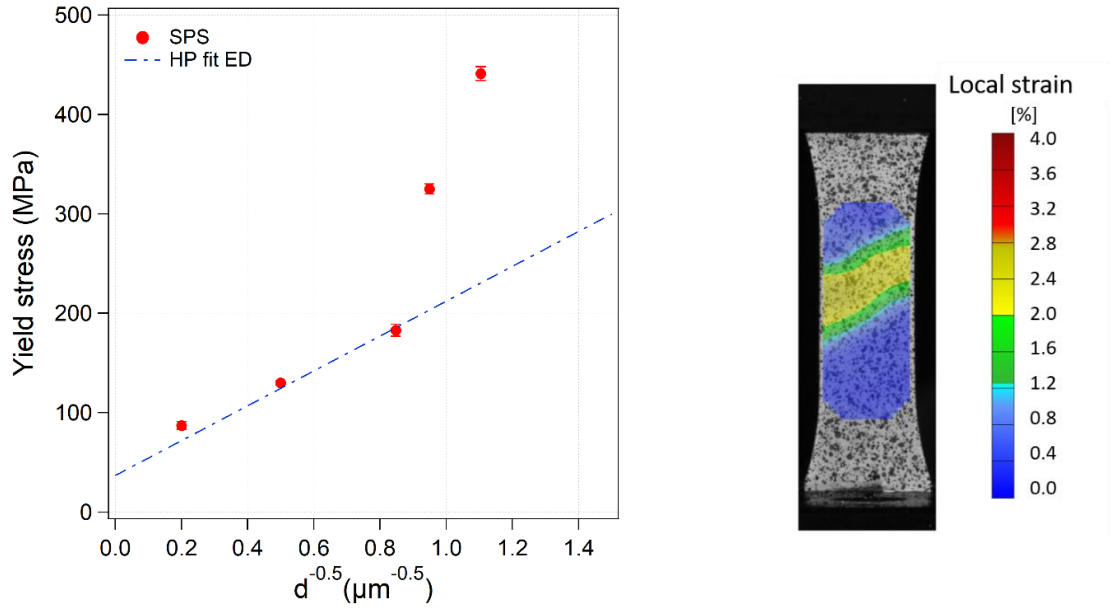

(a) (b)

Fig. 3-2 Influence de la taille de grains sur la limite d'élasticité (a). Cartographie de déformation obtenue par corrélation d'images qui montre une déformation hétérogène pour un échantillon UFG à une déformation vraie de $\varepsilon = 0.009$ (b).

La ductilité en fonction de la taille de grains a aussi été étudiée pour les échantillons frittés (**Fig. 3-3** (a)). Une ductilité moindre est observée pour les échantillons avec une taille de grains plus petite comme conséquence de la plus faible capacité d'écrouissage des UFG (Critère de Considère [16]). La différence est plus importante dans le cas de l'élongation à rupture, car la présence de petites porosités très proches dans les échantillons UFG facilite la coalescence des trous formés autour de celles-ci, donnant lieu à une rupture prématurée. Les faciès de rupture (**Fig. 3-3** (b)-(c)) montrent une rupture ductile pour tous les échantillons.

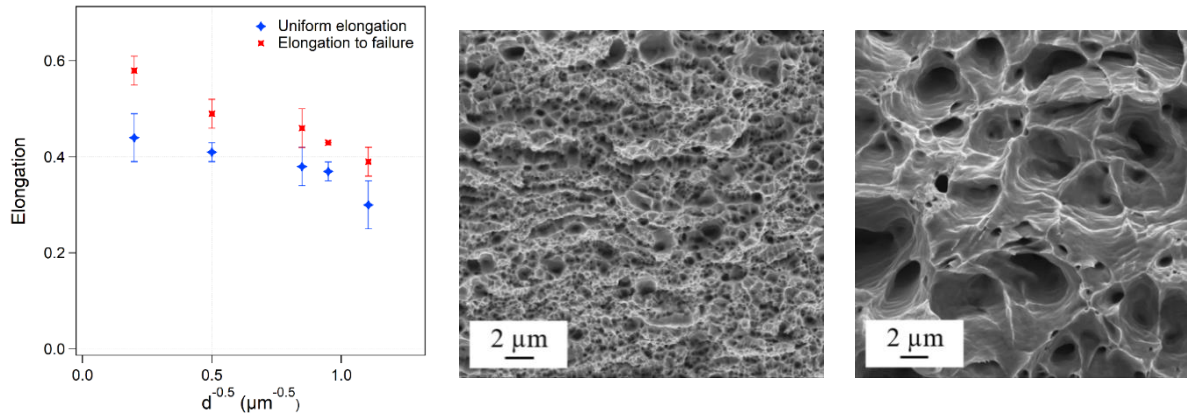

(a) (b) (c)

Fig. 3-3 Influence de la taille des grains sur la ductilité (a). Images MEB du faciès de rupture d'un échantillon UFG (d = 0.82 μm) (b) et d'un échantillon FG (d = 4 μm) (c).

L'évolution de la contrainte avec la déformation, c'est-à-dire l'écrouissage, est cruciale d'un point de vue technologique, car elle fournit des informations importantes sur la formabilité des matériaux. Egalement d'un point de vue physique, l'étude de l'écrouissage révèle des informations concernant les mécanismes de plasticité des métaux. L'évolution du taux d'écrouissage (θ_h) avec la contrainte pour des échantillons avec différentes tailles de grains est montrée dans la Fig. 3-4 (a). Il est montré une allure similaire pour tous les échantillons, avec des courbes décalées vers des valeurs de contrainte plus importantes pour les échantillons de petite taille de grains. Ce décalage provient des différences de contrainte et notamment de limite d'élasticité. Une normalisation du taux d'écrouissage est donc nécessaire (Fig. 3-4 (b)). Comme les résultats précédents l'indiquent, un taux d'écrouissage plus faible est observé pour les échantillons UFG.

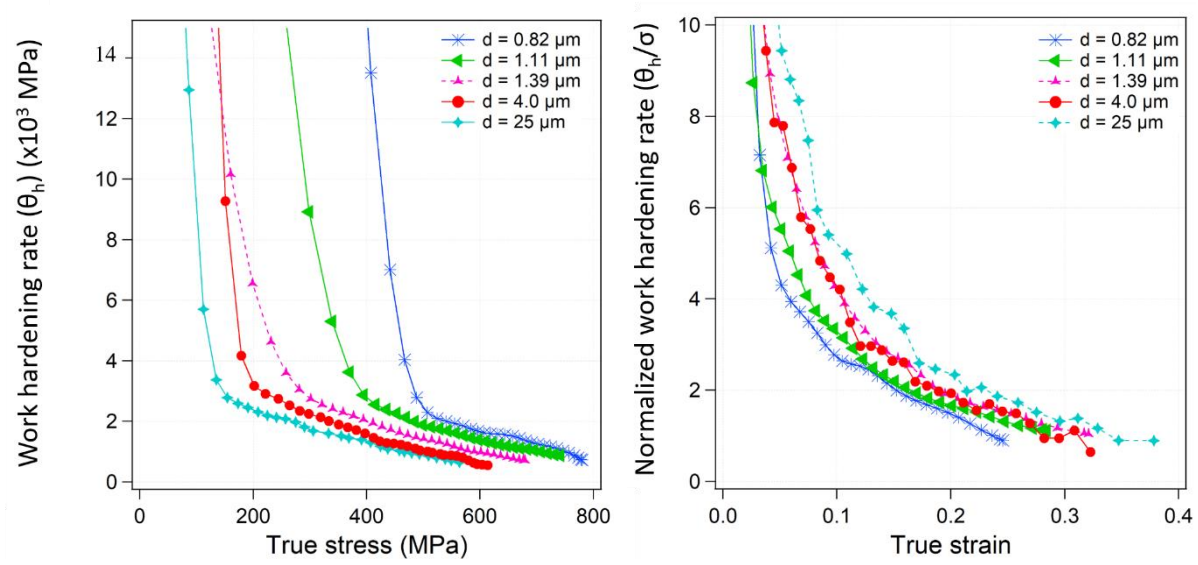

(a) (b)

Fig. 3-4 Evolution du taux d'écrouissage avec la contrainte vraie (a) et évolution du taux d'écrouissage normalisé avec la déformation vraie (b) pour cinq échantillons de Ni préparés par SPS.

Ainsi, l'écrouissage a été examiné avec le modèle de Mecking-Kocks [17–19], modèle physique basé sur la dynamique des dislocations. Un deuxième stade d'écrouissage relativement court est observé pour les échantillons UFG, ce qui suggère un glissement dévié généralisé très tôt dans la déformation. Ces conclusions ont été complétées par des analyses EBSD des échantillons après fracture. Des grains allongés et orientés dans la direction de la traction peuvent être observés (Fig. 3-5). Une différence est néanmoins visible entre l'échantillon de plus grande taille de grains (Fig. 3-5 (c)) et l'échantillon de taille de grains plus petite (Fig. 3-5 (a)). Ce dernier présente des grains plus équiaxes et moins orientés que le premier.

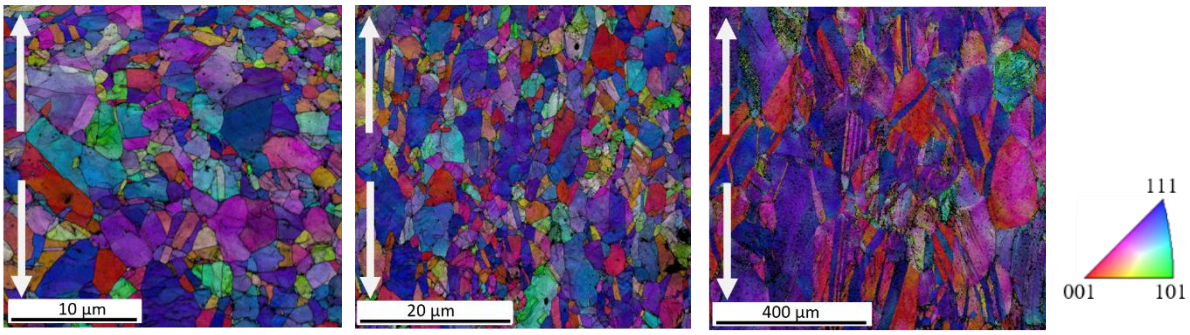

(a) (b) (c)

Fig. 3-5 Superposition des cartographies IPF (figure de pôles inverse) + IQ pour des échantillons déformés à rupture avec des tailles de grains d = 0,82 µm (a), d = 1,39 µm (b) et d = 25 µm (c) avec la direction de la traction comme référence. Les flèches blanches indiquent le sens de la traction.

Avec des cartographies Kernel, des faibles désorientations autour d'un point dans un grain peuvent être mesurées et liées à la présence des structures de dislocations. La présence considérable de faibles désorientations dans l'échantillon dont la taille de grain est la plus petite suggère un manque de cellules de dislocations et une accumulation préférentielle des dislocations aux JdGs (Fig. 3-6 (a)). Des désorientations plus importantes sont présentes dans l'échantillon de plus grande taille des grains, dans les JdGs et à l'intérieur des grains.

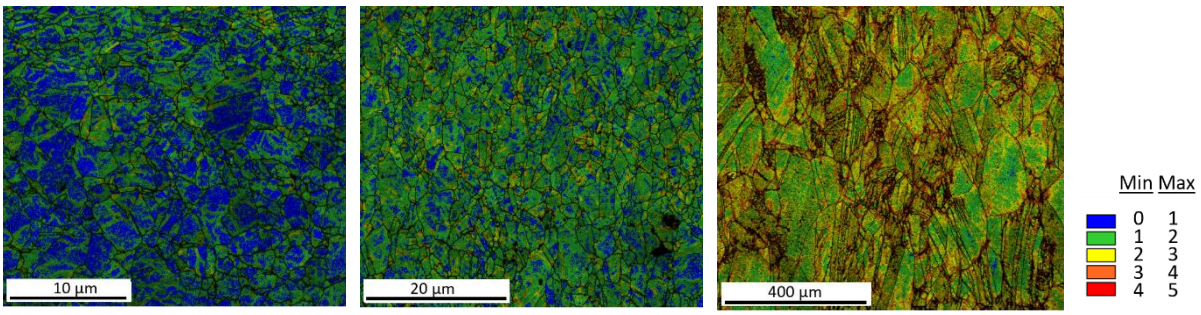

(a) (b) (c)

Fig. 3-6 Cartographies Kernel superposées sur des cartographies IQ pour des échantillons déformés à rupture avec des tailles des grains d = 0,82 µm (a), d = 1,39 µm (b) and d = 25 µm (c). La légende couleurs rapporte la désorientation Kernel en °.

Ces résultats ont été confirmés par les observations MET, où des zones de contraste diffus (Fig. 3-7 (a)) constituent la caractéristique principale du Ni UFG déformé, contrairement aux cellules de dislocations bien formées (Fig. 3-7 (b)) observées pour les échantillons FG. Des observations MET supplémentaires doivent être réalisées pour avoir une vision plus détaillée des mécanismes de déformation qui se produisent dans le régime UFG.

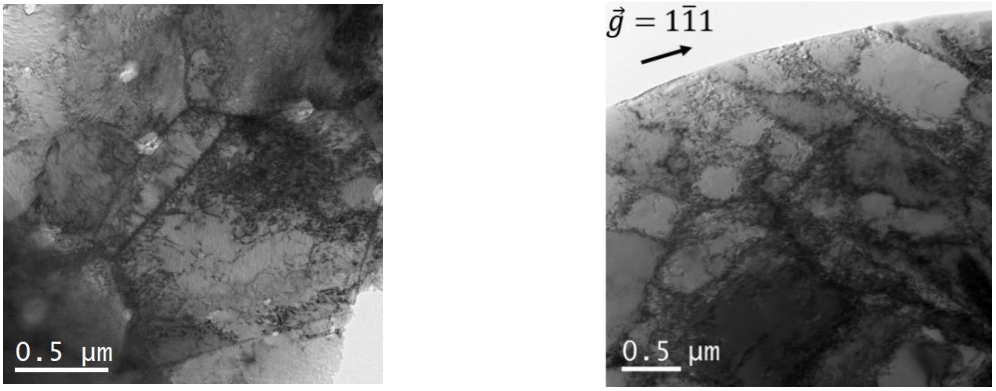

(a) (b)

Fig. 3-7 Images MET des grains dans l'échantillon avec une taille de grains d = 0,82 μm (a) et d'une partie d'un grain de l'échantillon avec une taille de grains d = 4,0 μm (b).

Les métaux UFG ont longtemps été étudiés dans le but d'obtenir des matériaux de très haute résistance. Néanmoins, la nécessité de trouver un bon compromis entre résistance et ductilité a motivé l'étude de microstructures présentant des tailles de grains comprises dans la gamme FG/UFG ainsi que des populations de tailles de grains différentes telles que les distributions bimodales. Les résultats concernant les propriétés mécaniques des échantillons de Ni frittés par SPS avec des tailles de grains différentes ont été présentées dans les paragraphes précédents. Tous les échantillons présentent une bonne combinaison de la résistance et de la ductilité, en particulier ceux du régime UFG. La relation entre la limite d'élasticité et la ductilité mesurée dans cette étude peut être tracée à côté des résultats d'échantillons de Ni obtenus avec différentes techniques de synthèse décrites dans la littérature (Fig. 3-8).

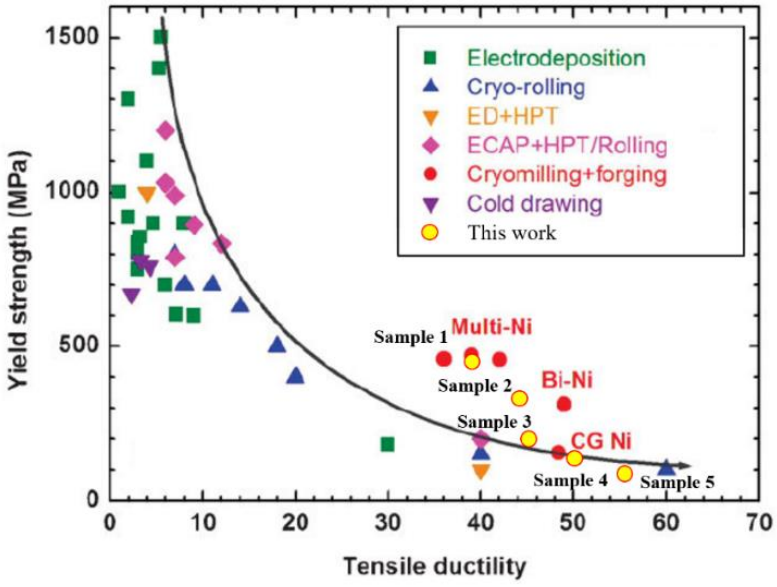

Fig. 3-8 Limite d'élasticité en fonction de l'allongement à rupture obtenue d'après [20]. Les points jaunes et rouges indiquent un bon compromis résistance mécanique/ductilité. Les points jaunes correspondent aux échantillons étudiés dans ce travail.

Les échantillons nanostructurés et UFG préparés selon les techniques d'électrodéposition (ED) et SPD sont présentés à l'extrémité gauche de la figure. Ils présentent une résistance élevée et une faible ductilité. À l'extrémité droite, les échantillons préparés par métallurgie des poudres sont représentés en rouge et en jaune. Les points rouges représentent des échantillons préparés par cryobroyage de poudres et consolidation par forgeage, lesquels présentent des tailles de grains dans la gamme FG (1-3 μm) et des microstructures à distribution de tailles bimodales ou multimodales. Au vu de ces résultats, une variation de la distribution granulométrique représente à ce jour le meilleur moyen de parvenir à un bon compromis. Néanmoins, les échantillons unimodaux de la gamme FG/UFG préparés par BM et SPS présentent également de très bonnes propriétés mécaniques.

4. ETUDE DE LA DIFFUSION AUX JDGS ET DE LA STABILITE THERMIQUE DU NI UFG OBTENU PAR MP

La diffusion aux joints des grains (JdGs) est un paramètre clé dans des nombreux phénomènes qui s'appliquent aux matériaux, à savoir le fluage, le frittage, l'oxydation, la recristallisation ou la croissance granulaire. Ces derniers se déroulent à haute température mais la diffusion aux JdGs à basse température ou même à température ambiante peut également modifier les propriétés de certains matériaux et, par exemple, limiter la durée de vie des métaux utilisés dans des dispositifs microélectroniques [21]. Une diffusivité élevée a été rapportée pour des échantillons nanocristallins produits par MP à partir de nanopoudres. Par conséquent, les échantillons UFG synthétisés à partir de poudres BM pourraient également présenter une diffusivité inhabituelle ultra-rapide. De plus, à l'instar du Ni UFG préparé par des techniques de SPD comme le « equal channel angular pressing » ou le « high pressure torsion » ([22],[23]), il est pertinent de penser que le BM pourrait entraîner la formation de joints de grains « modifiés par déformation » [24]. Les dislocations extrinsèques aux JdGs caractérisent l'état de « non-équilibre » de ces joints, et la relaxation par annihilation partielle peut être accomplie à des températures élevées par montée des dislocations [25]. Dans ce chapitre, la diffusion de JdGs à basse température a été étudiée pour trois échantillons synthétisés par frittage SPS dans le régime FG/UFG (Tableau 4-1).

Tableau 4-1 Caractéristiques des échantillons synthétisés pour l'étude de la diffusion aux JdG.

Echantillon	*Poudre*	*Densité relative (%)*	*Taille de grains (µm)*	*Gamme*
S1	Commerciale	96.0 (8)	3.2 ± 1.8 (3)	FG
S2	Poudre BM 3 h, 300 rpm et 8 g de MeOH	97.8 (9)	1.69 ± 1.25 (9)	FG
S3	Poudre BM 10 h, 350 rpm et 8 g de MeOH	98.1 (9)	0.86 ± 0.69 (5)	UFG

Dans l'étude de l'autodiffusion aux JdGs, quatre états différents ont été considérés pour chaque échantillon et sont résumés dans le Tableau 4-2. Le premier recuit de diffusion (E2) a été réalisé pour étudier la présence de chemins de diffusivité ultra-rapide. Ensuite, un deuxième recuit à 773 K (E3) a été choisi pour relaxer partiellement les JdGs hors-équilibre, s'ils étaient présents dans les échantillons. Enfin, un dernier recuit de diffusion (E4) a été réalisé dans les mêmes conditions que E2 pour étudier l'effet des recuits accumulés sur le comportement en diffusion des échantillons.

Tableau 4-2 Caractéristiques de chaque état de recuit. En gras les états correspondant aux recuits de diffusion.

Etat	*Condition*
E1	Etat initial après frittage
E2	**400 K pendant 3 jours**
E3	E2 + 773 K pendant 17 h
E4	**E3 + 400 K pendant 3 jours**

La diffusion aux JdGs est couramment étudiée par la détermination du coefficient de diffusion aux JdGs (D_{JdG}), pour lequel une valeur plus élevée signifie une diffusion plus rapide. La diffusivité à la température de cette étude pour du Ni pur peut être calculée ainsi :

$$D_{JdG} = \frac{1}{4t}\left(-\frac{\partial ln\bar{c}}{\partial y^2}\right)^{-1} \quad (4.1)$$

où t est le temps de recuit, y la distance de pénétration du traceur et $\bar{c}$ la concentration du traceur. Chaque échantillon présente une diffusivité ultra-rapide avec des profils de diffusion singuliers qui indiquent une hiérarchie différente de chemins de diffusivité (Fig. 4-1).

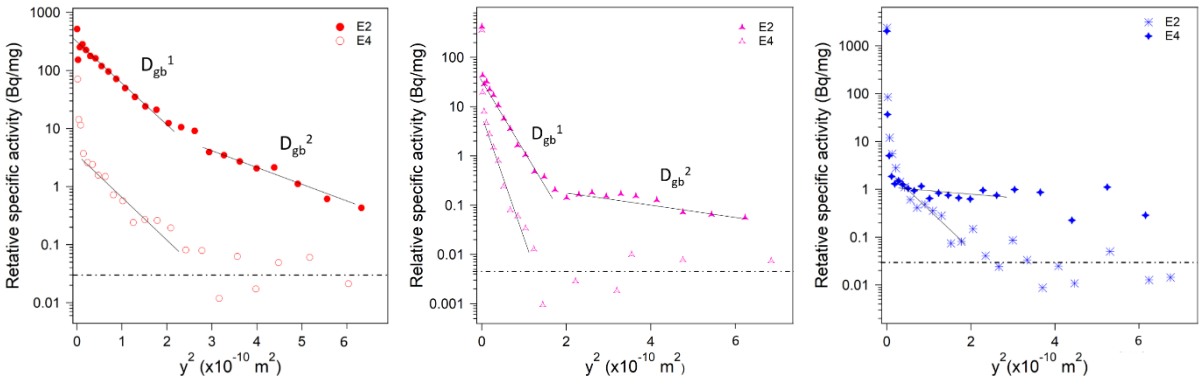

Fig. 4-1 Profils de pénétration des échantillons S1 (a), S2 (b) et S3 (c) pour les états E2 et E4 tracés en activité spécifique relative en fonction de y^2. Niveau du bruit de fond indiqué par une ligne pointillée.

L'échantillon S1 présente une similitude entre les premières pentes de chaque état (E2 et E4), ce qui suggère qu'aucun changement n'est opéré dans l'échantillon après les trois recuits. Dans les échantillons S2 et S3, un changement de pente des profils de diffusion est observé entre les états E2 et E4. Dans le cas de l'échantillon S2, le taux de diffusion inférieur mesuré après recuits successifs (E4) suggère une relaxation des JdGs. A l'inverse pour l'échantillon S3, l'augmentation de la diffusivité aux JdGs entre E2 et E4 suggère la formation de pores interconnectés lors du recuit, ce qui a été confirmé par l'observation au MEB de la section transversale (Fig. 4-2).

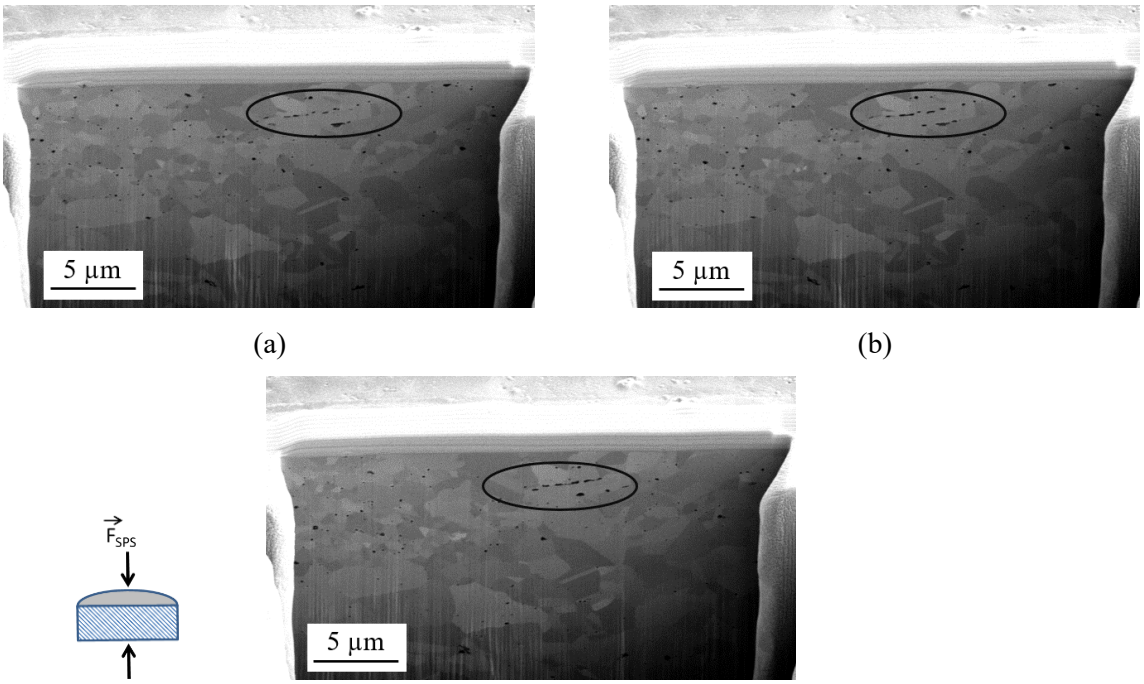

Fig. 4-2 Images MEB de l'échantillon S3 à l'état E4 après préparation par FIB (sonde ionique focalisée) à trois profondeurs consécutives. Indiqué en noir, la formation d'un chemin poreux continu.

Cette augmentation de la diffusion entrave la possibilité d'évaluer la présence de JdGs induits par la déformation dans S3 par ces moyens. S.V. Divinski [26] explique que les processus SPD n'engendrent pas tous des JdGs de diffusivité ultra-rapide, il est donc possible que le broyage ne les génère pas. Il expose également la possibilité de créer des joints de grains de « haute énergie » mais détendus, lorsque le SPD est effectué à des températures élevées par recristallisation. Il serait donc intéressant de poursuivre l'étude de la diffusivité aux JdGs dans les échantillons produits par BM et SPS.

Concernant l'échantillon S1 qui ne montrait pas des changement entre l'état E2 et E4, la préparation FIB et l'observation au MEB a révélé des porosités interconnectées complexes (Fig. 4-3). Des pores de grande taille situés principalement aux joints de grains se révèlent connectés quand on avance en profondeur dans l'échantillon.

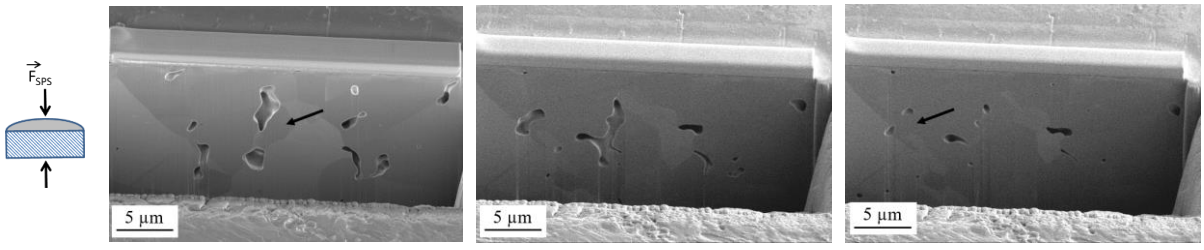

Fig. 4-3 Images MEB de l'échantillon S1 à l'état E1 après préparation par FIB à trois profondeurs consécutives. Les flèches indiquent deux pores qui s'interconnectent.

La grande pénétration du traceur (Fig. 4-1 (a)) et la stabilité du profil après différents recuits, suggère un régime cinétique de diffusion où le profil de diffusion est linéaire en $y^{6/5}$. La bonne linéarité des profils (Fig. 4-4) suggère que les porosités interconnectées seraient les principaux canaux de diffusion, avec des fuites vers les HAB relaxés.

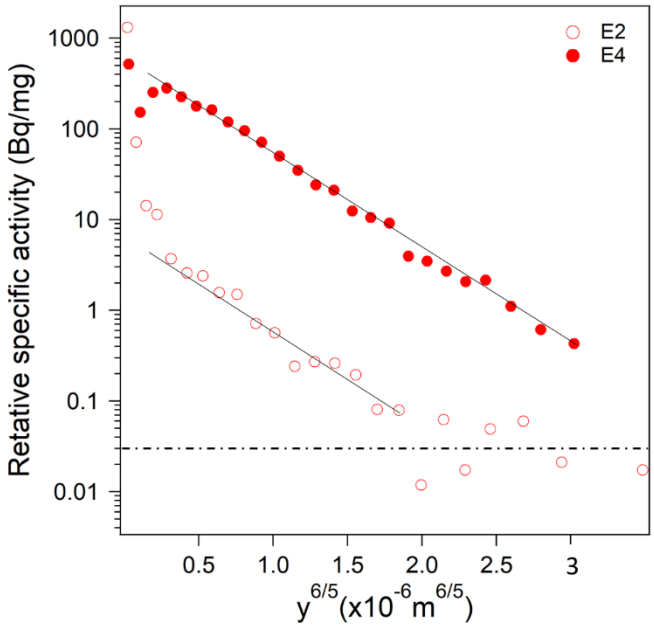

Fig. 4-4 Profils de pénétration de l'échantillon S1 dans les états E2 et E4 représentés en activité spécifique relative en fonction de $y^{6/5}$.

A partir de ces résultats, un coefficient de diffusion en « surface » (D_p) à travers les pores peut être estimé en utilisant l'hypothèse de S.V. Divinski *et al.* [27] pour une alliage γ-FeNi obtenu par frittage. Les valeurs obtenues sont $D_p = 1.40 \cdot 10^{-13}$ m^2/s et $D_p = 1.28 \cdot 10^{-13}$ m^2/s pour les états E2 et E4 respectivement. Ces valeurs pourraient servir de point de départ pour développer un modèle qui prend en compte les pores en tant que voies de diffusion ultra-rapide et aider à développer la compréhension actuelle de la diffusivité relative entre différents chemins de diffusion.

En ce qui concerne la stabilité thermique à haute température, le frittage rétrograde a été décrit par des mesures de dilatométrie dans des échantillons préparés à partir de poudres broyées à des températures supérieures à 1173 K (Fig. 4-5). L'échantillon S1 (préparé à partir de la poudre commerciale) ne présente pas un changement de volume persistant après refroidissement. Plus précisément, la densité relative dans S1 est de 96,1 (9) % avant la mesure et de 96,7 (9) % après, alors que la densité relative de l'échantillon S2 diminue de 98,3 (9) % à 94,3 (9) %. La différence de densité la plus importante est celle de l'échantillon S3 qui passe de 97,6 (9) % avant recuit, à 71,0 (9) % après refroidissement.

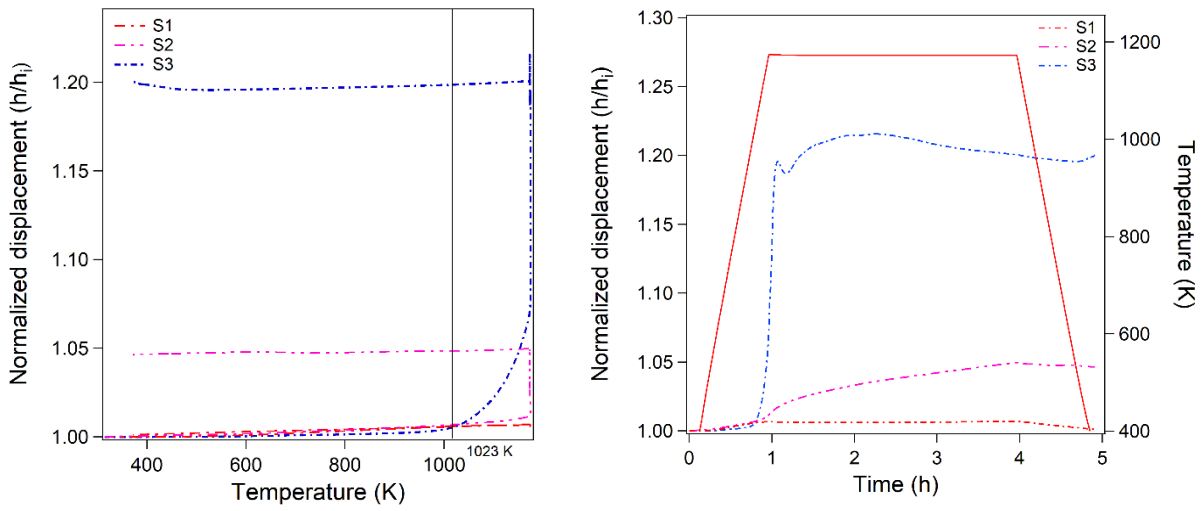

Fig. 4-5 Résultats de dilatométrie en déplacement normalisé par l'épaisseur initiale de l'échantillon en fonction de la température (a) et du temps (b). La ligne continue rouge en (b) correspond à la mesure de la température en fonction du temps.

La cinétique du processus de gonflement est clairement différente entre les échantillons S2 et S3. Dans le cas de l'échantillon S2, lorsque 1123 K est atteint, le volume augmente progressivement, tandis que dans l'échantillon S3, le changement s'effectue très rapidement et commence peu après le dépassement de la température de frittage. Dans le cas de nos échantillons, la densification rétrograde semble être liée au fluage du matériau sous des contraintes causées par la pression de gaz interne dans les pores. Les différences entre les structures de porosités peuvent ainsi rendre compte des divers comportements des échantillons S1, S2 et S3. Cependant, les résultats de l'étude sur la diffusion aux JdGs pour les échantillons S2 et S3 suggèrent que des défauts tels que des JdGs de haute énergie pourraient être présents dans ces échantillons et contribuer à l'instabilité à haute température. En effet, pour l'échantillon S3, des pores micrométriques peuvent être observés aux points triples (Fig. 4-6 (a)) ainsi que des chemins poreux continus (Fig. 4-6 (b)) provenant principalement de la coalescence des porosités de plus petite taille ayant diffusées par les JdGs. Dans le cas des porosités situées à l'intérieur des grains (Fig. 4-6 (c)), elles gardent leur taille nanométrique et ne participent pas à la densification rétrograde.

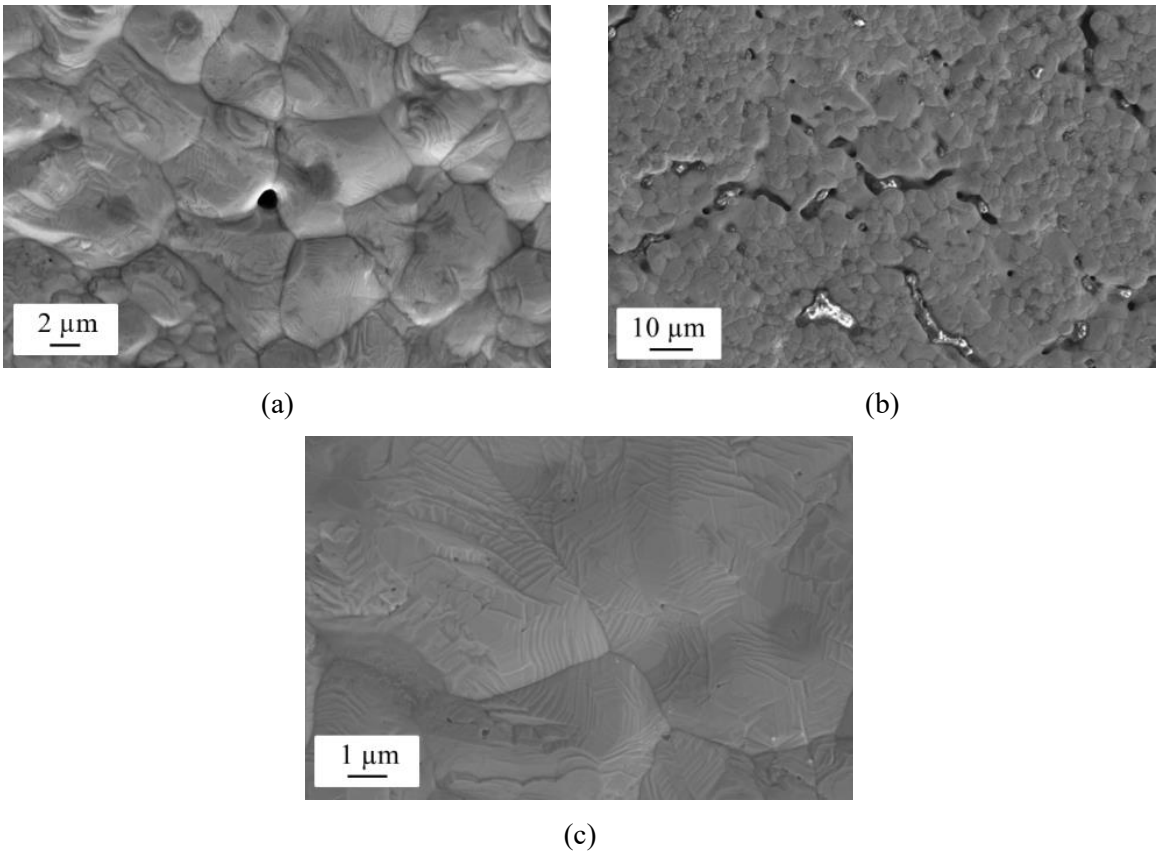

Fig. 4-6 Images MEB de la surface de l'échantillon S3 après recuit à 1173 K pendant 3 h, montrant un pore micrométrique situé sur un point triple (a), des chemins poreux continus (b) et des petites porosités nanométriques situées à l'intérieur des grains (c).

En ce qui concerne la stabilité de la microstructure, la taille de grains et la GBCD des trois échantillons sont stables jusqu'à 773 K. Néanmoins, une étude exhaustive de la stabilité thermique à des températures plus élevées et à des temps de recuit différents serait nécessaire pour compléter ces résultats.

5. CONCLUSIONS ET PERSPECTIVES

L'objectif de ce travail de thèse peut être divisé en trois parties. Une première partie consiste à explorer l'effet des paramètres de synthèse lors de la production de Ni FG/UFG préparé à partir de poudre modifiée par broyage et consolidée par SPS. Une seconde partie a pour objectif d'analyser l'effet de la taille des grains sur les propriétés mécaniques et les mécanismes d'écrouissage des échantillons élaborés par SPS. Enfin, une troisième partie étudie la diffusivité aux JdGs ainsi que la stabilité thermique à haute température.

Des échantillons de Ni UFG homogènes et sans oxydes ont été synthétisés à partir de poudres broyées. En maintenant une vitesse de broyage à moins de 350 rpm et le temps de broyage à moins de douze heures, différentes combinaisons de paramètres de broyage ont donné lieu à des échantillons de Ni avec une taille de grain comprise entre 0,69 et 1,1 µm avec peu ou pas de contamination, comme l'indiquent les mesures de DRX. Ces échantillons présentent des densités relatives supérieures à 95 % et une distribution de la nature des joints de grains (GBCD) dépendante de la taille de grains. Les structures de porosités rencontrées dans les échantillons préparés à partir de la poudre commerciale (S-PC) ou d'une poudre BM (S-PO) diffère en en taille, en morphologie et en emplacement. Des gros pores de forme irrégulière se retrouvent principalement dans les JdGs dans le cas de S-PC, et des petits pores géométriques situés principalement à l'intérieur des grains sont observés pour les échantillons S-P0. La GBCD des échantillons traités est caractérisée par une fraction de JdGs Σ3 élevée, qui diminue avec la taille de grain, et une fraction de LAGB faible, qui, à l'inverse, augmente avec la taille de grain. La distribution des angles de désorientation pour l'échantillon de plus petite taille de grain (S-P0) montre des caractéristiques intermédiaires par rapport aux échantillons traités exclusivement par SPD ou par SPS. Elle présente un pic aux angles de faibles désorientations et un autre pic aux angles de désorientations élevées. Enfin, un état initial de faibles contraintes internes est à signaler quelle que soit la poudre utilisée (commerciale ou BM), comme le montrent des analyses GOS obtenues par EBSD et des observations au MET.

Dans le but d'étudier exclusivement l'effet de la taille des grains dans la gamme FG/UFG sur les propriétés mécaniques, les conditions de synthèse (conditions de BM) ont été sélectionnées pour produire des échantillons avec des GBCD aussi proches que possible. Malgré un faible pourcentage de porosités, les échantillons préparés par SPS présentaient un allongement uniforme supérieur à 30 % dans tous les cas, ainsi qu'une résistance mécanique élevée. La combinaison de ces deux caractéristiques peut être observée à travers une bonne ténacité, spécialement pour les échantillons UFG, qui dépasse de loin les valeurs obtenues pour des échantillons préparés par SPD.

Une déviation de la limite d'élasticité par rapport à la relation HP a été décrite pour les échantillons UFG, ce qui est probablement la conséquence d'une déformation hétérogène. Cette déviation persiste à des niveaux de déformation plus élevés, ce qui soulève de nouvelles questions. La déformation hétérogène persiste-t-elle dans le domaine plastique ? L'origine du durcissement supplémentaire à des niveaux de déformation plus élevés est-il dû à d'autres caractéristiques de la microstructure ? Une évolution de l'écrouissage avec une taille de grain décroissante est observée vers des valeurs plus faibles du taux de durcissement normalisé, en particulier dans la gamme des UFG. Ainsi, le deuxième stade d'écrouissage est presque inexistant. Les recherches concernant l'état déformé des échantillons confirment l'absence de cellule de dislocations dans les échantillons UFG, ce qui suggère un glissement dévié généralisé ainsi qu'une annihilation précoce des dislocations dans le domaine plastique.

Les expériences de diffusion conçues pour étudier la diffusion aux JdGs ont permis de mieux comprendre la complexité des chemins de diffusion dans les échantillons de Ni préparés par SPS. Une diffusivité élevée a été observée pour tous les échantillons malgré des caractéristiques microstructurales différentes. Des profils de pénétration très variés indiquent une hiérarchie différente des voies de diffusion rapide pour chaque échantillon. La caractéristique ayant le plus grand impact sur la diffusion semble être la présence de différentes structures de porosités. Contrairement à des échantillons de Ni UFG préparés par d'autres techniques, une bonne stabilité microstructurale a été observée dans cette étude jusqu'à 773 K. Néanmoins pour l'échantillon présentant la plus petite taille de grain (S3), l'évolution de la localisation et de la taille des pores à basse température suggère une structure de porosité instable. Ce résultat est en corrélation avec le phénomène de densification rétrograde à haute température, observé exclusivement pour les échantillons faits à partir de poudres broyées qui présentent des porosités fermées. Indépendamment du faible impact de la porosité initiale sur les propriétés mécaniques, l'évolution des structures de porosités pourrait avoir un impact majeur sur la résistance mécanique et la ductilité.

L'ensemble de ces résultats montre que la nanostructuration des poudres par BM et la consolidation par SPS représentent une combinaison prometteuse pour produire du Ni UFG. Par rapport à d'autres techniques utilisées pour la synthèse des métaux UFG, cette méthode présente à la fois des avantages, tels qu'une bonne ductilité et une bonne stabilité microstructurale, et des inconvénients, tels qu'une limite d'élasticité plus basse et des structures de porosités complexes. Ainsi, choisir la métallurgie des poudres plutôt que la déformation plastique sévère dépendra des propriétés recherchées pour un matériau donné. Enfin, de nombreuses questions restent ouvertes pour de futures recherches. Il serait intéressant d'étudier les processus de restauration et de recristallisation lors du frittage. Aussi, une étude détaillée sur les mécanismes d'écrouissage permettrait de clarifier les résultats présentés dans ce manuscrit. De plus, de nouvelles analyses de diffusion seraient les bienvenues pour vérifier que le Ni UFG élaboré en combinant BM et SPS présente bien des JdGs de diffusivité ultra-rapide. Enfin, différents métaux et

alliages ainsi que d'autres propriétés telles les propriétés mécaniques à haute température, la diffusion aux JdGs dans d'autres régimes de diffusion ou le comportement à la corrosion des matériaux UFG pourraient être abordées..

6. RÉFÉRENCES BIBLIOGRAPHIQUES

[1] M. Suarez, A. Fernandez, J.L. Menendez, R. Torrecillas, H. U., J. Hennicke, R. Kirchner, T. Kessel, Challenges and Opportunities for Spark Plasma Sintering: A Key Technology for a New Generation of Materials, in: B. Ertug (Ed.), Sinter. Appl., InTech, 2013.

[2] C. Estournes, C. Maniere, L. Durand, Use of a deformable interface for the production of complex parts, WO2017/077028 A1, n.d.

[3] P. Ramakrishnan, History of powder metallurgy, Indian J. Hist. Sci. 18 (1983) 109–114.

[4] D.A. Levina, L.I. Chernyshev, N.V. Mikhailovskaya, Contemporary powder metallurgy: Achievements and problems, Powder Metall. Met. Ceram. 46 (2007) 202–205.

[5] L.A. Dobrzański, Goals and Contemporary Position of Powder Metallurgy, in: Powder Metall. - Fundam. Case Stud., 2017.

[6] W.B. James, Powder Metallurgy Methods and Applications, ASM Handb. Powder Metall. 7 (2015).

[7] T. Sekiguchi, K. Ono, H. Fujiwara, K. Ameyama, New Microstructure Design for Commercially Pure Titanium with Outstanding Mechanical Properties by Mechanical Milling and Hot Roll Sintering, Mater. Trans. 51 (2010) 39–45.

[8] Z. Zhang, D. Orlov, S.K. Vajpai, B. Tong, K. Ameyama, Importance of Bimodal Structure Topology in the Control of Mechanical Properties of a Stainless Steel, Adv. Eng. Mater. 17 (2015) 791–795.

[9] C. Sawangrat, O. Yamaguchi, S.K. Vajpai, K. Ameyama, Application of Harmonic Structure Design to Biomedical Co-Cr-Mo Alloy for imrpoved Mechanical Properties, Mater. Trans. 55 (2014) 99–105.

[10] J.M. Torralba, 3.11 - Improvement of Mechanical and Physical Properties in Powder Metallurgy, in: Compr. Mater. Process., Elsevier, 2014: pp. 281–293.

[11] M.A. Bousnina, A. dakhlaoui Omrani, F. Schoenstein, P. Madec, H. Haddadi, L.S. Smiri, N. Jouini, Spark plasma sintering and hot isostatic pressing of nickel nanopowders elaborated by a modified polyol process and their microstructure, magnetic and mechanical characterization, J. Alloys Compd. 504 (2010) S323–S327.

[12] J. Gubicza, H.-Q. Bui, F. Fellah, G.F. Dirras, Microstructure and mechanical behavior of ultrafine-grained Ni processed by different powder metallurgy methods, J. Mater. Res. 24 (2009) 217–226.

[13] Q.H. Bui, G. Dirras, S. Ramtani, J. Gubicza, On the strengthening behavior of ultrafine-grained nickel processed from nanopowders, Mater. Sci. Eng. A. 527 (2010) 3227–3235.

[14] J.K. Mackenzie, Second paper on statistics associated with the random disorientation of cubes, Biometrika. 45 (1958) 229–240.

[15] E.O. Hall, The deformation and ageing of mild steel: III discussion of results, Proc. Phys. Soc. Sect. B. 64 (1951) 747.

[16] A. Considère, Mémoire sur l'emploi du fer et de l'acier dans les constructions, Ann. Ponts Chaussées. IX (1885) 574–775.

[17] U.F. Kocks, H. Mecking, Physics and phenomenology of strain hardening: the FCC case, Prog. Mater. Sci. 48 (2003) 171–273.

[18] H. Mecking, U.F. Kocks, Kinetics of flow and strain-hardening, Acta Metall. 29 (1981) 1865–1875.

[19] D. Kuhlmann-Wilsdorf, Theory of plastic deformation:-properties of low energy dislocation structures, Mater. Sci. Eng. A. 113 (1989) 1–41.

[20] Y. Zhao, T. Topping, J.F. Bingert, J.J. Thornton, A.M. Dangelewicz, Y. Li, W. Liu, Y. Zhu, Y. Zhou, E.J. Lavernia, High Tensile Ductility and Strength in Bulk Nanostructured Nickel, Adv. Mater. 20 (2008) 3028–3033.

[21] P. Heitjans, J. Kärger, eds., Diffusion in Condensed Matter, Springer-Verlag Berlin Heidelberg, 2005.

[22] S.V. Divinski, G. Reglitz, I.S. Golovin, M. Peterlechner, R. Lapovok, Y. Estrin, G. Wilde, Effect of heat treatment on diffusion, internal friction, microstructure and mechanical properties of ultra-fine-grained nickel severely deformed by equal-channel angular pressing, Acta Mater. 82 (2015) 11–21.

[23] D. Prokoshkina, L. Klinger, A. Moros, G. Wilde, E. Rabkin, S.V. Divinski, Effect of recrystallization on diffusion in ultrafine-grained Ni, Acta Mater. 69 (2014) 314–325.

[24] A.A. Nazarov, A.E. Romanov, R.Z. Valiev, Models of the defect structure and analysis of the mechanical behavior of nanocrystals, Nanostructured Mater. 6 (1995) 775–778.

[25] S. Poulat, B. Décamps, L. Priester, In-situ transmission electron microscopy study of the accomodation in [101] tilt grain boundaries in nickel bicrystals, Philos. Mag. A. 79 (1999) 2655–2680.

[26] S.V. Divinski, Grain Boundary Diffusion in Severely Deformed Metals: State of the Art and Unresolved Issues, Diffus. Found. 5 (2015) 57–73.

[27] S.V. Divinski, F. Hisker, Y.S. Kang, J.S. Lee, C. Herzig, 59Fe Grain boundary diffusion in nanostructured γ-Fe-Ni, Z Met. 93 (2002) 265–272.

Ultrafine grained Ni processed by powder metallurgy: microstructure, mechanical properties and thermal stability

Abstract

The present manuscript concerns the synthesis of ultrafine grained (UFG) Ni by powder metallurgy, and the study of the influence of UFG microstructures on the mechanical behavior and physical properties. The possibilities of coupling ball milling and Spark Plasma Sintering are presented showing promising results. Highly dense homogeneous specimens are obtained, with average grain sizes d = 0.65 - 4 µm, and microstructures highlighted by a high fraction of Σ3 grain boundaries dependent on grain size. The mechanical properties in tensile testing for UFG samples are evaluated showing a good combination of strength and ductility, with little impact from porosities, the major drawback of powder metallurgy. The influence of grain size in the UFG regime on the mechanical properties is investigated, showing strength values that deviate from the expected behavior for grain refinement. Likewise, a reduced strain hardening capacity is depicted which correlates to the microstructural observations performed on the deformed state. High diffusivity measured by means of radiotracer experiments is observed in the sintered samples, displaying different penetration profiles that relate to diverse porosity structures. Such structures are also responsible for retrograde sintering observed exclusively in samples processed from BM powders.

Key words: Ultrafine grained metals, nickel, microstructural characterization, mechanical properties, grain boundary diffusion, thermal stability.

Nickel à grains ultrafins : microstructure, propriétés mécaniques et stabilité thermique

Résumé

La synthèse par métallurgie des poudres de nickel à grains ultrafins (UFG) a été effectuée, et l'effet de l'affinement de la microstructure sur le comportement mécanique et les propriétés physiques a été étudié. La possibilité de coupler le broyage et le frittage flash est étudiée avec des résultats prometteurs. Des échantillons de haute densité avec des tailles de grains d = 0.65 – 4 µm, caractérisés par une fraction élevée des joints de grains Σ3 et un faible niveau de contrainte ont été synthétisés. Les propriétés mécaniques des échantillons UFG montrent une bonne combinaison ductilité-résistance mécanique, avec un impact mineur des porosités présentes. L'étude de l'influence de la taille de grain dans le régime UFG sur les propriétés mécaniques montre une limite d'élasticité supérieure à celle attendue et une capacité d'écrouissage plus faible. Ces observations sont cohérentes avec la microstructure déformée à rupture, étudiée par diffraction d'électrons rétrodiffusés et microscopie électronique en transmission. Une haute diffusivité, mesurée par des expériences de traceurs radioactifs, montrent des profils de pénétration très différents liés aux structures de porosités diverses présents dans les échantillons. Ces différentes structures sont aussi responsables de la densification rétrograde observée, uniquement pour les échantillons frittés à partir de poudres broyées.

Mots clés: métaux à grains ultrafins, nickel, caractérisation microstructurale, propriétés mécaniques, diffusion aux joints de grain, stabilité thermique.